UNIVERSITÉ DE LILLE

THÈSE DOCTORALE

Caratérisation du contenu modal et de l'amplification dans les fibres optiques légèrement multimode

Auteur:
Jean YAMMINE

Directeurs:
Laurent BIGOT
Esben RAVN ANDRESEN

Une thèse soumise dans le cadre des conditions d'obtention
du diplôme de Docteur en Physique

PhLAM Laboratory

Novembre 8, 2019

Jury:

Président:	Y. QUIQUEMPOIS - Université de Lille
Rapporteur:	V. KERMENE - Université de Limoge
Rapporteur:	H. RIGNEAULT - Université de Aix-Marseille
Examinateur:	S. POPOFF - ESPCI
Examinateur:	M. BIGOT-ASTRUC - Prysmian Group
Directeur:	Esben Ravn ANDRESEN - Université de Lille
Directeur:	Laurent BIGOT - Université de Lille

UNIVERSITY OF LILLE

DOCTORAL THESIS

Characterization of modal content and amplification in few-mode optical fibers

Author:
Jean YAMMINE

Supervisors:
Laurent BIGOT
Esben RAVN ANDRESEN

A thesis submitted in fulfillment of the requirements
for the degree of Doctor of Physics

in the

PhLAM Laboratory

November 8, 2019

Jury:

President: Y. QUIQUEMPOIS - University of Lille

Referee: V. KERMENE - University of Limoge
Referee: H. RIGNEAULT - University of Aix-Marseille

Examiner: S. POPOFF - ESPCI
Examiner: M. BIGOT-ASTRUC - Prysmian Group

Supervisor: Esben Ravn ANDRESEN - University of Lille
Supervisor: Laurent BIGOT - University of Lille

Declaration of Authorship

I, Jean YAMMINE, declare that this thesis titled, "Characterization of modal content and amplification in few-mode optical fibers" and the work presented in it are my own. I confirm that:

- This work was done wholly or mainly while in candidature for a research degree at this University.
- Where any part of this thesis has previously been submitted for a degree or any other qualification at this University or any other institution, this has been clearly stated.
- Where I have consulted the published work of others, this is always clearly attributed.
- Where I have quoted from the work of others, the source is always given. With the exception of such quotations, this thesis is entirely my own work.
- I have acknowledged all main sources of help.
- Where the thesis is based on work done by myself jointly with others, I have made clear exactly what was done by others and what I have contributed myself.

Signed: Jean YAMMINE

Date: 08 November 2019

"Nous sommes comme les noix, Nous devons être brisés pour être découverts."

Gibran Khalil Gibran

UNIVERSITY OF LILLE

Abstract

PhLAM Laboratory

Doctor of Physics

Characterization of modal content and amplification in few-mode optical fibers

by Jean YAMMINE

Over the last few decades, the demand for data rate has increased rapidly in order to meet the social and economic needs of our society based on the massive exchange of information. In the near future, current telecommunications systems based on single-mode optical fibers will face difficulties in meeting this ever-increasing demand. In fact, despite the use of all the physical dimensions characterizing a guided wave in an optical fiber, the latter is approaching its fundamental limits, leading to what is known as "capacity crunch". In this context, new transmission systems are the subject of much research, based on the development of multi-core fibers or multi-mode fibers. These new types of fibers give access to an additional physical dimension, through the different open spatial channels (cores or modes). By using this spatial division multiplexing approach, these new systems can be used to exceed the announced saturation. However, different components of the transmission network must be developed and adapted for experimental use with this type of system. Among the aspects that require particular attention are the analysis of the modal content of multi-mode fibers and the optimization of the amplification process of the different co-existing beams in a multi-mode guide. The aim of this thesis was to contribute to the development of these two knowledges. In this work, we have demonstrated that the modal content of a few-mode fiber can be measured experimentally using the reconstruction of the fiber transmission matrix. This detection method has been used to characterize not only few-mode fibers with step index profiles, but also specialty fibers with ring cores supporting OAM modes. We also studied the temporal evolution of the different channels of the transmission matrix and developed an empirical model to predict this variation. We were also interested in the amplification process of a multi-modal transmission, so, during this thesis, new geometries of few-mode erbium-doped fibers were proposed for different applications: an annular core model capable of providing an equalized and flat gain for 26 spatial modes with a very low gain excursion was studied, as well as a ring-shaped doped step index fiber, capable of also amplifying ring modes. We have also introduced a ring-shaped doped step index fiber that can directly compensate for mode propagation losses in the line fiber.

UNIVERSITY OF LILLE

Abstract

PhLAM Laboratory

Doctor of Physics

Characterization of modal content and amplification in few-mode optical fibers

by Jean YAMMINE

Au cours des dernières décennies, la demande de débit de données a augmenté rapidement afin d'accompagner les besoins sociétaux et économiques de notre société basée sur l'échange massif d'information. Les systèmes de télécommunication actuels basés sur la fibre optique monomode vont dans un avenir proche rencontrer des difficultés pour répondre à cette demande sans arrêt grandissante. En effet, malgré l'exploitation de la totalité des dimensions physiques caractérisant une onde guidée dans une fibre optique, cette dernière se rapproche de ses limites fondamentales, conduisant à ce qui est connu sous le nom de « capacity crunch ». Dans ce contexte, les nouveaux systèmes de transmission font l'objet de nombreuses recherches, basées sur le développement de fibres multi-cœur ou de fibre multimodes. Ces nouveaux types de fibres donnent accès à une dimension physique supplémentaire, à travers les différents canaux spatiaux ouverts (cœurs ou modes). En utilisant cette approche de multiplexage spatial, ces nouveaux dispositifs peuvent être utilisés pour surpasser la saturation annoncée. Cependant, différentes composantes du réseau de transmission doivent être développées et adaptées afin d'être utilisées expérimentalement avec ce type de systèmes. Parmi les aspects qui demandent une attention particulière, on trouve l'analyse du contenu modal des fibres multimodes ou encore l'optimisation du processus d'amplification de différents faisceaux coexistant dans un guide multimode. Le but de cette thèse était de contribuer au développement de ces deux connaissances. Au cours de ce travail, nous avons démontré que le contenu modal d'une fibre légèrement multimode peut être mesuré expérimentalement en utilisant la reconstruction de la matrice de transmission de la fibre. Cette méthode de détection a été utilisée pour caractériser non seulement des fibres légèrement multimodes à saut d'indice, mais aussi des fibres de spécialité ayant des cœurs annulaires et supportant des modes OAM. Nous avons également étudié l'évolution temporelle des différents canaux de la matrice de transmission et développé un modèle empirique qui permet de prédire cette variation. Nous nous sommes également intéressés au processus d'amplification d'une transmission multimodale, ainsi, au cours de cette thèse, de nouvelles géométries de fibres dopées à l'erbium légèrement multimodes ont été proposées pour différentes applications : un modèle à cœur annulaire capable d'offrir un gain égalisé et plat pour 26 modes spatiaux avec une excursion de gain très faible a été étudié, de même qu'une fibre à saut d'indice dopée en forme d'anneau, capable d'amplifier également des modes annulaires. Nous avons également introduit une fibre à saut d'indice dopée en anneau qui peut compenser directement les pertes de propagation des modes dans la fibre de ligne.

Acknowledgements

Firstly, I would like to thank the members of my thesis committee: the president Mr. Yves QUIQUEMPOIS, the referees Mr. Herve RIGNEAULT and Mr. Vincent KERMENE, the examiners Mrs. Marianne BIGOT-ASTRUC and Mr. Sebastian POPOFF for accepting this role and dedicating their time in order to evaluate my thesis works. I am also thankful for their insightful comments and interesting questions which helped to see my work through other perspectives and widen my scientific point of view.

I would like to thank the director of this thesis Mr. Laurent BIGOT. I could have never chosen a better mentor to help me in my transition from a student to a researcher. Your motivation, patience (specially writing this manuscript) and wisdom helped me throughout the past 3 years and pushed me to breach limits I did not even know that I can reach. I will forever appreciate your impact on me as your Ph.D student as well as a person. Thank you for all the time you dedicated for me, even on weekends and off days, you were always available to me when I needed.

I would like to thank my supervisor Mr. Esben Ravn ANDRESEN, the genius that shaped and formed this thesis. Working with such an endless source of innovative ideas is the best thing a Ph.D student can ever wish for. Thank you for all that knowledge you helped me acquire and for all the time you passed in the laboratory room with me. I am sure that your future students will be as lucky as I was to work with you.

I would like to also mention and thank all the members of the PhLAM Photonics team at the IRCICA research institute. Being in a such friendly team helped me fit in and feel like I belong to this group. Thank you to all the other Ph.D students, especially Arsene Tandje with whom I worked on several topics, as well as the engineers and the researchers, especially the ones who contributed heavily in my work, notably Monica BOUET, Olivier VANVINCQ, Damien LABAT, Arnaud COTTERET and Stephane PLUS. Your contribution made my job so much easier.

Thanks to Guillaume LE COCQ and Jean-Baptiste TRINEL, the Ph.D students who laid the foundations for my thesis. Thank you for all the knowledge you passed to me even in the short period of time that we had together as labmates. I could never put into words how thankful I am, especially to Guillaume. Because of you I adapted to my new environment and I tried my best each and every day to reach that bar of expectation for a Ph.D student you set so high and far from a normal case. You being an idol for me was a major reason behind this work.

I would like to also thank my family: my parents Mireille and Chawky, my brother Georges and my two sisters Marie and Jessica. You supported me spiritually and mentally throughout this whole journey. Being able to see the look in your eyes during the Ph.D defense kept me calm and composed. Special thanks for my special Marie for being by my side during the redaction process. You made it easier than it must have been.

Last but certainly not least, I want to thank the person who start it all, my lovely Elsy. It was you who brought the very best of me and pushed me to potentials I could never reach without you. You were always there for me. Even in my lowest, you believed in me and you made me believe in myself. Thank you for your endless love, trust and support. I could not have done it without you.

Contents

List of Figures

List of Tables

List of Abbreviations

ASE	**A**mplified **S**pontaneous **E**mission
BS	**B**eam **S**plitter
CCD	**C**harge **C**oupled **D**evice
DGD	**D**ifferential **G**roup **D**elay
DMG	**D**ifferential **M**odal **G**ain
DMGD	**D**ifferential **M**ode **G**roup **D**elay
DML	**D**ifferential **M**odal **L**oss
DSG	**D**ifferential **S**pectral **G**ain
EDFA	**E**rbium **D**opped **F**iber **A**mplifier
EDP	**E**rbium **D**oping **P**rofile
FIR	**F**inite **I**mpulse **R**esponse
FM-EDFA	**F**ew **M**ode **E**rbium **D**oped **F**iber **A**mplifiers
FMF	**F**ew **M**ode **F**iber
GDS	**G**roup **D**elay **S**pread
HOM	**H**igher **O**rder **M**ode
HWP	**H**alf **W**ave **P**late
ICA	**I**ndependent **C**omponent **A**nalysis
LP	**L**inearly **P**olarized
MCF	**M**ulti **C**ore **F**iber
MCVD	**M**odified **C**hemical **V**apor **D**eposition
MDM	**M**ode **D**ivision **M**ultiplexing
MIMO-DSP	**M**ultiple **I**nput **M**ultiple **O**utput - **D**igital **S**ignal **P**rocessing
MMF	**M**ulti **M**ode **F**iber
MOF	**M**icro-structured **O**ptical **F**iber
MPLC	**M**ulti **P**lane **L**ight **C**onversion
MTIR	**M**odified **T**otal **I**nternal **R**eflection
MZM	**M**ach **Z**ehnder **M**odulator
NA	**N**umerical **A**perture
NF	**N**oise **F**igure
OAM	**O**rbital **A**ngular **M**omentum
OSA	**O**ptical **S**pectrum **A**nalyzer
PBG	**P**hotonic **B**and **G**ap
PBS	**P**olarization **B**eam **S**plitter
PCA	**P**rincipal **C**omponent **A**nalysis
PCE	**P**ower **C**onversion **E**fficiency
PDM	**P**olarization **D**ivision **M**ultiplexing
PMD	**P**olarization **M**odal **D**ispersion
QWP	**Q**uarter **W**ave **P**late
RIP	**R**efractive **I**ndex **P**rofile
SALS	**S**mall **A**ngle **L**ight **S**cattering
SAM	**S**pin **A**ngular **M**omentum
SDM	**S**patial **D**ivision **M**ultiplexing
SDM	**S**egmented **D**eformable **M**irror

SLM	**S**patial **L**ight **M**odulator
SM	**S**cattering **M**atrix
SMF	**S**ingle **M**ode **F**iber
SNR	**S**ignal to **N**oise **R**atio
SPM	**S**elf **P**hase **M**odulation
SVD	**S**ingular **V**alue **D**ecomposition
TE	**T**ransverse **E**lectric
TIR	**T**otal **I**nternal **R**eflection
TM	**T**ransverse **M**agnetic
TM	**T**ransmission **M**atrix
VOA	**V**ariable **O**ptical **A**ttenuator
VNA	**V**ector **N**etwork **A**nalyser
WDM	**W**avelength **D**ivision **M**ultiplexing
XPM	**C**ross **P**hase **M**odulation

Introduction

For the last decades, data rate demand has been growing in order to support our information driven society and economy. Accordingly, optical telecommunication has been advancing rapidly for the purpose of supplying this demand. Present long-haul commercial transmission systems, based on the use of the single-mode fiber, are finding difficulty to match this ever-growing demand. Despite the exploitation of the totality of its physical dimensions (time, wavelength, polarization and phase), this fiber type cannot surpass an upcoming capacity saturation, or what is called the capacity crunch [Richardson, Fini, and Nelson, 2013; Winzer, 2017]. Modern problems require modern solutions, so researchers all around the world are trying to develop new transmission systems, with another type of fiber at its core, offering an additional physical dimension in order to increase the transmission capacity. For that, the use of two fiber geometries is being investigated: the multi-core fiber and the multi-mode fiber. These types of fibers are considered to be the solution for the limited capabilities of the single-mode fiber, as they offer a fifth encoding dimension: the spatial dimension. These new systems offer to multiply the capacity by the number of their supported channels. As a simple approximation, a few-mode fiber guiding 10 modes offers the same transmission rate as 10 single-mode fibers. This technology is better known as the modal division multiplexing as the different modes of the few-mode fiber will act as independent transmission channels. However, modal division multiplexing systems are more challenging than this straightforward approximation. 2 major factors increase the difficulties facing this technology: the mode coupling and the amplification.

In order to use each mode as a separate channel, the information must be injected on its respective mode exclusively. Thus, selective excitation method of each mode is needed. In addition, during their propagation through the fiber, the different modes can couple for a variety of reasons. Each mode carrying its proper information, the mode mixing can be viewed as noise at the receiving end of the transmission, with different levels from a slight negligible noise to the loss of the entire information, depending on the coupling levels. Therefore, it is also mandatory to have a modal detection method in order to differentiate the mode signals.
The fact that this technology requires the use of the few-mode fiber instead of the single-mode one means that the fiber amplifiers used in the old systems must be replaced by new fiber designs adapted to the new systems. Thus, the new fiber amplifiers need to have the same properties as the old ones in addition to the ability of delivering an equal gain for all the spatial modes so the information can reach the end of a long distance transmission without losing any part during the propagation.

This thesis is founded on the study of these two major factors of the modal division multiplexing. This work has been partially supported by the Agence Nationale de la Recherche through the LABEX CEMPI (ANR-11-LABX-0007) and the

Equipex Flux (ANR-11-EQPX-0017), as well as by the Ministry of Higher Education and Research, Hauts de France council and European Regional Development Fund (ERDF) through the Contrat de Projets Etat-Region (CPER Photonics for Society P4S). Finally, we acknowledge financing from the project Fonds Unique Interministriel through FUI MODAL (FUI-AAP19), which includes multiple leaders on this research topic: Draka-Prysmian group, Nokia Bell labs France, CAILabs and our team from the PHLAM laboratory of the university of Lille, our team being based at the IRCICA institute. This thesis started at the second part of this project, so it is considered as the continuity of the previous works of our team on these topics, more specifically on the amplification axis. Further, this thesis proposed a new approach to the mode characterization axis in addition to other works already developed by our team members.

In this manuscript, we will discuss our works on both axes. We will start with an overview of the basic notions and theories required to comprehend our works in the first chapter. We will also situate our works more specifically in the large context of the modal division multiplexing. In the second chapter, we will be reviewing some of the already developed methods in order to characterize the modal content of a few-mode fiber. Further, we will describe our method in substantial details. The third chapter is dedicated to the different results obtained by our method on several fiber geometries. In the fourth chapter, we will showcase the continuity of the works of our previous team members on few-mode amplification. In addition to that, we will propose several new fiber amplifier designs that can be used for multiple applications. This chapter is supported by an appendix for better understanding of the used codes.

Chapter 1

Generalities

1.1 Introduction

During this chapter, the notions necessary for a good understanding of this manuscript will be presented. We will present these concepts successively, starting from the most general considerations of the light guiding mechanism in an optical fiber, to the different mode basis that can describe this guidance. We further show the great relationship between the optical fibers and the telecommunication world, describing some key components as the fiber amplifiers and ending this chapter with the limitations of today's fiber-based telecommunication systems and the upcoming capacity crunch which fueled a whole research domain in which this thesis takes part.

1.2 Light propagation

The basic function of any optical fiber is to guide light: light injected into one end should stay in the fiber until it emerges from the other side. In other words, it must be prevented from getting lost by reaching the outer surface and escaping there. This section is dedicated to describe basics of the guiding mechanisms in optical fibers.

1.2.1 Guiding mechanisms

Total internal reflection.

Light is an electromagnetic radiation wave formed by the association of an electric field, $\vec{E}$, and a magnetic field, $\vec{H}$. In an infinite homogeneous medium, these waves, in monochromatic cases, are considered as sinusoids, having frequencies defined by:

$$\omega = \frac{2\pi c}{\lambda} \tag{1.1}$$

where c is the speed of light in the vacuum and λ is the light's wavelength. Using Maxwell's equations, we arrive to the following Helmholtz equation [Jacquier, 2012]:

$$\vec{\nabla} \wedge \left(\frac{\vec{1}}{\varepsilon(\vec{r})} \nabla \wedge \vec{H} \right) = \left(\frac{\omega}{c} \right)^2 \cdot \vec{H} \tag{1.2}$$

$\varepsilon(\vec{r})$ represents the dielectric permittivity of the environment. If the considered medium is a non-magnetic one, the solution of this equation is:

$$\vec{H}(\vec{r},t) = \vec{h_0} \cdot e^{-i(\omega \cdot t - \vec{k} \cdot \vec{r})} \tag{1.3}$$

h_0 is the complex amplitude of the wave and $\vec{k}$ is the wave vector in a medium having a refractive index n defined as $k = n \cdot \omega / c$. If Oz is the axis of the propagation direction, the projection of the wave vector on this axis will be:

$$\beta = k_z = k \cdot \cos(\theta) \tag{1.4}$$

β is known as the propagation constant and θ is the angle between the wave propagation axis and the Oz axis. We can define the effective index n_{eff}: it is the refractive index encountered by the light while propagating in the direction of Oz as described in Figure 1.1:

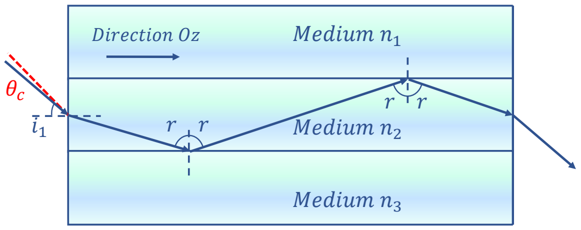

FIGURE 1.1: Description of the Total Internal Reflection (TIR) in a waveguide.

According to Equation 1.4, we define the condition for a wave to propagate in a homogeneous medium: the effective index of the wave must always be smaller than the refractive index of the guiding medium:

$$0 \leq n_{\text{eff}} \leq n \qquad for \quad 0 \leq \theta \leq \pi/2 \tag{1.5}$$

When the light propagating in a medium with a refractive index n_2 reaches an interface with a medium having a refractive index n_1 or n_3 , with $n_1 < n_2$ and $n_3 < n_2$, the light beam undergoes a total reflection if its incidence angle i exceeds a limit value i_{co} for which we have:

$$\sin(i_{\text{co}}) = n_1/n_2 \tag{1.6}$$

If we can arrange for a light beam in the middle of the index n_2 to be incident on the interface between the two media with an angle of incidence $i > i_{\text{co}}$, the light beam undergoes a total reflection and remains confined in the medium of index n_2: the principle of this light guidance is known as the phenomenon of total internal reflection (TIR).

A conventional optical fiber is a structure of the form mentioned above: a central medium with a refractive index n_{co} represents the confining region called "core". This medium is surrounded by a medium called "cladding", with a refractive index n_{cl}, with $n_{\text{cl}} < n_{\text{co}}$. For light guidance to be possible, the conditions that

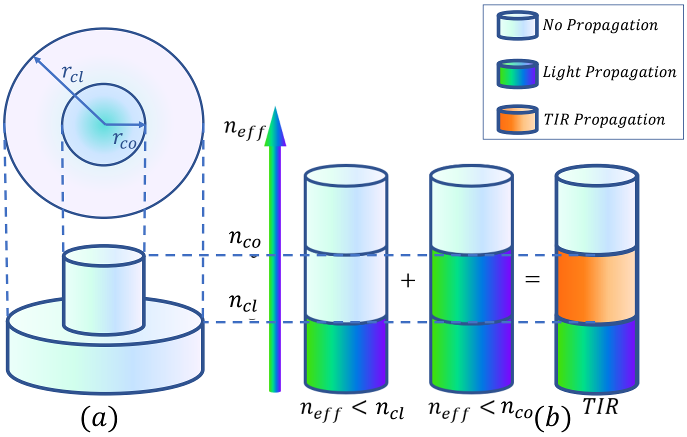

FIGURE 1.2: (a) Conventional optical fiber structure with a r_{co} core radius and a r_{cl} cladding radius.(b) Effective index diagram of a light beam inside a conventional optical fiber.

ensure full internal reflection must be met. Figure 1.2 shows the propagation conditions for a light beam in mediums with refractive index n_{cl} and n_{co}. The light beam can be guided within a conventional optical fiber if its propagation is possible in the core but not in the cladding, thus its effective index satisfies the following condition:

$$n_{\mathrm{cl}} \leq n_{\mathrm{eff}} \leq n_{\mathrm{co}} \tag{1.7}$$

In addition, a light beam can be injected into an optical fiber if its coupling angle at the air-core interface is less than a defined value θ_{co}:

$$\sin(\theta_{\mathrm{co}}) = n_{\mathrm{co}} \cos(i_{\mathrm{co}}) = n_{\mathrm{co}} \sqrt{1 - \sin^2(i_{\mathrm{co}})} \tag{1.8}$$

These conditions provide TIR guidance. If $n_{\mathrm{eff}} \leq n_{\mathrm{cl}}$, the light spreads into the cladding and the confinement is lost.

The light guiding capacity of an optical fiber is characterized by the numerical aperture (NA) of the fiber. A higher NA means the fiber can couple more light:

$$NA = \sin(\theta_{\mathrm{co}}) = \sqrt{n_{\mathrm{co}}^2 - n_{\mathrm{cl}}^2} \tag{1.9}$$

Modified total internal reflection.

In the previous section, we considered a conventional fiber with an uniform core refractive index n_{co} and an uniform cladding refractive index n_{cl}. In this section, we are interested in the propagation of a light wave in a structured medium with a refractive index n_1 in which inclusions with refractive index n_2 are integrated periodically. To clarify things, Figure 1.3 shows an optical fiber with a micro-structured cladding: such fibers are known as micro-structured optical fibers (MOF). The effective index of the fundamental mode of the cladding is called n_{fsm}. It is wavelength-dependent. At long wavelengths, it can also be seen as the surface average of the inclusions of refractive index n_2 and of the background medium of refractive index n_1. The core index is equivalent to the index of the host structure, n_1, and Equation 1.7 then becomes:

$$n_{\text{fsm}} \leq n_{\text{eff}} \leq n_1 \tag{1.10}$$

The mode is guided in a similar way to the TIR, hence the origin of the name modified total internal reflection (MTIR). We must mention that MOF having inclusions with refractive index higher that the index of the host structure do exist. Such fibers prohibite the light guiding for some specific wavelengths via a so-called photonic band gaps (PBG) effect. We will limit this mention just here and will not dig deep into the details of this guidance regime for the sake of simplicity of the manuscript and because we will not be using this regime in all the steps conducted during this work.

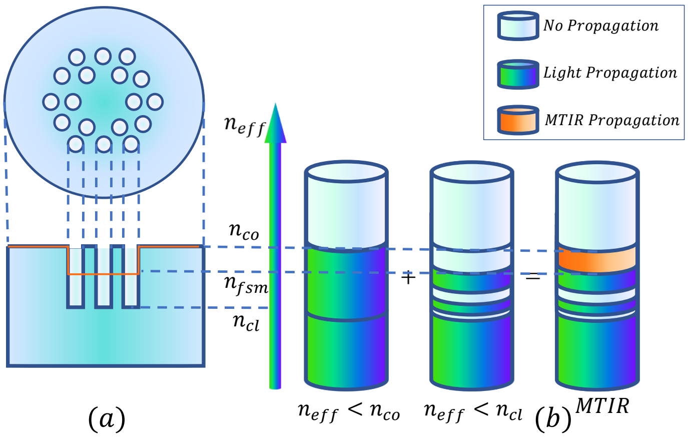

FIGURE 1.3: (a) Conventional optical fiber structure with a r_{co} core radius and a r_{cl} cladding radius.(b) Effective index diagram of a light beam inside a conventional optical fiber.

1.2.2 Propagation modes: Vector modes.

In the previous section, we saw that the guidance of light in an optical fiber must satisfy the conditions of TIR obtained using geometrical optics approach. It can be also considered that, when light is reflected on the core-cladding interface, the wave interferes with itself. Only the beams verifying the constructive inferference condition are then guided: these are the transversal modes [Bures, 2009; Yariv, 1997].

Eigenvalues equation

As mentioned in the previous section, light is an electromagnetic wave. An optical beam can be described as a sum of a group of monochromatic waves, however for simplicity, we will consider it as a monochromatic wave in the following section, with a frequency ω defined by the Equation 1.1. The electric field $\vec{E}$ and the magnetic field $\vec{H}$ of such a wave are given by the following equations:

$$\vec{E}(\vec{r},t) = \vec{E}(r,\theta,z)e^{-i\omega t} \tag{1.11}$$

$$\vec{H}(\vec{r},t) = \vec{H}(r,\theta,z)e^{-i\omega t} \tag{1.12}$$

From Maxwell's equations, we can develop the following system of equations based on $\vec{E}$ and $\vec{H}$, in the case of a dielectric where the surface density of free charges and the current density vector are null:

$$\vec{\nabla} \times \vec{E} = -\mu_0 \frac{\partial \vec{H}}{\partial t} \tag{1.13}$$

$$\vec{\nabla} \cdot \epsilon_0 n^2 \vec{E} = 0 \tag{1.14}$$

$$\vec{\nabla} \times \vec{H} = \epsilon_0 n^2 \frac{\partial \vec{E}}{\partial t} \tag{1.15}$$

$$\vec{\nabla} \cdot \mu_0 \vec{H} = 0 \tag{1.16}$$

μ is the magnetic permeability, ϵ is the electric permittivity and the index $_0$ is used to reference the physical variables of the vacuum. Using this equation system, and the fact the frequency can be defined as $\omega = k/\sqrt{\mu\epsilon}$, we can write :

$$\vec{\nabla} \times \vec{E} = i\sqrt{\frac{\mu_0}{\epsilon_0}} k\vec{H} \tag{1.17}$$

$$\vec{\nabla} \times \vec{H} = -i\sqrt{\frac{\epsilon_0}{\mu_0}} kn\vec{E} \tag{1.18}$$

In a fiber similar to the one described in Figure 1.2, we can introduce the parameters U,W and the normalized frequency V as :

$$U^2 = r_{\mathrm{co}}^2(k_0^2 n_{\mathrm{co}}^2 - \beta^2) = r_c^2 k_0^2 (n_{\mathrm{co}}^2 - n_{\mathrm{eff}}^2) \tag{1.19}$$

$$W^2 = r_c^2(\beta^2 - k_0^2 n_{\mathrm{cl}}^2) = r_c^2 k_0^2 (n_{\mathrm{eff}}^2 - n_{\mathrm{cl}}^2) \tag{1.20}$$

$$V = \sqrt{U^2 + W^2} = r_{\mathrm{co}} k_0 \sqrt{n_{\mathrm{co}}^2 - n_{\mathrm{cl}}^2} \tag{1.21}$$

where the wave vector of free space is given by $k_0 = 2\pi/\lambda$. The normalized frequency V determines the number of guided modes and depends only on the opto-geometrical parameters of the fiber: the core refractive index, the cladding refractive index, the diameter of the core and the wavelength. The eigenvalues equation of the guided modes in a step index fiber is defined by:

$$(\nu n_{\mathrm{eff}})^2 \left(\frac{V}{UW}\right)^4 = \left(\frac{n_{\mathrm{co}}^2 J'_\nu(U)}{UJ_\nu(U)} + \frac{n_{\mathrm{cl}}^2 K'_\nu(W)}{WK_\nu(W)}\right) \cdot \left(\frac{J'_\nu(U)}{UJ_\nu(U)} + \frac{K'_\nu(W)}{WK_\nu(W)}\right) \tag{1.22}$$

where J'_ν is the derivative of the Bessel function J with respect to the argument U, and K'_ν is the derivative of the Bessel function K with respect to the argument W. The discrete solutions of this equation give values of U and W specific to each guided mode according to the fiber's parameters: n_{co}, n_{cl} and V.

TM and TE modes

The transverse and longitudinal components of the vector modes have specific values which are not zero. However, there are two groups of modes for which one of the two longitudinal components is zero: the transverse electric (TE) modes, with no electric field component in the direction of propagation, and the transverse magnetic (TM) modes, with no magnetic field component in the direction of propagation. These modes are obtained for $\nu = 0$. In such case, using the properties of Bessel's functions we can obtain :

$$J_0'(U) = -J_1(U) \quad \text{and} \quad K_0'(W) = -K_1(W) \tag{1.23}$$

and the eigenvalues Equation 1.24 for TE and TM modes:

$$\left(\frac{n_{\text{co}}^2 J_1(U)}{UJ_0(U)} + \frac{n_{\text{cl}}^2 K_1(W)}{WK_0(W)}\right) \cdot \left(\frac{J_1(U)}{UJ_0(U)} + \frac{K_1(W)}{WK_0(W)}\right) = 0 \tag{1.24}$$

The first part of the Equation 1.24 is the eigenvalues equation of the $\text{TM}_{0\text{m}}$ modes and the second part is the eigenvalues equation of the $\text{TE}_{0\text{m}}$ modes. The discrete solutions of these two equations give the modes increasing eigenvalues $U_{01}, U_{02}, ...U_{0\text{m}}$ corresponding to $\text{TM}_{0\text{m}}$ and $\text{TE}_{0\text{m}}$ modes. These modes have a circular symmetry in a step index fiber.

Hybrid modes HE and EH

The TE and TM modes are obtained if $\nu = 0$. If $\nu \neq 0$, the solutions of Equation 1.15 are obtained by applying the following variable changes:

$$x = \frac{J_\nu'(U)}{UJ_\nu(U)} \qquad c = \nu^2 n_{\text{eff}}^2 \frac{V^4}{(UW)^4} \qquad b = \frac{K_\nu'(W)}{WK_\nu(W)}$$

thereafter, the Equation 1.22 becomes:

$$n_{\text{co}}^2 x^2 + xb(n_{\text{co}}^2 + n_{\text{cl}}^2) + (n_{\text{cl}}^2 b^2 - c) = 0 \tag{1.25}$$

and its solution, while $n_{\text{cl}}^2 b^2 \ll c$, can be obtained by:

$$\Delta = [b(n_{\text{co}}^2 - n_{\text{cl}}^2)]^2 + 4n_{\text{co}}^2 c = 0 \tag{1.26}$$

$$x_\pm = \frac{-b}{2}\left(\frac{n_{\text{cl}}^2}{n_{\text{co}}^2} + 1\right) \pm \frac{1}{2}\sqrt{\left[b\left(-\frac{n_{\text{cl}}^2}{n_{\text{co}}^2} + 1\right)\right]^2 + \frac{4c}{n_{\text{co}}^2}} \tag{1.27}$$

The two solutions of this equation correspond to two different groups of hybrid modes HE_{lm} and EH_{lm}. All the components of the electric field e_{x}, e_{y} and e_{z} and the magnetic field h_{x}, h_{y} and h_{z} have non-zero values. The $-$ sign corresponds to HE modes and the $+$ sign to EH modes.

Mode cut-off

If we examine the asymptotic limits of the solutions calculated in the previous parts (the limit for $U \to V$ and the limit for $V \to \infty$), we find the cut-off frequencies V_c of the modes, the order of appearance of the modes and the n_{eff} values for a fixed V value. The HE_{11} mode exists always and it is called the fundamental mode. In order to obtain other guided modes, the value of the normalized frequency V must exceed the cut-off value V_c of each mode for it to exist: these are the higher order modes (HOM). The cut-off frequencies of a step index fiber with a $NA = 0.85$ for up to $V = 10$ are presented in Figure 1.4.

Fibers supporting only the fundamental mode are known as single-mode fibers (SMF) , while others supporting more than one mode are referred to as multi

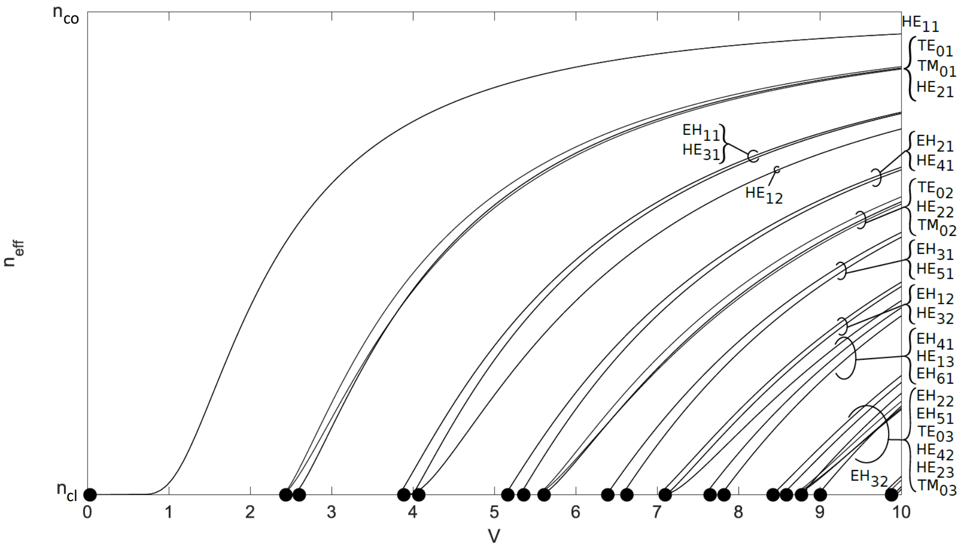

FIGURE 1.4: The evolution of n_{eff} values for up to $V = 10$ for a $NA = 0.85$ conventional step index fiber. The black dots show the cut-off frequency of each mode.

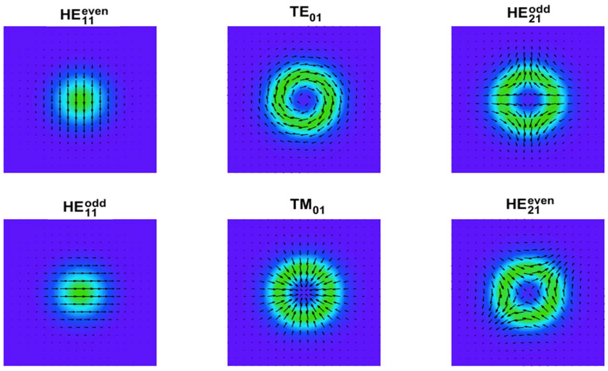

FIGURE 1.5: Electric field direction and transverse intensity of the first 6 vector modes.

mode fibers (MMF). We must mention that MMFs with a small number of modes are known as few-mode fibers (FMF).

1.2.3 Propagation modes : Linearly polarized modes.

Weakly guiding fibers

The index profiles of almost all the optical fibers exhibit only a small index contrast, so that the fiber can be assumed to be only "weakly guiding". In this situation, the calculation of the fiber modes is greatly simplified. The wave equations of a fiber are given by [Bures, 2009]:

$$(\vec{\nabla}_{\mathrm{t}}^2 + k^2 n^2 - \beta^2)\vec{e} = -(\vec{\nabla}_{\mathrm{t}} + i\beta z)(\vec{e}_t \cdot \vec{\nabla}_t \ln(n^2)) \tag{1.28}$$

$$(\vec{\nabla}_{\mathrm{t}}^2 + k^2 n^2 - \beta^2)\vec{h} = [(\vec{\nabla}_{\mathrm{t}} + i\beta z) \wedge \vec{h}] \wedge \vec{\nabla}_{\mathrm{t}} \ln(n^2) \tag{1.29}$$

In the weakly guiding approximation, the small value of the index contrast $\Delta n = n_{\mathrm{co}} - n_{\mathrm{cl}}$ allows to neglect the term $\vec{\nabla}_{\mathrm{t}} \ln(n^2)$ as it presents negligible value in the wave equations 1.28 and 1.29. Thus, these equations become scalar and we can talk about linearly polarized (LP) modes. Δn affects greatly the polarization: if $n_{\mathrm{co}} \neq n_{\mathrm{cl}}$, the TE and TM polarization states are reflected differently on the core-cladding interface while in the case of weakly guidance, both polarization states behave in a similar way. In fact, when $\Delta n \approx 0$, the fiber tends towards a uniform medium of index $n \approx n_{\mathrm{co}} \approx n_{\mathrm{cl}}$ and the wave's longitudinal components become negligible. The fields are practically transverse and given by [Bures, 2009]:

$$H_{\mathrm{t}} \approx \sqrt{\frac{\epsilon_0}{\mu_0}} n \cdot \vec{z} \times E_{\mathrm{t}} \qquad \text{thus} \qquad E_{\mathrm{t}} \times H_{\mathrm{t}}^* \cdot \vec{z} \approx n\sqrt{\frac{\epsilon_0}{\mu_0}} |E_{\mathrm{t}}|^2 \tag{1.30}$$

where H^* is the complex conjugate of the magnetic field H. Since the fiber is guiding, the wave is always inhomogeneous: its amplitude depends on the coordinates $(x; y)$ or $(r; \phi)$.

Eigenvalue equation

For transitionally invariant waveguides, the weakly guided fields can be written:

$$\vec{E}(r, \phi, z) = \vec{e}_{\mathrm{t}}(r, \phi) e^{i\beta z} \tag{1.31}$$

$$\vec{H}(r, \phi, z) = \vec{h}_{\mathrm{t}}(r, \phi) e^{i\beta z} \tag{1.32}$$

with e_{z} and $h_{\mathrm{z}} = 0$. We define the vectors $\vec{x}$ and $\vec{y}$ as the two polarization directions. Since the longitudinal components are negligible, we can write the following system of equations:

$$\vec{e}_{\mathrm{x}} = \vec{x} \cdot \Psi_{\mathrm{l}}(r, \phi) \rightarrow h_{\mathrm{x}} = -\sqrt{\frac{\epsilon_0}{\mu_0}} n_{\mathrm{eff}} \cdot e_{\mathrm{y}} \qquad \text{polarisation } \vec{y} \tag{1.33}$$

$$\vec{h}_{\mathrm{y}} = \vec{y} \cdot \Psi_{\mathrm{l}}(r, \phi) \rightarrow h_{\mathrm{y}} = \sqrt{\frac{\epsilon_0}{\mu_0}} n_{\mathrm{eff}} \cdot e_{\mathrm{x}} \qquad \text{polarisation } \vec{x} \tag{1.34}$$

where $F_{\mathrm{l}}(r; \rho)$ is the field amplitude at any point $(r; \phi)$ of the transverse section and l is an integer called the azimuthal modal number. For these modes to be invariant for a rotation of 2π, their equations have to respect:

$$e_{\mathrm{x,y}} = \Psi_{\mathrm{l}}(r, \phi) = \Psi(r) \left\{ \begin{array}{c} \cos(l\phi) \\ \sin(l\phi) \end{array} \right\} \tag{1.35}$$

The cosine solutions correspond to LP "even" modes and the sine solutions correspond to the LP "odd" modes. The difference between even and odd modes is a $\pi/2$ rotation of the fields around the propagation axis. While in weakly guidance conditions, using the wave equations 1.28 and 1.29, we can write for both polarization directions:

$$(\nabla_{\mathrm{t}}^2 + k^2 n^2 - \beta^2)\left(\left\{\begin{array}{c} e_{\mathrm{y}} \\ h_{\mathrm{x}} \end{array}\right\} \text{or} \left\{\begin{array}{c} e_{\mathrm{x}} \\ h_{\mathrm{y}} \end{array}\right\}\right) = 0 \tag{1.36}$$

This equation must be satisfied on the core-cladding interface and everywhere inside the fiber core. By applying the value of ∇_{t}^2 in Equation 1.36 we obtain :

$$\frac{\partial^2 \Psi_1(r)}{\partial r^2} + \frac{1}{r}\frac{\partial \Psi_1(r)}{\partial r} + \left(k^2 n^2 - \beta^2 - \frac{l^2}{r^2}\right)\Psi_1(r) = 0 \tag{1.37}$$

It is the scalar wave equation that determines the propagation constants β of the LP scalar modes. It must be satisfied at the boundaries: $\Psi_1(r)$ and $\frac{d\Psi_1(r)}{dr}$ are continuous on both interfaces. This wave equation is the differential equation of the Bessel functions J_l and Y_l or the modified Bessel functions I_l and K_l, according to $k^2(n^2 - n_{\mathrm{eff}}^2)$. To find the solutions of this equation, for a step index fiber with n_{co} as the core's index, n_{cl} as the cladding index, and r_{co} as the core radius, we must reject the solutions for $r = 0$ and $r \to \infty$ while having $n_{\mathrm{cl}} < n_{\mathrm{eff}} < n_c$. Thus, the possible solutions of the Equation 1.37 are:

- Inside the fiber's core, $r < r_{\mathrm{co}}$ and $n_{\mathrm{cl}} \leq n_{\mathrm{eff}} \leq n_c \Longrightarrow k^2(n_{\mathrm{co}}^2 - n_{\mathrm{eff}}^2) > 0$. In such conditions, the Bessel function Y_l diverges for $r = 0$, hence the solution is the Bessel function J_l.

- In terms of the cladding, $r > r_{\mathrm{co}}$ et $n_{\mathrm{cl}} < n_{\mathrm{eff}} \Longrightarrow k^2(n_{\mathrm{cl}}^2 - n_{\mathrm{eff}}^2) < 0$. In these conditions, the Bessel function I_l diverges for $r \to \infty$, hence the solution is the Bessel function K_l.

Using the same values for U, W and V as the ones mentioned in the Equations 1.19, 1.20 and 1.21 respectively, we can write the solutions of the Equation 1.37 as:

$$\Psi_1(r) = \left\{\begin{array}{ll} \frac{J_l(Ur/r_{\mathrm{co}})}{J_l(U)} & \text{if} \quad r \leq r_{\mathrm{co}} \\ \frac{K_l(Wr/\nabla_{\mathrm{co}}^2)}{K_l(W)} & \text{if} \quad r > r_{\mathrm{co}} \end{array}\right\} \tag{1.38}$$

For $r = r_{\mathrm{co}}$, the denominators ensure the continuity of $\Psi_1(r)$. In order to establish the eigenvalue equation, we take the conditions of the continuity of the derivative of $\Psi_1(r)$ at the core-cladding interface:

$$U\frac{J_{l+1}(U)}{J_l(U)} = W\frac{K_{l+1}(W)}{K_l(W)} \quad \text{or} \quad U\frac{J_{l-1}(U)}{J_l(U)} = -W\frac{K_{l-1}(W)}{K_l(W)} \tag{1.39}$$

The 2 forms of Equation 1.39 are identical. This is the eigenvalue equation. The solutions of this equation are series of discrete U_{lm} values where m is an integer that represents the order of the solution, which is a function of the effective indices n_{eff}, which allows us to find the propagation constants β of the guided modes. Each mode has a unique U_{lm} value. Note that for all optical fibers there is at least one solution, the one that corresponds to the value of $l = 0$ and $m = 1$: this is the fundamental mode.

These modes have two different degeneracy types: spatial degeneracy between even and odd modes (as mentioned by the Equation 1.35) and polarization degeneracy, x and y, depending on the polarization state of the mode's electric field. Vector modes are considered the natural modes of the optical fiber and consist of spatially inhomogeneous states of polarization. As shown in Figure 1.4, some

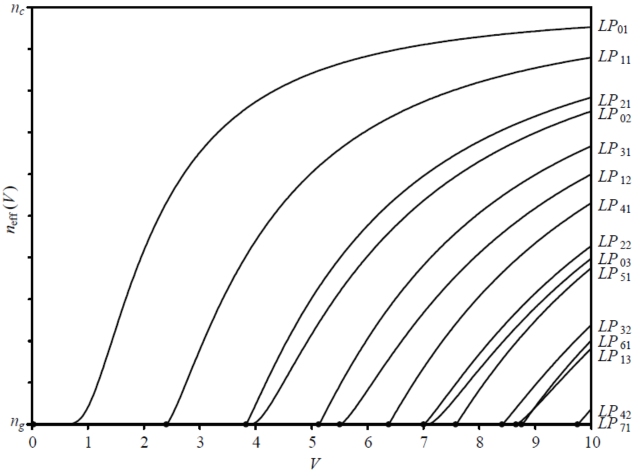

FIGURE 1.6: n_{eff} values for the first 10 LP modes for a $\Delta n = 0.3$ conventional fiber. The black dots show the cut-off frequency of each mode.

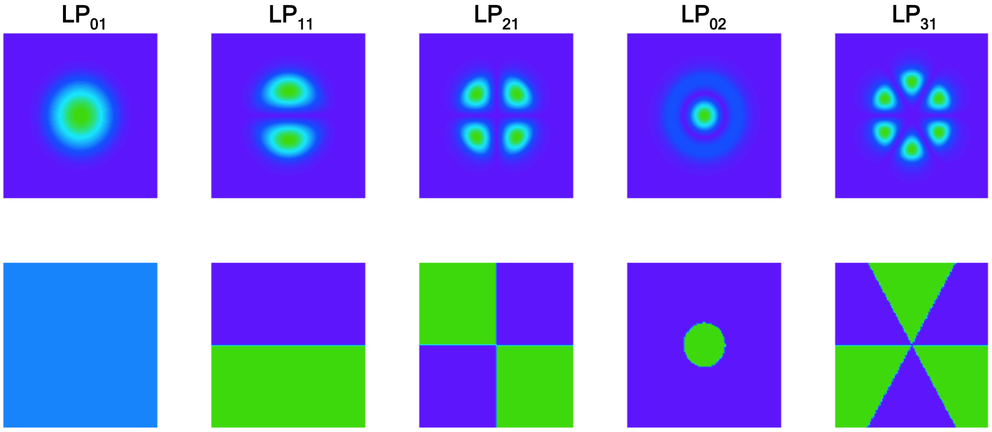

FIGURE 1.7: Field transverse intensity distribution of the first 5 LP modes.

of these modes share very close propagation constants. These modes are likely to couple during their propagation due to this slight difference. Under the weak guidance approach, these modes form the LP modes: the LP modes are in fact linear combinations of the vector modes under the weak guidance approximation. The resulting cut-off frequencies of the first 10 LP modes are shown in Figure 1.6 and the field transverse intensity distributions of the first 5 LP modes are showed in Figure 1.7. Table 1.1 shows the possible combinations to form the LP modes using the vector modes depending on the l value. Table 1.2 shows the spatial and polarization degenerate states of the first 4 LP mode groups.

TABLE 1.1: The vector modes combinations leading to the conversion to the LP mode basis using the weakly guidance approach.

l	LP	Vector modes
$= 0$	$\mathrm{LP}_{0,m}$	$\mathrm{HE}^{(e,o)}_{1,m}$
$= 1$	$\mathrm{LP}_{1,m}$	$\mathrm{HE}^{(e,o)}_{2,m}, \mathrm{TE}_{0,m} \quad or \quad \mathrm{TM}_{0,m}$
> 1	$\mathrm{LP}_{l,m}$	$\mathrm{HE}^{(e,o)}_{l+1,m}, \mathrm{EH}^{(e,o)}_{l-1,m}$

TABLE 1.2: The degeneracy states of the first 4 LP mode groups.

Mode	Spatial degeneration	Polarization degeneration
$\mathrm{LP}_{0,1}$	$\mathrm{LP}_{0,1}$	$\mathrm{LP}^{x}_{0,1}, \quad \mathrm{LP}^{y}_{0,1}$
$\mathrm{LP}_{1,1}$	$\mathrm{LP}^{(e)}_{1,1}, \quad \mathrm{LP}^{(o)}_{1,1}$	$\mathrm{LP}^{(e),x}_{1,1}, \quad \mathrm{LP}^{(o),x}_{1,1}, \quad \mathrm{LP}^{(e),y}_{1,1}, \quad \mathrm{LP}^{(o),y}_{1,1}$
$\mathrm{LP}_{2,1}$	$\mathrm{LP}^{(e)}_{2,1}, \quad \mathrm{LP}^{(o)}_{2,1}$	$\mathrm{LP}^{(e),x}_{2,1}, \quad \mathrm{LP}^{(o),x}_{2,1}, \quad \mathrm{LP}^{(e),y}_{2,1}, \quad \mathrm{LP}^{(o),y}_{2,1}$
$\mathrm{LP}_{0,2}$	$\mathrm{LP}_{0,2}$	$\mathrm{LP}^{x}_{0,2}, \quad \mathrm{LP}^{y}_{0,2}$

1.2.4 Propagation modes: Orbital angular momentum modes

Energy, momentum and angular momentum are some of the most fundamental physical quantities in classical and quantum electrodynamics. The electromagnetic angular momentum in a vacuum is defined as :

$$\vec{M} = \epsilon_0 \vec{r} \times (\vec{E} \times \vec{H}) \tag{1.40}$$

where ϵ_0 is the electric permittivity in the vacuum. Angular momentum can be divided into spin angular momentum (SAM) and orbital angular momentum (OAM): SAM is associated with photon spin and is manifested as circular polarization. OAM is linked to the spatial distribution of the electric field [Beth, 1936; Jackson, 1998]. Considering a light wave with an electric field proportional to $e^{il\phi}$, this wave has an OAM of $l\hbar$ per photon [Allen et al., 1992], where l is the topological charge, ϕ is azimuthal angle, and $\hbar$ is Plank's constant h divided by 2π.

In the case of a weakly guiding fiber, the electric and magnetic fields given by the Equations 1.31 and 1.32, can be separated into azimuthal and radial parts:

$$\vec{E}(r,\phi,z,t) = e(\vec{r}) \left\{ \begin{array}{c} e^{i\sigma\phi} e^{il\phi} \\ ie^{i\sigma\phi} e^{il\phi} \\ e^{i\nu\phi} \end{array} \right\} e^{i\beta z - i\omega t} = 0 \tag{1.41}$$

$$\vec{H}(r,\phi,z,t) = e(\vec{r}) \left\{ \begin{array}{c} e^{i\sigma\phi} e^{il\phi} \\ ie^{i\sigma\phi} e^{il\phi} \\ e^{i\nu\phi} \end{array} \right\} e^{i\beta z - i\omega t} = 0 \tag{1.42}$$

where $\sigma = 0$ for linear polarization, $\sigma = 1$ for right circular polarization and $\sigma = -1$ for left circular polarization. $\nu = l + \phi$ is the total angular momentum (SAM + OAM). The term $e^{il\phi}$ indicates that these fiber modes do have a OAM. The term $e^{i\sigma\phi}$ assure that the mode has a circular polarization. OAM modes are formed, just like the LP modes, from the fiber's vector mode basis using the combinations shown in Table 1.3 [Brunet and Rusch, 2016]. The OAM modes can

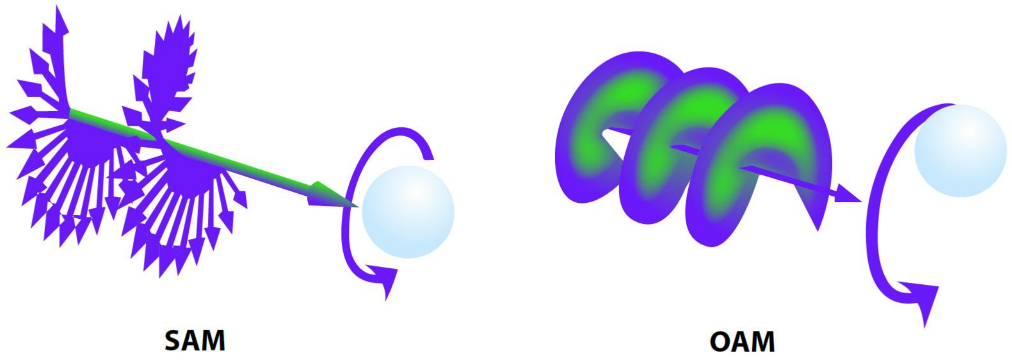

FIGURE 1.8: Representation of SAM and OAM.

TABLE 1.3: The vector modes combinations leading to the conversion to the OAM mode basis.

OAM	Vector modes
$OAM^{\pm}_{0,m}$	$\mathrm{HE}^{(e)}_{1,m}, \mathrm{HE}^{(o)}_{1,m}$
$OAM^{\mp}_{\pm 1,m}$	$\mathrm{TE}_{0,m}, \mathrm{TM}_{0,m}$
$OAM^{\pm}_{\pm l,m}$	$\mathrm{HE}^{(e)}_{l+1,m}, i\mathrm{HE}^{(o)}_{l+1,m}$
$OAM^{\mp}_{\pm l,m}$	$\mathrm{EH}^{(e)}_{l-1,m}, i\mathrm{EH}^{(o)}_{l-1,m}$

also be defined as the modes with a perfectly circular polarization and a perfectly helecoidal phase. Using this definition, the OAM modes can then be obtained from a combination of LP modes in the weak guidance approximation. However, in a real fiber propagation, the polarization of the OAM mode is rarely perfectly circular and the polarization state tends to have an elliptical form with axis that rotate according to the azimutal position in the fiber. This state change is due to the spin-orbit coupling which will not be detailed in this manuscript. Tandje, a fellow PhD student of our team, studied in great detail this phenomenon and its impact on the modal distribution of the fiber [Tandjè, 2019]. Given the fact that the majority of my works were experimental, we will stick to the first definition of the OAM modes, given by Table 1.3 throughout this manuscript. Since OAM modes are made of a combination of vector modes having the same propagation constant β (except the OAM$^{\mp}_{11}$), these modes are propagation invariant. This can be better understood using the spatial dependent part of the OAM mode combination:

$$\psi = \psi_a e^{i\beta_a z} + \psi_b e^{i\beta_b z} \tag{1.43}$$

where ψ is the OAM mode field, ψ_a and ψ_b are the 2 vector modes that can combine into a OAM mode according to Table 1.3, β_a and β_b being their propagation constants. For the OAM modes, $\beta_a = \beta_b$ and thus the phase of both parts of the combination is the same, therefore the OAM modes is propagation invariant (except the $\mathrm{OAM}_{11}^{\mp}$). The transverse distribution of the electric field of the first 5 OAM mode groups and their respective phases are represented in Figure 1.9. The circular polarization and the orbital angular momentum directions can be aligned or anti-aligned, as shown in the Figure 1.10.

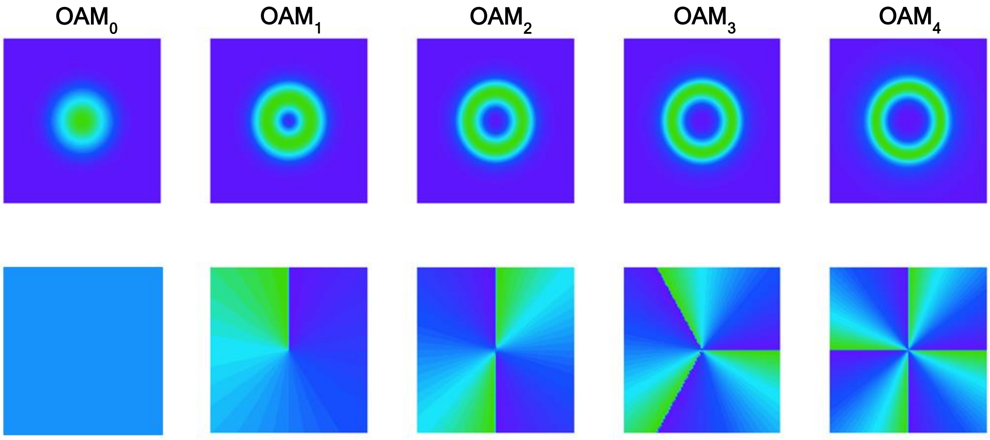

FIGURE 1.9: Field transverse distribution of the first 5 OAM modes on the top row and their corresponding phases on the bottom row.

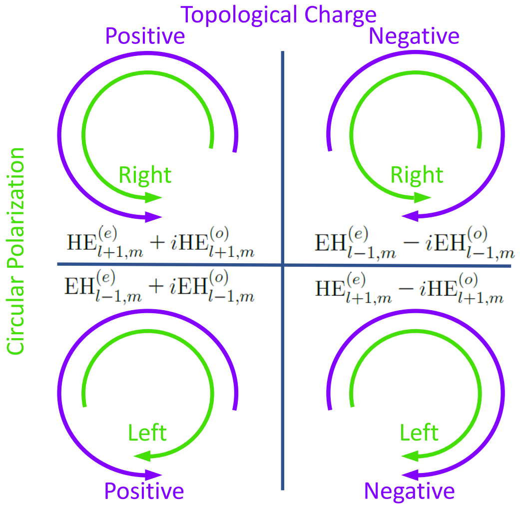

FIGURE 1.10: The four degenerate states of the OAM mode basis for $l > 1$ [Brunet and Rusch, 2016].

In the previous paragraphs, we have discussed the light propagation mechanism through a optical fiber. We have also described the vector modes that can be guided in the fibers, and the combination that can be used in order to obtain the

LP mode basis and the OAM mode basis. These basis will be used in the later sections of this manuscript.

1.3 Optical fibers and telecommunications

1.3.1 General overview

From the telephonic services to optical endoscopy, optical fibers are used in many fields, but nowhere more than high data rate telecommunications. The optical fiber presents the perfect solution for the explosion of information traffic due to the enormous growth of the Internet, computer networks, electronic commerce. Its low attenuation and possible preservation of high signal integrity make long distance signal transmission possible. The optical fiber presents a large bandwidth, elementary for high rate transmissions. The information security is not a real concern for the optical fiber systems due to their dielectric nature: accessing to the signal is impossible without access to the fiber itself, which can be easily detected. The fiber's physical properties present many advantages: it's very light comparing to the traditional metallic lines used before, it has small dimensions and it is a non-conductive component, so the electromagnetic and radio waves have no effects on the signal within.

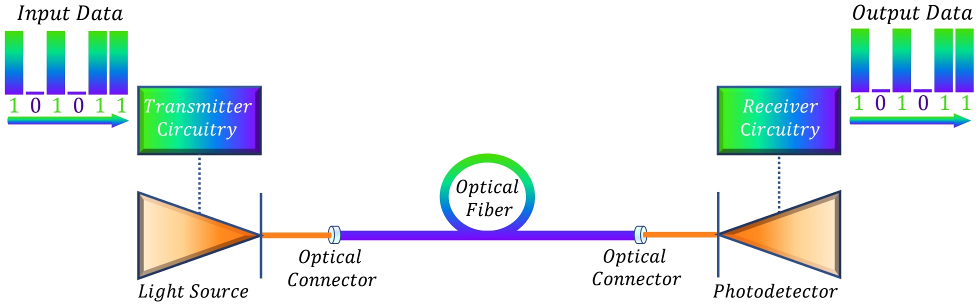

FIGURE 1.11: Basic fiber optic communication system.

Fiber optics are just a carrying support of light beams containing encoded information from one point to another, therefore its use must be combined with a suitable system. A basic fiber optic system consists of a transmitting device that encodes an electrical signal onto a light carrier, an optical fiber cable that carries the light, and a receiver that detects the light signal and converts it back into an electrical signal. Such a system is shown in Figure 1.11.

1.3.2 Amplifiers

In optical communication networks, signals travel through fibers for very large distances without significant attenuation ($\approx 0.2\,\mathrm{dB}\cdot\mathrm{km}^{-1}$ for the presently used

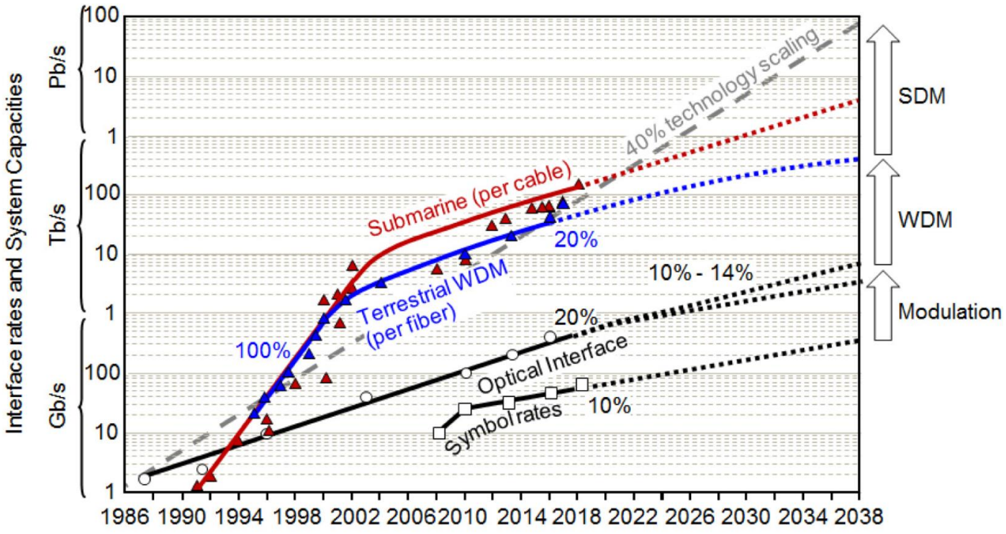

FIGURE 1.12: Evolution of commercial optical transmission systems over the past 30 years and extrapolations for the coming 20 years [Winzer, 2017].

line SMFs type $G652$). However, when distances become hundreds of kilometers, the signal attenuation becomes a non negligible effect and the restitution of the signal power becomes necessary so it can be detected at the other side of the transmission system. The first in-line amplifiers were opto-electronic regenerators, transforming the light signal into electronic signal to be amplified, then re-transformed into light signal and coupled into the fiber. These systems were limited at a data rate of 2.5 Gb/s [Winzer, 2017]. The invention of optical amplifiers, and in particular of the erbium doped fiber amplifier (EDFA) was the game-changer [Mears et al., 1987; Desurvire, Simpson, and Becker, 1987]. This technology started a new era of optical transmission: it provides in-line broadband amplification of signal without requiring electronics i.e., the signal does not need to be converted to electrical signal before amplification. The evolution of commercial optical transmission systems over the past 30 years and extrapolations for the coming 20 years is shown in Figure 1.12. The amplification is entirely optical, does not need to change the propagation medium of the light (the light passes from one fiber to another doped one), independent of data rate, independent of the light's polarization state and possible for a large bandwidth. A basic EDFA system is illustrated in Figure 1.13. This technology was first used in the TAT-12/13 cable system back in 1996, connecting the US to the UK and France, supporting up to 10 Gbit/s [Trischitta et al., 1996]. An EDFA quality is measured by its gain, the ratio between the signal output power P_s^{out} and the signal input power P_s^{in} is given by:

$$G_{\mathrm{dB}} = 10 \log \left(\frac{P_s^{out}}{P_s^{in}} \right) \tag{1.44}$$

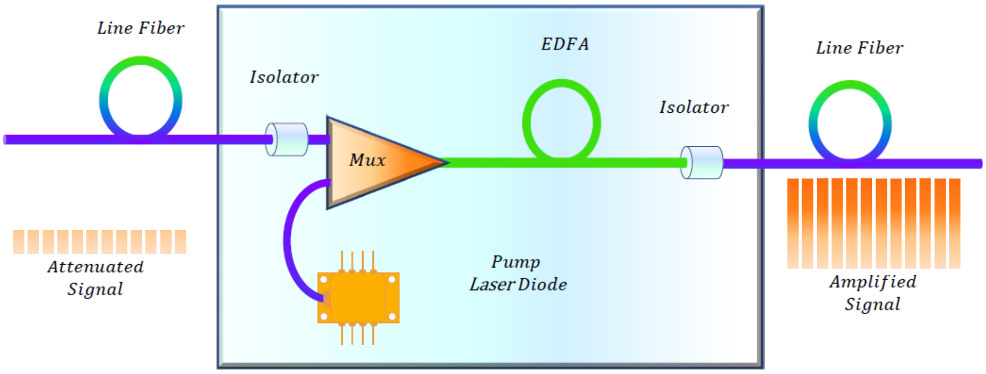

FIGURE 1.13: A basic EDFA system.

Erbium spectroscopy

Erbium is one of the 28 rare earth elements. Trivalent erbium ions, Er^{3+}, have optical fluorescent properties particularly useful for fiber amplifiers especially those used in the telecommunication networks. Its electronic configuration is given by :

$$Er^{3+} : 1s^2 2s^2 2p^6 3s^2 3p^6 3d^{10} 4s^2 4p^6 4d^{10} 5s^2 5p^6 4f^{11}$$

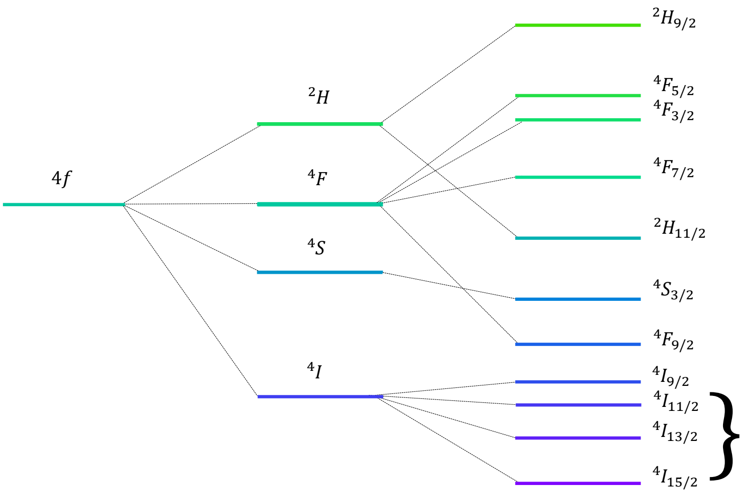

FIGURE 1.14: degenerate levels of Er^{3+} $4f$ level [Bigot, 2002].

The amplification mechanism implies the $4f$ level electrons. Once the ions are introduced into the glass matrix of the fiber's core, the $4f$ level degeneracy obtained from spin-orbit coupling is lifted due to contributions from ion-lattice interaction

(Stark splitting) as shown in Figure 1.14.
EDFAs use only three of the levels shown in Figure 1.14 and $4I_{15/2}$ level serves as the ground level. The transition between the fundamental level and the $4I_{13/2}$ level corresponds to the operation wavelength used in optical communications (between 1530 nm and 1625 nm). Third used level is the $4I_{11/2}$ with a transition centered near 980 nm, the wavelength mainly used to pump the EDFAs.

EDFAs operating mechanism.

EDFAs spectral properties: The Er^{3+} ions have a wide spectrum band when introduced into the fiber's glass core. This property gives the possibility to the EDFAs to operate over a wide spectral range, covering the C band between 1530 nm and 1565 nm) and also the L band (between 1565 nm and 1625 nm) in some conditions (C for conventional and L for long wavelength). Figure 1.15 shows the absorption and emission cross sections for the Er^{3+} ions when introduced in an aluminosilicate Er-doped fiber.

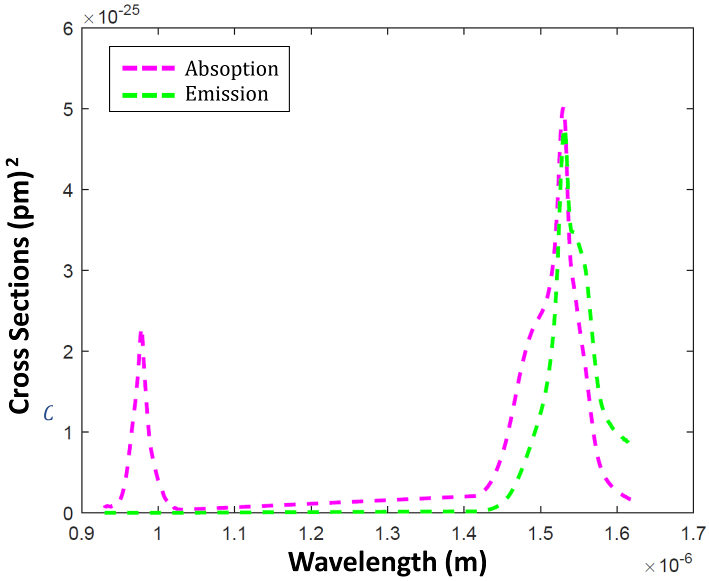

FIGURE 1.15: Absorption and emission cross section of the Er^{3+}.

Amplified spontaneous emission: In the absence of any radiation, the ions are in their ground state $4I_{15/2}$. If a light beam with a wavelength corresponding to the energy gap between the electronic states is incident on the system, the ions will be excited to the higher levels. Such a radiation will be referred to as the pump beam. If its wavelength is chosen at 980 nm, the pump beam will excite the Er^{3+} ions to the $4I_{11/2}$ level. Because of the short lifetime (few μs) of this energy level, the electrons are transferred to the metastable level $4I_{13/2}$ (about 10 ms lifetime). The pump can also operate at 1480 nm, exciting the ions directly into the metastable level, but this configuration whereas it reduces the difference between the signal and pump wavelengths and leads to larger optical noise level. The possible transitions, illustrated in Figure 1.16 from the $4I_{13/2}$ state to the ground state are provided by :

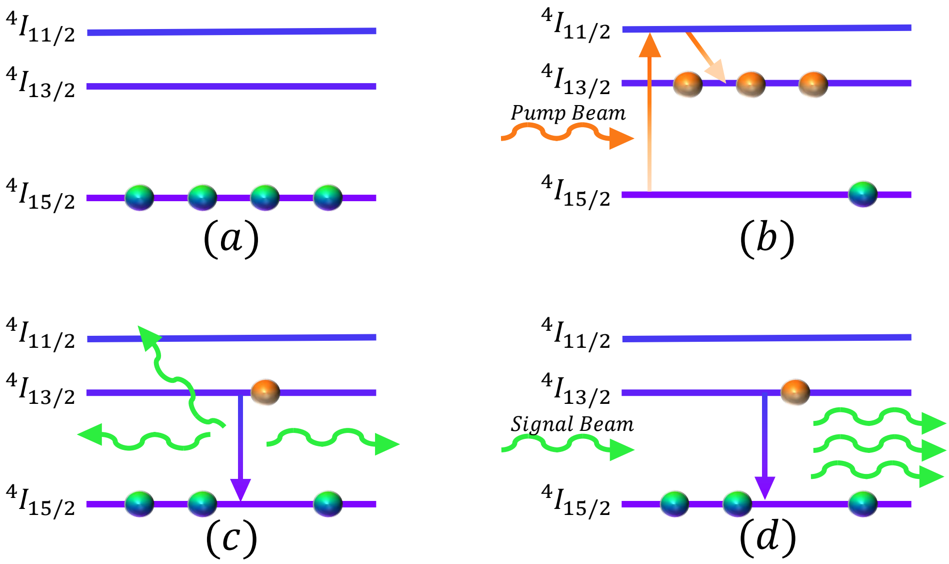

FIGURE 1.16: (a) All ions in the ground state. (b) Pump absorption and relaxtion of the ions to the $4I_{13/2}$ state. (c) Spontaneous emission. (d) Stimulated emission.

- Spontaneous Emission : spontaneously emitted photons have no phase relationship with one another. It can take place in the entire bandwidth of transition and can even travel backwards. This, therefore, contributes to noise. A fraction of the spontaneously emitted photons will be emitted in a direction which is within the numerical aperture of the fiber and will, therefore, be captured and guided. Such photons, in turn, may interact with rare earth ions and be amplified as well. The amplified spontaneous emission (ASE) is one of the major limitations of amplifying fibers because, on the one hand, it disrubts the signal by adding noise, thus decreasing the signal-to-noise ratio and, on the other hand, duplicate spontaneous photons consume gain that does not benefit to useful photons and thus decrease the gain of the signal.

- Stimulated Emission : the stimulated emission takes place in the wavelength window 1520 to $1620\ \mathrm{nm}$ (C and L-bands) if a data signal with the corresponding wavelength is fed into the fiber. The newly generated photons by stimulated emission are responsible for amplification of signal as they travel along the fiber.

Population equations. In the previous sections, we mentioned that EDFAs operate using three of the degenerate energy levels shown in Figure 1.13. In fact, if the electronic states are spaced closely enough, which is the case for $4I_{13/2}$ and $4I_{11/2}$ levels, the ion relaxes non-radiatively from the higher to the lower state through emission of multiple phonons in order to conserve the total energy. This non-radiative transition is fast and enables us to suppose that the EDFAs operate mainly as a two-levels system : between the $4I_{13/2}$ and the $4I_{15/2}$ states. Let N_{T} denote the Er^{3+} ions total concentration inside the fiber's core and $N_i(t)$ the ions population of the ith energy state at a given time t. N_{T} has the same value at every position of the fiber, therefore we can write [Giles and Desurvire, 1991]:

$$N_{\mathrm{T}}(x,y) = N_1(x,y,z,t) + N_2(x,y,z,t) \tag{1.45}$$

N_1 being the population of the ground state $4I_{15/2}$ and N_2 being the population of the $4I_{13/2}$ state. As already explained, due to the fast non-radiative transition between the third and second energy levels, we neglect the population of the $4I_{11/2}$ state and consider it directly represented in N_2. The efficiency of the pump can be described by its capacity to excite ions and can be evaluated by the coefficient of the population inversion η_2 :

$$\eta_2(z) = \iint \frac{N_2(x,y,z,t)}{N_{\mathrm{T}}(x,y)} dxdy \tag{1.46}$$

1.3.3 Influencing factors of EDFAs.

The Er^{3+} ions energetic gap between the metastable and ground levels allows high levels of stimulated emissions to occur in the C-band range mainly and in the L-band range as detailed in the previous sections. So EDFA can be used to amplify signals but the gain of different signal wavelengths is different, due to multiple factors of the EDFA itself which can heavily influence its performances:

The influence of the fiber length on the EDFA's gain: The length change of EDFA directly affects its amplifying ability. 2 cases are distinguished for this parameter: the single wavelength and multiple wavelengths. In the case of a single wavelength, the optimized length is given by the maximal delivered gain value. When the length of the EDFA is less than the optimal value, the gain is limited because of the limitation of the stimulated emission, consequently, while when the length of EDFA is more than the optimal value, the gain starts to decrease after a certain length because the pump does not have enough energy to create a sufficient population inversion all along the amplifier, especially in the last portion of the fiber. In this case, the unpumped region of the fiber absorbs the signal, thus resulting in signal loss rather than gain in that section. For both fiber lengths, the gain is less than the optimized value. For a multiple wavelengths transmission, the optimization is controlled by the flatness of the delivered gain spectrum: although the optimized fiber length might not deliver the maximal gain value for the shortest wavelengths, delivering a equalized gain for all the wavelengths is the main criteria, which leads to a compromise leading to secure a length were the overall spectrum of the gain for all the wavelengths is as flat as possible. A shorter fiber length will result in a spectrum were the short wavelengths present higher gain than the later ones, whereas a fiber length longer than its optimized value illustrate the re-absorption of the gain of the short wavelength. Figure 1.17(a) illustrates the influence of the fiber length on a single-mode EDFA: the blue spectrum shows the flat gain of the EDFA in its optimized conditions and the optimized length $L_{\mathrm{opt}} = 3.7$ m. The red gain spectrum is delivered for $L = 1.7$ m and the green gain spectrum is $L = 5.7$ m.

The influence of the Er^{3+} concentration on the EDFA's gain: Er^{3+} doping concentration has a significant effect on the gain too. For a specific fiber, if Er^{3+} doping concentration is too heavy, the pump efficiency is greatly reduced and consequently the signal gain due to ion-ion interactions. However, in a low doped concentration scheme, the excited state will be depleted and so the optical signal amplification is limited to the smaller ion number available and thus more fiber length is necessary. Figure 1.17(b) illustrates the influence of the Er^{3+} concentration on a single-mode EDFA: the blue spectrum shows the flat gain of the EDFA in its optimized conditions and the optimized doping concentration $C_{\text{opt}} = 10 \times 10^{24}$ ions/m^3. The red gain spectrum is delivered for $C = 5 \times 10^{24}$ ions/m^3 and the green gain spectrum is $C = 15 \times 10^{24}$ ions/m^3. All 3 spectra are obtained for the optimized fiber length of C_{opt}. We should mention that we can obtain 3 very similar flat gain spectrum for the 3 different doping concentrations of ions if the fiber length is changed: $L = 2.5$ m for the highest concentration, $L = 3.7$ m and $L = 7.2$ m for the lowest concentration.

The influence of the signal wavelength on the EDFA's gain: The Er^{3+} ions cross sections spectra are presented in Figure 1.15 and are clearly wavelength dependent. Therefore, the amplification of a signal with multiple wavelength channels will depend on these cross sections and will not be flat over the whole spectrum. Although the gain difference between different wavelengths for a single amplification can be viewed as a slight difference, for a long distance transmission deploying multiple EDFAs, these differences are amplified by each EDFA and can destroy the integrity of the signal at the detection end of the transmission. Gain flattering filters are then used after each EDFAs. These filters introduce wavelength-dependent losses and the signal will then have a flat amplification leaving the EDFA.

The influence of the signal power on the EDFA's gain: The signal power has a significant effect on the EDFA's behavior: when the signal has a low power, gain increases linearly with the signal power. When the signal power becomes more important, the amplifier operates in what is called saturation regime and the gain decreases if the signal power is increased. This phenomena is wavelength-dependent. Figure 1.17(c) illustrates the influence of the signal power on a single-mode EDFA: the blue, red and green spectrum show flat gains of the EDFA in its optimized conditions. The lowest the initial signal power is, the higher gain spectrum is obtained.

The influence of the pump power on the EDFA's gain: Pump power is an important factor that affects the gain of the EDFA. When the pump power is less than the optimal value, the gain of each channel starts to decrease, which makes the flatness of the gain spectrum worse. In fact, the pump power is not sufficient to create an efficient population inversion to provide the necessary number of excited ions. When the pump power is more than the optimal value, the EDFA enters another saturation regime, which deteriorates the amplification efficiency and the flatness of the gain is risked. Figure 1.17(d) illustrates the influence of the pump power on a single-mode EDFA: the blue, red and green spectrum show flat gains of the EDFA in its optimized conditions. The highest the pump power is, the higher gain spectrum is obtained.

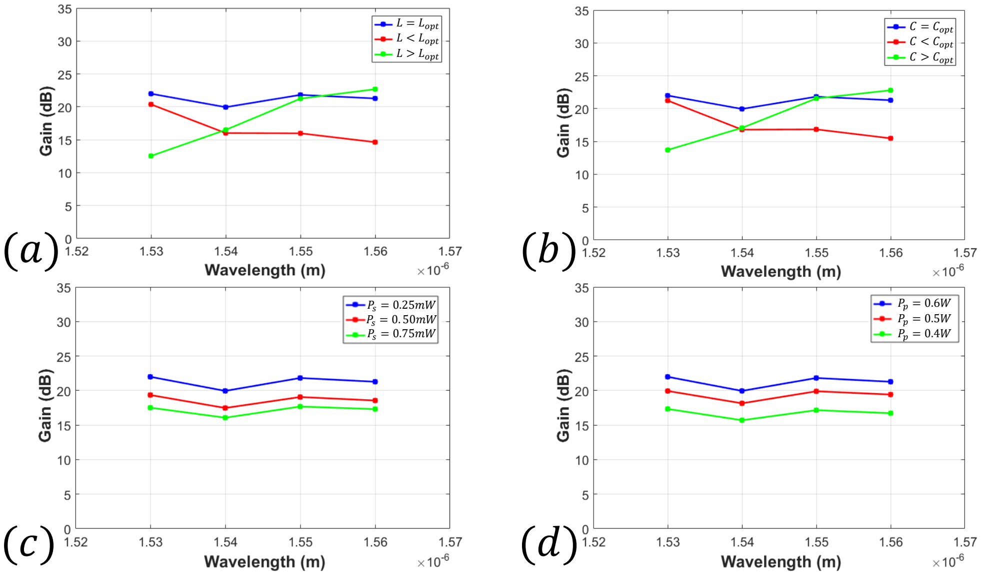

FIGURE 1.17: Influence of the (a) fiber length, (b) Erbium doping concentration, (c) signal power and (d) pump power on the performance of a single-mode EDFA.

1.3.4 Multiplexing

In telecommunications, multiplexing is a method by which multiple analog or digital signals are simultaneously combined and transmitted using a single fiber. Multiplexing divides the capacity of the communication channel into several logical channels, one for each message signal or data stream to be transferred. Several types of multiplexing exist and are deployed in the telecommunication networks all around the world. We will scout some of the types which can be useful to a better understanding of the following of this manuscript.

Wavelength division multiplexing

Wavelength division multiplexing (WDM) is a technology that consists in the combination of numerous optical signals at different wavelengths onto a single optical fiber. A basic WDM setup is presented in Figure 1.18 (a). WDM enables bidirectional communication (in case EDFA is not employed) as well as multiplication of signal capacity. WDM systems can combine signals with multiplexer (typically an arrayed waveguide grating) and split them apart with a demultiplexer, and with the proper fiber cable, the two can be done simultaneously. WDM systems are popular with telecommunications companies because they allow them to expand the capacity of the network without laying more fibers [Yamada et al., 2001]. The wavelengths must be chosen separated enough so the signals do not interact with each other, which would degrade the transmitted information. Note that this technology was only possible due to the wide amplification bandwidth of the EDFA, and was considered as a revolutionary progress in the mid 90s.

Polarization division multiplexing

Polarization division multiplexing (PDM) is a physical layer method of multiplexing signals, allowing two channels of information to be transmitted on the

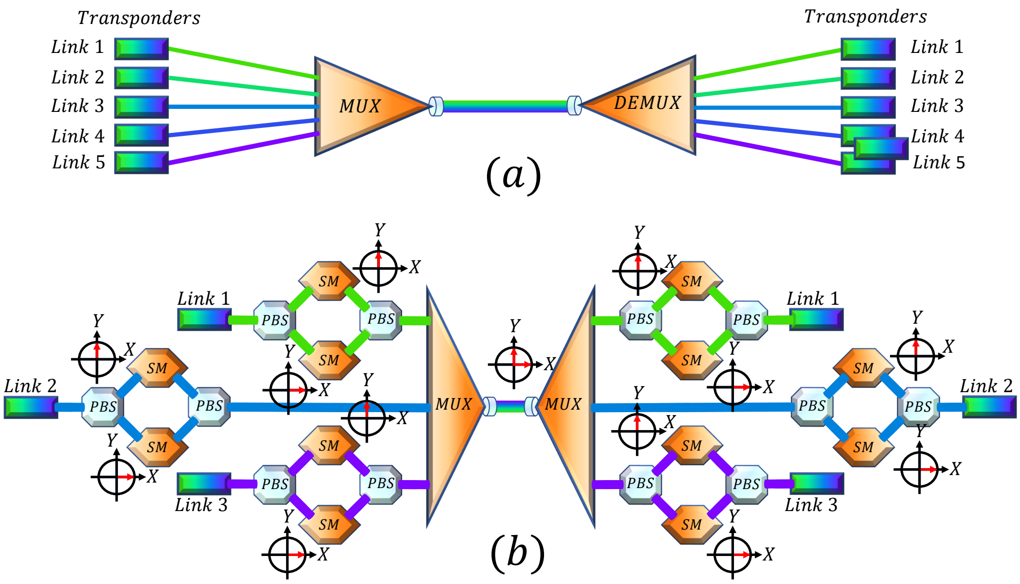

FIGURE 1.18: (a) WDM basic setup. (b) PDM basic setup combined with a WDM setup.

same carrier wavelength of a given spatial mode by using light beams of two orthogonal polarization states [Glance, 1987], or left and right circularly polarized light beams through the same optical fiber [Bozinovic et al., 2013]. PDM can be combined with the WDM technique, multiplying by a factor of 2 the latter's capacity. Multiple polarization signals can be combined to form new states of polarization, which is known as parallel polarization state generation. A basic PDM setup is presented in Figure 1.18 (b).

Spatial division multiplexing

The multiplicity of modes propagating within FMFs or MMFs explains that, from the point of view of information theory, the latter has potentially a greater capacity than regular SMFs used presently in the transmission networks. The exploitation of the spatial domain, which is regarded as the last unexplored physical dimension in optical communication, creates an additional degree of freedom in the transmission of information. This technology is known as spatial division multiplexing (SDM). It is widely used in the electronic and wireless domains [Foschini, 2002], increasing the capacities considerably. In the optical domain, multiple modes co-propagating over FMFs and parallel-signal transmission over coupled or uncoupled multi-core fiber (MCF) are currently regarded as new-emerging SDM technologies to be exploited in optical communication [Venghaus and Grote, 2017]. A MCF is an optical fiber containing more than one fiber core, the different cores acting as separate waveguides, if they are well separated from each other, so that light can independently propagate through, providing a new set of separated channels that can go along with other multiplexing methods. In both MCFs or FMFs, the possibility exists to operate either in a uncoupled or strongly coupled regime. For a FMF with one core, the modes are considered as the new set of channels. Figure 1.19 shows the basic physical difference between the fibers cited in this section and the ordinary SMF used in the telecommunication network.

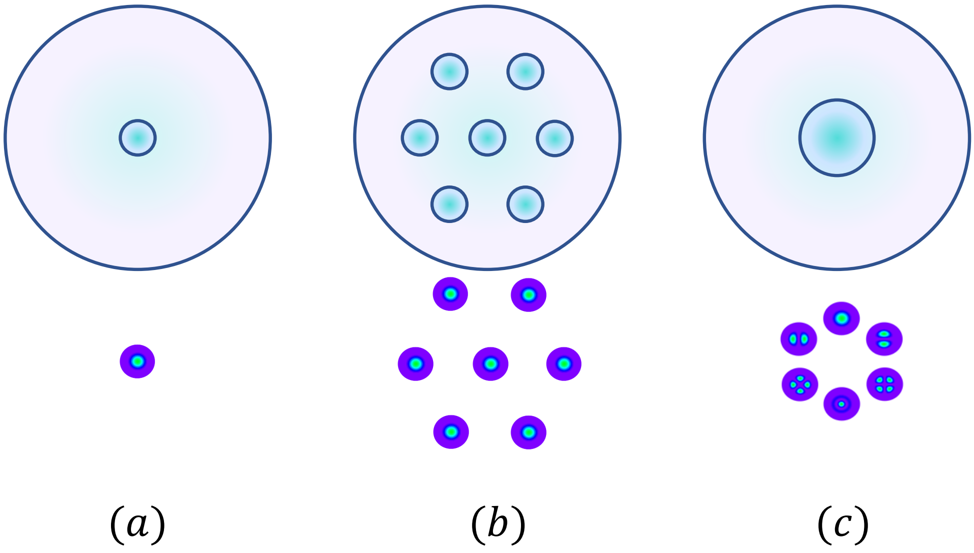

FIGURE 1.19: (a) SMF, guiding only the LP_{01} mode. (b) MCF, guiding one LP_{01} mode per core. (c) FMF, guiding up to six LP modes.

Multiple Input Multiple Output

While propagating in a single-mode transmission fiber, time shift exists between different signal polarization states. Therefore, at the reception end of the transmission line, it is necessary to correct the effect of polarization state change and the impact of time delay undergone by the beam. Some digital treatments should be added to compensate the effects of the polarization dispersion, but also the effect of group velocity dispersion: this is known as multiple input multiple output digital signal processing (MIMO-DSP). A MIMO $n \times n$ is formed of $n \times n$ finite impulse response (FIR) filters, with n depending on the number of channels to differentiate.

There are 2 categories of optical MIMO implementation in MMF: dispersive multiplexing and modal multiplexing [Stuart, 2000, Amphawan, 2011]. Both categories have great potential for increasing the channel capacity of a MMF link: the first one relies on the excitation of a large number of modes in order to increase the number of signal channels while modal multiplexing strives to confine a channel to as few-modes as possible so as to minimize cross-talk (X-talk) between channels. We should mention that the modal multiplexing seems to have a greater potential. Its limited number of modes presents higher precision in the design of the mode multiplexer and lower crosstalk between the channels, which results in a higher efficiency of its individual channels, compared to the to dispersive multiplexing where the random fluctuations in power modal coupling with time makes the prediction of each channels more challenging and difficult. We should also mention that the modal multiplexing can be divided into 2 sub-categories according to the coupling levels of the used FMFs: the weakly coupled and the strongly coupled regime. For the strongly coupled fibers, the challenge is to minimize the differential mode group delay (DMGD) to keep a small group delay spread (GDS) by adapting the fiber designs and apply compensating techniques, so that all modes can be simultaneously MIMO processed at the reception with as low a complexity as possible [Molin et al., 2018]. It is also possible to impose strong mode coupling to the fiber so that the GDS increases with the square root of the propagation distance and not linearly as in the weakly-coupled regime. In the weakly-coupled regime, the challenge is to design fibers with minimum coupling between modes.

In the case of a PDM transmission using two different states of polarization, for a given spatial mode, MIMO 2×2 is used. In a more general case, such as a transmission with PMD, each element of the channel matrix is an impulse response itself. The channel matrix estimated by the MIMO is similar to the transmission matrix (TM), which is a subject of the Chapter 2 of this manuscript.

1.3.5 Limitations

Various physical parameters limit the maximum capacity achievable in optical telecommunications, related to the propagation properties of the light wave in the optical fiber, such as the nonlinear effects and the various dispersion types.

Polarization dispersion.

As mentioned in the Equations 1.33 and 1.34, and by the Table 1.2, transverse modes have a degeneracy in polarization. Due to manufacturing imperfections and strains, the fiber's core might not be perfectly circular all the way from the input to the output face. This miniature defects of the fiber core are randomly distributed. Add to that all the thermal and mechanical stresses imposed on the fiber (bends, twists) the polarization degeneracy of the transverse mode is lifted, creating two different modes having orthogonal polarization states but the same transverse spatial distribution. These new modes present distinct propagation constants, which result in a different traveling speed for each of them. At the output of a long distance transmission, these modes will experience what is known as polarization mode dispersion (PMD). The two polarization components of a signal will slowly spread and split a unique input pulse. Therefore, the pulse spreading effects have a mean polarization-dependent time-differential, also called the differential group delay (DGD) proportional to the propagation distance L:

$$DGD = L \cdot (\Delta\beta) \tag{1.47}$$

where $\Delta\beta$ is related to the difference in group velocities along the two principal states of polarization [Agrawal, 2002]. Because of the imperfections are random, the type of the birefringence is random by nature along the fiber, both for its amplitude and its orientation. Thus, the DGD between the polarization states and the polarization mixing both have random variations along the fiber. Therefore, the PMD-induced pulse spread is a result of the interplay of these 2 contributions. It is characterized by the root mean square value of the DGD, obtained after averaging over random birefringence changes:

$$\sigma_{\mathrm{T}} \approx D_{\mathrm{p}}\sqrt{L} \tag{1.48}$$

where σ_{T} is the variance $\sigma_{\mathrm{T}}^2 = \langle (DGD)^2 \rangle$ and D_p is a PMD coefficient, with a value of nearly $0.04\mathrm{ps}/\sqrt{\mathrm{km}}$, for today's best SMF fibers, which is a measure of the strength and frequency of the imperfections. Figure 1.20 (b) shows the effects of the PMD in a birefringent fiber: after traveling through the fiber length, the pulse is divided into two spatially identical pulses, having two orthogonal polarization states with different propagation speeds [Frignac, 2003].

Modal dispersion.

Each transverse mode in a MMF has its own effective index with a specific wavelength dependence. Thus, the information contained in a mode propagates with a distinct speed with respect to the other modes: this is a kind of generalization of what has been explained just before for the polarization dispersion. The group index n_G designates the index of the pulse envelope, function of the wavelength and of the effective index n_eff defined by the Equation 1.49:

$$n_\mathrm{G} = n_\mathrm{eff} - \lambda \frac{\partial n_\mathrm{eff}}{\partial \lambda} \tag{1.49}$$

If no precaution is used when injecting a light beam in a MMF, its power will be distributed over the different supported modes. Each mode having its own propagation speed, when the output is reached, a DMGD will occur, resulting in temporal broadening of the signal, which is typically the situation used for short distance transmission with MMF. The effect of modal dispersion depends on the distance traveled by the signal: if it is short, these effects will have limited impact. However, over long distances, modal dispersion strongly affects the maximum rate, knowing that the duration of a symbol must be greater than the difference in propagation time between the fastest mode and the slowest mode. The GDS is defined as:

$$GDS = \frac{L}{c} \Delta n_\mathrm{G,max} = DMGD \cdot L \tag{1.50}$$

The spread being proportional to the length of the fiber L, the maximum data transmission rate in the fiber is then inversely proportional to L in a case where a single channel utilize all the modes.

In the case of a MDM transmission, the modal dispersion is viewed a bit differently:

- In the case where we have X-talk between the different channels, the effect of the modal dispersion is similar to the PMD.
- In the case where the channels are completely independent without any X-talk between the modes, the modal dispersion has no impact on the transmission.

Chromatic dispersion.

The wavelength dependence of the effective index causes a chromatic dispersion to the propagated signals, characterized by the dispersion parameter D:

$$D = \frac{-2\pi c}{\lambda^2} \beta_2 \tag{1.51}$$

with β_2 given by:

$$\beta_2 = \frac{1}{c} \frac{\partial n_\mathrm{cl}}{\partial \omega} \tag{1.52}$$

The dispersion parameter, in $[\mathrm{ps} \cdot \mathrm{nm}^{-1} \cdot \mathrm{km}^{-1}]$ represents the difference in propagation time observed after one kilometer of fiber between two spectral components spaced by $1\ \mathrm{nm}$. The dispersion regime is defined by normal or anomalous according to that if $D < 0$ $(\beta_2 > 0)$ or $D > 0$ $(\beta_2 < 0)$ respectively. The finite spectral width of the laser source generating the light signal causes the propagation of the different spectral components at different speeds. Consequently, the signal will be expanded temporally, which makes it impossible to recover the original transmitted data if a pulse starts to overlap with its neighbors in the case of incoherent communications. We should mention that, in coherent communications, we can actually compensate the chromatic dispersion numerically. This temporal expansion caused by the chromatic dispersion of a symbol determines the maximum allowed bit rate. Inter-symbol interference occurs when the pulse expansion becomes temporally greater than the time of a symbol. The accumulated chromatic dispersion increases proportionally to the fiber length. Figure 1.20 (a) shows the chromatic dispersion of a signal pulses propagation through a fiber: after a certain distance, the different wavelengths traveling at different speeds stretch the pulse envelope, risking the integrity of the transmitted information.

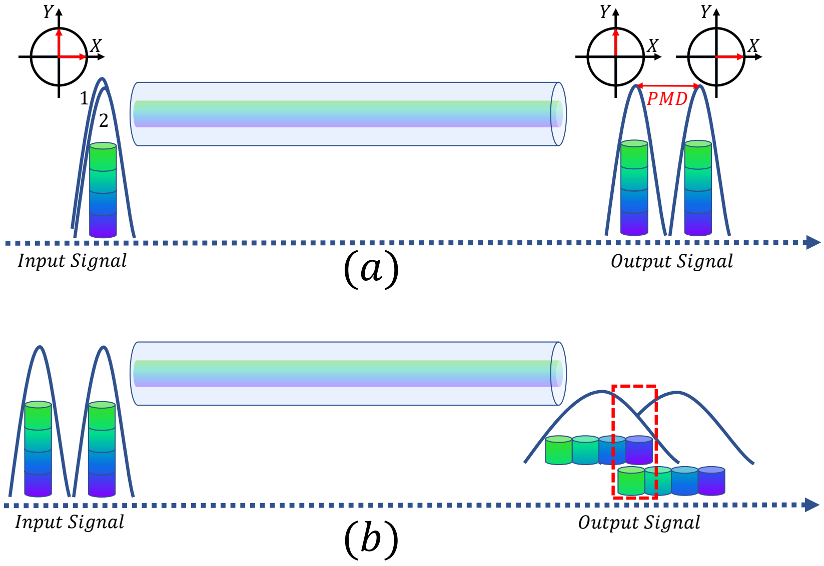

FIGURE 1.20: (a) Polarization mode dispersion of two signal pulses with different polarization states. (b) Chromatic dispersion for a multi-wavelength signal, shows the different traveling delay at the output of the fiber.

Nonlinear effects.

The maximum capacity of the fibers can be limited by other factors than dispersion such as the nonlinear effects, especially the Kerr effect. Its physical origin is a nonlinear polarization generated in the medium, which itself modifies the propagation properties of the light. The Kerr effect is the effect of a nearly instantaneous nonlinear response, which can be described as a modification the refractive index: if the power is high enough, the refractive index can be modified from its initial value n_0 following the equation:

$$n = n_0 + n_2|E|^2 \tag{1.53}$$

n_0 is also known as the linear refractive index, n_2 is thus the nonlinear refractive index which presents the modification to the refractive index n according to the beam's electric field E. n_2 is expressed by:

$$n_2 = \frac{3\chi^{(3)}}{8n_0} \tag{1.54}$$

with $\chi^{(3)}$ representing the third orfer nonlinear electric susceptibility.
Due to the index variation caused by the Kerr effect, a phase shift in the pulse can be created, leading to a frequency broadening that increases its sensitivity to the chromatic dispersion: this is known as the self phase modulation (SPM). A similar effect can be observed between two different pulses, when the optical power of the first pulse modifies the refractive index, the impact on the other channel is known as the cross phase modulation (XPM). XPM effect is two times more efficient than the SPM effect, limiting heavily the maximum capacity of the WDM transmissions [Agrawal, 2012].

Other nonlinear effects have smaller contributions on limiting the capacity of the fibers using WDM:

- Four-wave mixing (FWM) is a nonlinear inter-modulation phenomenon, whereby interactions between two or three wavelengths produce two or one new wavelengths.
- The nonlinear response of a transparent optical medium to the optical intensity of light propagating through the medium is very fast (Kerr effect), but not always instantaneous. In particular, a non-instantaneous response is caused by vibrations of the glass network that composes the core/cladding materials. When these vibrations are associated with optical phonons, the effect is called Raman scattering, whereas acoustical phonons are associated with Brillouin scattering.

All these effects are a result of the material response due to the high signal power. Using a limited signal power, these effects can have little to no impact.

Capacity crunch.

Today's long-distance optical telecommunications systems are based on SMFs. These systems have already taken advantage of all degrees of freedom offered to light wave in a single-mode fiber, namely, frequency, polarization, amplitude, and phase. Further multiplicative growth must explore new degrees of freedom that do not exist in SMFs. Due to the fast growth of capacity requirement of optical networks, it has been foreseen that future bandwidth demands will exceed the maximum achievable capacity of SMF-based networks due to fiber nonlinear effects [Mitra and Stark, 2001; Mecozzi and Essiambre, 2012]. The term "capacity crunch" was first applied to communication networks at the start of the decade [Agrawal, 2012], and signaled the recognition that the transmission capacity of an optical fiber is not limitless. The capacity limit C in $\mathrm{bits/s}$ can be determined by:

$$C = B\log_2\left(1 + \frac{e^{-(I/I_0)^2}I}{I_\text{n} + (1 - e^{-(I/I_0)^2})I}\right) \tag{1.55}$$

B is the spectral bandwidth in Hz, I is the initial signal intensity, I_n is the noise intensity and I_0 the nonlinear intensity scale indicating the departure from the linear behavior. Once the maximum capacity of individual fibers is reached, the "install more cables" approach can be adopted but is probably not the best solution in terms of cost. Therefore, a new approach giving a more robust solution is already under research. As mentioned in the previous section, the SDM provides an additional degree of freedom thanks to the multiplicity of modes presented in the FMFs/MMFs, or the number of cores of the MCFs.

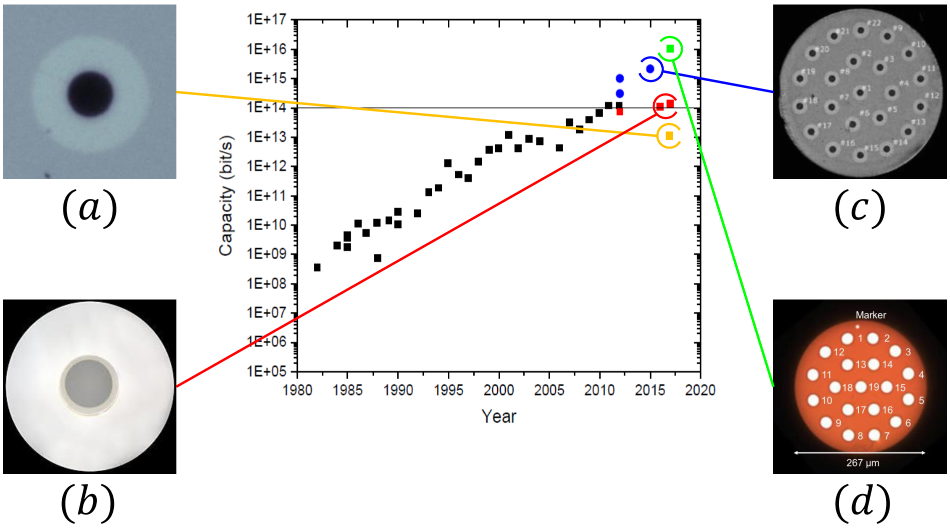

FIGURE 1.21: Demonstration of capacity increase of the data transmission from 1980 to the present. The capacities obtained using the SDM and MDM techniques are highlighted by the colors, with a example of the used fiber: (a) air-core fiber, (b) graded-index FMF, (c) 22-core single-mode MCF and (d) 6-modes 19-core MCF.

Although we did not plan any telecommunication transmission during this thesis, it fits well to mention some of the highest achieved rates till this day as our work is based on the FMFs for MDM transmissions. Figure 1.21 shows the evolution of the maximum capacities of the optical transmission networks with these different used technologies: MDM transmission based on the use of FMFs is already under tests. (a) In 2018, a 12 OAM mode MIMO-free transmission over a 1.2 km air-core fiber was demonstrated, with a total aggregate capacity of 10.56 Tbit/s [Ingerslev et al., 2018]. (b) In the same year, a graded-index few-mode fiber was used to demonstrate a net transmission rate of 138 Tbit/s at a spectral efficiency of 34.91 bit/s/Hz over 590 km [Weerdenburg et al., 2018]. The SDM technique using MCFs is also a subject of many study. (c) In 2015, a 2.15 Pbit/s transmission over 31 km of a homogeneous 22-core single-mode multi-core fiber was demonstrated [Puttnam et al., 2015]. In some cases, both SDM and MDM techniques are combined in order to achieve higher capacity rates. In 2018, ultradense SDM transmission was used for a 11.3 km 6-mode 19-core fiber using the C+L band, achieving a record fiber capacity of 10.16 Pbit/s with an aggregate spectral efficiency of 1099.9 bit/s/Hz [Soma et al., 2018].

1.4 Conclusion: Thesis frame

This chapter was dedicated to recall the basic notions needed in order to better evaluate the work presented in the next chapters of this manuscript. Starting from the simple guiding mechanism inside a conventional or micro-structured optical fiber (TIR, MTIR), to the different types of solutions of the propagation equations descendant from the Maxwell equations. These solutions helped us to demonstrate that light beams propagate inside any fiber verifying specific conditions, creating the basis of vector modes. We then used this basis in order to form others, yet more practical and usable modal basis. If the fiber fits the weak guiding approximation, the LP basis can be used. We can also choose to operate using the OAM basis, which presents its own characteristics according to the used fibers.
Once the mode basis was detailed, we described the relation between the optical fibers and the telecommunications field, detailing the fiber amplifiers and the amplification systems, going through the different types of multiplexing (WMD, PDM, SDM) and the different factors limiting the actual transmission networks, from the different types of dispersion (chromatic, modal, polarization) to the multiple nonlinear effects (Kerr, SPM, XPM) inside the core of the fiber.
Due to this capacity limit, solutions must be searched for and theories are being investigated in order to push further all the limits, such as SDM using MCFs or FMFs. This technology faces two major challenges before it can be commercially used in new transmission networks: the first resides in the detection of the modal content and quantifying the inter-mode coupling (in the case of FMFs) or the inter-core coupling (in the case of MCFs), while the second challenge represents the ability to equally amplify the different spatial channels (FMF's modes, MCF's different cores).
In the following chapters of this work, we will introduce a new modal content detection method able to sort an output optical signal of a tested FMF and separate its different modes, while giving full information about the weight of each mode and the coupling between them. In addition, we will explore a new type of FM-EDFAs capable of equally amplifying a number of modes.

Chapter 2

Modal detection methods

2.1 Introduction

SDM transmissions based on MCFs or mode division multiplexing (MDM) based on FMFs have the potential for increased capacity and avoid the upcoming saturation described in section 1.3.5. In the simplest approximation, a MCF with N cores is thought of as N independent parallel channels, each being the equivalent of a SMF link. The same approximation can be done for a FMF guiding N modes, as the different modes can be utilized as independent channels. This approximation is insufficient, apart from very short links: the cores of a MCF generally couple among each other leading to energy transfer between cores also known as inter-core X-talk. Similarly, the different modes of a FMF couple among each others. The level of X-talk will hence dictate the length of the fiber than can be used for a given modulation format and the level of complexity of the DSP that has to be applied at the fiber end. The X-talk is a function of the effective index differences between modes (here, the modes of 2 different cores) and also the overlap integral between them. This is explained by the coupled-mode theory [Snyder, 1972]. This parameter is quite sensitive to strain, temperature, etc. which must be expected to vary both as a function of distance and time. In order to achieve efficient MDM transmission networks, a major concern should be taken into account: what is the interaction between these new channels ?
In this thesis, we focused on the MDM technology based on the use of FMFs where the HOMs would be explored to act as separated transmission channels. To be able to answer this question, we must have the knowledge of the modal content of the fiber: how the X-talk between degenerated modes within a mode family evolve in time, a mode family being a grouping of modes whose effective indices are very close (the two polarization states of the modes $\mathrm{LP}_{1,1}^{(e)}$ and $\mathrm{LP}_{1,1}^{(o)}$, for example). In addition to that, we must know how the X-talk between any two mode families evolves in time. For that, we will describe in this chapter the different used methods to analysis and study the modal content of a FMF. We will then introduce our approach to characterize the content of a FMF inspired by the previous works, and describe it in great detail, from the experimental setup all the way to the data analysis.

2.2 The transfer matrices

The propagation of waves in heterogeneous media, such as the optical fibers, is a very fundamental problem of optical physics. A deeper approach for the study of complex media lies in the TM retrieval. The TM gives access to the single and the multiple-coupling components and the input field - output field correlations. This feature can be used in order to access the mode content of the fiber and the X-talk between the different modes. In this section, we will describe the mathematical origins of the TM. We will show that, regardless of the nature of any transitive media, being a scattering medium or an optical fiber, as long as we stay in a linear regime, it is possible to model the propagation of the light within it in a very simple way. In other words, the medium is considered as a black box, having a specific number of inputs and outputs linked by a defined channel fully described by this matrix.

2.2.1 Singular value decomposition

Before jumping into the mathematical demonstration of the transfer matrices, we will revisit a tool of linear algebra that will be used extensively during the different detailed works in order to offer a better understanding of this calculation method. The Singular Value Decomposition (SVD) is a generalization of the matrix diagonalization process. The diagonalization of a matrix $\boldsymbol{L}$ is only possible if it can be expressed as $\boldsymbol{L} = \boldsymbol{JEJ}^{-1}$. By definition, the matrix $\boldsymbol{E}$ is a diagonal matrix and $\boldsymbol{J}$ is an invertible square matrix, therefore this process only makes sense for square matrices. In contrast, the SVD can be applied to all matrices of any dimensions, breaking up a matrix $\boldsymbol{M}$ of $m \times n$ dimensions into 3 matrices as following:

$$\boldsymbol{M} = \boldsymbol{UHV}^{\dagger} \tag{2.1}$$

The symbol † represents the conjugate transpose operation in case of a complex matrix. The matrix $\boldsymbol{U}$ is an orthogonal unit matrix representing the basis of the output modes while $\boldsymbol{V}$ is an orthogonal unit matrix representing the basis of the input modes. We should mention that in contrast with the ordinary diagonalization, $\boldsymbol{U}$ and $\boldsymbol{V}$ are different matrices, which can have different dimensions m and n. $\boldsymbol{H}$ is a diagonal matrix with positive real terms λ_i called singular values [MIT OpenCourseWare, 2016]. A simple illustration of this process is shown in Figure 2.1.

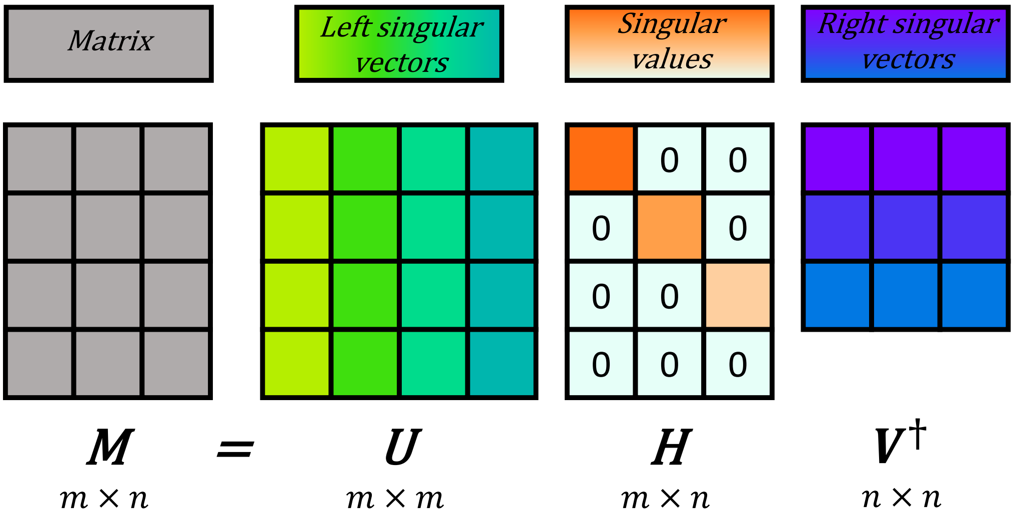

FIGURE 2.1: SVD process of a $m \times n$ matrix.

The values of the terms λ_i represent the amplitude transmission of each of the independent modes of the system. The normalized singular values are given by:

$$\bar{\lambda}_\mathrm{i} = \frac{\lambda_\mathrm{i}}{\sqrt{\frac{1}{N}\sum_\mathrm{i} \lambda_\mathrm{i}^2}} \tag{2.2}$$

Where N is the number of the singular values. For that, SVD became a widely used technique to decompose a matrix $\boldsymbol{M}$ and expose many of its useful and interesting properties. It is commonly used in the analysis of physical systems, such as waveguides and optical fibers. SVD allows the break down of the propagation waves into independent transmission channels [Popoff, 2012]. Each channel is characterized by its proper input and output modes and its proper transmission energy fraction: the first channel has a transmitted amplitude of $\lambda_1{}^2$. Its input mode is the first singular vector of the matrix $\boldsymbol{V}$, located on its first row, while its output mode is the first singular vector of the matrix $\boldsymbol{U}$, located on its first column.

It is very important to note that the channels given by the SVD do not necessarily correspond to physical modes, being the proper modes of the fiber. A first reason is the orthogonality made by the SVD: as described above, the singular vector matrices $\boldsymbol{U}$ and $\boldsymbol{V}$ are orthogonal , which is not necessarily the case for an optical fiber: theoretically, the guided modes of a fiber are orthogonal (in the weakly guided approximation), however, due to the different manufacture imperfections, bends, twists... this orthogonality is generally broken and we can have some coupling between the different modes. During our studies, we used this method on FMFs guiding no more than 30 modes. This approach has been successfully used on MMFs guiding more than 400 modes [Carpenter, Eggleton, and Schröder, 2016].

2.2.2 The scattering matrix

In order to better understand the TM of a system, we will start with a brief explanation of the general scattering matrix (SM). The SM provides the complete description of the link between the input flux coming at a given system and the output flux scattering away from it. This connection is provided by determined input-output channels. A better description can be provided using a model with a phase-coherent disordered region connected to 2 lossless waveguides as illustrated in Figure 2.2 [Beenakker, 1997; Rotter and Gigan, 2017].

The SM is defined as the complex matrix that connects the input expansion coefficients with the output coefficients [Rotter and Gigan, 2017]. As shown in Figure 2.2, a^+ and b^- are the amplitudes of the incoming waves to the disordered media, whereas a^- and b^+ are the amplitude of the outgoing waves. Thus, the coefficient vector describing the input amplitudes can be written as [Beenakker, 1997]:

$$c^{\mathrm{in}} = (a_1^+, a_2^+, \dots a_N^+, b_1^-, b_2^-, \dots b_N^-) \tag{2.3}$$

and the output amplitudes can be written as:

$$c^{\mathrm{out}} = (a_1^-, a_2^-, \dots a_N^-, b_1^+, b_2^+, \dots b_N^+) \tag{2.4}$$

where the first N coefficients refer to the waves on the left side of the system and the second N coefficients represent the waves on the right side of the system. The

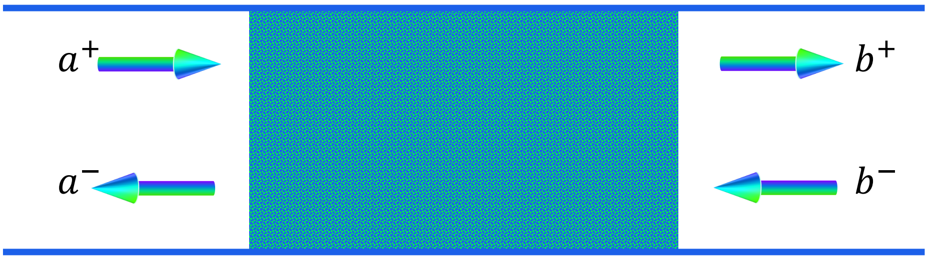

FIGURE 2.2: Illustration of the modeled disordered region between the 2 lossless waveguides [Beenakker, 1997].

SM, $\boldsymbol{S}$, can then be defined as the link factor between these 2 matrices [Beenakker, 1997; Rotter and Gigan, 2017]:

$$c^{\text{out}} = \boldsymbol{S}c^{\text{in}} \tag{2.5}$$

Thus $\boldsymbol{S}$ is a $2N \times 2N$ complex matrix that can be expressed as:

$$\boldsymbol{S} = \begin{pmatrix} r & t' \\ t & r' \end{pmatrix} \tag{2.6}$$

The 4 elements of $\boldsymbol{S}$ are $N \times N$ matrices: r are the reflection amplitudes of the input modes from the left and r' are the reflection amplitudes of the input modes from the right, while t are the transmission amplitudes of the scattering from left to right and t' are the transmission amplitudes of the scattering from right to left. Due to the flux conservation proprieties of the scattering theory [Rotter and Gigan, 2017], the matrix $\boldsymbol{S}$ is a unitary matrix. As a consequence, $\boldsymbol{S}^{\dagger}\boldsymbol{S} = 1$ and the 4 Hermitian matrices $tt^{\dagger}$, $t't'^{\dagger}$, $1 - rr^{\dagger}$ and $1 - r'r'^{\dagger}$ all have the same set of eigenvalues $T_1, T_2, \ldots T_N$, with values between 0 and 1 (in a flux normalized basis) [Beenakker, 1997]. Using the polar decomposition [Mello, Pereyra, and Kumar, 1988; Martin and Landauer, 1992], based on the singular value decomposition of $\boldsymbol{S}$, the later can be written as:

$$\boldsymbol{S} = \begin{pmatrix} U & 0 \\ 0 & V \end{pmatrix} \begin{pmatrix} -\sqrt{1-T} & \sqrt{T} \\ \sqrt{T} & \sqrt{1-T} \end{pmatrix} \begin{pmatrix} U' & 0 \\ 0 & V' \end{pmatrix} \tag{2.7}$$

where U, V, U' and V' are 4 unitary matrices of $N \times N$ and $T = \text{diag}(T_1, T_2, \ldots T_N)$ is a diagonal matrix of $N \times N$ dimensions containing the transmission eigenvalues on its diagonal.

2.2.3 The transmission matrix

In contrast with the SM connecting the input waves into any medium to the output waves scattered away from this medium, the TM is the matrix linking all the waves on one side (left or right) to their corresponding waves on the other side (right or left), through defined channels. Thus, instead of the c^{in} and c^{out} given by Equations 2.3 and Equation 2.4, we can define c^{left} and c^{right} as

$$c^{\text{left}} = (a_1^+, a_1^+, \dots a_N^+, a_1^-, a_1^-, \dots a_N^-) \tag{2.8}$$

$$c^{\text{right}} = (b_1^+, b_1^+, \dots b_N^+, b_1^-, b_1^-, \dots b_N^-) \tag{2.9}$$

where the first N coefficients refer to the incoming waves and the second N coefficients represent the outgoing waves. Similarly to the SM, the TM, $\boldsymbol{M}$, can then be defined as the link factor between these 2 matrices [Beenakker, 1997]:

$$c^{\text{right}} = \boldsymbol{M} c^{\text{left}} \tag{2.10}$$

Thus $\boldsymbol{M}$ is a $2N \times 2N$ complex matrix. Using the same polar decomposition as for the Equation 2.7, $\boldsymbol{M}$ can be expressed as:

$$\boldsymbol{M} = \begin{pmatrix} V & 0 \\ 0 & V'^{\dagger} \end{pmatrix} \begin{pmatrix} \sqrt{1/T} & \sqrt{1/T \; - 1} \\ \sqrt{1/T \; - 1} & \sqrt{1/T} \end{pmatrix} \begin{pmatrix} U' & 0 \\ 0 & U^{\dagger} \end{pmatrix} \tag{2.11}$$

We should note that the TM present a serious convenient when compared to the SM: the TM of a number of medium separated by lossless spaces (or even not separated) is the product of their individual TMs : $\boldsymbol{M} = \boldsymbol{M}_1 \boldsymbol{M}_2 \dots \boldsymbol{M}_N = \prod_{n=1}^{N} \boldsymbol{M}_n$. This concept can be extended to the study of optical fibers. The TM thus links the electric field at the entry side of fiber to the electric field at the exit side of it. Such a matrix model is not new. Many approaches use matrices to describe the propagation of waves or their transport properties as will be described in the following sections.

2.3 Signal modal content detection methods.

The questions raised in the introduction of this chapter fueled the research for an efficient method to access the modal content of FMFs, quantify the X-talk between the different modes and give a time-evolving description to it. In the following sections we will point out some of the methods already reported in the literature.

2.3.1 The C^2 method

As mentioned before, several methods exist to characterize at least partially the information on the modal content of a FMF. A simple example is to observe the trace obtained by using a reflectometer, capable of showing the number of supported modes due to their DGD. The cross-correlation imaging, or more simply the C^2 imaging, is an optical low-coherence interferometry method, based on the cross-correlations between the fiber output and an external reference beam [Schimpf, Barankov, and Ramachandran, 2011]. C^2 is a measure of similarity of two signal beams as a function of the displacement of one relatively to the other.

C^2 analyzes the slowly varying envelope of the signal which contains the necessary information in order to obtain the correct modal weights, profiles, relative group-delays, and dispersion of all the modes without making any assumptions about the optical properties nor the modal content of the FMF under test. Figure 2.3 shows a schematic of the experimental setup, which is inspired by a Mach-Zehnder interferometer.

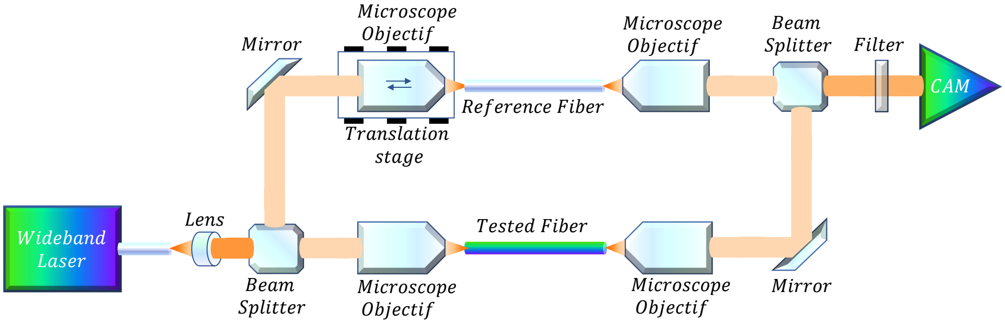

FIGURE 2.3: Schematic of the C^2 experimental setup.

The tested fiber is placed in the first arm of the interferometer, while a reference fiber is placed in the other arm. In the reference arm, a well controlled translation stage is used to apply optical path variations to the reference beam, controlling both the fiber input and the coupling lens in order to ensure the stability of the reference beam through the process. The optical path variations correspond to different temporal delays between the beams of the 2 arms: these variations are used to scan a span of temporal delays, registering an interference image formed by the collimated beams of both arms at the camera for each scanning step. The pixels of the camera form the spatial resolution of this method: the stack of images enable the trace of the cross-correlation between the 2 arms for each pixel. The match between the controlled temporal delay and the DGD of a HOM of the tested fiber is visualized with a peak on the cross-correlation trace. The main advantage of this method is to be able to compare the tested fiber with a fiber with known dispersion. Also, interference between HOMs does not appear in these measurements if a SMF is used at the reference arm, which can simplify the analysis. The electric field registered by the camera is given by a superposition of the reference field and the tested fiber output field. In the frequency domain, this field can be written as:

$$E_{\mathrm{m}}(x,y,\omega) = \sum_{\mathrm{m}=1}^{N} \alpha_{\mathrm{m}} e_{\mathrm{m}}(x,y) A_{\mathrm{m}}(\omega) e^{i\phi_{\mathrm{m}}} + e_{\mathrm{r}}(x,y) A_{\mathrm{r}}(\omega) e^{i\phi_{\mathrm{r}}} \tag{2.12}$$

where m is the HOM order for N existing HOMs, α_{m} is the real modal weight, e_{m} and e_{r} are the near-field images of the transverse modes for the tested fiber and the reference fiber respectively, with A_{m} and A_{r} as their amplitudes and ϕ_{m} and

ϕ_r as their phases. Thus, at any given delay stage, the intensity image captured by the camera will be :

$$I(x,y) = \int_{-\infty}^{+\infty} |E_{\mathrm{m}}(x,y,\omega)|^2 \frac{d\omega}{2\pi} \tag{2.13}$$

Knowing that the cross-correlation phase varies slowly as a function of the delay compared to the phase mismatch between the reference arm and the tested fiber arm, the intensity $I(x,y)$ can thus be expressed as [Schimpf, Barankov, and Ramachandran, 2011]:

$$I(x,y) = I_0(x,y) + \sum_{\mathrm{m}=1}^{N} 2\alpha_{\mathrm{m}} \sqrt{i_{\mathrm{r}}(x,y) i_{\mathrm{m}}(x,y)} c_{\mathrm{mr}} |\tau - \tau_{\mathrm{mr}}| \cos(\Phi) \tag{2.14}$$

where I_0 is a background term, i_{r} and i_{m} are the normalized intensity distributions of the reference and the HOM of order m. c_{mr} is the cross-correlation function between the variable delay τ and the group delay difference τ_{mr}. Φ is a phase term. The envelope trace of c_{mr} contains the required information about the dispersive properties of the modes. For fiber modes with distinct dispersive behavior, the peaks present in the envelope will be different for each mode. Figure 2.4 illustrates an expected envelope trace for a 2 modes fiber. This method offer limited information about the modal content of a FMF. However, as we will be discussing in the following sections, more advanced methods exist offering better and more complete information about the guided modes and their characteristics.

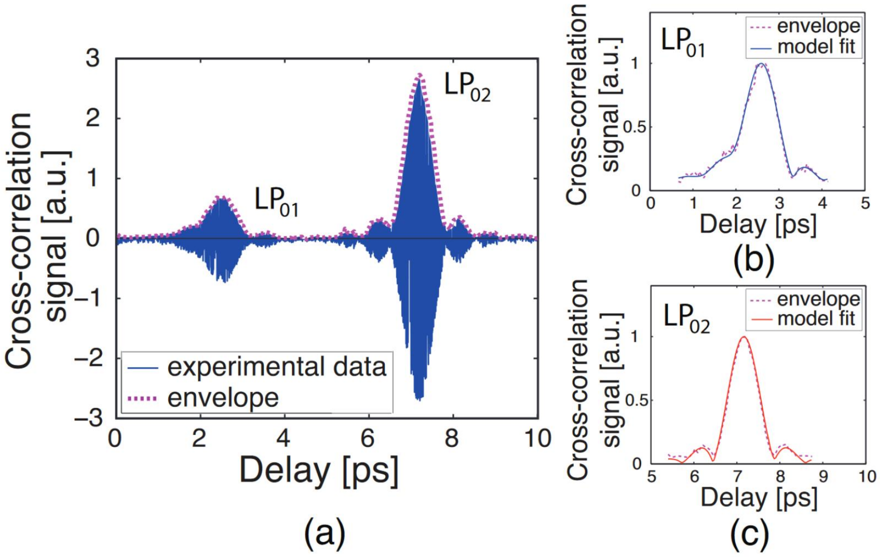

FIGURE 2.4: C^2 experimental trace for a 2 modes fiber: (a) Cross-correlation trace for the entire image, (b) the envelope of the experimental data for the first peak corresponding to the LP_{01} with a model fit of the mode and (c) the envelope of the experimental data for the second peak corresponding to the LP_{02} with a model fit of the mode [Schimpf, Barankov, and Ramachandran, 2011].

2.3.2 The S^2 method

The spatially and spectrally resolved imaging technique, known as S^2 measurement technique, is capable of quantifying the number and type of modes propagating in a fiber. In fact, it is an interferometric method that studies the spatial and spectral interference between the different propagating modes [Nicholson et al., 2008]. Using this technique, one can access specific information about the modal content of the studied fiber: the profiles of the mode fields, the optical powers proportion of each mode and the beat spectrum from which we can deduce group delay differences between modes.
During S^2 measurements, we inject light into a FMF (or any MMF) in a specific way in order to excite several HOMs, either using a mode converter, or using a light beam slightly shifted from the center of the fiber's core. At the other end of the fiber, we collect the light on a transverse surface, mainly a charge-coupled device (CCD) camera, perpendicular to the face of the fiber: this is the spatial resolution. We also have to use a tunable laser source to scan over a range of several wavelengths: this is the spectral resolution. An example of the experimental setup is presented in figure 2.5.

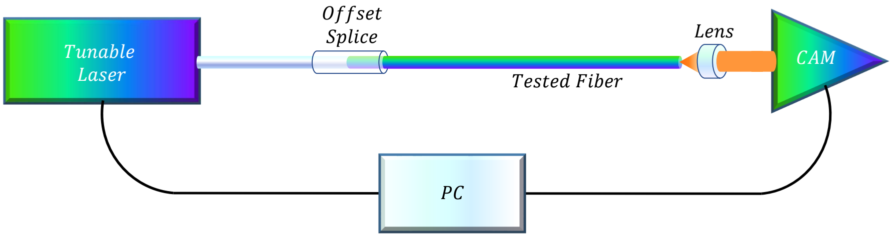

FIGURE 2.5: Schematic of the S^2 experimental setup.

The images taken contain all the spectral and spatial information, but we have to take a picture for each wavelength (generally more than one picture per wavelength in order to average them), and as a result we will have a large number of images to analyze in order to access the desired information.

Conventional S^2: If we consider that the majority of the beam power is guided by the fundamental mode (with field E_0), the HOMs field E_{m} are related to the fundamental mode field E_0 by the constant α_{m} [Nicholson et al., 2008]:

$$E_{\mathrm{m}}(x,y,z,\omega) = \alpha_{\mathrm{m}} \cdot E_0(x,y,z,\omega) \exp^{i\omega\tau_{\mathrm{m}}} \tag{2.15}$$

where τ_{m} is the propagation time delay between the HOM number m and the fundamental mode, given by $\tau_{\mathrm{m}} = L\Delta n_{\mathrm{g}}/c$ with L the fiber length and Δn_{g} is the difference between the group indices. This expression is only valid for short spectral range, where the modes normalized field profiles are independent of z and ω and the group indices are also independent of ω for all modes. Due to the fact that the HOMs power is relatively low compared to the fundamental mode, the interference between the HOMs can be neglected and we only take into account the interference between the dominant mode and each of these modes. The total intensity can be described by

$$I(x,y,\omega) = I_0(x,y)\left(1 + \sum_{\mathrm{m}=1}^{N} \alpha_{\mathrm{m}}^2 + 2\sum_{\mathrm{m}=1}^{N} \alpha_{\mathrm{m}} \cos(\omega\tau_{\mathrm{m}})\right) \tag{2.16}$$

I_0 is the optical intensity of the dominant mode and N is the number of the guided modes. We can notice that in this equation, only one constant term is present and several oscillating terms. These oscillating terms express the beats between the fundamental mode and the HOMs. Figure 2.6 shows the resulting spectrum of a S^2 measurement.

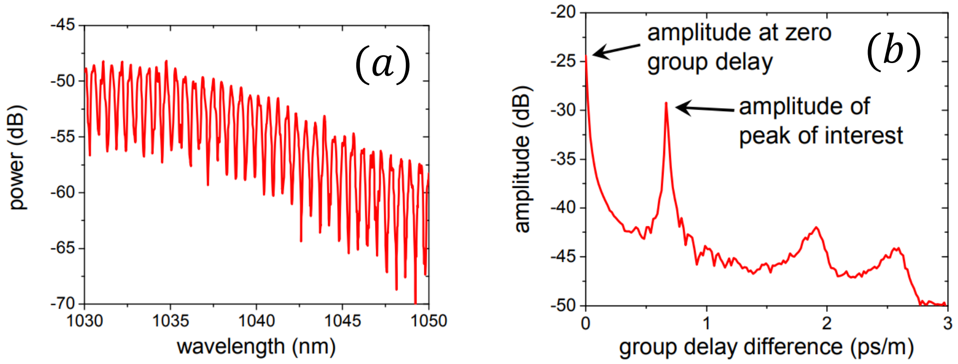

FIGURE 2.6: (a) Optical spectrum measured at an arbitrary (x,y) point and (b) the Fourier transform of the optical spectrum in (a) showing multiple beat frequencies [Nicholson et al., 2008].

However, the classical S^2 approach presents several limitations:

- We have seen that the S^2 technique can deliver good results in the case where the powers of the HOMs are relatively low compared to the power of the fundamental mode, which allows us to neglect the interference between the HOMs, and obtain a beat spectrum of N peaks if the number of these modes is N. However, this approximation is not entirely valid since even with low powers, the interference between the HOMs cannot be neglected and additional peaks can be seen in the beat spectrum.
- Another limitation of this technique is the fact that if several beats have very close frequencies, the peaks related to these beats concur and are almost confused in the beat spectrum. These 2 beats seem to have one peak and it will be very difficult to separate them, especially if they are spatially

correlated.

Advanced S^2 analyses were developed in order to solve these problems. We will describe briefly their theory without deep details because we will not use any of these methods during the different stages of this work.

Advanced S^2, Principal Component Analysis: Theoretically, each mode family should have a consistent beating with itself, different from the other mode families interactions. Therefore, the correlation between the data points can be explored for additional information that could not be accessed to using the classical approach. The principal component analysis (PCA) decompose the measured data in principal components of beat figures and their associated spectrum, based on their correlation [Sévigny et al., 2014; Li and Wang, 2014]. This method can separate mixed beats at the same group index differences, mixed using the classical S^2 analysis, due to their lack of spatial correlation.

Advanced S^2, Independent Component Analysis: Although the PCA can isolate the uncorrelated beats, the measured data presents generally some correlation between different beats, making them "immune" to the PCA step and thus the beats will remain mixed after this step. These mixed signals can be separated assuming their information exchange is minimal, thus making them kind of independent. This is defined as the independent component analysis (ICA). This method can be applied on the mixed beats post the PCA in order to separate them into uncorrelated independent signals. [Sévigny et al., 2014].

2.3.3 Selective Mode Excitation

Precise modal excitation in optical fibers is of interest for improving the transmission capacity of FMFs and MMFs. Using a phase mask containing regions of either 0 or π phase delays that takes the shape of the far-field phase of the desired modal pattern, selective mode excitation has been demonstrated [Carpenter and Wilkinson, 2011; Ip et al., 2011]. In 2012, Carpenter proposed a method based on highly selective binary phase masks calculated using techniques from computational holography. The generated mode masks have near perfect theoretical quality under the constraints of the actual operating system [Carpenter and Wilkinson, 2012]. That technique employed the use of a simulated annealing based algorithm to create masks having the highest possible overlap with the far-field of the mode for a fixed beam waist incident on the screen of the spatial light modulator (SLM) for all the modes. Hence, there is no need of physical modification of the setup in order to excite different modes, but a simple reprogramming of the SLM can adapt the mask to the mode waist. Figure 2.7 illustrates the experimental setup used for this method.
A Mach–Zehnder modulator (MZM) is used to modulate the beam of the C-band tunable laser controlled by a vector network analyzer (VNA). A variable optical attenuator (VOA) is used to control the beam power at all time. The polarization controller aligns the polarization state of the beam with the polarizing beam splitter (PBS) axis. The SLM modifies the beam before its injection in the tested fiber in the Fourier plane. The emerging beam is received at a photodiode connected to the VNA. The modal characteristics of the fiber were investigated over

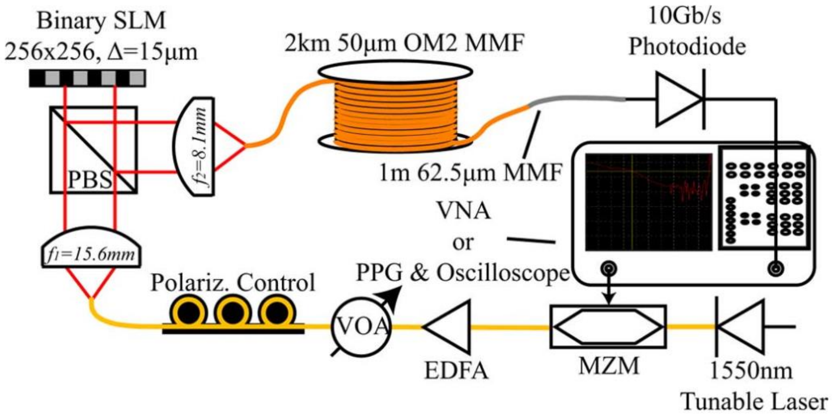

FIGURE 2.7: Illustration of the experimental setup used to characterize a MMF by selective mode excitation [Carpenter and Wilkinson, 2012].

the C-band for 2 km of OM2 grade MMF having a core of 50 μm. In this paper, the rotational dependence of modal performance, a study of the chromatic dispersion and a study on the improvement of the modal dispersion were also investigated but we will limit ourselves with the modal characterization study for this manuscript.

In an ideal fiber, the guided modes can be organized into mode groups having degenerate propagation constants as shown throughout Chapter 1. In reality, this degeneracy is broken due to the fabrication imperfection of the fiber, specially on the core-cladding interface, bends, twists and all the other sorts of stresses on the fiber. However modes within a mode group still share almost identical propagation constants, leading to strong mode coupling within the same family. For the HOMs which have a larger proportion of their field propagating in the cladding, this difference become higher and higher which leads to a larger spread of group delays within a mode group. By individually launching each mode, it is possible to measure the modal characteristics of the fiber. Figure 2.8 shows the results of a measurement using this method.

We can see that for the low order modes, this method can detect them easily (one peak per mode group) due to the difference between their propagation constants resulting in a different time delay. The mode groups having closer propagation constants are mixed in the same peak. This is the same problem faced for the classical S^2 method 2.3.2. In addition to that, higher order mode groups have more diffuse peaks with less consistent mode group propagation delay (wide spread peaks).

2.3.4 The transmission matrix based methods

The characterization of the transmission proprieties of various mediums using the TM has been the subject of many studies. In 2010, Popoff reported a method to measure experimentally the monochromatic TM of a thick random scattering

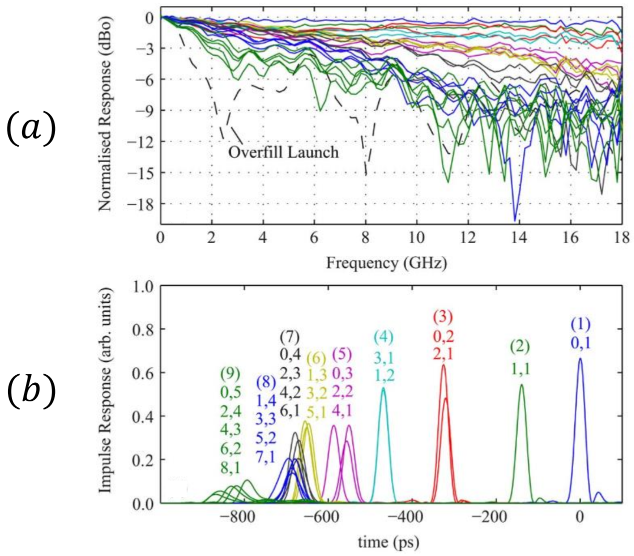

FIGURE 2.8: a) Normalized frequency response for all 25 modes at 1548.5 nm. (b) The Fourier transform of those same frequency responses representing the impulse response in the time-domain [Carpenter and Wilkinson, 2012].

sample using a SLM to control the injected beam through the tested medium [Popoff et al., 2010a]. Later that year, the same team performed an imaging experiment through an opaque material using the same method [Popoff et al., 2010b]. These works won't be detailed in this manuscript as they are not applied directly on optical fibers, but they are considered as cornerstones for the use of the TM in order to access the information on how light propagates through a disordered media. Many researches were inspired by these works and interested in adapting such an experimental method to characterize optical fibers. In 2011, a similar method was proposed to better understand the light propagation through a MMF [Cizmar and Dholakia, 2011]. In this work, a SLM was used to manipulate the light shape before it enters the fiber so the output beam can have a specific shape. We won't be detailing this work in this manuscript since their was no clear measurement of the TM, but only a beam shape manipulation combined with an optimization algorithm to obtain certain shapes at the output end of the fiber.

In 2014, Carpenter was able to measure the TM of a fiber guiding 110 spatial and polarization modes using 2 SLMs at both ends of the fiber [Carpenter, Eggleton, and Schröder, 2014]. The experimental setup is illustrated in Figure 2.9.
An ASE source is filtered and polarized to approximate a high-bandwidth channel. A polarization controller is then used to ensure the polarization state of the incoming beam is split evenly between two regions of the SLM, corresponding to the horizontal and vertical polarization axes of the system. Each mode of the fiber in each polarization is launched one at a time into the fiber under test. At the receiving end, a symmetrical design permits to a second SLM to play the role of a mode demultiplexer, except some of the power entering the system is tapped off with a beam splitter (BS) so it can be directed towards a polarization diverse imaging system. For each mode in each polarization, the receiver SLM

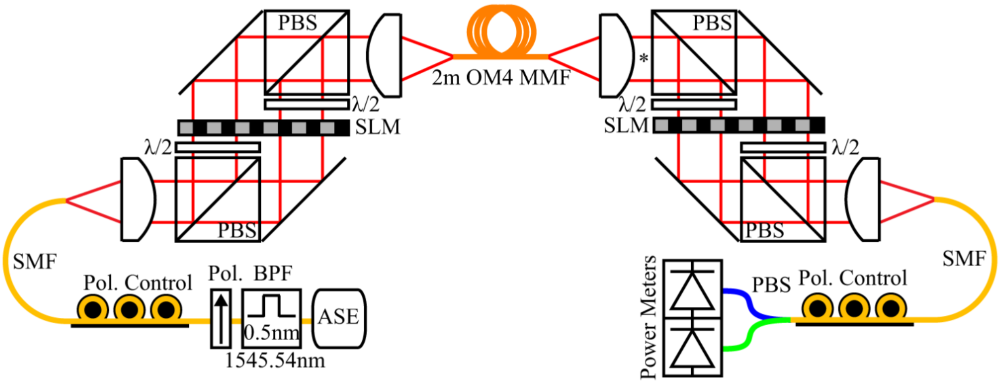

FIGURE 2.9: The mode decomposition and mode generation setup. The asterisk marks the place at which the beam is sampled by the polarization diverse imaging system [Carpenter, Eggleton, and Schröder, 2014].

displays phase masks for each mode basis and polarization one at a time to measure the amplitude of each mode. The phase of the modes within a polarization is then found by adding together the phase masks for the different basis modes with varying phase shifts and measuring the variation on a power meter. When the phase mask is conjugated with the incoming beam, the power will be maximized. However in order to know how different launched modes will interfere, it is necessary to define all the phases of the TM relative to the same phase reference. To achieve this, each mode at the transmitter is superposed with a reference mode, being the fundamental mode due its polarization only degeneracy. The corresponding phase masks for the mode of interest and the reference mode are interfered on the SLM at the receiver to measure their relative phase.
The tested fiber was a $2\ \mathrm{m}$ length of OM4 grade $50\ \mu\mathrm{m}$ core MMF guiding up to 110 spatial and polarization modes. The results are presented in Figure 2.10(a) that shows the amplitude of the TM, where the white lines delimit the different degenerated groups, according to their propagation constants: the modes of each mode group have close propagation constants, thus are very likely to couple during the propagation. Meanwhile, the difference of the propagation constants between these mode groups is large enough, so there is no important coupling between them. This can be seen on the diagonal blocks of the amplitude of the TM. Figure 2.10(b) shows the singular values given by the performed SVD on the TM. The singular values refer, by definition to the relative loss of the different channels [Carpenter, Eggleton, and Schröder, 2014]. We can see that the loss of the first 90 modes have approximately the same values, but the losses of the last 20 modes drastically increase. This increase is largely due to the last degenerated mode group being close to its cut-off at the used wavelength for this fiber.

In 2015, Ploschner reported a TM measurement for a commercial MMF guiding up to 500 modes at the measurement wavelength of $1064\ \mathrm{nm}$ [Plöschner, Tyc,

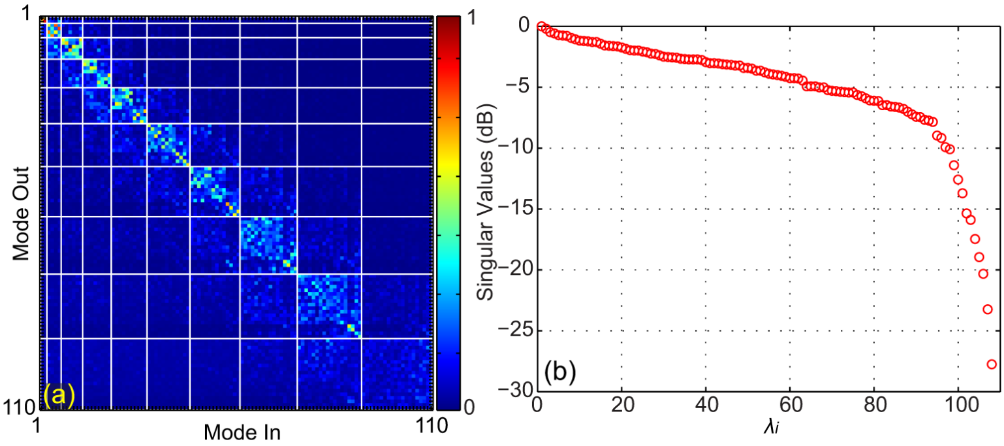

FIGURE 2.10: (a) Amplitude of the mode transfer matrix for all 110 modes. (b) Singular values of that mode transfer matrix representing mode dependent loss [Carpenter, Eggleton, and Schröder, 2014].

and Čižmár, 2015]. The experimental setup used for is measurement is presented in Figure 2.12. A SLM is used to split the initial laser beam into 3 separate paths. The first path is reflected by a mirror, then coupled into a SMF in order to be used as a reference beam for the image detection. The 2 other beams have their polarization states converted into orthogonal states and overlap using a series of HWP, polarization beam displacers, before traveling through a $4F$ telescope in order to have the spot at the fiber face matching the Fourier transform of the SLM plane. In order to obtain circular polarization states, a QWP is used before the fiber. The emerging beam travels through a second QWP to convert the polarization states back to linear, then it is combined with the reference beam emerging from the SMF using a BS. The 2 polarization states are then split using a PBS: one CCD camera is used to record the interference image of each polarization separated beam, thus having a simultaneous measurement for both polarization states.

In order to measure the TM, the SLM is used to scan the face of the tested fiber. Figure 2.12(a) shows the scanning method used by Ploschner, following an orthogonal grid of focalized spots called focal points. This method was used to characterize a 10 mm and a 100 mm long fiber, but due to the similarity of the results we will be limiting ourselves to the results of the 10 mm MMF. Figure 2.12(b) shows one third of the measured TM called M. Each row contains the amplitudes and the phases of all output focal points for each input focal points, presented on the column of this matrix. In order to better illustrate the measured TM, Ploschner used the theoretical calculated scalar modes of this fiber, presented in Figure 2.12(c), to create a conversion matrix T that will enable M to be expressed in the basis of the theoretical calculated modes using $M_0 = TMT^\dagger$, where M_0 is the TM expressed in the basis of its own modes and the $T^\dagger$ presents the transpose conjugate of T. T is illustrated in 2.12(d) and M_0 is presented in 2.12(e). The non diagonal behavior of M_0 is largely due to the unavoidable misalignments

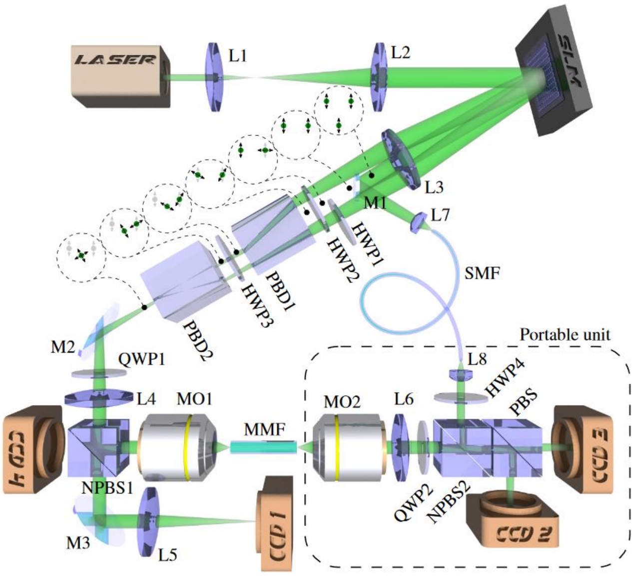

FIGURE 2.11: Experimental setup of the TM measurement method proposed by Ploschner [Plöschner, Tyc, and Čižmár, 2015].

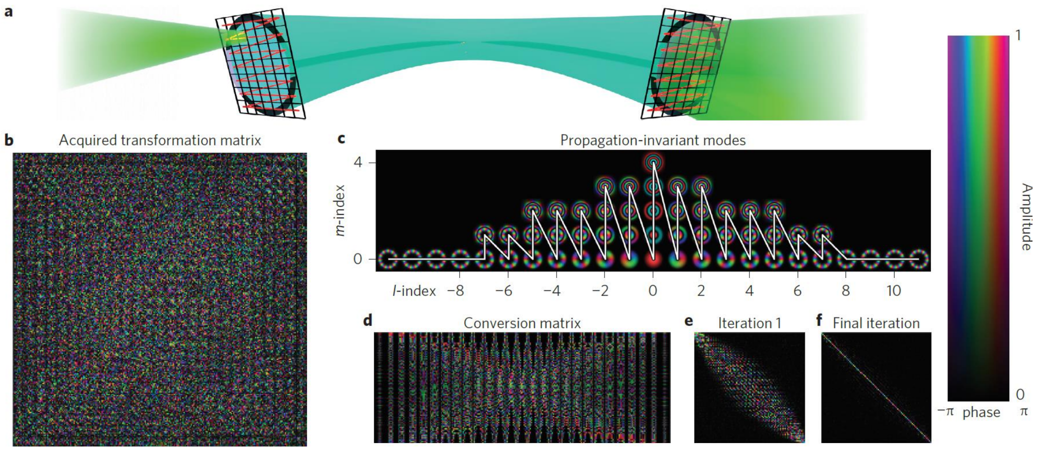

FIGURE 2.12: (a) Illustration of the input and output focal points, (b) experimentally measured TM M, (c) theoretical calculated fiber scalar modes, (d) conversion matrix T, (e) converted matrix M_0 before the optimization and (f) converted matrix M_f after the optimization. [Plöschner, Tyc, and Čižmár, 2015].

encountered in any experimental setup. Therefore an optimization algorithm is used to surpass the contributions of such misalignments. M_f is the TM delivered after the optimization process is completed, with a great diagonal behavior carrying over 93% of the total transmitted power [Plöschner, Tyc, and Čižmár, 2015].

In 2016, the Carpenter team reported a TM measurement of a 420 modes fiber, using basically the same experimental setup as in their 2014 work[Carpenter, Eggleton, and Schröder, 2016]. The ASE source was replaced by a tunable CW laser source, in order to extend the optical TM measurement into the time domain: a TM measurement was performed over a large bandwidth, spanning from $1525\ \mathrm{nm}$ to $1566.7\ \mathrm{nm}$, separated closely enough to be Fourier transformed in order to obtain TM as a function of time. The spatial characterization is insured by the SLM, while a swept-wavelength interferometry (SWI) gives access to the spectral/temporal dimension of the measure. The tested fiber was a $2\ \mathrm{m}$ of $62.5\ \mu\mathrm{m}$ core graded-index MMF (Thorlabs GIF625). Such a fiber supports 306 spatial and polarization modes organized into 17 degenerate mode groups at $1550\ \mathrm{nm}$. The results are presented in Figure 2.13.

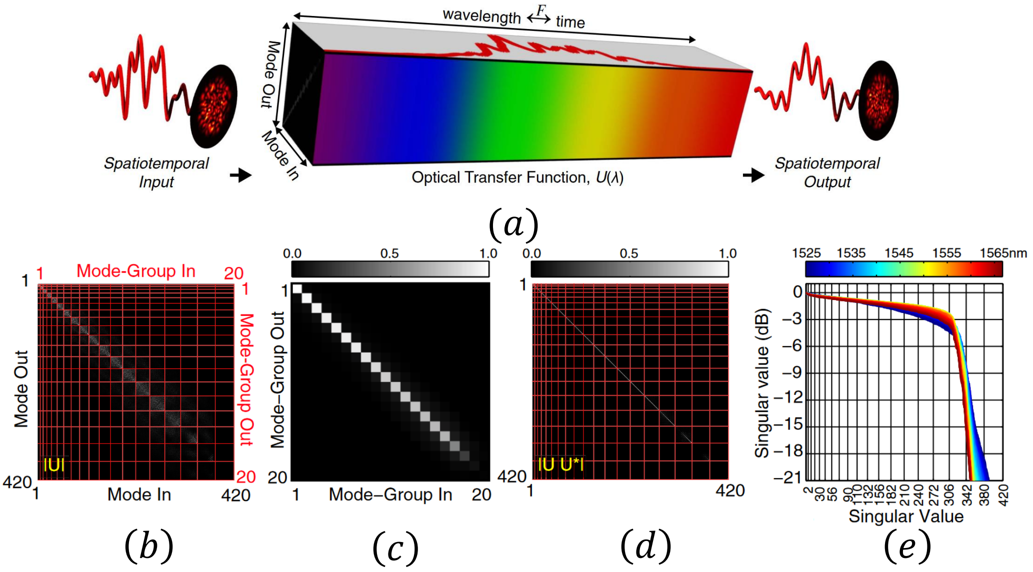

FIGURE 2.13: (a) Optical transfer function of a linear scattering medium. It consists of the optical TM measured as a function of wavelength, which can also be Fourier transformed into the time domain, (b) amplitude of the 420×420 optical transfer matrix, (c) transfer matrix of (b) summarized in terms of a 20×20 matrix of power coupling between the near-degenerate mode groups , (d) measured $|UU^*|$, (e) Wavelength-dependent singular values of the singular value decomposition of U [Carpenter, Eggleton, and Schröder, 2016].

One can see on Figure 2.13(b) that, similarly to their previous work, the mode groups are effectively independent with little to no coupling between them, while heavy coupling occurs inside a mode group delimited by the red lines. This can be verified by the diagonal blocks of the amplitude of the TM. Figure 2.13(c) shows a transfer matrix summarizing the 420×420 TM by representing each degenerate mode group as one element of the matrix: clearly, the coupling between these elements is weak, but increases gradually with the HOMs. Due to the fact that this basis also generates approximately unitary transfer matrices, they are also straightforward and stable to invert. This is verified on Figure 2.13(d) by the nearly perfect diagonal matrix resulting from the $|UU^*|$. The effect of the modal cut-off can be seen in all the graphs as the power seems fading along the diagonal.

The SVD resulting singular values are shown on Figure 2.13(e) with the spectral dependence illustrated by the different colors. Similarly to the previous study, the first 306 modes present close losses values, while the HOMs closer to their cut-offs see significant losses increase.

In 2018, Florentin reported a fast measurement of the "focusing matrix" of a 1.6 m long MMF guiding up to 104 modes per polarization using a common path reference. The measurement was performed at 1064 nm in less than 1 minute [Florentin et al., 2018]. Figure 2.14 shows the experimental setup used by Florentin to measure the TM. A continuous laser source at 1064 nm is used to generate the testing beam. The polarization of the beam is controlled using a PBS and a half wave plate (HWP), whereas its size is magnified using a first telescope. In order to shape the wavefront of the beam, a segmented deformable mirror is used.

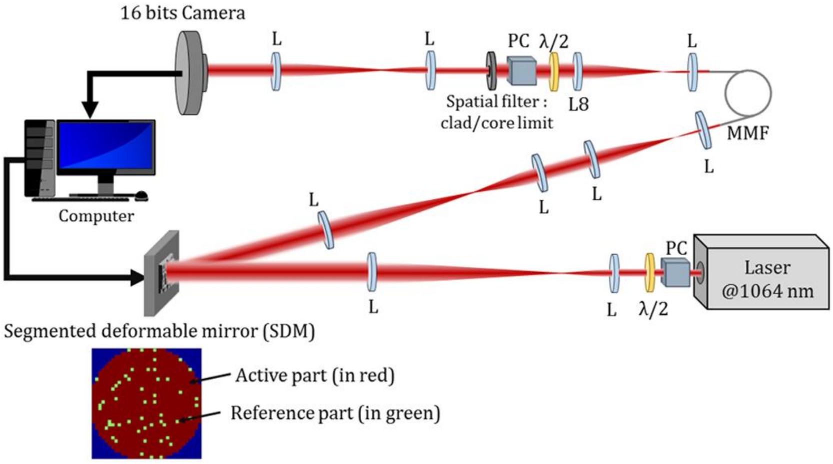

FIGURE 2.14: Experimental setup of the TM characterization based on the use of the common path reference [Florentin et al., 2018].

This method applies a common path reference, which means that the reference beam propagates through the fiber along side the signal beam. The reference beam was generated using 5% of the segmented deformable mirrors (50 mirrors), randomly distributed across the mirrors surface. The 50 reference mirrors displayed 4 different phase values so the phase can be retrieved using phase stepping interferometry. Thus, the reference output is formed by a combination of fiber modes that were excited by the beam reflected off these 50 mirrors: any other 50 mirrors result in another reference output. The rest of the mirrors (900 mirrors) are divided into a 34×34 binary basis, displaying each a random phase distribution. The beam propagates through a $8F$ lens scheme so the image of the mirrors in focused on the fiber input face. The emerging output beam is magnified and has its polarization controlled by a second set of PBS and HWP and is registered on the camera. The recorded images are used to express the TM of the system in a 900×16384 dimension, where 900 is the number of input phases and 16384 is the number of pixels of the used camera. The inset of Figure 2.14 shows an example of distribution of the pixels on the segmented deformable mirrors for respectively the reference (green) and shaped input wavefront (red). As a consequence of the common path reference, the reference field is random and unknown. Therefore the measured TM contains a contribution of the speckle field of the reference, as well as the real system TM as $TM = TM_{\text{real}} \times R$. However, keeping the same 50 mirrors for the whole measurement as well as the same fiber configuration result in a fixed reference speckle, which means the obtained TM has a physical meaning. To better illustrate the quality of the measured system TM, Florentin chose to show the focusing operator of the TM given by $O_{\text{foc}} = TM \cdot TM^{\dagger}_{\text{norm}}$, where $TM^{\dagger}_{\text{norm}}$ is the normalized conjugate transpose of the measured TM. This operator is shown in Figure 2.15.

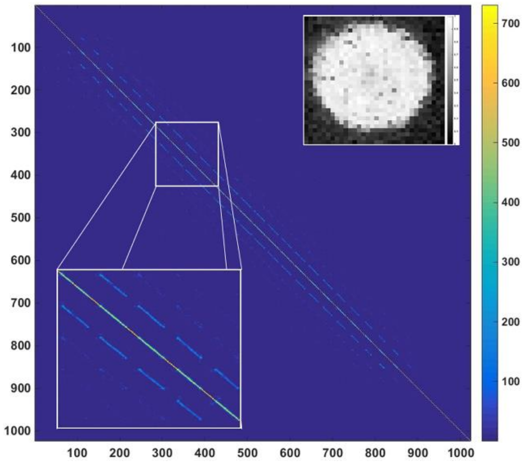

FIGURE 2.15: Focusing operator O_{foc} of the measured system TM with a zoom on the diagonal in lower inset [Florentin et al., 2018].

The normalized focusing efficiency on the MMF cross-section is shown in the upper inset of Figure 2.15. O_{foc} indicates the capability of the system to focus on any pixel of the fiber output cross section. Given the fact that the focus spot is larger than one pixel of the used camera, the spot cover more than one pixel at a time. This is translated by the presence of the low intensity lines parallel to the diagonal in Figure 2.15.

2.4 Implemented method

In this section, we will be describing our implemented method for modal content detection. This method was the center of works for the first part of the thesis, and aims to characterize the modal content of any fiber by defining its TM. Using a SLM , we can control the input position of the beam on the input face of the fiber, so we can cover a large panel of injection conditions. Combining the use of the SLM with an off-axis holography setup, we are able to isolate the TM of the fiber itself which gives us access to the needed information. By compensating all the contributions of the experimental setup using an optimization algorithm, we will be able to access the TM of the fiber itself and thus its modal content in a given configuration. In this section, we will be describing in great details the different parts used to put together our experimental method. This method was heavily inspired by the works mentioned in the previous section.

2.4.1 Off-axis holography

A hologram is a physical structure that diffracts light into an image that appears to be three dimensional and which can be seen with the naked eye. Scientifically, a hologram is a photographic recording of a light field, rather than an image formed by a lens. Classical holography employs photographic plates as a recording media, needing chemical processing in order to reconstruct the hologram. However, digital holography uses a CCD camera for hologram recording and a numerical method for hologram reconstruction, thus adding more flexibility and speed to the holographic process while negating the need of the chemical process. The progress of the electronic image acquisition devices and the calculation machines have made digital holography an attractive tool to several domains, from endoscopy [Coquoz et al., 1995] to biomedical micro-imaging [Boyer et al., 1996]. In order to measure the TM, one must have access to the amplitude of the emerging field at the output end of the fiber, which is provided naturally by the use of the CCD cameras. In addition to that, the TM measurement requires the phase information as well, which is not given directly by the camera. For that, we chose to apply the off-axis holography method in order to acquire the complex field of the emerging beam: the fact of having a slight angle between the signal and the reference beam can enable a measurement of the phase and amplitude of the interference images with a single recorded hologram.

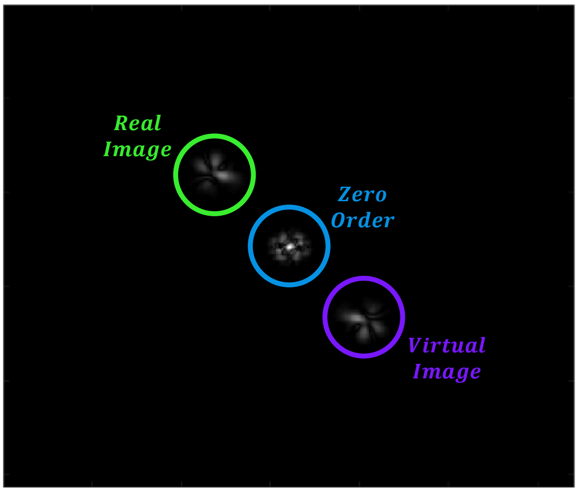

FIGURE 2.16: Fourier transformation of a reconstructed holographic image highlighting the zero order of diffraction, the real image and the virtual image.

This technique applies some reconstruction operation in the frequency domain. A 2D Fourier transformation is applied to the interference image. The reconstructed holographic images contains a zero order of diffraction and two conjugated images: the virtual image and the real image, as shown in figure 2.16. The off-axis holography provides a well needed separation between these three elements so they appear at different locations in the reconstructed images [Leith, Upatnieks, and Haines, 1965]. The elimination of the undesired terms of the images results in an enhancement of image quality: the zero order of diffraction and the virtual image can be eliminated in the frequency domain of an off-axis hologram, which will enhance the contrast of the reconstructed image and reduces the noise produced by parasitic reflections. The resulting image contains all the needed information in order to build the TM of the fiber.

2.4.2 Scanning method

Thanks to the off-axis holography method, we now have access, with one reference and with one step, to the complex field on each pixel of the camera. Each one of these pixels will be considered as a localized output mode. The associated localized input modes is a set of different injection conditions on the input face of the tested fiber: at the input face of the fiber, any beam will couple into a fraction of all the guided modes of the fiber according to the overlap between the electric fields of both of them. Changing the injection conditions at the entry of the fiber will result in unique overlap fractions for each condition. In order to have a complete behavior of the modal content of the fiber, we aim to cover as much injection conditions as possible. It is then possible to proceed with the reconstruction of the TM column by column by measuring the complex field resulting from each localized input mode sent, in our case, by the SLM. The most obvious solution would be to use a canonical basis, which will be known as the pixel basis [Plöschner, Tyc, and Čižmár, 2015]. This consists of turning on a single pixel or a small matrix of neighbored pixels of the SLM, measuring the resulting field on the camera. Using a $4F$ telescope, each pixel matrix would result in a focalized gaussian beam at a specific position on the face of the fiber. This procedure is then repeated for each small matrix until the gaussian beam positions cover the whole area of the core of the fiber. We should mention that the selected pixels are not just turned on, but applied together with a saw-tooth phase mask with a horizontal periodicity, in our setup, so the first order of diffraction is the only order that is injected in the fiber, eliminating the beam part that is not modified by the SLM but reflected by its protective window. However, using the pixel basis poses a major problem : the amplitude of the field modulated by the small number of pixels for each localized input mode is relatively small. The measurement would then be very sensitive to noise contributions.

For that, it is advisable to choose a basis which maximizes the number of turned on pixels for each localized input mode, thus benefiting from the maximum power on the input beam. For this approach, we used another scanning basis, called the angle basis: the totality of the pixels will be used to diffract the input beam, which is a plane wave. We use the SLM screen as a diffraction grating by displaying a saw-tooth phase mask with desired horizontal and vertical periodicity, so we can change the reflection angle of the beam. Combined with an optical telescope in the $6F$ configuration, the angle change will enable us to localize the beam on a defined spot: we scan the fiber face with this beam spot so we cover all the possible injection positions in the fiber. A comparison between these 2 methods is illustrated in Figure 2.17. We should mention that we used both these techniques during our experimental tests. The better results of the second technique led to the decision of adapting this technique for the rest of the works, since it enables to have larger power for each localized input mode, thus increasing the immunity of the measurement from the noise contributions. We should note that for both

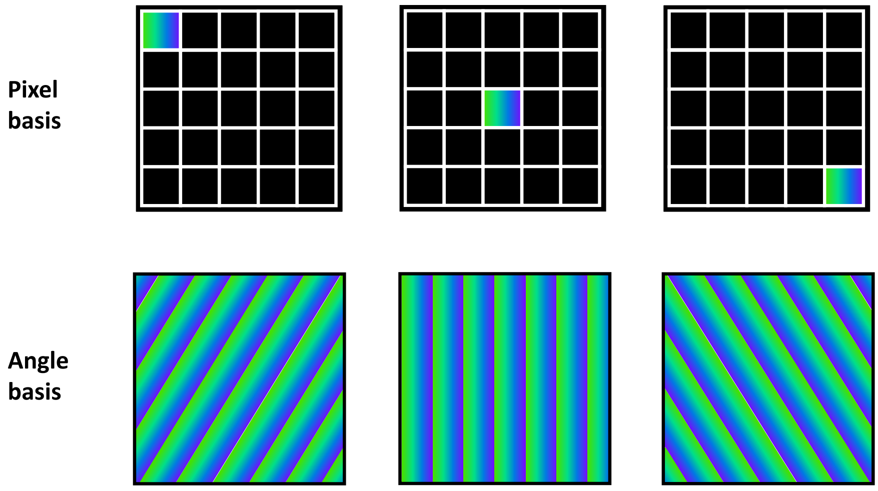

FIGURE 2.17: A simple comparison between the 2 scanning basis: the pixel basis displays a one directional (horizontal) diffraction grating on a number of neighbored pixels, while the angle basis displays a combined horizontal and vertical diffraction grating on all the pixels.

techniques, we kept the same experimental setup except for the telescope, which changed from a $4F$ configuration for the pixel basis, in order to obtain the image of the SLM on the face of the fiber, to a $6F$ configuration for the angle basis in order to have the Fourier transformation of the SLM at the face of the fiber.

2.4.3 Experimental setup

The TM measurement requires the control of the incident beam at the input face of the fiber and the measurement of the complex field at its output end. The experimental setup is similar to the one presented in figure 2.18.

We use a coherent laser source (Yenista Tunics T100S) at a wavelength of $1550nm$. A polarization-maintaining fiber optic coupler (not shown in the figure) divides the laser into two different beams: the signal beam and the reference beam. (I) The signal beam is collimated, passes through a PBS and (II) reaches the screen of a two-dimensional SLM (Meadowlark P1920-1625-HDMI). The polarization axis of the signal fiber, the PBS, and the SLM are all aligned. We use the SLM screen as a diffraction grating so we scan the fiber face with our beam spot to cover all the possible injection positions in our fiber using the method described in the previous section 2.4.2. Each angle is considered as a localized input mode. (III) Between the SLM and the fiber, we use a HWP to generate the desired polarization state, either horizontal or vertical (quarter-wave plate QWP for circular polarization states), then the beam is focalized using a micro-lens on the face of the fiber. (IV) After its propagation, (V) the beam emerges from the tested fiber, is collimated, passes through another HWP and a PBS. The HWP will convert one polarization component of the emerging beam into a linear polarization, parallel to the axis of the PBS. Then, the signal beam reaches a non-polarizing BS.

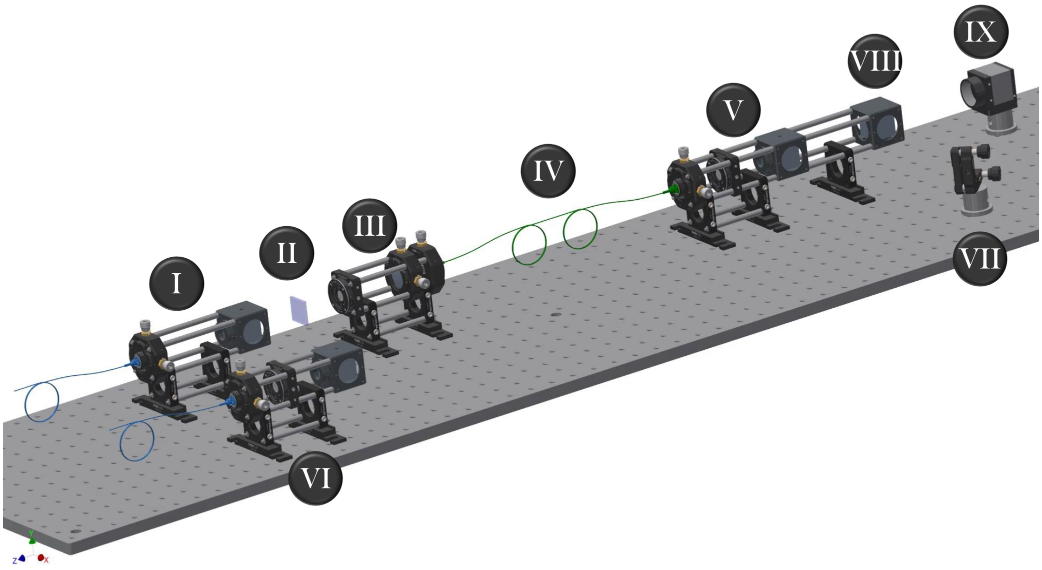

FIGURE 2.18: Experimental setup of the TM measurement method.

On the other output of the fiber optic coupler, (VI) the reference beam travels approximately an equal optical path as the signal beam through a polarization maintaining fiber, while passing through a HWP and a PBS which are aligned in the same direction as the HWP and PBS of the emerging signal beam. (VII) A mirror is used to guide the reference beam into the BS, (VIII) where it joins the signal beam. (IX) The two beams reach the end of their paths at the screen of an infrared camera (Hamamatsu C-10633), with an angle slightly higher than 0 degree, enabling off-axis holographic recording. On the camera, an interference image appears as a result of the interference between signal and reference beams. An interference image is registered for each localized input mode, and for each combination of input and output polarization. The images form four stacks, one stack for each polarization combination. Four acquisitions are needed with different angles between the axis of the HWP and polarization axis of the SLM: the first acquisition for the input and output HWP at 0 degree, a second acquisition with 0 degree for the input HWP and 45 degrees for the output HWP, the third acquisition with 45 degrees at the input and 0 at the output, and the last one with both HWPs at 45 degrees. In this example, we chose to operate with a resolution of 25×25 localized input modes, and therefore each stack contains 625 images.

Phase monitoring We chose to implement a phase monitor for the phase variation that can occur during a measurement: we selected one localized input mode, having a relevant output amplitude, preferably the localized mode responsible for the maximum intensity at the camera. This localized input mode is displayed on the SLM screen between each 2 localized input modes, and its resulted interference images are also registered, playing the role of the phase reference. Thus, an additional set of 625 images for the phase reference is obtained. These stacks will be the data from which we will extract the TM of the fiber itself as described in the next section. In addition, the use of the angle basis induce a phase variation for each pixel on the SLM. This variation is also calculated by tracing the phase variation of the central pixel of the SLM, which is aligned with the center of the input gaussian beam on the SLM screen. These 2 contributions are compensated from the the TM to surpass the phase fluctuations of the surrounding of the setup itself, since the later is not isolated.

Localized input basis choice For any given fiber, the size and the set of positions of the localized input modes must be adapted to the core of the fiber: it is critical to have a localized input basis that covers the entire core of the fiber. This fact is ensured by the choice of the 3 lenses of the $6F$ telescope and the range of angles used for the angle basis. For a better understanding of this choice, Figure 2.19 illustrates 4 of the possible cases of the localized input basis choices.

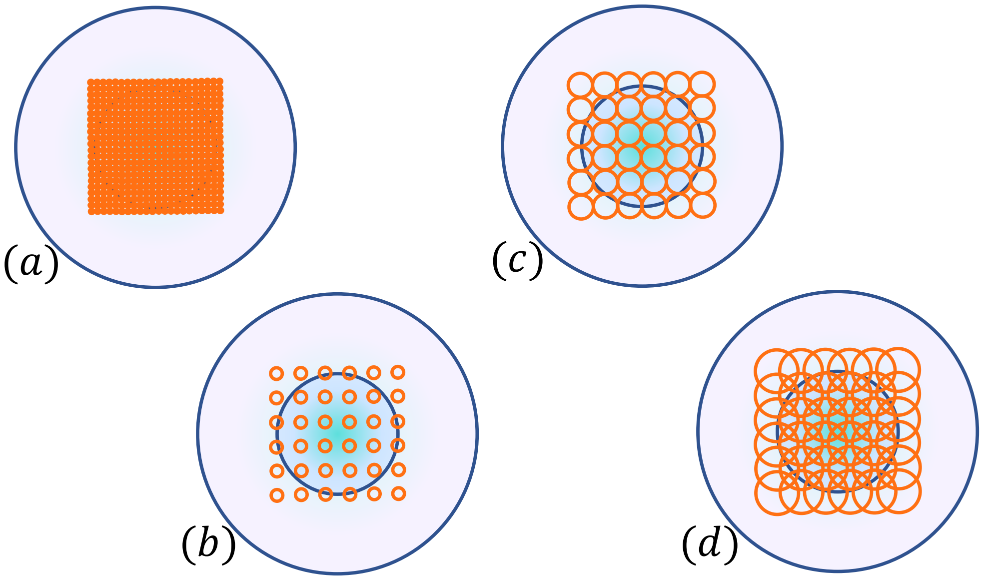

FIGURE 2.19: 4 different cases of the possible localized input basis choices.

Figure 2.19(a) shows the best choice for such a measurement: the localized spots are as small as possible, covering the maximal area of the core without having an overlap between them, ensuring a orthogonal basis. This basis can cover the maximal number of injection conditions offering a high resolution measurement. The quality of this choice can be better understood when compared to the other basis. Figure 2.19(b) shows a small spot basis which does not cover the entirety of the area of the core: the omitted areas due to the bad positioning of the localized input modes refers to possible injection condition that can have unique excitation properties for the guided fiber modes as described in Section 2.4.2, thus a part of the coupling information can be lost using such basis. Figure 2.19(c) shows a better positioned basis but with relatively larger spots. Although the positioning and the orthogonality of the basis can be seen, the use of smaller spots leaves some areas uncovered. In addition, the number of localized input modes inside the core area is small which can have a low resolution measurement. Figure 2.19(d) shows an input basis with good positioned modes covering the whole core area. However, it can be seen that the orthogonality of the basis is lost and the different modes overlap: this can be seen experimentally as added losses to the guided modes of the fiber, since the overlap between the guided modes and each localized input mode have a small value.

We should mention that the choice of the localized input basis is also a crucial point to be considered when changing the tested fiber, in case that the new fiber to be tested have a different core structure or a different core diameter. In our case, the chosen localized input basis was a 25×25 basis, close to the example illustrated in Figure 2.19(c). This choice offered a well balanced compromise between the number of localized modes and their size and position on the face of the fiber.

2.4.4 Data treatment

Following the experimental procedure described in section 2.4.3, we will obtain 4 stacks of images, 1 for each polarization combination. The data analysis step can thus begin: each stack is analyzed on its own in the first step as described in Figure 2.20.

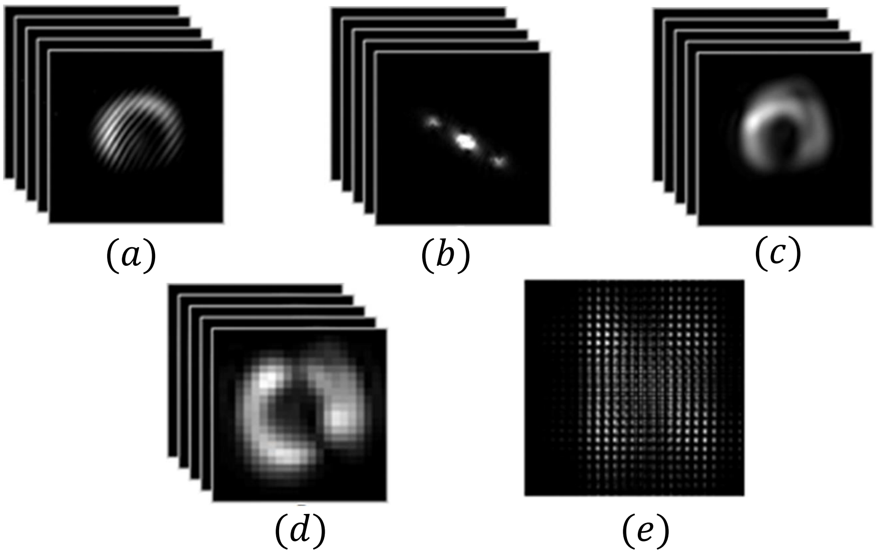

FIGURE 2.20: (a) Stack of interference images for 1 polarization combination. (b) Fourier transformation of the stack. (c) Inverse Fourier transformation of the filtered stack. (d) Down sampling of the images. (e) The transmission matrix of the stack. Only the amplitude of the complex-valued matrices is shown.

First, a two-dimensional Fourier transformation is applied on each image of the stack as shown in Figure 2.20(a). The result is a stack of images with 3 peaks in the Fourier domain. We then apply a filter on the images to isolate the real image of the first-order and translate it to zero spatial frequency (the center of the image), described by Figure 2.20(b). This step will enhance the contrast of the reconstructed image and reduces the noise produced by parasitic reflections. Figure 2.20(c) shows the stack of images after an inverse Fourier transformation is applied, thus obtaining a stack of images of the electric field. We then down sample and resize the images to reduce the calculation time, while retaining of the information on the output electric field, from 320×256 (the resolution of our camera), to 25×25, matching the number of elements in an image to the number of images in the stack as shown in Figure 2.20(d). This stack of images is reshaped into a two-dimensional complex matrix $\boldsymbol{P}$ that will contain all the localized input modes in its rows, and all the localized output modes in its columns as shown in Figure 2.20(e). Given the fact that the experimental setup is not isolated, phase fluctuations can occur. For that we have chosen to trace the phase variations of the setup during the measurement as mention in Paragraph 2.4.3. These contributions are compensated from the matrix $\boldsymbol{P}$ using the following equation:

$$\boldsymbol{Q} = \boldsymbol{P} \cdot e^{(-i(\phi_{\text{monitor}} + \phi_{\text{pixel}}))} \tag{2.17}$$

Where ϕ_{monitor} is the calculated phase contribution using the monitor localized input mode and ϕ_{pixel} is the phase contribution traced for the central pixel of the SLM. The matrix $\boldsymbol{Q}$ is one quadrant of the system TM (one polarization combination out of four possible) containing contribution from the fiber itself as well as all the other optical components between the SLM and the camera, with all their misalignments. This matrix is expressed in the basis of the localized modes and has a 625×625 elements.

The 4 quadrants (matrix $\boldsymbol{Q}$) of the system TM are combined to form the total system TM, T_{kl}, that links all the input and output localized modes and their polarization states. The indices k and l refers to the input and output elements of the matrix respectively. Figure 2.21 shows an example of the total system TM, T_{kl}, having 1250×1250 elements.

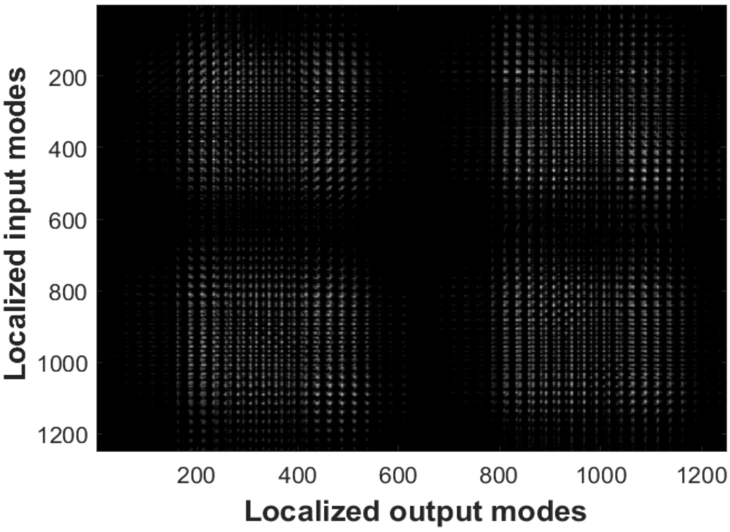

FIGURE 2.21: The total system TM T_{kl}. Only the norm of the complex-valued matrix is displayed.

As a first step in the data treatment which will factor the system TM T_{kl} into fiber TM H_{kl} and misalignment operators, we perform a SVD on the system TM T_{kl}, as described in Section 2.2.1:

$$\mathrm{T}_{\mathrm{kl}} = \boldsymbol{USV}^{\dagger} \tag{2.18}$$

The first matrix $\boldsymbol{U}$ contains the left-singular vectors of the input basis, $\boldsymbol{S}$ is a diagonal matrix formed by the singular values and $\boldsymbol{V}$ contains the right-singular vectors. The matrix $\boldsymbol{S}$ will give us indications about the number of guided modes: a significant singular value marks the presence of a guided mode. In our current example, we have 10 significant singular values (cf Figure 2.22), hence 10 guided modes. The first 10 singular vectors contained in $\boldsymbol{U}$ and $\boldsymbol{V}$ are used to define the modal content of the fiber. An example of the singular vectors of $\boldsymbol{U}$ and $\boldsymbol{V}$ are displayed in Figure 2.23

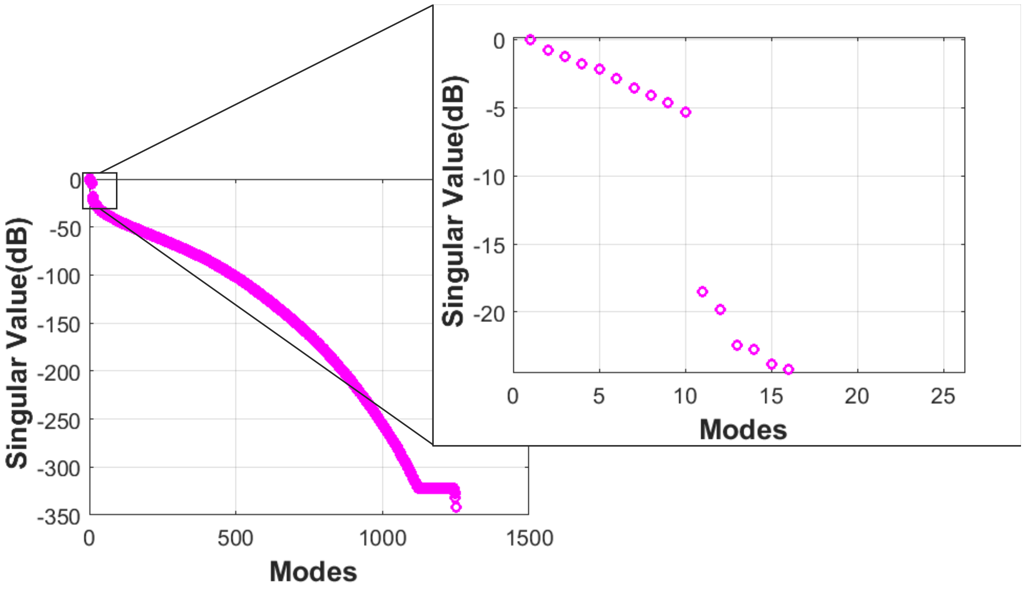

FIGURE 2.22: The singular values found in the singular value decomposition of the system TM T_{kl} in a logarithmic scale.

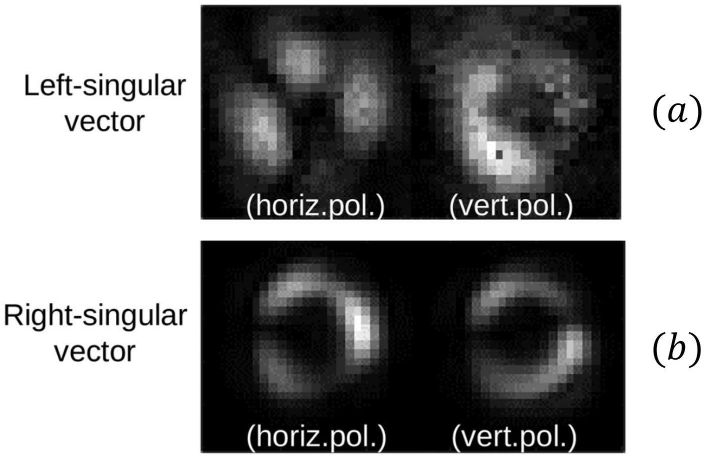

FIGURE 2.23: Comparison of (a) a left-singular vector and (b) a right-singular vector extracted from the singular-value decomposition of the system TM T_{kl}.

At this point, the singular vectors given by the $\boldsymbol{U}$ and $\boldsymbol{V}$ do not represent the proper modes of the fiber, but will be used to retrieve the modes: the SVD gives access to a orthogonal singular vector basis of independent guided channels in the fiber having the lowest possible losses. It is possible to find linear combinations of these singular vectors having high overlap with the calculated fields of the guided modes of the fiber. This is done by compensating the misalignments and the contribution of all the optical components between the SLM and the camera during the optimization process: an iterative optimization algorithm makes a guess for the misalignment parameters at the input and the output of the fiber, represented by the indices in and out respectively, as presented in Table 2.1.

TABLE 2.1: Misalignment parameters to be evaluated in the optimization process.

Symbol	Misalignment
dx	Horizontal transversal shift
dy	Vertical transversal shift
$d\theta_x$	Horizontal angle shift
$d\theta_y$	Vertical angle shift
$\phi^{(2)}$	Second order phase shift
dM	Scale factor

From the basis of calculated mode fields $\Psi_{\mathrm{k}}(x, y)$ given by Table 1.1 the algorithm generates a basis of modified calculated input and output mode fields $\Psi_{\mathrm{k}}^{(\mathrm{in})}(x, y)$ and $\Psi_{\mathrm{l}}^{(\mathrm{out})}(x, y)$ by applying the "misalignment operators" $M^{(\mathrm{in})}(x, y)$ and $M^{(\mathrm{out})}(x, y)$:

$$\Psi_{\mathrm{k}}^{(\mathrm{in})}(x, y) = M^{(\mathrm{in})}(x, y)\Psi_{\mathrm{k}}(x, y) \tag{2.19}$$

$$\Psi_{\mathrm{l}}^{(\mathrm{out})}(x, y) = M^{(\mathrm{out})}(x, y)\Psi_{\mathrm{l}}(x, y) \tag{2.20}$$

where

$$\begin{aligned} M^{(\mathrm{in})}(x, y) = &\exp\left(j\phi_{\mathrm{in}}^{(2)}(x^2+y^2)\right) \\ &\times\mathcal{F}^{-1}\exp\left(j2\pi f_x dx_{\mathrm{in}} + j2\pi f_y dy_{\mathrm{in}}\right)\mathcal{F} \\ &\times\exp\left(\frac{j2\pi}{\lambda}x\sin(d\theta_{x,in}) + \frac{j2\pi}{\lambda}y\sin(d\theta_{y,in})\right) \end{aligned} \tag{2.21}$$

and

$$\begin{aligned} M^{(\mathrm{out})}(x, y) = &\exp\left(j\phi_{\mathrm{out}}^{(2)}(x^2+y^2)\right) \\ &\times\mathcal{F}^{-1}\exp\left(j2\pi f_x dx_{\mathrm{out}} + j2\pi f_y dy_{\mathrm{out}}\right)\mathcal{F} \\ &\times\exp\left(\frac{j2\pi}{\lambda}x\sin(d\theta_{x,out}) + \frac{j2\pi}{\lambda}y\sin(d\theta_{y,out})\right) \end{aligned} \tag{2.22}$$

where $\mathcal{F}$ and $\mathcal{F}^{-1}$ denote forward and inverse Fourier transform and f_x and f_y

the spatial frequencies. The parameters dM_{in} and dM_{out} are left out of the misalignment operators, but in the algorithm they are basically used as scaling parameters, amounting to $(x, y) \to (dM_{\text{in}}x, dM_{\text{in}}y)$ and $(x, y) \to (dM_{\text{out}}x, dM_{\text{out}}y)$.

In order to express the transmission matrix using the guided mode basis, the algorithm calculates the projection coefficients between the modified calculated basis and the singular vectors:

$$\mathrm{C}_{\text{km}}^{(\text{in})} = \langle \Psi_{\text{k}}^{(\text{in})}(x, y) | \boldsymbol{U}_{\text{m}}(x, y) \rangle \tag{2.23}$$

$$\mathrm{C}_{\text{lm}}^{(\text{out})} = \langle \Psi_{\text{l}}^{(\text{out})}(x, y) | \boldsymbol{V}_{\text{m}}(x, y) \rangle \tag{2.24}$$

and calculates the penalty functions

$$P_{\text{in}} = 1 - \frac{1}{N} \sum_{\text{km}} |\mathrm{C}_{\text{km}}^{(\text{in})}|^2 \tag{2.25}$$

$$P_{\text{out}} = 1 - \frac{1}{N} \sum_{\text{lm}} |\mathrm{C}_{\text{lm}}^{(\text{out})}|^2 \tag{2.26}$$

with $N = 10$ the number of modes guided by the fiber. P_{in} (P_{out}) takes values in the interval $[0; 1]$, is equal to zero for perfect likeness between the calculated input (output) mode space and the mode space of the retained left-singular (right-singular) vectors, and equal to one for no likeness. The optimizations of input and output parameters are done separately. A summarized flowchart of the optimization process is shown in Figure 2.24: the index i refers to the order of the input parameter under test. When $i = 1$, the first parameter $\mathrm{Param}_{i=1}^{(\text{in})}$ is optimized using the initial parameter values given at the start of the algorithm. However, $\mathrm{Param}_{i=2}^{(\text{in})}$ is optimized using the initial values for all the parameters except $\mathrm{Param}_{i=1}^{(\text{in})}$, which will have its previously optimized value. This index i is regularly changed until optimizing the totality of the input parameters, evaluating the penalty function P_{in} along the way. Once $i = i_{\text{max}}$, the first iteration is completed. The algorithm then forces a second iteration, so $\mathrm{Param}_{i=1}^{(\text{in})}$ will be optimized using the optimized values of the previous iteration as initial values. After the second iteration, the algorithm compares the penalty functions of both iterations: if the penalty function value of the first iteration is larger than the second one (which is generally the case since the first iteration started from a perfect alignment condition with 0 as a value for all the parameters), the algorithm starts a new iteration based on the values of the second iteration as an initial starting point. This process is repeated until the penalty function of 2 consecutive iterations are relatively the same, having their minimized value and giving access to a modified mode basis $\Psi_{\text{k}}^{\text{in}}$ having the best possible matching with the calculated fiber modes Ψ_{k}. The same exact procedure is used for the output modes separately.

Once the algorithm converges to the smallest value of P_{in} and P_{out}, the optimizing parameters are at their optimized values as a group. At this point, the algorithm re-calculates $\mathrm{C}_{\text{km}}^{(\text{in})}$ and $\mathrm{C}_{\text{lm}}^{(\text{out})}$ for a last time: these matrices are the operators responsible for the basis change from the localized input and output basis in which the system TM T_{kl} is expressed, to the fiber mode basis in which the isolated fiber TM H_{kl} is expressed. This TM is constructed as

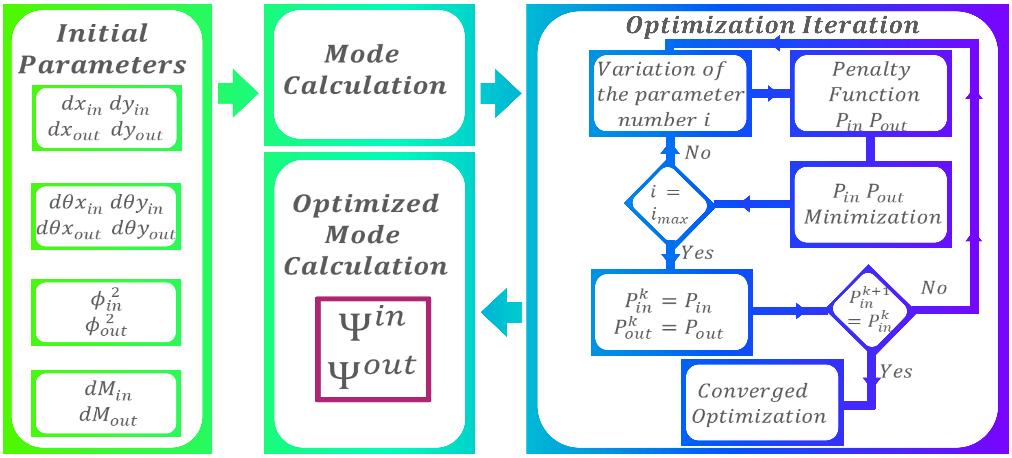

FIGURE 2.24: Summarized flowchart of the optimization process.

$$H_{kl} = C^{(in)}_{km} \cdot (C^{(out)}_{lm})^{\dagger}, \tag{2.27}$$

The resulting matrix is similar to the matrix presented in Figure 2.25. A visual gauge of the quality of the solution found by the algorithm can be obtained by comparing a left-singular (right-singular) vector to the closest semblance of it that can be constructed by a linear combination of the $\Psi^{(in)}(x,y)$ ($\Psi^{(out)}(x,y)$) onto which the algorithm has converged. Such a comparison is given in Figure 2.26.

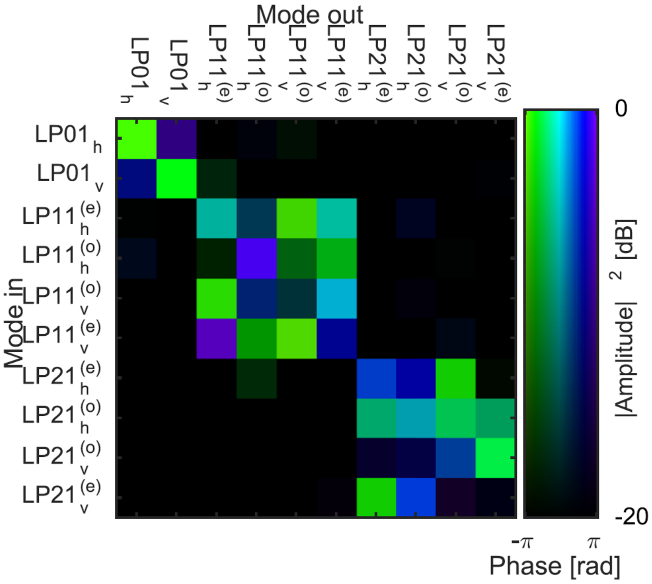

FIGURE 2.25: An example of the fiber TM H_{kl} in the LP mode basis.

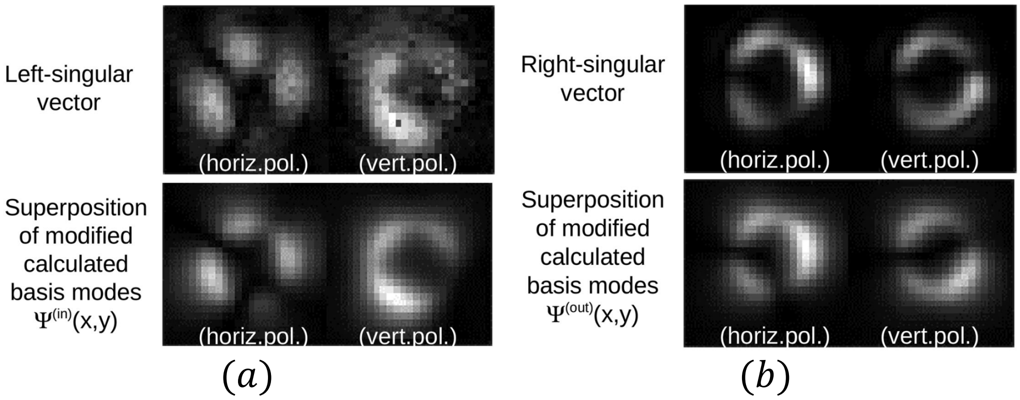

FIGURE 2.26: Comparison of (a) a left-singular vector and (b) a right-singular vector shown in figure 2.22 with a linear combination of the modified calculated basis modes found by the iterative optimization algorithm. Only the norm of the fields is shown.

The fiber TM $\mathrm{H_{kl}}$ is expressed in the basis of its own modes. We should mention the doubly graduated color map of Figure 2.25, where the color codes represent the phase and the saturation codes represent the norm-squared amplitude of the complex-valued fiber TM $\mathrm{H_{kl}}$. With the current setup, the measurement of the entire TM takes around 25 minutes when a basis of 25×25 localized modes is used. The optimization code can deliver trustworthy results after 3 to 4 iterations, which takes around 10 minutes of calculation time, depending on the initial values of the optimization parameters.
To highlight the important role of the optimization process, Figure 2.27 illustrates the same transmission matrix as Figure 2.25 without the compensation of the misalignment contributions. We should mention that for this example, the highest transversal shift was less than $1.5\ \mu\mathrm{m}$ for both in and out beams, the highest angle shift was less than $0.18\ \mathrm{rad}$. The scale factor was about 0.9 for the output beam and 0.8 for the input beam, while the second order phase correction applied for the output beam was about $20\ \mathrm{rad}/\mu\mathrm{m}^2$ and close to 0 for the input beam. These compensation are quite small but impact the result of the detection method heavily, thus the fundamental job of the optimization process can be validated.

We should mention that this result can be achieved using a multitude of ways other than ours. For example, the SVD operation is not mandatory: one can achieve the same expression of the fiber TM $\mathrm{H_{kl}}$ without the use of the SVD. For example, one can use the localized input and output modes in order to find the best matching combination of them with the calculated modes of the fiber. In fact, we chose to apply the SVD on the system TM $\mathrm{T_{kl}}$ in order to access some interesting information, as the number of guided modes and the shapes of the principle singular vectors of this matrix. It is also an excellent way to avoid the insignificant vectors, which present insignificant singular values. These noise vectors are filtered and discarded from our optimization process thanks to the SVD. An

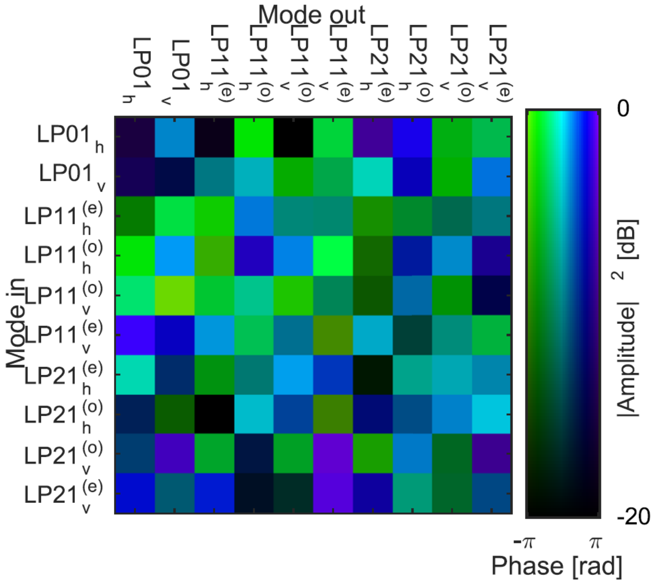

FIGURE 2.27: An example of the fiber TM H_{kl} in the LP mode basis without the optimization process.

additional feature that should be mentioned is the choice of the optimized variable: in the example given in this chapter, the aim of the optimization process is to find the combination of the modified calculated modes Ψ_k^{in} and Ψ_l^{out} that best matches each singular vector of the matrices $\boldsymbol{U}$ and $\boldsymbol{V}$, as shown in Figure 2.26. It is possible to reverse this calculation, so the optimization algorithm aims to find the combination of the significant singular vector from the matrices $\boldsymbol{U}$ and $\boldsymbol{V}$ that best matches the modified calculated modes Ψ_k^{in} and Ψ_l^{out}, as will be shown in Section 3.2 of the next chapter.

2.5 Conclusion

In this chapter, we reviewed the different methods to characterize the modal content of MMFs, from the C^2 to the standard and advanced versions of S^2, all the way to the TM based methods. We further continued to describe in details our implemented method, based on the measurement of the TM of the fiber. We detailed the various building stones of this method, from the acquisition method of a complex optical field, to the off-axis holography. We showed the adapted scanning basis that we used to enhance the performance of the SLM in this type of application. The experimental setup was detailed, followed by the data treatment including the optimization process that we used to extract the fiber's TM out of the acquired stack of images. The next chapter will be dedicated to showcase the different results delivered by this method on transmission line FMFs and even specialty fibers.

Chapter 3

Modal detection results

3.1 Introduction

In Chapter 2, we described in detail our implemented method to characterize the modal content of FMFs based on the measurement of the TM. This method has been applied to test several fiber types. This thesis was a part of the project FUI MODAL, in collaboration with Draka/Prysmian group, CAILabs and Nokia. Draka/Prysmian group developed a passive step index fiber design that was considered as the transmission fiber of a possible MDM transmission. Our implemented method was used to detect the guided modes of this fiber design and the results will be discussed in the following sections. In addition to that, we used this method to test another type of fiber, mainly a specialty ring core fiber made by our team at the FiberTech Lille platform. This method was also used to test the fundamental properties of the TM itself and applied in order to characterize the time evolution of the TM over a 2 days span.

3.2 Step index fibers

As part of the project FUI MODAL, Draka/Prysmian group developed a passive step index fiber design that was considered as the transmission fiber of a possible MDM link. Several fabrications of this fiber was issued, each one having a specific design targeting a specific propriety of the fiber. From these iterations, we have mainly used 2 for our experimental studies: the FMF L111 having a RIP close to an ideal step, presenting a $\Delta n_{\text{eff}}^{\text{min}}$ of 0.9×10^{-3} and guiding up to 7 mode groups at 1550 nm (24 modes in total degenerated in space and polarization) and the FMF L113 with an inner depressed trapezoidal-index structure with a $\Delta n_{\text{eff}}^{\text{min}}$ of 1.6×10^{-3} and guiding up to 6 mode groups at the same wavelength (20 modes in total degenerated in space and polarization) [Bigot-Astruc et al., 2019]. Figure 3.1 shows comparison between the theoretical and experimental RIP of these fibers. The main difference between these 2 fibers resides in their mode dependent losses, which will be later discussed in following Section 4.6.3. The depressed index zones at the center of the core of the L113 is designed to reduce the n_{eff} of the LP_{02}, thus increasing its different with the n_{eff} of the LP_{21}. The intensity distribution as well as the relative phase of each mode are shown in Figure 3.2 for both LP and OAM modes. These modes were calculated using a vector mode solver developed by our team based on the experimental RIP on the fibers and will be used for the optimization process of our method in order to rebuild the modes of the fiber using its isolated TM.

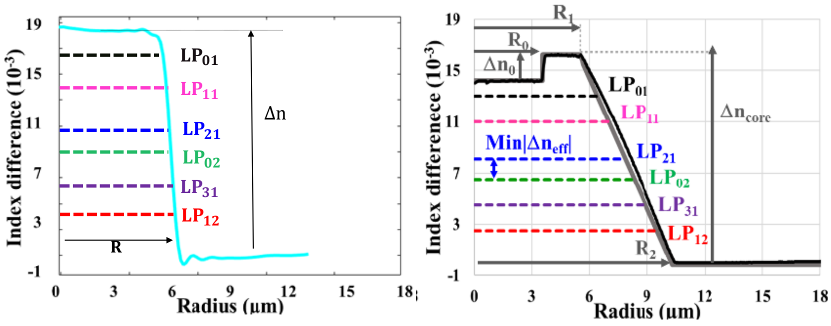

(*a*) (*b*)

FIGURE 3.1: Experimental and theoretical index profiles of the fiber designs: (a) FMF L111 with a step-index structure and (b) FMF L113 with a trapezoidal-index structure [Bigot-Astruc et al., 2019].

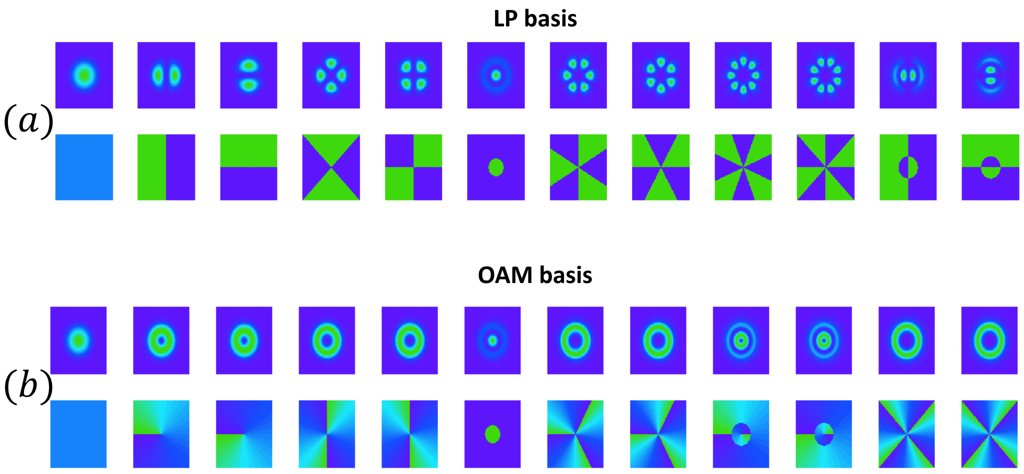

FIGURE 3.2: The intensity distribution as well as the relative phases of the guided modes of the FMF L111 and L113 in the (a) LP and (b) OAM basis.

3.2.1 FMF L111

The first studied fiber using our experimental method to detect its modal content was the FMF L111. A 1 m-long fiber was characterized at 1550 nm using the same angle basis scanning method and the $6F$ telescope for the experimental setup described in Section 2.4.3. The choice of the short fiber length for this study was due to the available materials used: in order to characterize a longer fiber, we need to have a SLM with faster response time, a perfectly stable coherent laser source and the experimental setup should be isolated in order to limit all the noise contributions that can alter our interferometric method performance. The TM of this fiber was measured in the LP basis using HWP at both ends of the fiber for a first measurement, then we replace the HWP with QWP in order to obtain circular polarization at both ends of the fiber in order to measure the TM in the OAM basis. Figure 3.3 shows the FMF L111 isolated TM $\mathrm{H}_{\mathrm{kl}}^{(\mathrm{L111})}$ using both basis.

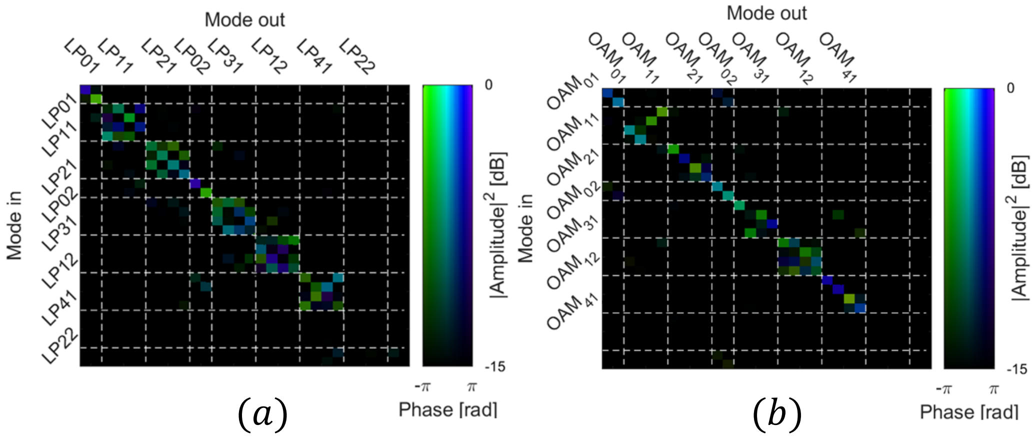

FIGURE 3.3: The isolated TM $\mathrm{H}_{\mathrm{kl}}^{(\mathrm{L111})}$ for the FMF L111 in the (a) LP basis and the (b) OAM basis measured using our implemented method.

We should mention the doubly graduated color map of Figure 3.3, where the color codes represent the phase and the saturation codes represent the norm-squared amplitude of the complex-valued fiber TM. In the case of our study, a mode group contains the degeneracy states of a given spatial mode, therefore, the fundamental mode degenerate into 2 polarization modes formed the first mode group, while the second mode group was formed by 4 polarization and spatial degenerate states of the LP_{11} mode. These mode groups are delimited on our TM by the white doted lines. For the OAM basis, the second order modes were not a part of our study so, even though they are well presented on the TM, we won't be mentioning them. For the TM in the LP basis, we can clearly see the low to non-existing coupling between the different mode groups: 79% of the total amplitude of the TM elements is presented on the diagonal blocks while 21% of this amplitude is spread on the remaining elements. Meanwhile, inside each mode group, we can see high coupling levels: 28% of the TM amplitude is presented on the diagonal itself, which means that the majority of this amplitude belong to the elements of the diagonal blocks indicating the coupling between the members of the same mode group. The LP modes are the results of vector mode combinations, given by Table 1.1, having close but different effective index or propagation constants. This fact enhances the coupling within a same mode group as we can see in our TM. On the other hand, the TM of the FMF L111 in the OAM mode basis presents similar or even lower coupling levels for the non-diagonal elements.

Our OAM mode groups, have the similar composition as the LP basis, present low X-Talk between them for our measured TM, with 83% of the total amplitude of the TM elements presented on the diagonal blocks. However, within each mode group, we can see the that the majority of the input power of each member is focused mainly on one member of the same mode group. The coupling within a mode group is significantly decreased using this mode basis, which can be better understood by observing the increasing amplitude localized on the diagonal of the TM itself to 48%. This is largely due to the nature of the OAM modes, being a complex combination of the same vector mode as given by Table 1.3, thus having the same propagation constant for both its elements. The different degenerate spatial and polarization OAM modes are less likely to couple within the same mode group, as has been suggested by other teams [Ramachandran, Kristensen, and Yan, 2009, Ramachandran and Kristensen, 2013]. Nevertheless, some coupling still occur due to the different bends, twists and mechanical stresses which could have been applied on the fiber while measuring the TM.

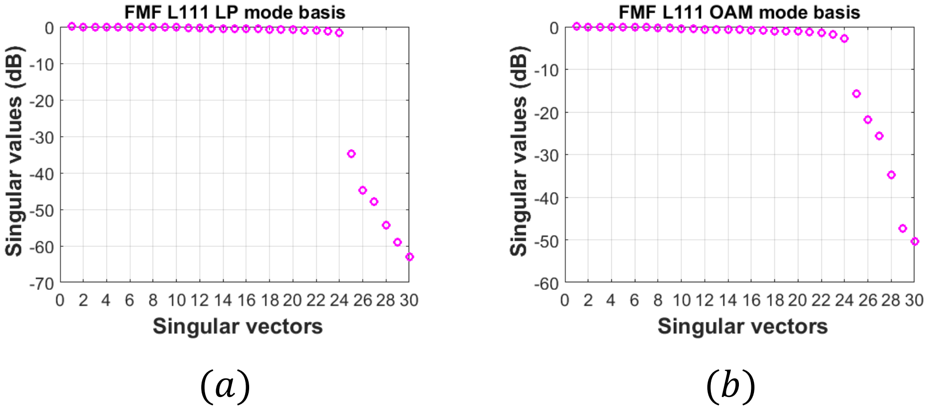

FIGURE 3.4: The singular values of the $\mathrm{H}_{\mathrm{kl}}^{(\mathrm{L111})}$ of (a) the LP and (b) the OAM mode basis.

Another way to visualize the number of guided modes of a fiber is by evaluating the singular values delivered by applying the SVD on the isolated fiber TM: $\mathrm{H}_{\mathrm{kl}}^{(\mathrm{L111})}$ is fragmented into 3 matrices as following:

$$\mathrm{H}_{\mathrm{kl}}^{(\mathrm{L111})} = \boldsymbol{USV}^{\dagger} \tag{3.1}$$

where $\boldsymbol{S}$ is the singular value diagonal matrix, $\boldsymbol{U}$ is the matrix containing the output singular vectors and $\boldsymbol{V}$ is the input singular vector matrix. As mentioned in the Section 2.2.1, $\boldsymbol{U}$ and $\boldsymbol{V}$ are 2 orthogonal matrices. The fact that our fiber TM $\mathrm{H}_{\mathrm{kl}}^{(\mathrm{L111})}$, expressed in both basis as shown in Figure 3.3, is not perfectly diagonal but has diagonal blocks indicates that the the modes experience some couplings. Therefore, the singular vectors of $\boldsymbol{U}$ and $\boldsymbol{V}$ do not represent the proper modes of the fiber itself, but a basis of orthogonal independent guided channels, which offers the highest possible overlap with the proper modes of the fiber. These singular vectors are sorted following the increasing order of their losses, given by the singular value matrix *S* as shown in Figure 3.4. For both the LP and the OAM mode basis, we can clearly see the steady low increase in these channels losses until the 24th mode, at which the loss increases drastically: the 25th mode is beyond its cut-off frequency, thus the losses increase sharply and the mode is not guided.

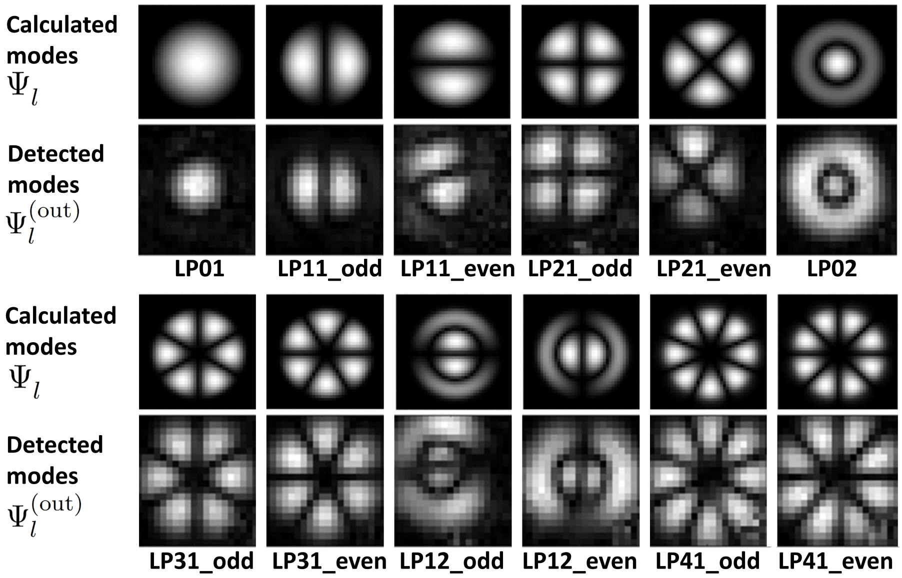

FIGURE 3.5: Comparison between the theoretical modes Ψ_l and the experimentally detected modal content at the output end of the FMF L111 $\Psi_l^{(\text{out})}$ in the Fourier domain.

The input fiber face is in the Fourier plane regarding the SLM screen thanks to the $6F$ telescope in between them. In order to validate the performance of the reconstruction of the fiber TM, we compared the detected modal content using our method to a calculated one using a vector mode solver developed by our team members to calculate the intensity distributions of the spatial degenerate LP modes guided by the FMF L111 using its measured RIP. These modes are referred to in Equation 2.19 as Ψ_k and Ψ_l. The optimization process of our method gives us access to the singular vectors superposition that best matches the calculated mode basis Ψ_k. The results of these superposition are considered as the guided modes experimentally detected, which are referred to in Equation 2.19 as $\Psi_k^{(\text{in})} = M^{(\text{in})} \cdot \Psi_k$ and $\Psi_l^{(\text{out})} = M^{(\text{out})} \cdot \Psi_l$. Figure 3.5 shows a comparison between the theoretical and the experimentally detected modal content of the fiber. The high similarity between the calculated basis and the detected modal content stands out, as the penalty functions given by Equations 2.25 and 2.26 both have values less than 10%.

3.2.2 FMF L113

Following the positive results obtained from the modal content analysis of the FMF L111, the next step of our study was to repeat the same characterization on the FMF L113. This characterization was also interesting to test the consistency of our method. The same exact procedure was used for the FMF L113: a 1 m-long fiber was characterized at 1550 nm using the angle basis scanning method and the

$6F$ telescope for the experimental setup of Section 2.4.3. The TM was measured for both LP and OAM basis. Figure 3.6 shows the FMF L113 isolated TM $\mathrm{H}_{\mathrm{kl}}^{(\mathrm{L}113)}$ using both basis. We can see for the TM of both basis that the number of guided modes is 24 instead of 20. Although the fiber design targets the guiding of 20 modes, the presence of the 4 extra modes is mainly due to the short length fiber tested, and the fact that this mode group is close to its cut-off frequency for this design.

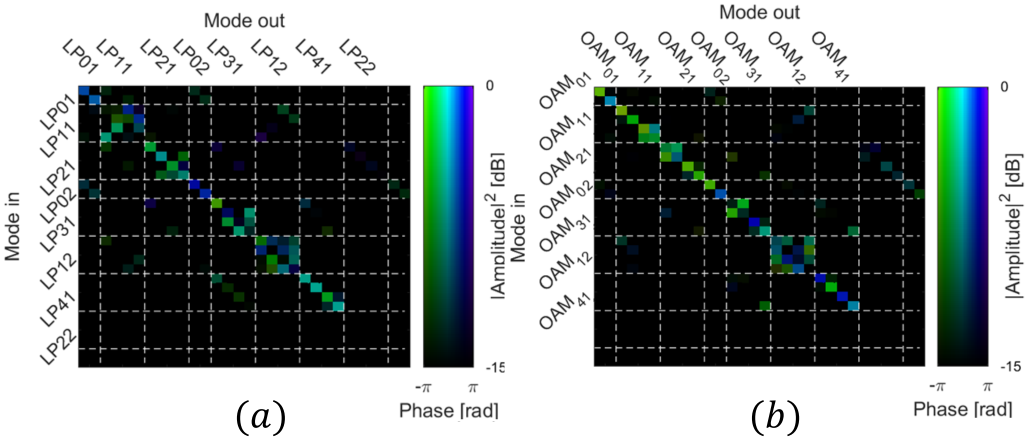

FIGURE 3.6: The isolated TM $\mathrm{H}_{\mathrm{kl}}^{(\mathrm{L}113)}$ for the FMF L113 in the (a) LP basis and the (b) OAM basis measured using our implemented method.

For this study, the group modes are the same groups defined for the previous FMF L111. For $\mathrm{H}_{\mathrm{kl}}^{(\mathrm{L}113)}$ expressed in the LP basis, we can clearly see the low to non-existing coupling between the different mode groups: all the significant elements belong to the mode groups blocks on the diagonal of our TM, carrying over 80% of the total amplitude of the TM elements. We should mention that our measurement indicates that the coupling within each mode group obtained for $\mathrm{H}_{\mathrm{kl}}^{(\mathrm{L}113)}$ is relatively lower than the coupling obtained for $\mathrm{H}_{\mathrm{kl}}^{(\mathrm{L}111)}$ described in the previous section, with 44% of the total amplitude of $\mathrm{H}_{\mathrm{kl}}^{(\mathrm{L}113)}$ presented on its diagonal. For the TM measured in the OAM basis, the same effect is observed with even less coupling levels: 82% of the total amplitude is presented on the diagonal blocks, with more than 54% on the diagonal itself. In a more macroscopic view, both fibers have the same guiding properties with diagonal TM, guiding the same mode groups. The losses properties given by the singular values of the SVD of the fiber TM $\mathrm{H}_{\mathrm{kl}}^{(\mathrm{L}113)}$, shown in Figure 3.7, present high similarity when compared to the singular values distributions obtained by the SVD of the fiber TM $\mathrm{H}_{\mathrm{kl}}^{(\mathrm{L}111)}$, shown in Figure 3.4, for both mode basis. We should recall that the singular values do not represent directly the modal dependent losses of the fiber, but the losses of the singular vectors of the SVD of the fiber TM $\mathrm{H}_{\mathrm{kl}}^{(\mathrm{L}113)}$.

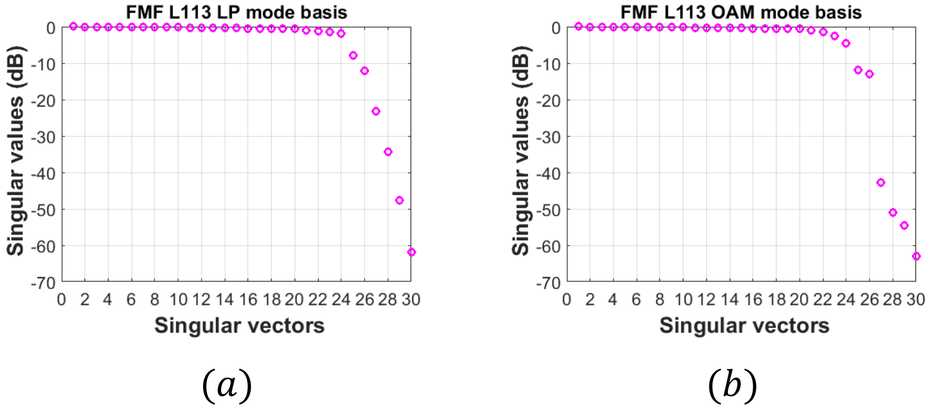

FIGURE 3.7: The singular values of the $\mathrm{H}_{\mathrm{kl}}^{(\mathrm{L113})}$ of (a) the LP and (b) the OAM mode basis.

3.2.3 Selective exitation

We were also interested in the possibility of the excitation of a specific mode using our method: we created phase masks that can be displayed on the SLM so we can effectively excite the exact mode of the fiber at the specific conditions (bends, twists ...) that were present during the measurement of the TM. We should mention that at the time when we conducted this study, we used the pixel basis in order to characterize the fiber TM, thus the telescope located between the SLM and the tested fiber was a $4F$ telescope in order to obtain the image of the SLM of the fiber face. These masks are formed using 4 elements as shown in Figure 3.8: the normalized intensity distribution of the detected mode I, its phase ϕ, a saw-tooth phase mask and the product of multiplying I by a random matrix R.
To better understand how the selective masks are created, we will describe an example of this process using the detected fiber mode $\mathrm{LP}_{41}^{(e)}$. As described in Section 2.4.2, a saw-tooth mask is used at the localized input modes in order to isolate the first diffraction order, which will be later injected into the fiber. Therefore, the saw-tooth phase mask is necessary to deviate the generated mode in the same direction and angle of the central localized input modes. Thus, the generated mode will have its center aligned with the center of the core at the input face of the fiber. The saw-tooth mask is generated with the same period T_{st} as the central localized input mode, as shown in Figure 3.8(a). The phase of the detected mode, shown in Figure 3.8(b), and the saw-tooth phase mask are then multiplied as mentioned in Equation 3.2: if a gaussian beam is incident on the mask displaying this product on the screen of the SLM, the reflected beam will carry the phase ϕ_n and first order of diffraction will be incident on the core of the fiber, with both their centers aligned.

$$\mathrm{Mask}_{n,\mathrm{phase}} = \mathrm{mod}\left(\frac{2\pi P^{(\mathrm{x,y})}}{T_{\mathrm{st}}} \times \phi_n^{(\mathrm{x,y})}\ , 2\pi\right) \tag{3.2}$$

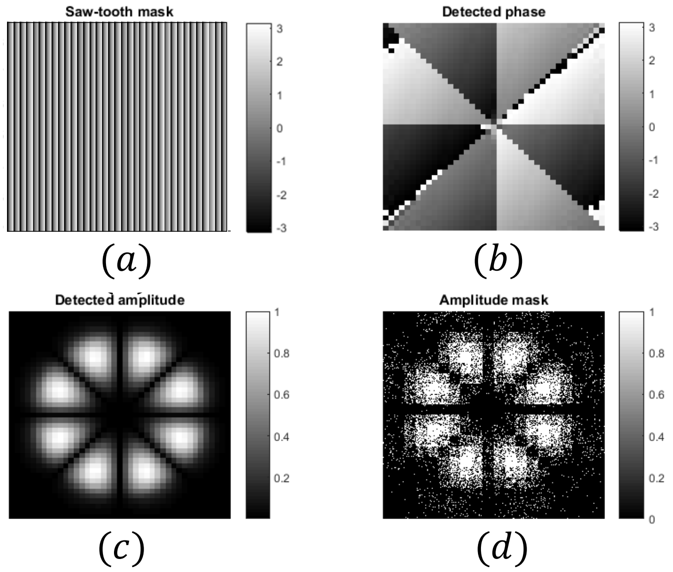

FIGURE 3.8: Generation process of the mask for a selective mode excitation of the proper fiber mode $\mathrm{LP}_{41}^{(e)}$: (a) the saw-tooth phase mask used for the central localized mode, (b) the detected phase of the mode, (c) the normalized intensity distribution of the mode and (d) the resulting matrix after multiplying the random matrix R by the normalized intensity amplitude distribution of the mode.

where $P^{(\mathrm{x,y})}$ is the SLM pixel with (x,y) as its coordinates. The SLM presents a phase resolution of 255 levels for an interval of $[0;2\pi]$. Thus for the smaller intervals, the resolution level decreases and this can reduce the diffraction efficiency of the SLM. In order to surpass this limitation, a random matrix R is generated, having the dimensions of the SLM screen (1152×1920) and values between 0 and 1. This matrix will be used in order to re-sample these phase variations into larger intervals, thus optimizing the diffraction properties of the SLM. It can be also considered as a method to shape the amplitude using a phase only SLM. The normalized intensity distribution I_n, illustrated in Figure 3.8(c), and the matrix R are used in order to create the amplitude mask of the mode n as following:

$$\mathrm{Mask}_{n,\mathrm{amplitude}} = \begin{cases} I_n^{(\mathrm{x,y})} & \text{if } R^{(\mathrm{x,y})} > I_n^{(\mathrm{x,y})} \\ 0 & \text{if } R^{(\mathrm{x,y})} < I_n^{(\mathrm{x,y})} \end{cases} \tag{3.3}$$

The resulting $\mathrm{Mask}_{n,\mathrm{amplitude}}$ is shown in Figure 3.8(d). For each pixel of the mask, we evaluate the value of the normalized intensity distribution of the mode. The smaller values of the normalized intensity distribution, which can be a result of the background noise of the camera and the calculation error, are then multiplied by 0 in order to omit them from contributing to the final mask, while preserving the higher values in order to give the created mask the shape of the corresponding mode amplitude. The final mask is obtained by multiplying the phase mask and the amplitude mask.

$$\mathrm{Mask}_n = \mathrm{Mask}_{n,\mathrm{amplitude}} \times \mathrm{Mask}_{n,\mathrm{phase}} \tag{3.4}$$

Figure 3.9(a) illustrates the final mask of the $\mathrm{LP}_{41}^{(e)}$ fiber mode. Once this mask is displayed on the SLM screen, a gaussian beam is injected onto the mask, with

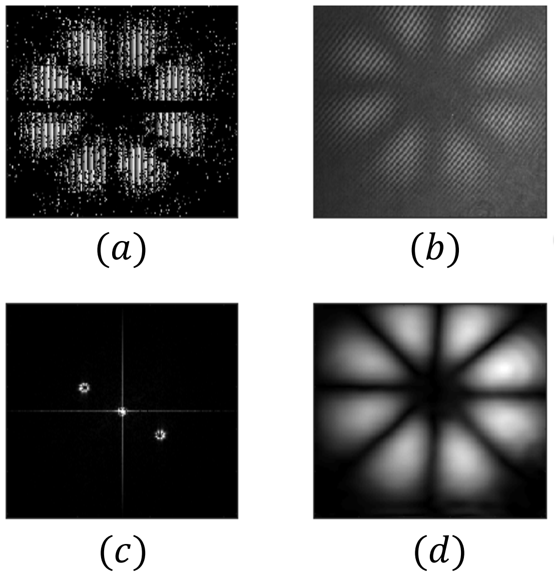

FIGURE 3.9: (a) The final selective excitation mask of the $\mathrm{LP}_{41}^{(e)}$ fiber mode and the data process used to recover the excited mode: (b) the interference image, (c) the Fourier transformation and (d) the inverse Fourier transformation of the filtered image.

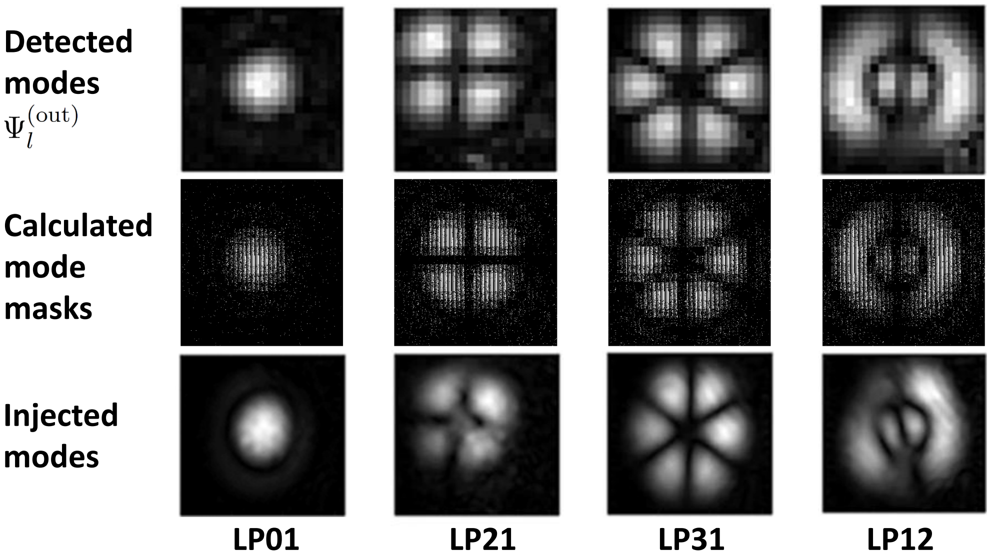

FIGURE 3.10: Comparison between the distribution of intensity of the detected LP modes of the FMF L111 $\Psi_l^{(\mathrm{out})}$, the calculated masks able to excite each mode and the resulting intensity distribution registered at the camera for each one of them.

its center aligned with the center of the mask. Thus, the reflected beam off the SLM screen represents the generated mode and is then injected using the same $6F$ telescope used for the TM measurement into the fiber. At the output end, the emerging beam is combined with a reference beam and the interference image on the camera, shown in Figure 3.9(b), is registered. These images is then processed using a similar process to the one of Section 2.4.4: a two-dimensional Fourier transformation is applied to the registered interference images (cf Figure 3.9(c)). The real image of the first order is then filtered and translated to the zero spatial frequency, before applying another two-dimensional Fourier transformation to obtain the selectively excited mode as shown in Figure 3.9(d). Figure 3.10 shows a comparison between the detected intensity distribution of the LP basis of the FMF L111 (Ψ_l^{out}), the calculated masks able to selectively excite the mode and the resulting intensity distribution registered at the camera, which is nothing but the selectively injected mode emerging from the fiber.

3.3 Ring core fibers

3.3.1 Modal content characterization

Ring core fibers guiding OAM modes are a part of the different research topics that our team is heavily invested in. After the characterization of both step index FMFs as part of the project FUI MODAL, we were interested in studying a ring core fiber using our method. We used a ring core fiber fabricated by our team at the FiberTech Lille technology platform. The fiber refractive index difference as well as a scanning electron micrograph are presented in Figure 3.11 (a) and (b) respectively.

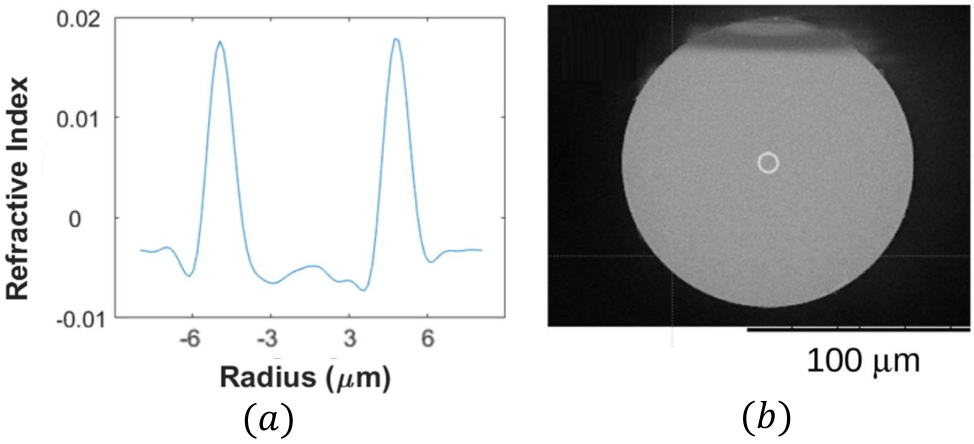

FIGURE 3.11: (a) The tested ring core fiber refractive index difference and a (b) scanning electron micrograph of its face.

We modeled the fiber using its fitted refractive index curve and predicted the presence of 10 guided vector modes which are listed in Table 3.1 along with their calculated effective indices.

From the calculated vector mode fields, we construct a basis of linearly polarized, helical-phase modes which will be used in order to characterize this fiber, based on the combinations given by Table 3.2. The modes are denoted as (l, pol), where l is the topological charge (or the number of 2π phase turns per period) and pol is the polarization vertical v or horizontal h. The intensity distributions of these

TABLE 3.1: The vector modes of the ring core fiber and their calculated effective indices.

Mode	n_{eff}
$\text{HE}_{1,1}^{(e)}, \text{HE}_{1,1}^{(o)}$	1.448482
$\text{TE}_{0,1}$	1.447199
$\text{HE}_{2,1}^{(e)}, \text{HE}_{2,1}^{(o)}$	1.447143
$\text{TM}_{0,1}$	1.447077
$\text{HE}_{3,1}^{(e)}, \text{HE}_{3,1}^{(o)}$	1.444285
$\text{EH}_{1,1}^{(e)}, \text{EH}_{1,1}^{(o)}$	1.444289

modes and their relative phases are also presented in Figure 3.12. Our choice of mode basis was motivated by the fact that our method can use any type of mode basis in order to detect the modal content of the fiber. Indeed, the measured fiber TMs using other more conventional basis will be also shown and the results will be compared in the following paragraph.

TABLE 3.2: The linearly polarized, helical-phase mode basis.

#	(l, pol)	Constituent vector modes
1	$(0, h)$	$\text{HE}_{11}^{(e)}$
2	$(0, v)$	$\text{HE}_{11}^{(o)}$
3	$(-1, h)$	$(\text{TE}_{01} - j\text{TM}_{01}) + (\text{HE}_{21}^{(e)} - j\text{HE}_{21}^{(o)})$
4	$(1, h)$	$(\text{HE}_{21}^{(e)} + j\text{HE}_{21}^{(o)}) + (\text{TE}_{01} + j\text{TM}_{01})$
5	$(1, v)$	$(\text{HE}_{21}^{(e)} + j\text{HE}_{21}^{(o)}) - (\text{TE}_{01} + j\text{TM}_{01})$
6	$(-1, v)$	$(\text{TE}_{01} - j\text{TM}_{01}) - (\text{HE}_{21}^{(e)} - j\text{HE}_{21}^{(o)})$
7	$(-2, h)$	$(\text{EH}_{11}^{(e)} - j\text{EH}_{11}^{(o)}) + (\text{HE}_{31}^{(e)} - j\text{HE}_{31}^{(o)})$
8	$(2, h)$	$(\text{HE}_{31}^{(e)} + j\text{HE}_{31}^{(o)}) + (\text{EH}_{11}^{(e)} + j\text{EH}_{11}^{(o)})$
9	$(2, v)$	$(\text{HE}_{31}^{(e)} + j\text{HE}_{31}^{(o)}) - (\text{EH}_{11}^{(e)} + j\text{EH}_{11}^{(o)})$
10	$(-2, v)$	$(\text{EH}_{11}^{(e)} - j\text{EH}_{11}^{(o)}) - (\text{HE}_{31}^{(e)} - j\text{HE}_{31}^{(o)})$

A $1.5\,\text{m}$-long fiber was characterized at $1550\,\text{nm}$. The choice of a short fiber length is for the same reasons as described for the FMF L111. The TM of this fiber was measured using HWP at both ends of the fiber in order to have linear polarization states for the input and output beams, so we can use the mode basis defined in Table 3.2 to isolate the fiber TM from the the interfacing components contributions. The HWP was also used while measuring the TM in the LP mode basis given by Table 1.1, while QWP was used for the measurement in the OAM mode basis given by Table 1.3. The ring core fiber TMs expressed in the mode basis defined in Table 3.2 is presented in Figure 3.13(a). As a point of comparison, the TM expressed in the standard LP mode basis is presented in Figure 3.13(b) and the TM expressed in the OAM mode basis is presented in Figure 3.13(c).

As expected, the matrix elements of significant amplitude are found in three blocks on the diagonal constituted by the three mode families with $|l| = 0, 1, \text{ and } 2$. Just like in the case of both step index FMFs, the small effective index differences within a mode group allow its members to couple freely in the presence of small

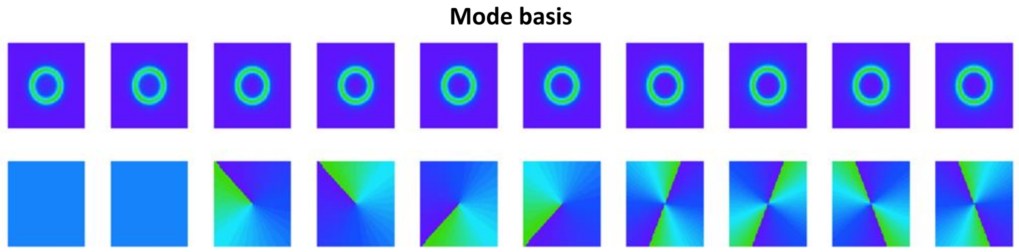

FIGURE 3.12: The intensity distributions and the relative phases of the tested ring core fiber.

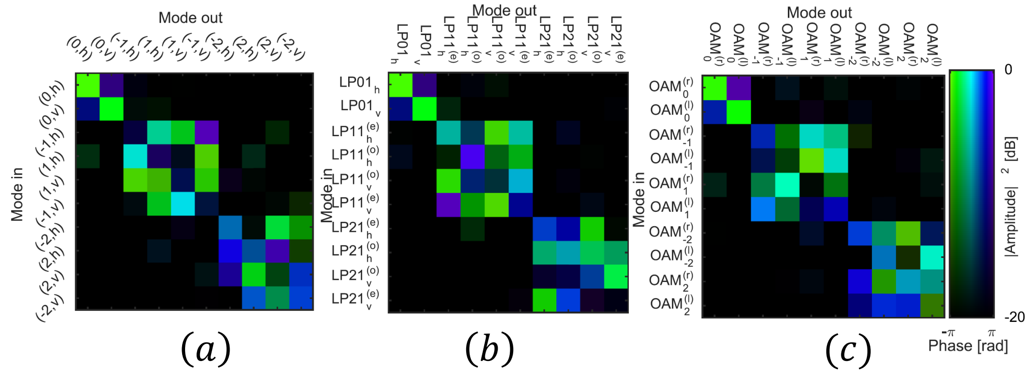

(a) (b) (c)

FIGURE 3.13: The ring core fiber TM expressed using (a) the mode basis defined in Table 3.2, (b) the standard LP mode basis and (c) standard OAM mode basis [Yammine et al., 2019].

perturbations of the fiber, while the large effective index differences between different mode groups impede coupling. For all three mode basis, the similarity of the distribution of the elements of the TM is remarkable which validates the fact that the chosen mode basis has no impact on the resulting detected modes, as long as this mode basis present a physical meaning. The singular values obtained by applying the SVD to the isolated fiber transmission matrix are presented in Figure 3.14.

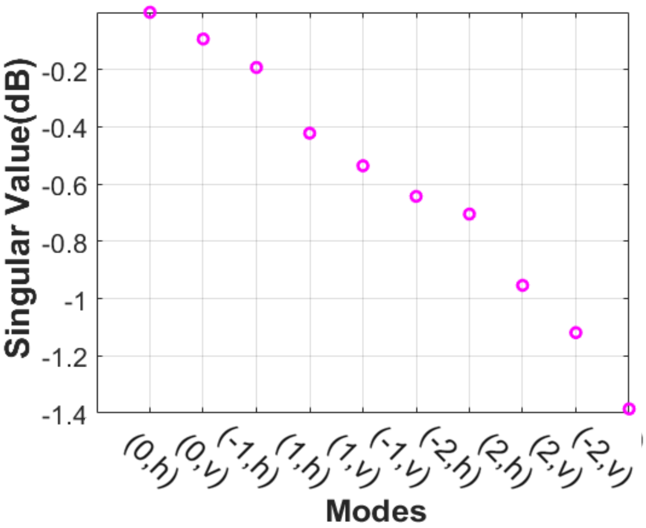

FIGURE 3.14: The singular values of the fiber TM of the linearly polarized, helical-phase mode basis defined in Table 3.2.

3.3.2 Time dependence of the TM

In any SDM transmission, it is essential to quantify and control the X-Talk between the different used channels, being the different cores for a MCF or the different modes for a FMF. As described in Section 2.1, experimental measurements show that the inter-core X-Talk can vary over time by as much as 10 dB. However, to the best of our knowledge, the time evolution of the X-Talk between the different modes of a FMF has not been studied yet, which raises two fundamental questions: how does the X-Talk between degenerate modes within a mode family evolve in time ? How does the X-Talk between any two mode families evolve in time ? These questions are not straightforward to address because we do not have easy access to the individual spatial channels of a FMF. However, this access can be provided by our method which can be used to conduct this study: we used our method to perform a time-resolved measurement and isolate the TM of the ring core fiber of the previous section, thus evaluate the temporal behavior of the multi-mode channel represented by the FMF. In order to do that, the experimental procedure detailed in Section 2.4.3 was repeated each 2 hours over a 2 days span: as mentioned in Section 2.4.4, the entire measurement can take up to 25 minutes using a localized input mode basis of 25×25, but we chose to split the start of 2 consecutive measurements for 2 hours in order to allow more relaxation time. Our setup was built in a non-isolated environment, but we tried to keep the surrounding conditions as stable as possible, specially the fiber itself, because any modification of its conditions can change the channels of the TM, thus the time-resolved matrix must be repeated from the start. The temperature was also maintained at a relatively stable level.

We start the investigation of the temporal evolution of the fiber TM by examining the amplitudes and the phases of each element of the fiber TMs.
Figure 3.15 presents the temporal variation of the TM:

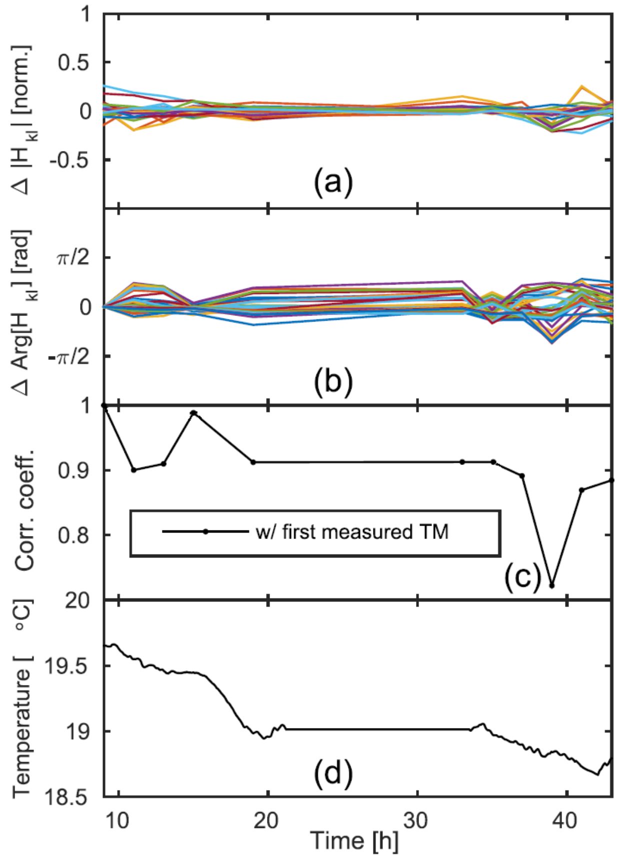

FIGURE 3.15: Temporal evolution of the fiber TM: (a) Normalized amplitude variation of fiber TM elements, (b) Phase variation of TM elements. Curves for fiber TM elements with a negligible amplitude (less than 0.18) are not shown, (c) Similarity index between the first measured fiber TM and the ones measured at t_i and (d) Log of the temperature in the vicinity of the fiber during the measurement window. [Yammine et al., 2019].

- (a) presents the temporal variation of the normalized amplitude defined as

$$\Delta|\mathrm{H_{kl}}|(t_\mathrm{i}) = \frac{|\mathrm{H_{kl}}(t_\mathrm{i})| - \langle|\mathrm{H_{kl}}(t_\mathrm{i})|\rangle_\mathrm{i}}{\langle|\mathrm{H_{kl}}(t_\mathrm{i})|\rangle_\mathrm{i}}, \tag{3.5}$$

  which describes the fractional amplitude variation from its mean normalized to the average over the time index i.

- (b) presents the temporal variation of the phase defined as

$$\Delta\mathrm{Arg}[\mathrm{H_{kl}}(t_\mathrm{i})] = \mathrm{Arg}[\mathrm{H_{kl}}(t_\mathrm{i})] - \mathrm{Arg}[\mathrm{H_{kl}}(t_0)] \tag{3.6}$$

  which can take on values in the interval $[-\pi;\pi]$. Only the curves for those fiber TM elements whose mean amplitude > 0.18 are shown (27 out of 36 elements contained in the diagonal blocks) because of the higher relative noise on the remaining elements. It can be appreciated that the variations are quite small, the amplitude varying only within 25% of the mean and the phase only within $\pi/2$. From the fact that there are no large phase jumps we conclude that the time resolution of our fiber TM measurement $(40\,\mathrm{min})$ is sufficient to resolve the slow drift under our experimental conditions.

- (c) We further examine the time evolution of the fiber TM by computing the similarity index between the first measured fiber TM at time t_0 with those measured at later times t_i. We define the similarity index as

$$\mathrm{SI}_{0\mathrm{i}} = \frac{\sum_{\mathrm{k,l}} \mathrm{H}^*_{\mathrm{kl}}(t_0)\mathrm{H}_{\mathrm{kl}}(t_\mathrm{i})}{\sqrt{\sum_{\mathrm{k,l}} |\mathrm{H}_{\mathrm{kl}}(t_0)|^2}\sqrt{\sum_{\mathrm{k,l}} |\mathrm{H}_{\mathrm{kl}}(t_\mathrm{i})|^2}} \tag{3.7}$$

  where * denotes element-wise complex conjugation. The similarity index remains above 70% throughout which, again attests to the slow drift of the fiber TM.

- (d) For reference, the temperature in close vicinity of the fiber was monitored during the measurements

An equivalent, but perhaps slightly more illustrative, representation of the same dataset is presented in Figure 3.16. For each element, all 11 complex-valued fiber TM elements acquired at times t_i are plotted in the complex plane. Horizontal and vertical lines represent the real and imaginary axes, and the circles are guides to the eye with radius equal to the absolute value of the matrix element. This illustration allows us to observe that the drift in the fiber TM can be attributed mainly to a drift in the phase since all the 11 plotted points per subfigure overwhelmingly tend to lie on the circles. This representation does not however provide any insight on the correlation between the phase variations of the different elements, which is the topic of the next paragraph.

3.3.3 Parametrization of the TM

Furthermore, we tried to find a parametrization of the fiber TM that can describe its temporal evolution. We started out from the stack of fiber TMs $\boldsymbol{H}_{\mathrm{kl}}(t_\mathrm{i})$ and the observation made in the previous paragraph that mainly the phase variation of the fiber TM needs to be taken into account. We hence create the two-dimensional matrix $\Delta\Phi_{\{\mathrm{kl}\}\mathrm{i}}$ in the composite index $\{\mathrm{kl}\}$ and the temporal index i:

$$\Delta\Phi_{\{\mathrm{kl}\}\mathrm{i}} = \mathrm{Arg}[\mathrm{H}_{\mathrm{kl}}(t_\mathrm{i})] - \mathrm{Arg}[\mathrm{H}_{\mathrm{kl}}(t_0)], (\mathrm{k}, \mathrm{l}) \in \mathcal{D} \tag{3.8}$$

where $\mathcal{D}$ is the group of indices (k, l) of the diagonal blocks of the fiber TM. The $\Delta\Phi_{\{\mathrm{kl}\}\mathrm{i}}$ matrix has a dimension of 36×11 (number of elements in the diagonal blocks × number of time points). We take the singular value decomposition of the resulting matrix:

$$\Delta\Phi_{\mathrm{kl}} = \boldsymbol{USV}^\dagger. \tag{3.9}$$

The $\Delta\Phi_{\{\mathrm{kl}\}\mathrm{i}}$ matrix is shown in Figure 3.17(a). We applied the SVD on this matrix and obtained the singular values of $\boldsymbol{S}$ which are shown in Figure 3.17(b). As can be seen, there is one significant singular value (which can be extended to include the first 5 singular values), which is way less than the number of elements of the matrix or the number of the elements of the diagonal blocks of the fiber TM. This fact allows us to find a parametrized model that can predict the phase variations based on the singular vectors of the SVD of $\Delta\Phi_{\{\mathrm{kl}\}\mathrm{i}}$. The first singular value

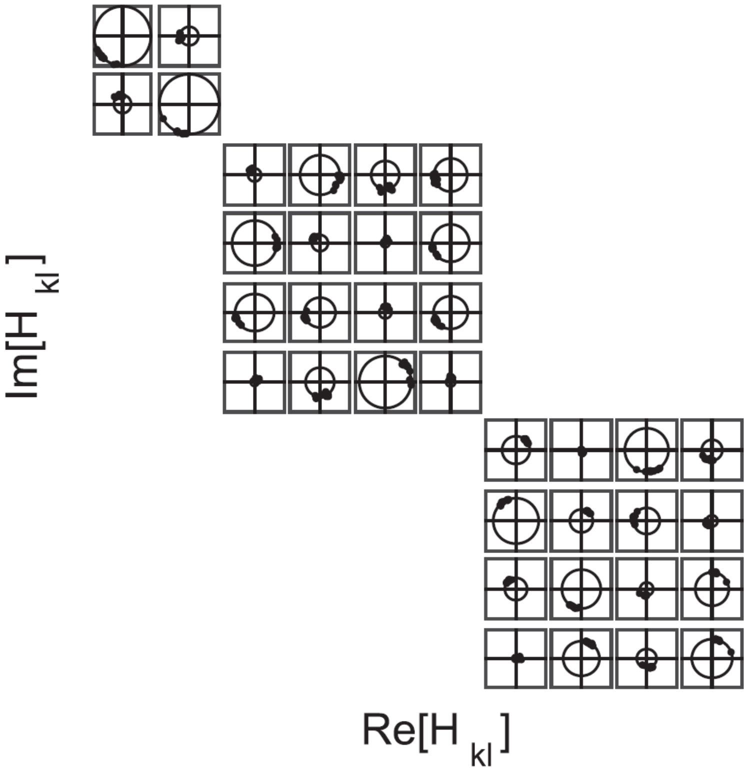

FIGURE 3.16: Representation in the complex plane of the fiber TM elements measured at different times. Horizontal and vertical lines represent the real and imaginary axes. Depicted circles are guides to the eye and have radius equal to the time-averaged norm of the fiber TM element. [Yammine et al., 2019].

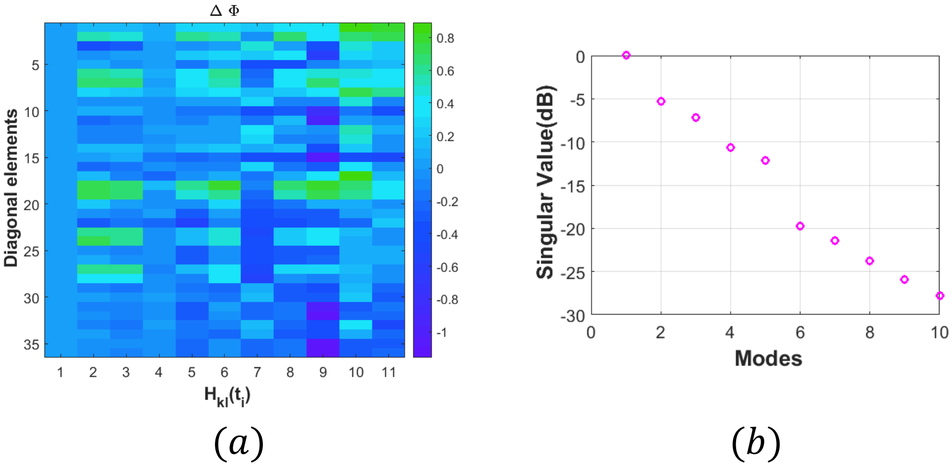

FIGURE 3.17: (a) The $\Delta\Phi_{\{kl\}i}$ 36×11 matrix and (b) the singular values obtained of its SVD.

accounts for 35% of the singular weight; the first three for 69%, and the first five for 88%. For now, we retain only the first singular vector which which equals to taking the first column of $\boldsymbol{U}$, $\mathrm{U}_{\{\mathrm{kl}\}1}$, with which we can construct an empirical, parametrized version of the fiber TM in the parameter α:

$$\mathrm{H}_{\mathrm{kl}}^{(\mathrm{param})}(\alpha) = \begin{cases} \mathrm{H}_{\mathrm{kl}}(t_0) \cdot e^{(j\alpha U_{\{\mathrm{kl}\}1})} & ,(\mathrm{k},\mathrm{l}) \in \mathcal{D} \\ \mathrm{H}_{\mathrm{kl}}(t_0) & ,(\mathrm{k},\mathrm{l}) \notin \mathcal{D} \end{cases} \tag{3.10}$$

The drift is thus mathematically expressed as a complex-valued "drift" operator, identifiable as the matrix being multiplied onto $\mathrm{H}_{\mathrm{kl}}(t_0)$ in the Equation 3.10. In Figure 3.18 this drift operator is presented.

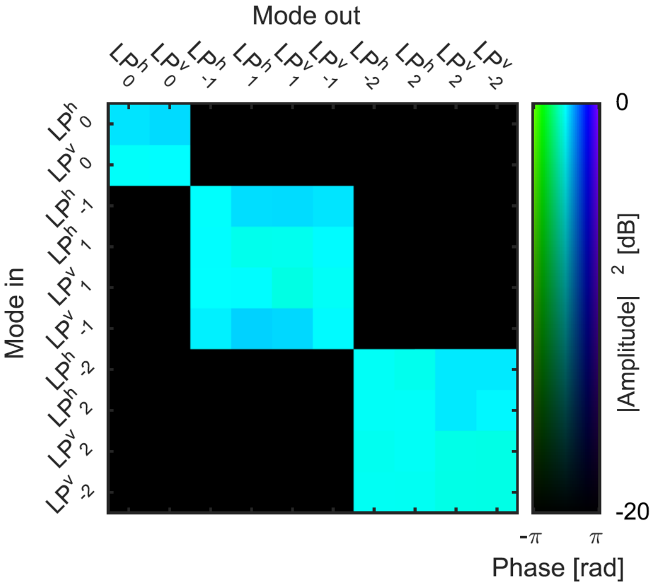

FIGURE 3.18: First singular vector of $\Delta\Phi$ drift operator (in complex form), in the case of parametrization in one parameter [Yammine et al., 2019].

We now check whether the parametrized TM is a good model of the multi-modal channel represented by the fiber. To do so, for each fiber TM of the fiber TM stack we identify the α value that results in the best similarity index using:

$$C_{\mathrm{i}}^{(\mathrm{param})} = \frac{\sum_{\mathrm{k,l}} [\mathrm{H}_{\mathrm{kl}}^{(\mathrm{param})}(\alpha)]^* \mathrm{H}_{\mathrm{kl}}(t_{\mathrm{i}})}{\sqrt{\sum_{\mathrm{k,l}} |\mathrm{H}_{\mathrm{kl}}^{(\mathrm{param})}(\alpha)|^2} \sqrt{\sum_{\mathrm{k,l}} |\mathrm{H}_{\mathrm{kl}}(t_{\mathrm{i}})|^2}}. \tag{3.11}$$

The results are summarized in Table 3.3. It can be appreciated that this simple parametrization in only a single parameter gives a very decent description of the measured TMs with its 36 significant elements, with similarity index systematically above 91%. The same values are also shown in Figure 3.19 as squares.

To put things in perspective, we tried to include more parameters in the model, so we expanded the model of Equation 3.11 to take into account 3 singular vectors, $\mathrm{U}_{\{\mathrm{kl}\}1}$, $\mathrm{U}_{\{\mathrm{kl}\}2}$ and $\mathrm{U}_{\{\mathrm{kl}\}3}$. Thus, the model included 3 parameters α, β and γ as follows:

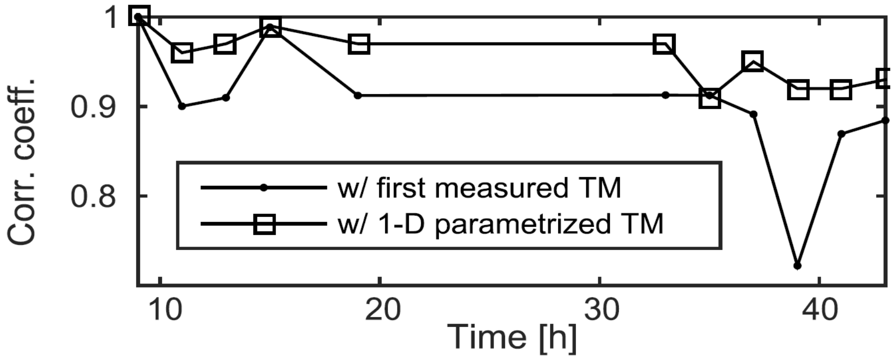

FIGURE 3.19: Similarity index between the TM parametrized in one parameter and the fiber TM measured at time t_i represented by squares and compared to the similarity index between the first measured fiber TM and the ones measured at t_i represented by the dots [Yammine et al., 2019].

TABLE 3.3: Similarity index with the TM parametrized in one parameter.

Time[h]	α	Similarity Index
9	0.00	1.00
11	1.54	0.96
13	1.49	0.97
15	0.17	0.99
19	1.48	0.97
33	1.48	0.97
35	−0.15	0.91
37	1.61	0.95
39	3.04	0.92
41	1.43	0.92
43	1.41	0.93

$$\mathrm{H}_{\mathrm{kl}}^{(\mathrm{param})}(\alpha) = \begin{cases} \mathrm{H}_{\mathrm{kl}}(t_0) \cdot e^{(j\alpha \mathrm{U}_{\{\mathrm{kl}\}1})} \cdot e^{(j\beta \mathrm{U}_{\{\mathrm{kl}\}2})} \cdot e^{(j\gamma \mathrm{U}_{\{\mathrm{kl}\}3})} & ,(\mathrm{k},\mathrm{l}) \in \mathcal{D} \\ \mathrm{H}_{\mathrm{kl}}(t_0) & ,(\mathrm{k},\mathrm{l}) \notin \mathcal{D} \end{cases} \tag{3.12}$$

The results are summarized in Table 3.4. It can be seen that this expanded parametrization using 3 parameters gives a better description of the measured TMs than the single parameter model with its 36 significant elements, with similarity index systematically above 95%. However, the increase in the similarity is minimal, whereas the increase of the degree of difficulty of the problem is much greater.
It is clear that parametrizing the TM in more parameters will result in ever better

TABLE 3.4: Similarity index with the TM parametrized in three parameters.

Time[h]	α	β	γ	Similarity Index
9	0.00	0.00	0.00	1.00
11	1.50	0.80	−0.60	0.99
13	1.45	0.85	−0.35	0.99
15	0.20	−0.05	0.20	0.99
19	1.55	0.35	0.60	0.97
33	1.55	0.95	0.40	0.98
35	−0.05	−1.20	0.90	0.97
37	1.75	0.95	1.05	0.97
39	2.80	−1.75	−1.80	0.96
41	1.45	−1.40	0.25	0.96
43	1.50	−0.20	0.95	0.95

concordance with the measured fiber TMs. Using all 10 vector modes of the $\boldsymbol{U}$ matrix with the right parameters would eventually lead to the exact initial TM. Nevertheless, we can conclude from our results that, in our measurement conditions, drift results in changes to the fiber TM that are highly correlated between matrix elements. Thus, even a low-dimensional parametrization with number of parameters much smaller than the number of matrix elements involved, even if the number of parameters is just one, can describe the measurement very well.

3.4 Discussion

In this chapter, we presented the results of the modal content analysis for several fiber geometries using our implemented method based on the measurement of the full TM of the fiber. The full fiber TM is a direct measurement of the linear behavior of the fiber. Thus, it contains more information than indirect measurements like time-averaged X-Talk and bit-error ratio. As such, fiber TM measurements could be a good basis for developing empirical multi-modal channel models but could also be a good basis for comparison with various multi-modal channel models that have been developed [Antonelli et al., 2013; Ho and Kahn, 2011]. In order to explain the group-delay effects, a wavelength resolved TM measurement is required [Carpenter, Eggleton, and Schröder, 2016]. The tested fibers lengths were very short, between 1 m and 1.5 m but it is of the same length scale as some of the multi-mode components which would be required for potential future multi-modal fiber optic communication networks, like mode filters or multi-mode amplifiers. So our method could have an appeal for characterizing this type of multi-mode components.

In the case of a SDM transmission, the time evolution of transmission quality in MCF has been the subject of several papers. In effect, experimental measurements show that inter-core X-Talk can vary over time by as much as 10 dB [Macho, Morant, and Llorente, 2015; Luís et al., 2016; Puttnam et al., 2017]. The variability of the inter-core X-Talk must be known in order to design a MCF network that can guarantee a certain minimum performance in all conditions. Channel models for MCF have been proposed in order to provide tools to assist in designing MCF networks [Alves et al., 2017; Alves and Cartaxo, 2017; Alves and Cartaxo, 2018; Gan et al., 2018]. The very same issues are expected to be present in FMFs. Nevertheless, to the best of our knowledge, FMFs have not yet been subjected to the same level of scrutiny as their MCF counterparts in what concerns their temporal behavior. At the end of this chapter, the time evolution of the TM matrix of a FMF and its channels was investigated over a two-days span. Due to our experimental approach, we were able to notice that phase drifts are the major contributors for the time variation of the channels of a FMF in our experimental conditions.

This method is subject to further upgrades, mainly to reduce the required time to deliver the final result: as the time scale of drift likely decreases as a function of the length of the fiber, the measurement time reduction can enable us to characterize long distance fibers, such as transmission fibers and reduce the noise contribution from the fiber's entourage. The current time to measure a fiber TM, defining the temporal resolution, is about 25 minutes. In principle this could be sped up in a number of ways that we have not yet implemented. We currently measure the four combinations of input and output polarizations separately, as described in Section 2.4.3. Measuring them simultaneously in a two-polarization setup enables an immediate 4 times gain on the measurement time, in addition to eliminating the source of error which is phase drift between measurement of different polarization combinations. Another way to reduce the required time for a measurement is to reduce the number of localized input modes: using the 625 localized input modes of the 25×25 basis is a massive over-sampling to measure 24 guided modes for the step index fiber of Section 3.2 and the 10 guided modes for the ring core fiber of Section 3.3. We could also envision employing another wavefront shaping device, such as a SLM with shorter response time, a segmented deformable mirror or a acousto-optic deflector (AOD). During the last few months of this thesis, our team proposed a Master 2 internship, in order to adapt our experimental method to the use of two AODs as the wavefront shaping devices instead of the SLM. The SLM that we used in our experimental setup presented in Section 2.4.3 (Meadowlark P1920-1625-HDMI) has a standard liquid crystal response time of 33 ms, which can be converted to a frequency of 30 Hz. We should mention than SLMs with higher frequencies do exist. The AOD that we implemented can operate at a frequency of 52.5 MHz. However, this potential speed increasing is limited by the response time of the used camera. During his 4 months internship, Adrien CARRON worked on this task. In the part of his internship, Adrien got the chance to work on the experimental setup based on the two AODs and managed, in this little time window, to assemble an operating experimental setup, with several modification from the one presented in Section 2.4.3 in order to implement the two AODs. Figure 3.20 illustrates a schematic of his adapted experimental setup, which was used in his final report.
The first results obtained using this experimental setup were not perfect. The resulting fiber TM of the FMF L113 using this method is displayed in Figure 3.21(a) for the LP mode basis and in Figure 3.21(b) for the OAM mode basis. The difference is clear between the results of the two AODs setup and the results of the SLM setup for the same L113 presented in Figure 3.6. We should recall that the matrices of Figure 3.21 are preliminary results. Unfortunately, the short one and a half months of experimental works ended before Adrien managed to find and optimize the experimental setup. However, his remarkable efforts and great progress

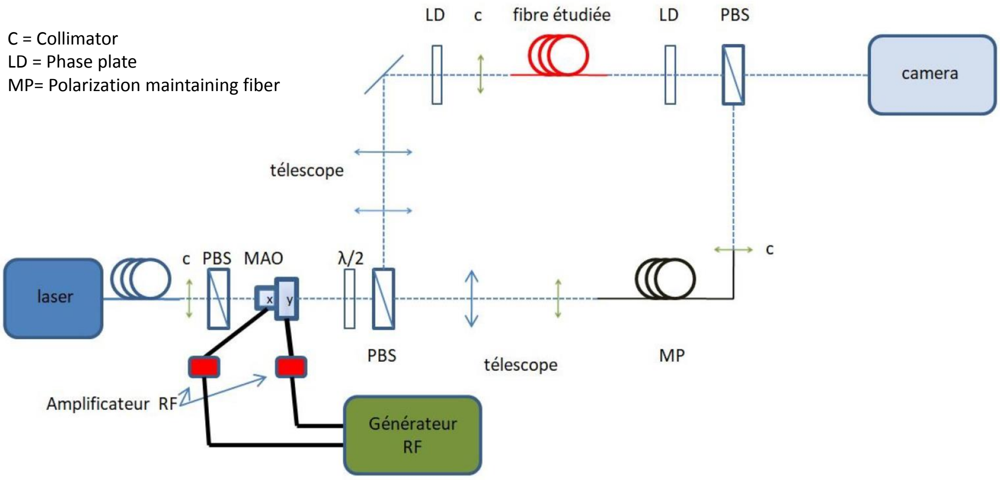

FIGURE 3.20: Schematic of the experimental setup using the two AODs in order to generate the localized input modes.

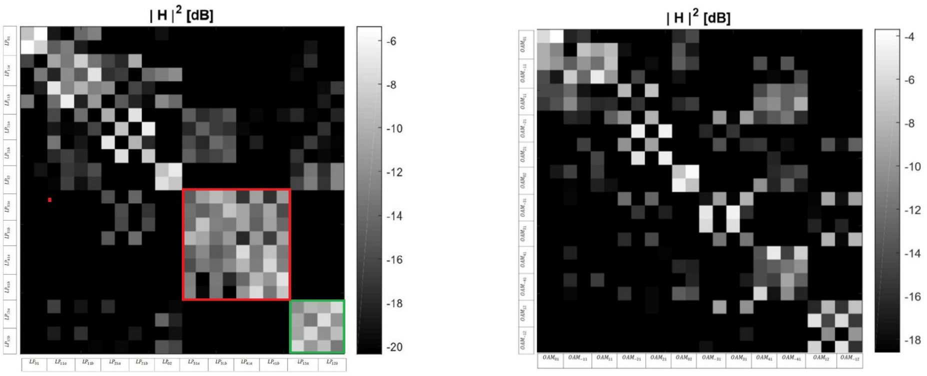

(a) (b)

FIGURE 3.21: The isolated TM for the FMF L113 in the (a) LP basis and the (b) OAM basis measured using the two AODs experimental setup.

gave us a first lead on updating our experimental setup, which can be pursued and continued during future works. Finally, the data treatment and optimization process time can also be shortened, which can give us the ability of quicker characterization, maybe even live characterization of the different channels of the fiber.

3.5 Conclusion

In this chapter, we showed the different works and results that we obtained during this thesis using our implemented method described in Chapter 2. Several fiber geometries were investigated, from step index fibers to ring core fibers, in order to highlight that our method does not have a geometric preference for the tested fiber. Our method was used to characterize short fiber lengths comparable to some multi-mode components. In addition to that, the time dependence of the TM was also characterized over a two-days span, from which we concluded that the temporal drift that can occur is mainly due to the phase drifts in our experimental conditions. We further showed how a simple, low-dimensional parametrization of the fiber TM, gives a good description of the temporal evolution of the multi-modal channel it represents over the same time span. We believe that our approach could aid in developing accurate channel models for FMF optic transmission systems as well as a deeper understanding of FMFs.

Chapter 4

Few-mode amplification

4.1 Introduction

The amplification process is one of the corner stones of any long distance telecommunication transmission system. It provides the necessary power boost so the signal can reach its destination with significant amount of power for any detection and decryption to be possible. The study of this process for MDM transmission made a focal part of this thesis. There are different types of amplifiers that can be used in the context of MDM: parametric amplifiers [Zhao et al., 2013], Raman amplifiers [Ryf et al., 2011] and the few-mode Erbium doped fiber amplifiers (FM-EDFA). In this chapter, we will focus on the FM-EDFA as it has demonstrated the greatest potential in the context of MDM, compared to the later two, from its reliability to its cost. We will start by reviewing the previous works conducted in this field, from more than 25 years until now. Then, we will describe the different works on this topic that we have done during this thesis, based on the previous works of our team. First, we will show the latest tests and results on a fiber design developed by Trinel during his thesis in our team: it is a micro-structured core FM-EDFA capable of generating equal gain for 10 LP modes, using a pair of custom-made MUX-DEMUX manufactured by CAILabs for this particular fiber. In a second part of this chapter, we will describe the design and the fabrication of an all-solid ring core FM-EDFA, capable of amplifiying OAM modes in a more familiar annular fiber guiding up to 26 modes (6 OAM mode groups, consisting of 4 modes and the pair of OAM_0 modes). After that, we will show numerical works and studies of a step-index FM-EDFA, doped in an annular fashion. This study illustrates the amplification process of OAM modes in a step-index fiber. At the end of this chapter, we will discuss the power conversion efficiency of each of these designs and compare them to the presently used single-mode EDFA.

4.2 Key parameters of FM-EDFA

FM-EDFAs have an architecture similar to single-mode EDFAs presented in the first chapter, with a core that can guide multiple modes at the signal wavelengths. In consequence, the number of modes significantly increases at the pump wavelengths. The challenges facing the FM-EDFAs consist in having a flat gain over all the signal wavelength band with low noise figure (NF, described later in appendix 4.8), just like in the single-mode EDFAs case. However, in addition to these "old" challenges, the gain needs to be equalized over all the signal modes. Thus, the designs of the FM-EDFAs must take into account the gain difference for a particular mode over spectrum called differential spectral gain (DSG), the gain difference for a particular wavelength between the different signal modes called differential modal gain (DMG) and the difference of gain between all the signal channels called total gain excursion (ΔG). These different parameters are presented in Figure 4.1.

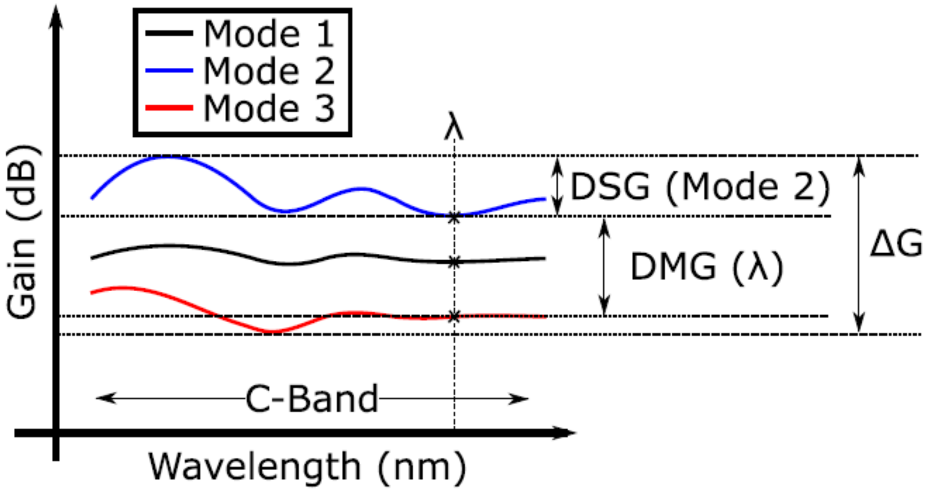

FIGURE 4.1: Evolution of gain as a function of signal wavelength for different modes in a non-equalized gain configuration [Trinel, 2017].

From the amplification medium point of view, the amplification process is a product of the overlap γ between the transverse distribution of light intensity at the pump wavelength, the transverse distribution of the light intensity of the different signal modes and the transverse Erbium doping profile (EDP). In order to reduce the value of ΔG, two different parameters can be explored: the shape of the pump beam and the shape of the EDP. Multiple studies have been conducted on this subject and will be reviewed in details in the next section.

4.3 State of the art

Well before MDM, the gain differential issue in multi-mode configuration was the subject of multiple studies. Back in 1990, Desurvire studied for the first time the impact of using a multi-mode pump beam on the gain. The combination of LP_{01} and LP_{11} modes at the pump wavelength reduces the overlap γ with the LP_{01} at the signal wavelength, thus reducing the efficiency of the amplifier [Desurvire, 1990]. In 1991, Nykolak presented the first experimental study of a multi-mode amplifier [Nykolak et al., 1991]. In 2000, Spellmeyer presented a two-stage multi-mode EDFA to reduce noise level [Spellmeyer, 2000]. Even if the problematic was different, these works can be useful for the MDM as they study the same parameters: the shape of the pump beam and the shape of the EDP.

As we go through the different works since 2011, we will be using the fiber type to categorize these works, as shown in Figure 4.2:

- the conventional FM-EDFAs, the most common and studied type [Jung et al., 2011; Ip et al., 2011; Bai et al., 2012; Sleiffer et al., 2012; Le Cocq et al., 2012; Ip et al., 2013; Jung et al., 2013b; Jung et al., 2013a; Jung et al., 2014b; Jung et al., 2014a; Simonneau et al., 2015; Lopez-Galmiche et al., 2016; Wakayama et al., 2016; Fontaine et al., 2016; Ryf et al., 2016; Eznaveh, 2017; Wakayama et al., 2017; Zhang et al., 2018; Gaur, Kumar, and Rastogi, 2018],

- the micro-structured FM-EDFAs, which provides a high EDP customization capability [Le Cocq et al., 2013; Trinel et al., 2018],

- the cascaded FM-EDFAs, combining different type of fibers simultaneously in order to obtain a more flattened gain [Salsi et al., 2012; Wada et al., 2016].

- the ring core FM-EDFAs, guiding modes with very similar spatial intensity distributions [Ono et al., 2015; Kang et al., 2015; Deng et al., 2017; Jung et al., 2017b; Wang et al., 2017; Jung et al., 2017a].

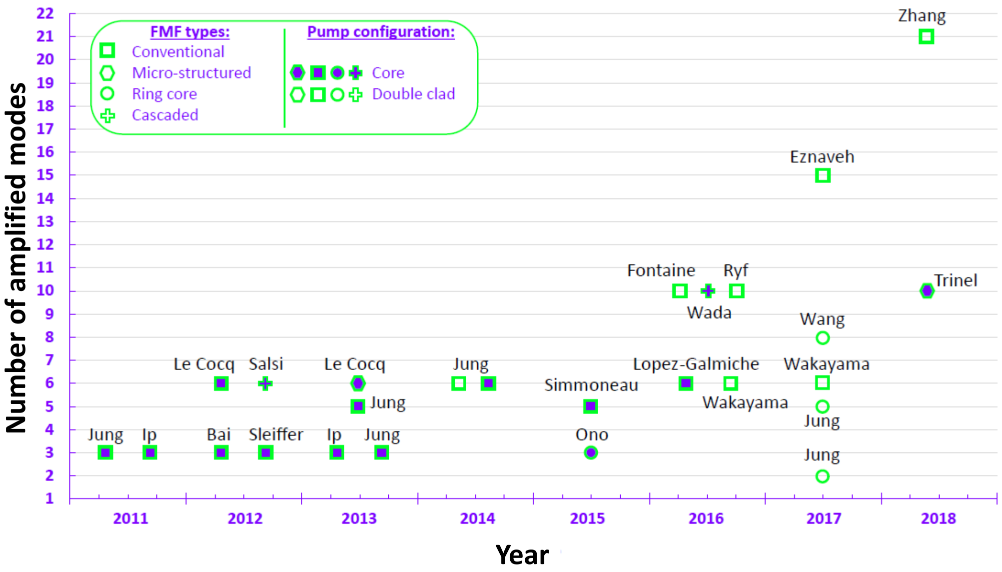

FIGURE 4.2: Evolution of the number of amplified modes in the context of the MDM since 2011.

As mentioned previously, in order to achieve spectral and modal gain equalization, the shape of the pump beam can be explored. This can be done by modifying the contribution of each mode at the pump wavelength to the whole pumping beam. The pump can be guided in the core of the fiber, or using an inner cladding, with n_{ic} as refractive index, surrounding the fiber's core where the signal propagates, as shown in Figure 4.3.

Due to the high number of modes at the pump wavelength, the core-pumped FM-EDFAs have the advantage of providing a large number of possible combinations regarding their respective fractions of the total pump power. The main limitation of this approach is the generation of specific mode profiles that can generate significant power losses and thus increase the need of the pump power

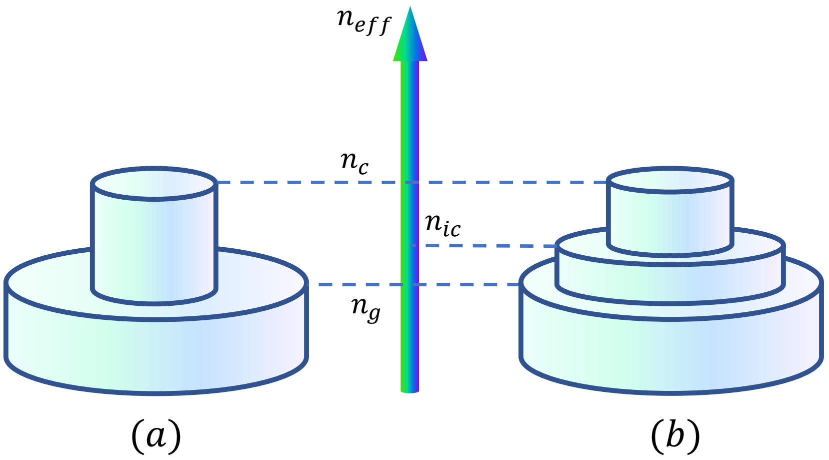

FIGURE 4.3: Conventional fiber structure and a double clad fiber structure.

level. The first theoretical results on pump beam shaping for FM-EDFAs, in the context of modal multiplexing, were reported by Bai in 2011. The use of LP_{11}, LP_{21} or a combination of LP_{01} and LP_{21} modes with a uniformly doped FM-EDF was proposed. These modes are generated using specific wave plates. For a 3 mode FM-EDFA, this strategy can greatly reduce the modal gain excursion for a specific wavelength [Bai et al., 2011]. These theoretical results were confirmed experimentally in 2012 [Bai et al., 2012]. The same fiber was used in line for data transmission (30 Tbit/s over 50 km) requiring the use of a MIMO 6×6. The shaping of the pump beam is performed both in the co-propagative direction with a LP_{21} mode and in the counter-propagative direction with LP_{11} mode [Ip et al., 2011]. In 2012, Sleiffer presented a transmission record using 3 mode FM-EDFA a MIMO 6×6 (73.7 Tbit/s over 119km) [Sleiffer et al., 2012]. In 2013, Ip and his group reported a transmission over a longer distance (3 Tbit/s over 700km) involving the same 3 mode FM-EDFA used in his previous work [Ip et al., 2013]. This technique was also used by Jung in 2011, who adopted the same amplifier scheme proposed by Bai, but replaced the phase plates with an off-center injection of the pump beam in order to excite the LP_{21} mode (co-propagative) [Jung et al., 2011]. Jung reused this technique by adding a counter-propagative LP_{21} mode pump for a 5 mode FM-EDFA in 2013 and a 6 mode FM-EDFA in 2014 [Jung et al., 2013b; Jung et al., 2014b]. The results of the 6 mode FM-EDFA show a gain larger than 20 dB with a modal gain excursion of less than 2 dB over a spectral range from 1535 nm to 1560 nm, using a 0.34 W pump power. In 2016, Lopez-Galmiche reported a 6 mode FM-EDFA using a photonic lantern to generate the spatial modes both at the signal and pump wavelengths [Lopez-Galmiche et al., 2016]. The LP_{21} mode group was chosen to shape the pump beam. This FM-EDFA provided a gain larger than 10 dB for a gain excursion equal to 9 dB over a spectral range from 1530 nm to 1565 nm and a pump power of 0.57 W.

Beyond this first approach, the inner cladding pumping configuration has the advantage of providing a homogeneous transverse intensity distribution of the pump beam. In addition, uncooled multi-mode laser diodes can be used as pump sources, giving higher power limits and making these systems more suitable for future application. The main disadvantage of this approach is the low conversion efficiency of the pump power due to the difficulty in reaching the saturation power in the core. With this approach, Jung demonstrated in 2014 a 6 mode FM-EDFA providing an average gain larger than 20 dB for a 4 dB modal excursion and requiring more than 3 W of pump power [Jung et al., 2014a]. In 2016, Wakayama proposed a 6 mode FM-EDFA, with an Erbium doped area wider than the core in order to optimize the pump absorption. In this configuration, the pump power was 7.9 W for a gain larger than 20 dB with a gain excursion about 3.3 dB over a spectral range from 1535 nm to 1562 nm [Wakayama et al., 2016]. The same year, Fontaine reported a 10 mode MM-EDFA providing a gain larger than 15 dB for a modal excursion of less than 2 dB over a spectral range from 1525 nm to 1560 nm and requiring 9 W of pump power [Fontaine et al., 2016]. This FM-EDFA was also used by Ryf in a 10 modes MDM transmission, reaching a rate of 111.4 Tbit/s over 121 km with the need of a MIMO 20×20 treatment [Ryf et al., 2016]. In 2017, the same team reported a 15 mode FM-EDFA using a fiber guiding 36 spatial modes at 1550 nm. Only 15 of these 36 spatial modes were selected for amplification to reduce the modal gain excursion. It provides a gain of 15 dB at 1550 nm, with a modal gain excursion not exceeding 0.5 dB using 10W for pump power. Note that this FM-EDFA is characterized mode by mode and that no cross-talk information is provided. The same year, Wakayama reported a 6 modes C and L-band (1535 nm to 1602 nm) FM-EDFA, offering a gain over 16 dB with a modal gain excursion of 2.3 dB for the C-band and 5 dB for the L-band. The pump powers were 7.9 W and 8.1 W for the C and L-band demonstrations, respectively [Wakayama et al., 2017]. In 2018, Gaur proposed a theoretical design of 20 mode dual core FM-EDFA, with an amplification of more than 21 dB and a 1.75 dB gain excursion over a spectral range from 1530 nm to 1560 nm. The pump power variation was from 0.255 W to 0.335 W [Gaur, Kumar, and Rastogi, 2018]. The same year, Zhang presented a cladding-pumped 21 mode FM-EDFA, with an average gain of 15 dB for all modes, with a modal gain excursion of 3 dB over the C-band and a pump power of 2.9 W [Zhang et al., 2018].

The second approach consists in adapting the EDP in order to favor the equalization of the gain. This approach enables to decrease the pump power budget compared to the first approach. However, the constraint is transferred to the manufacturing of the preform itself. Kang proposed, in 2012, a theoretical design of FM-EDF: a ring-shaped transverse distribution of Erbium should favor gain equalization for the 3 modes, LP_{01} and the LP_{11} mode group [Kang et al., 2012]. At the same time, our group demonstrated the realization and characterization of a 6 mode FM-EDFA with a similar ring-shaped Erbium distribution to help the gain equalization of non-centered modes (the LP_{11} and LP_{21} mode groups). This FM-EDFA uses centered pump modes in order to couple a maximum of pump power into the core of the fiber. This ring distribution effectively reduces the modal gain excursion between non-centered modes to 0.4 dB at 1550 nm [Le Cocq et al., 2012]. In 2015, Simmoneau used this FM-EDFA for a 5 mode transmission, each mode carrying a rate of 100 Gbit/s over 80 km of FMF with low complexity signal processing (MIMO 4×4) for the LP_{11} and LP_{21} mode groups and a conventional MIMO 2×2 for the LP_{01} mode [Simonneau et al., 2015]. This work demonstrates an average gain of 16.3 dB for a gain excursion of 8 dB using a 0.27 W pump power. The ring-shaped distribution FM-EDFA were widely used by Jung combined with the pump beam shaping approach [Jung et al., 2011; Jung et al., 2013a; Jung et al., 2014a].

In 2012, Ip proposed to use a complex transverse distribution to achieve a 10 mode FM-EDFA. In this configuration, the pump beam shaping involves ten groups with specific fractions of the total pump power in order to achieve a very low gain modal excursion [Ip, 2012]. In the following year, more transverse Erbium distributions were presented, inspired by the ring-shaped distribution: ring shaped distribution with a centered peak and the double ring distribution. These distributions resulted in a 3 mode FM-EDFA using a LP_{01} pump mode [Jin et al., 2013] and a 6 mode FM-EDFA using a combination of LP_{01} and LP_{41} pump modes [Kang et al., 2013]. However, conventional preform manufacturing techniques (especially Modified Chemical Vapor Deposition (MCVD)) can hardly achieve complex distribution and are limited to circular or quasi-circular symmetry.

In order to surpass these limits, an alternative approach based on a micro-structured core has been proposed by our team [Le Cocq et al., 2013] in the MDM context. This approach allows to "pixelate" the core of the fiber and then achieve complex EDP, not necessarily in a cylindrical symmetry. Following this approach, a 6 mode micro-structured core FM-EDFA has been designed and realized in 2013 to provide equalized gain for the off centered modes, LP_{11} and LP_{21} mode groups, with an average gain of 21.7 dB and a total gain excursion of 2.7 dB. In 2018, our team reported a new design of a 10 mode FM-EDFA with multicore pedestal core [Trinel et al., 2018]. This work will be described in great details later in this chapter.

Another possibility for achieving an equalized gain between the different modes is to concatenate fibers with different Erbium distributions, rather than limiting it to a single type of fiber with a complex distribution. In 2012, this technique was used by Salsi: a FM-EDFA with a ring-shaped distribution made in our laboratory [Le Cocq et al., 2012] and combined to a FM-EDFA with a homogeneous Erbium distribution [Salsi et al., 2012]. This configuration provides an amplification of 6 modes simultaneously, with a gain larger than 18 dB for a total gain excursion of 6 dB. In 2016, Wada proposed the same type of configuration for a 10 mode FM-EDFA using the LP_{11} mode group as the pump mode [Wada et al., 2016]. This amplifier provides a gain larger than 15 dB with a total gain excursion of 6 dB, but the mismatch of the index profiles between the two FM-EDFs induces a strong coupling between the modes, which tends to favor the equalization of the measured gains.

Another approach to obtain gain equalization suggested a new configuration of FM-EDFA, where the ring profile is not only used for the transverse distribution of Erbium but also for the refractive index profile. In 2015, Ono proposed a 3 mode FM-EDFA design, capable of reducing the differential modal gain to about 1.8 dB while pumping with the LP_{01} mode and 1.6 dB while pumping with the LP_{11}. These values have to be compared to 9.2 dB and 6.1 dB representing the DMG values that were obtained for a step index FM-EDFA [Ono et al., 2015]. Later that year, Kang proposed a theoretical air-hole ring-core FM-EDFA capable of providing a uniform gain for 12 OAM modes from the groups $|L| = 5$, 6 and 7 over the C-band. The gain provided was about 20 dB for a differential modal gain of $0.25\ \mathrm{dB}$ when pumping with the $\mathrm{OAM}_{(8,1)}$ [Kang et al., 2015]. In 2017, Jung presented for the first time, an OAM FM-EDFA for lower order modes, based on an air-hole fiber design. This fiber provides significant mode splitting between the $|L| = 1$ modes and the adjacent vector modes, and a gain of $15.7\ \mathrm{dB}$ is obtained using a cladding pumped amplifier configuration over an operational wavelength range from $1545\ \mathrm{nm}$ to $1600\ \mathrm{nm}$ [Jung et al., 2017b]. Later then, Deng proposed a theoretical OAM FM-EDFA based on circular photonic crystal fiber, supporting 18 OAM modes, providing a gain larger than $20\ \mathrm{dB}$ with a small differential modal gain of less than $0.2\ \mathrm{dB}$ over the C-band [Deng et al., 2017]. Still in 2017, Wang reported an OAM FM-EDFA based on an annular-core photonic lantern, with a gain of $22.1\ \mathrm{dB}$ for the $|L| = 1$ mode group and $16.7\ \mathrm{dB}$ for the $|L| = 2$ mode group over the C-band. The differential modal gain is about $5.4\ \mathrm{dB}$. This FM-EDFA contains 5 SMFs input of dissimilar size inside a low refractive index capillary and a pure fluorine-doped central fiber core. During adiabatic tapering, each input fundamental mode can evolve into a specific LP mode at the output and OAM modes can be then expressed as a superposition of two degenerate LP modes [Wang et al., 2017]. Finally, Jung reported another ring-core FM-EDFA with a cladding pump configuration, capable of amplifying 5 LP modes of nearly $10\ \mathrm{dB}$ with a differential modal gain less than $1\ \mathrm{dB}$ [Jung et al., 2017a].

4.4 Micro-structured FM-EDFA with inclusions

Upon my arrival at the laboratory, in 2016, our team members were working on new designs of FM-EDFAs. Conventional preform manufacturing techniques, mainly MCVD, can hardly achieve complex doping profiles and are limited to circular or quasi-circular symmetry designs. As described in the section 4.3, our team have suggested the use of micro-structure approach in order to obtain complex doping profiles [Le Cocq et al., 2013]. However, manufacturing difficulties and poor gain performances for its 6 amplified modes led the team to find a better design.

4.4.1 Design

During his thesis, Trinel was interested in studying an alternative approach that combines the advantages of micro-structuring the core for the realization of complex EDP, while being achievable by conventional processes [Trinel et al., 2018]. The design he proposed is a micro-structured core consisting of 19 secondary cores with refractive index $n_2 = 1.452$, embedded in a pedestal geometry with refractive index $n_1 = 1.448$. This design has a micro-structured core equivalent to a coupled-cores multi-core fiber due to the refractive index difference $n_2 - n_1$ as shown in Figure 4.4.
In the following, the cores with refractive index n_2 will be mentioned as inclusions. As explained by Trinel in his PhD thesis [Trinel et al., 2018], this design has several advantages:

- the MCVD process combined with the solution doping gives access to the fabrication of Erbium doped preforms with large panels of glass composition, especially aluminosilicate cores compatible with WDM,

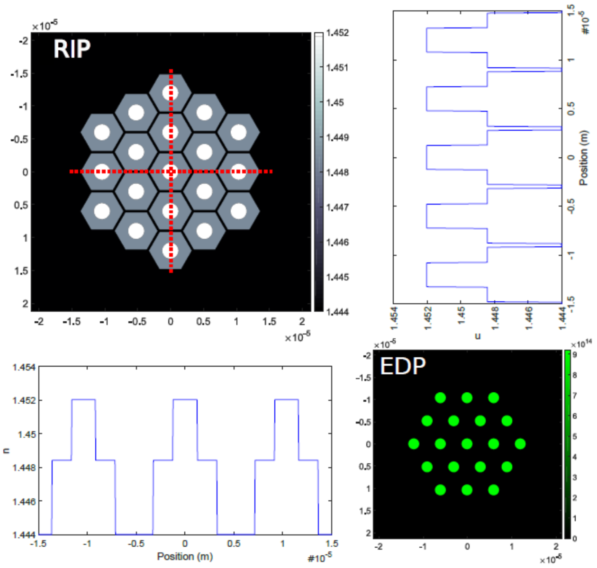

FIGURE 4.4: The $2D$ RIP and EDP of the micro-structured core FM-EDFA theoretical design [Trinel et al., 2018].

- the quantity of raw material available from one single preform is sufficient for the fabrication of a 19-elements FM-EDFA, in contrast with the previous micro-structured fiber design Le Cocq et al., 2013,
- RIP and EDP imperfections of the MCVD preform do not have a significant impact on the properties of the final fiber,
- this FM-EDFA is all-solid, in order to avoid complications related to the use of air holes.

4.4.2 Fabrication

This design was manufactured by the FiberTech Lille platform at our laboratory using mastered MCVD processed preforms, combined with the stack and draw technique. The fabrication process is well detailed in the PhD thesis of Trinel [Trinel et al., 2018]. Figure 4.5 shows the obtained index profile of the preform, which is very close to the targeted design. We should mention that the "hole" in the center of the inclusion has no significant impact on the final fiber structure, nor its modal content.
The dimensions of the final fiber must be such that the distance between two inclusion centers (known as pitch) is 6 μm, to ensure the guidance of 10 modes in the C-band. The core of the preform is also doped with Er^{3+} and Al^{3+} to allow amplification in the C-band. The pitch measured by optical and scanning electron microscopy is about 6 μm. The "pixels" composing the core are regularly arranged and correspond perfectly to the geometry targeted. The pixels of the outer ring are slightly deformed, which could be corrected by using pure silica rods of different sizes to better fill the gaps at the interface between the elements constituting the core and those constituting the optical cladding of the fiber. This

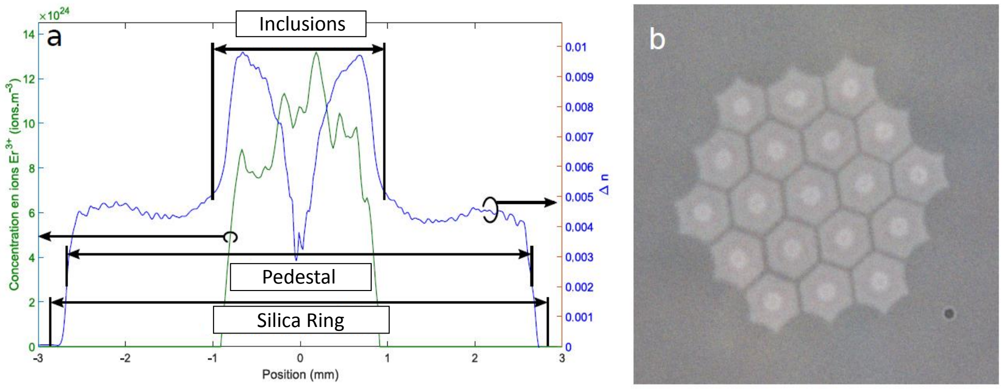

(a) (b)

FIGURE 4.5: Realization of the geometry of the 10-mode amplifying fiber: (a) index profile of the MCVD preform produced with a core, a pedestal zone with a higher index than that of the surrounding pure silica cladding, distribution of the Er^{3+} concentration. (b) Image by optical microscopy of the cleaved face of the manufactured fiber [Trinel et al., 2018].

demonstrates the feasibility of this fiber geometry with controlled manufacturing methods in our laboratory.

4.4.3 Manufactured fiber

Based on measurements of the RIP and EDP of the preform and the manufactured fiber dimensions, the index profile as well as the 2D distribution of Erbium dopant are reconstructed in order to simulate the performance of the fiber and compare it to the theoretical design. The performance of this design is tested using the amplification modeling code described in Appendix 4.8.
The performance is optimized using a pump beam shaping determined by a modified gradient method developed by Le Cocq during his thesis in our team [Le Cocq, 2014]. The optimized pump shape for the micro-structured fiber is a combination of 4 modes distributed as shown in Table 4.1. The obtained results using the optimized configuration are summarized in Table 4.2 and are also very close to those of the theoretical design, which seems logical since the two fiber geometries are very close. The modal and spectral gain, shown in Figure 4.6, show very close results when compared to that of the theoretical configuration.

TABLE 4.1: Pump beam shape composition [Trinel et al., 2018].

Modes	Fraction
LP_{31}^{odd}	0.23
LP_{12}^{even}	0.26
LP_{12}^{odd}	0.36
LP_{03}	0.15

TABLE 4.2: Simulated performances of the theoretical and manufactured 10 mode FM-EDFA under the same conditions [Trinel et al., 2018].

Parameters	Theoretical	Manufactured
L_{opt}	1.68 m	24.5 m
Gain_{mean}	19.2 dB	19.4 dB
ΔG	2.4 dB	2.5 dB
$\Delta G/\mathrm{Gain}_{mean}$	0.125 dB	0.129 dB
DMG	$0.5, 0.6, 0.9, 1.1$ dB	$0.7, 0.7, 0.9, 1$ dB

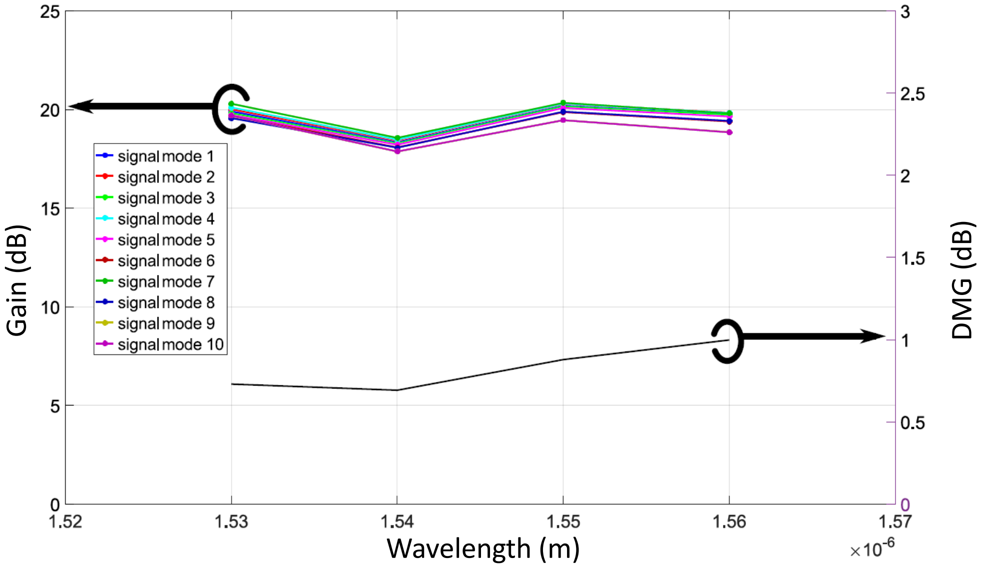

FIGURE 4.6: Spectral and modal gain and DMG simulated from the characteristics of the manufactured 10 FM-EDFA [Trinel et al., 2018].

4.4.4 Characterization

In order to characterize experimentally the amplifying performance of the produced fiber, the proper transverse profiles of the signal and pump modes have to be generated. In order to do this, the team chose to use the multi plane light conversion (MPLC) technology based MUX developed by CAILabs, a partner of the project FUI MODAL. With this technology, it is possible to convert the fundamental modes from different SMFs to a transverse profile corresponding to the modes guided by the fiber: the fundamental mode of the SMFs is reshaped after passing through several custom-made phase plates resulting in the desired transverse profiles for the signal and pump beams [Labroille et al., 2016].
Using an identical spatial multiplexer at the fiber output, the DEMUX demultiplex the signal beams for independent analysis, while providing a symmetrical system. Thus, it is possible to analyze separately the different signal modes in order to determine the level of induced X-talk between the modes and measure the output power of each signal mode so we can calculate the gain of the different modes, the DMG,... The experimental set-up, as well as the signal and

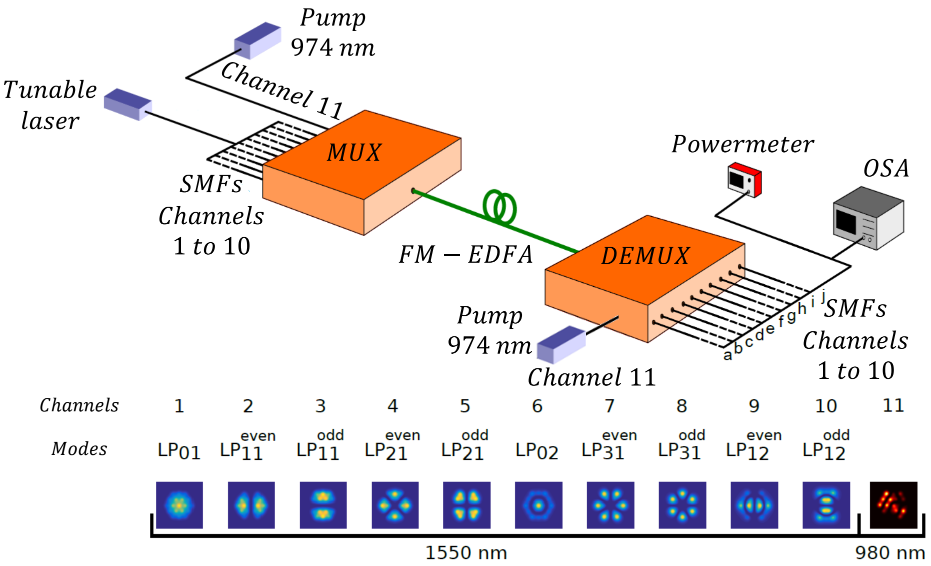

FIGURE 4.7: Experimental set-up of the 10 mode FM-EDFA and its signal and pump modes transverse distributions [Trinel et al., 2018].

pump modes transverse distributions are shown in Figure 4.7. During the first few weeks of my thesis, the various elements of the experimental set-up of the MUX/Fiber/DEMUX system were being assembled. I was able to use this system in order to characterize its performances. Gain, X-talk and system losses measurements were conducted:

Gain study The gain was characterized using a $14\ \mathrm{m}$ long fiber, with a $0.25\ \mathrm{W}$ pump in co and counter-propagating configuration. The set-up is similar to the one presented in Figure 4.7. In order to fully characterize the gain of the system, 2 studies were conducted:

- The modes are dispatched over a bandwidth of wavelengths spanning from $1548\ \mathrm{nm}$ to $1552.5\ \mathrm{nm}$, with a difference of $\Delta\lambda = 0.5\ \mathrm{nm}$, one wavelength corresponding to a given mode. The modes are injected with the same power of $-11\ \mathrm{dBm/mode}$. At the output, each channel spectrum is observed separately using an optical spectrum analyzer (OSA). The input and output spectra of the LP_{01} are shown in Figure 4.8. For each channel, the majority of the power is presented at the relative wavelength that was used to inject this mode at the input. For example, the LP_{01} was injected at $1548\ \mathrm{nm}$. If we connect the LP_{01} output channel to the OSA, the majority of the power is presented at the same wavelength, while small noise contributions are viewed at the other wavelengths as shown in Figure 4.8(b). This test thus provides a first estimation of the gain and also provides a first visualization of the X-talk of the system. If another output channel is connected to the OSA, the resulting spectrum will have nothing but noise contributions. As we can see on Figure 4.8(b), the output spectrum does not present a net gain due to the multiple losses presented in the setup.
- In order to study the flatness of the modal gain of this system in the case of WDM transmission, we chose to successively inject the same wavelength

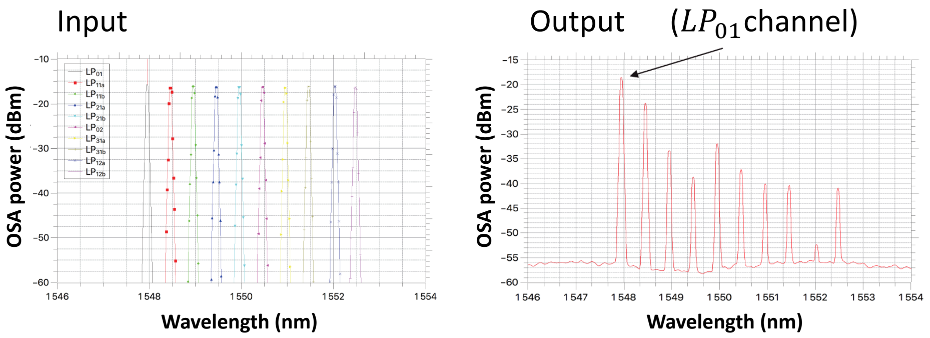

(a) (b)

FIGURE 4.8: (a) Input and (b) output spectrum of the gain characterization study of the MUX/Fiber/DEMUX system.

comb on the different channels and evaluate the gain values obtained at the receiver end. Figure 4.9 shows the results for all the modes spanning over a bandwidth from 1530 nm to 1565 nm with a difference of $\Delta\lambda = 5$ nm.

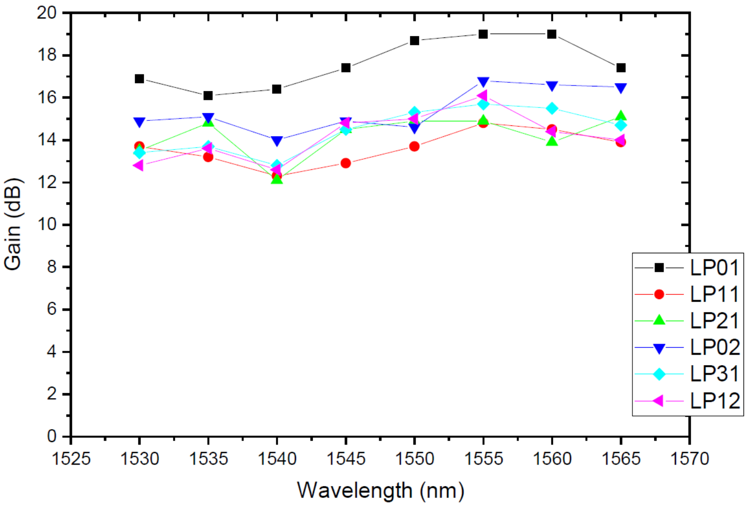

FIGURE 4.9: Experimental result of the gain measurement for the 10 mode FM-EDFA.

Once the losses are compensated, the amplifier delivers a mean value of gain of $\text{Gain}_{\text{mean}} = 14.9$ dB with a differential gain $\Delta G = 6.9$ dB. We can see that all the mode present the same behavior over this bandwidth, a relatively flat modal gain with some absorption at the smaller wavelengths.

X-talk study In order to study the coupling level between the different channels of this system, we used the set-up shown in Figure 4.10. This time, the tunable laser was replaced by an ASE source that will be filtered on a bandwidth of few nanometers centered around a chosen wavelength. This setup will allow us to avoid the beam beats related to the configuration of the multi-passage interferometer represented by the FMF. In order to study the X-talk, each mode was injected separately at the same wavelength (1610 nm) with the same input power. The choice of the wavelength was adapted in order to minimize the signal absorption by the erbium ions while being in a wavelength range acceptable for the MUX and DEMUX. The power of each output channel was evaluated using a power meter.

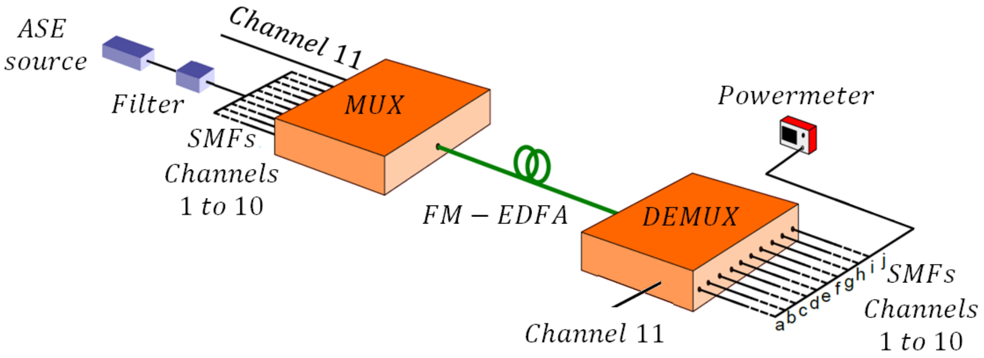

FIGURE 4.10: Experimental set-up used to characterize the X-talk of the 10 mode FM-EDFA.

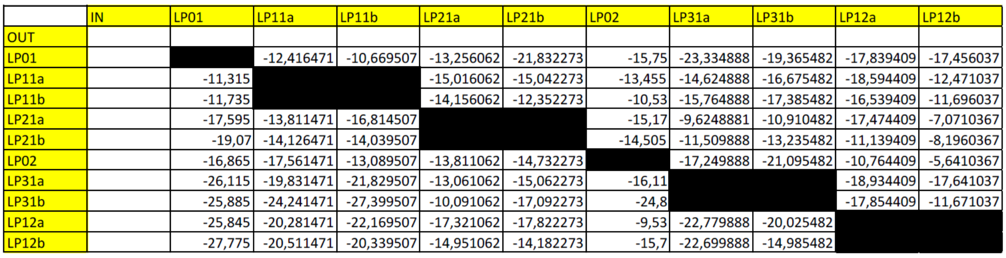

	IN	LP01	LP11a	LP11b	LP21a	LP21b	LP02	LP31a	LP31b	LP12a	LP12b
OUT											
LP01			-12,416471	-10,669507	-13,256062	-21,832273	-15,75	-23,334888	-19,365482	-17,839409	-17,456037
LP11a		-11,315			-15,016062	-15,042273	-13,455	-14,624888	-16,675482	-18,594409	-12,471037
LP11b		-11,735			-14,156062	-12,352273	-10,53	-15,764888	-17,385482	-16,539409	-11,696037
LP21a		-17,595	-13,811471	-16,814507			-15,17	-9,6248881	-10,910482	-17,474409	-7,0710367
LP21b		-19,07	-14,126471	-14,039507			-14,505	-11,509888	-13,235482	-11,139409	-8,1960367
LP02		-16,865	-17,561471	-13,089507	-13,811062	-14,732273		-17,249888	-21,095482	-10,764409	-5,6410367
LP31a		-26,115	-19,831471	-21,829507	-13,061062	-15,062273	-16,11			-18,934409	-17,641037
LP31b		-25,885	-24,241471	-27,399507	-10,091062	-17,092273	-24,8			-17,854409	-11,671037
LP12a		-25,845	-20,281471	-22,169507	-17,321062	-17,822273	-9,53	-22,779888	-20,025482		
LP12b		-27,775	-20,511471	-20,339507	-14,951062	-14,182273	-15,7	-22,699888	-14,985482		

FIGURE 4.11: X-talk matrix of the signal modes at 1610 nm for the MUX/Fiber/DEMUX system.

Figure 4.11 shows the X-talk matrix of the system. The mean value of X-talk in this matrix is −16.3 dB, with values ranging from a best of −27.8 dB to a worst of

-5.6 dB. We should mention that the maximum value for a long distance transmission, with several FM-EDFAs, should probably not exceed 18 dB per amplifier if we consider the penalties that can be supported by QPSK modulation format [Bigot, Cocq, and Quiquempois, 2015]. After a global look at the resulting X-talk matrix, the X-talk values are nearly acceptable, especially for the first five mode groups. However, the higher order modes, notably the input LP_{12b} present very high X-talk levels. This could be due to a bad mode matching between the calculated and the proper mode of the fiber.

Loss study In order to evaluate the system losses, the fiber linking the MUX/DEMUX was voluntarily cut 1 m after the MUX and the DEMUX and its output face was cleaved. The cleaved face was connected to a powermeter as shown in Figure 4.12.

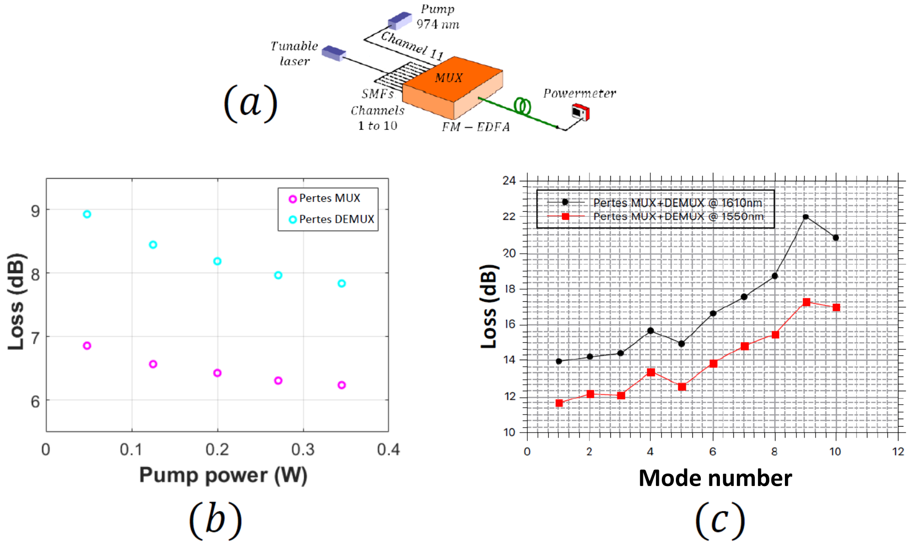

FIGURE 4.12: (a) Experimental set-up used to study the losses of the MUX and the DEMUX, (b) the measured losses for each the MUX and the DEMUX at the pump wavelength 977 nm for different power levels and (c) the measured losses for the MUX and the DEMUX at the signal wavelengths 1550 nm and 1610 nm for the different modes.

The losses of the MUX and the DEMUX at the pump wavelength 977 nm were measured and are shown in Figure 4.12. As can be seen, both devices do not present the same level of losses. At the different pump power levels, the MUX presents higher losses levels than the DEMUX, with a difference larger than 1 dB. However, for both devices, the losses level can be considered high, with a minimal value of 6.2 dB for the DEMUX for a pump power of 0.35 W. We can also see that the losses are power-dependent, with decreasing values for higher power levels: the losses of the DEMUX decrease from 8.3 dB for a pump power of 0.05 W all the way to 7.8 dB for a pump power of 0.35 W.
The losses of both MUX at the signal wavelengths 1550 nm and 1610 nm were also measured and are shown in Figure 4.12. As can be seen, the losses have high values, with a minimal value of nearly 12 dB for the fundamental mode LP_{01} at

$1550\ \mathrm{nm}$ and $14\ \mathrm{dB}$ for the same mode at $1610\ \mathrm{nm}$. The losses are wavelength-dependent, with larger losses occurring in the L-band. We can also see that the losses are mode-dependent, with values increasing from nearly $12\ \mathrm{dB}$ for the LP_{01} all the way up to $22\ \mathrm{dB}$ for the LP_{12a} mode. These losses can have multiple sources:

- the temperature: after using the system for a several hours duration, we could sense experimentally the temperature of the MUX and DEMUX rising, which can alter their performances.

- mode shaping: the technology used for our MUX and DEMUX was based on a single phase plate to simultaneously shape the modes at the signal and pump wavelengths using the MPLC methods as described in Section 4.4.4 and detailed by Labroille [Labroille et al., 2016]. It is plausible that the calculated mode profiles does not match perfectly the guided modes of the fiber, due to the difference between the simulated fiber profile and the real fiber profile: even if the X-talk values indicates that each shaped mode by the devices couple preferably with the targeted proper mode of the fiber, this can be due to symmetry considerations and a low overlap between the shaped mode and the other modes of the fiber and not necessarily the prefect match with its target.

- saturation regime: the high power of the pump beam can saturate the absorption capacity of the erbium ions, thus bleaching the fiber and giving the impression that the losses decrease at high pump powers. The saturation effect can be seen on Figure 4.12(a), where the losses levels tend to have a more stable variation for the high pump powers. However, the losses values remains relatively high even with the high pump powers (more than $5\ \mathrm{dB}$). In order to validate this theory, we simulated a step index FM-EDFA with the same properties as the FM-EDFA used in this system: the core diameter, the modal content at the signal wavelength, the absorption level and the doping concentration. The $\mathrm{LP}_0 1$ mode was used as a pump beam at $980\ \mathrm{nm}$ while no signal was injected in this fiber. Figure 4.13 shows the different absorption losses for the different pump powers of our simulated step-index FM-EDFA. We can see the same behavior of the absorption as in Figure 4.12(b), with some differences in the values of the losses, because Figure 4.13 illustrates only the pump absorption losses without considering extra losses.

The obtained results show a bit of difference regarding the calculated values for the real fiber profile. As a result of the different tests above described on this system, one can easily see the high levels of losses presented in this system. However, we should mention that this system can be considered as the first to apply the MPLC technology using a single phase plate to reshape both beams at the signal and the pump wavelengths, which had severe consequences on the losses of this system, especially at the signal wavelength. This system is still under study in order to maximize its potential and deliver the awaited level of gain. Although this design shows a huge advantage in feasibility and manufacturing compared to the other micro-structured fiber designs, the micro-structuring itself remains challenging if one was to compare it with the conventional ways. In this logic, we

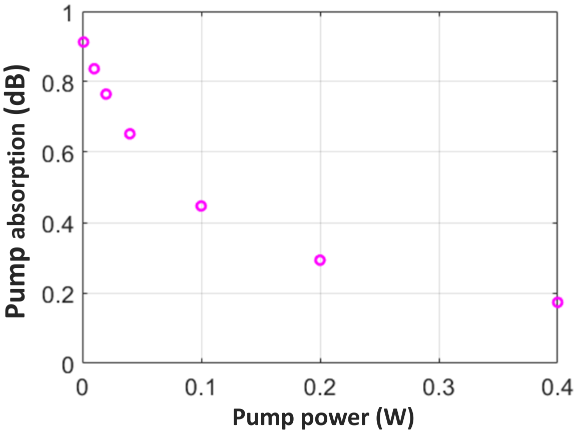

FIGURE 4.13: The absorption losses of a step-index FM-EDFA having the same characteristics as the micro-structured FM-EDFA used in the experimental setup presented in Figure 4.12(a).

chose to study other designs capable of delivering an equalized gain for a FMF based MDM transmission.

4.5 Ring core FM-EDFA

4.5.1 Design

Given the fact that the amplification process is largely governed by the overlap γ between the transverse distribution of light intensity at the pump wavelength, the transverse distribution of the light intensity of the different signal modes and the EDP, having a design where this overlap is well mastered for all the modes will improve gain equalization and very low DMG and ΔG values. As described in the state of the art section 4.3, ring core FM-EDFA designs present a very good candidate for this kind of job. That's why, during this thesis, we were interested in developing a new ring core FM-EDFA design capable of generating high levels of gain while providing a low level of DMG for a significant number of modes. In order to highlight the motivation that drove us to consider this type of fibers, Figure 4.14 shows a basic simple comparison between theoretical step index FM-EDFA design and ring core one. The RIP, EDP and guided signal mode groups are all normalized to their maxima respectively in order to better illustrate their positioning inside a one dimensional cut of the fiber. In the case of the ring core fiber, it is hard to differentiate the trace of the mode groups due to their high confinement in a same region. The overlap values between the guided mode groups at the signal wavelength and the EDP are presented as well and calculated using the following equation:

$$\Gamma_{k,i} = \iint E_{k,i}(x,y)\frac{N_{\mathrm{t}}(x,y)}{N_{\max}(x,y)}dxdy \tag{4.1}$$

where $N_{\mathrm{t}}(x, y)$ is the $2D$ EDP, and $E_{k,i}$ is the $2D$ complex electric field of the mode i at the wavelength k.

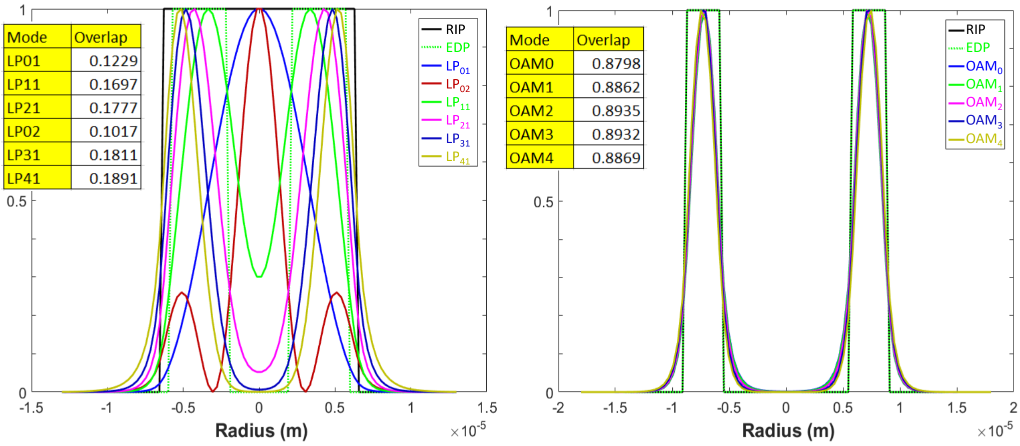

Mode	Overlap
LP01	0.1229
LP11	0.1697
LP21	0.1777
LP02	0.1017
LP31	0.1811
LP41	0.1891

Mode	Overlap
OAM0	0.8798
OAM1	0.8862
OAM2	0.8935
OAM3	0.8932
OAM4	0.8869

(a) (b)

FIGURE 4.14: RIP, EDP and the signal mode groups one dimensional traces for a 10 modes: (a) step index FM-EDFA, (b) ring core FM-EDFA. The tables report the overlap between the EDP and the signal mode groups for both fiber geometries.

As can be seen, the ring core design enhances this overlap, with similar high values for all the mode groups, between 87.9% and 89.3%, comparing to the low values presented by the step index fiber ranging between 10.1% and 18.9%. Practically, all the mode groups "see" the same number of excited Erbium ions while propagating through the doped ring core fiber, resulting in a low DMG and ΔG equalized gain. In addition, as shown is the previous chapter, OAM modes provides lower X-talk levels, thus the use of these fiber designs, which are naturally ideal to guide the OAM modes, can enable a more efficient MDM transmission.

4.5.2 Theoretical performance

We start investigating a general ring core FM-EDFA. The design must aim to reduce the coupling between the guided modes by maximizing the effective index difference, Δn_{eff}, between them. This can be done by attributing specific values to the inner radius of the ring r_{i}, the outer one r_{o} and the refractive index difference between the ring core and the cladding, Δn. This study was conducted by Tandje, a fellow PhD student of our team working on special ring core fiber designs for telecommunication transmissions [Tandjè, 2019]. The aim of this design was to optimize the passive properties of the fiber and its modal content characteristics. We will later adopt this design as the basis of the optimization of an active fiber.
We proposed a fiber guiding up to the $|L| = 6$ group of OAM modes (26 modes), having a $\Delta n = 22.5 \times 10^{-3}$, which is well mastered in our manufacturing abilities. Thus, we conducted a study in order to get the optimized values of r_{i} and r_{o}. Figure 4.15 shows a map that can be used to choose the best pair $(r_{\mathrm{i}}, r_{\mathrm{o}})$. The green area covers the radius combinations where the fiber guides up to $|L| = 5$, thus these pairs will not be evaluated. The blue area covers the radius combinations

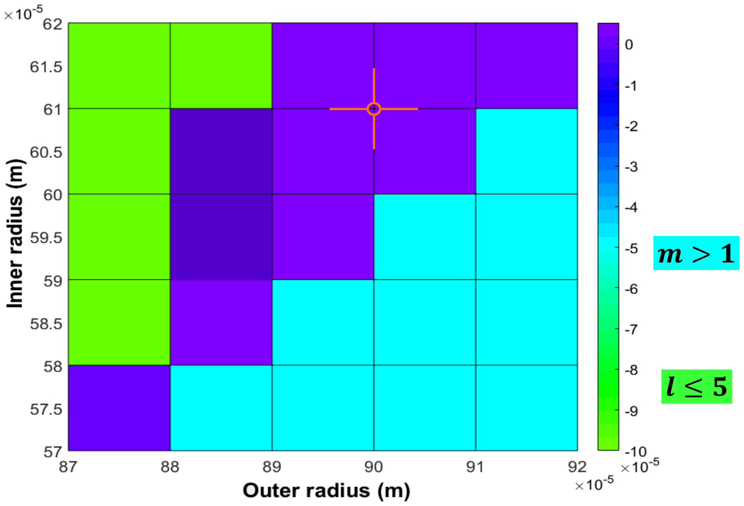

FIGURE 4.15: Determination of the best inner and outer radius combination in order to have maximum effective index difference between the guided modes and the suited modal content.

where the second order OAM modes are guided, which must be avoided too. The purple area covers the radius combinations that respect all the targeted conditions. We should mention that within the purple area, the $(r_\mathrm{i}, r_\mathrm{o})$ pairs present different characteristics: although the design guides up to the $|L| = 6$ group, the last group of modes can be close to its cut-off frequency and the mode may be lost as is the case for the dark purple areas. Another criteria that can drive us to the quest of the best $(r_\mathrm{i}, r_\mathrm{o})$ pair is the value of the effective index difference between the modes, Δn_eff: a high value of Δn_eff indicates lower coupling levels between the modes. The orange marker points out the chosen values for our design, having a $r_\mathrm{i} = 6.1\ \mu\mathrm{m}$ and a $r_\mathrm{o} = 9\ \mu\mathrm{m}$. All the modes of this design are far from their cut-off frequency and present the highest difference between their effective indices n_eff available, presented in Table 4.3. The RIP, EDP and the intensity distribution of the guided modes of this structure are calculated and are represented in Figure 4.16. These intensity distribution are calculated using a vector mode solver developed by our team.

At the pump wavelength, this fiber guides up to $|L| = 11$ OAM mode groups. The $|L| = 0$ OAM groups has two OAM modes, while each OAM group for $|L| \geq 1$ have four OAM modes, as described in Table 1.3. In order to completely describe how each pump mode impacts the DMG among the guided modes at the signal wavelength, we tested all the pump modes individually. In each simulation run, only one pump mode was launched into the fiber. The pump power was set to 0.3 W and the input signal power was set to $12\ \mu\mathrm{W/mode/wavelength}$ for four wavelengths spreading over the C-band. The fiber length is chosen as the optimized value for each pump configuration, given the most flat gain possible over the studied bandwidth, evaluated by the $\Delta G/\mathrm{Gain}_\mathrm{mean}$ ratio: a low ratio values represent a flatter gain spectrum. The erbium concentration is fixed to $2.5 \times 10^{25}\ \mathrm{ions/m^3}$.

Due to the circular symmetry of the ring core fiber, the simulated ΔG, using the different pump modes of each OAM mode group are nearly identical as shown in Figure 4.17. The observed variation of the ΔG for different pump modes is

TABLE 4.3: The vector modes of the ring core fiber and their calculated effective indices.

Mode	n_{eff}
$\text{HE}_{1,1}^{(e)}, \text{HE}_{1,1}^{(o)}$	1.458249
$\text{TE}_{0,1}$	1.457924
$\text{HE}_{2,1}^{(e)}, \text{HE}_{2,1}^{(o)}$	1.457855
$\text{TM}_{0,1}$	1.457773
$\text{HE}_{3,1}^{(e)}, \text{HE}_{3,1}^{(o)}$	1.456688
$\text{EH}_{1,1}^{(e)}, \text{EH}_{1,1}^{(o)}$	1.456677
$\text{HE}_{4,1}^{(e)}, \text{HE}_{3,1}^{(o)}$	1.454779
$\text{EH}_{2,1}^{(e)}, \text{EH}_{1,1}^{(o)}$	1.454773
$\text{HE}_{5,1}^{(e)}, \text{HE}_{3,1}^{(o)}$	1.452171
$\text{EH}_{3,1}^{(e)}, \text{EH}_{1,1}^{(o)}$	1.452167
$\text{HE}_{6,1}^{(e)}, \text{HE}_{3,1}^{(o)}$	1.448919
$\text{EH}_{4,1}^{(e)}, \text{EH}_{1,1}^{(o)}$	1.448897
$\text{HE}_{7,1}^{(e)}, \text{HE}_{3,1}^{(o)}$	1.445074
$\text{EH}_{5,1}^{(e)}, \text{EH}_{1,1}^{(o)}$	1.445026

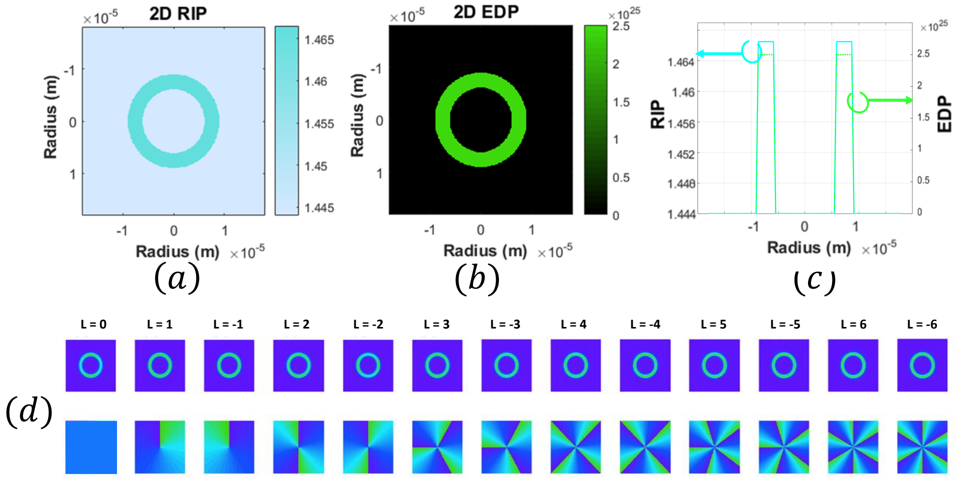

FIGURE 4.16: Two-dimensional representations of the (a) RIP and the (b) EDP, (c)one dimensional cut of the RIP and the EDP, and (d) the intensity and phase distributions of the guided modes at 1550nm of the ring core FM-EDFA theoretical design.

expected, even though very minimal, as the pump mode intensity varies according to the mode order. The physical origin of the ΔG results from differences in the overlap of the pump modes, signal modes and the EDP. Another parameter that can be used to optimized the pump mode is the ratio of the ΔG and the mean value of the gain. Figure 4.17 summarizes the different values of the ΔG, the mean gain values, their ratio and the power conversion efficiency (PCE) of this design. The resulting ΔG values are close, spanning between 3.45 dB and

TABLE 4.4: Parameters of the 6 mode ring core FM-EDFA design numerical study.

Parameters	Values
$\text{Power}_{\text{Pump}}$	0.3 W
$\text{Power}_{\text{Signal}}$	12 μW/mode/wavelength
Er^{3+}	2.5×10^{25} ions/m^3

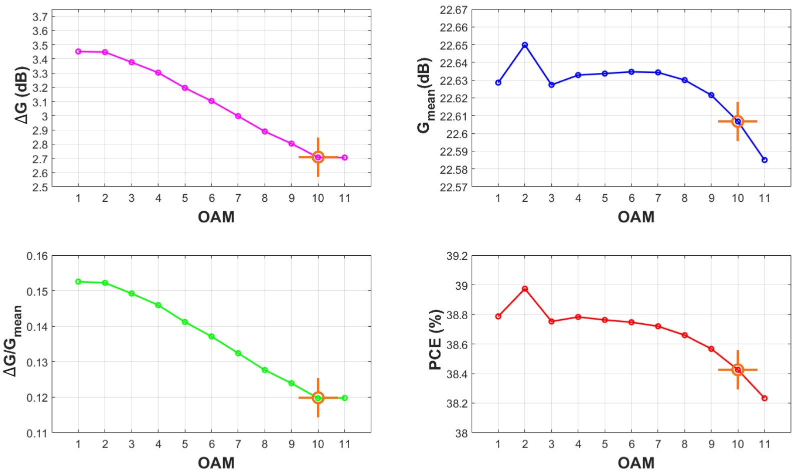

FIGURE 4.17: Evaluation of the performance of the 6 mode ring core FM-EDFA while modifying the pump beam mode between the 11 guided OAM modes at the pump wavelength.

2.71 dB, given by the $|L| = 11$ mode group. Meanwhile, the mean gain values are also very close, ranging between a maximal value of 22.65 dB given by the $|L| = 2$ mode group and a minimal value of 22.58 dB. However, the best compromise is provided by minimal value of the $\Delta\text{G}/\text{Gain}_{\text{mean}}$ ratio, obtained for the $|L| = 10$ mode group, which we chose to go forward in our study as the pump mode. The best PCE level is 38.97% obtained using the $|L| = 2$ mode group.

TABLE 4.5: Simulated results of the 6 mode ring core FM-EDFA design.

Parameters	Values
L_{opt}	1.92 m
$\text{Gain}_{\text{mean}}$	22.61 dB
ΔG	2.71 dB
$\Delta\text{G}/\text{Gain}_{\text{mean}}$	0.12 dB
DMG	0.64, 0.56, 0.70, 0.73 dB
PCE	38.42%

The performance of this design is tested using the amplification modeling code described in Appendix 4.8. The parameters of this study are summarized in Table 4.4. Figure 4.18 presents the spectral and modal gain spectrum, in addition to the DMG provided by the ring core FM-EDFA theoretical design for four wavelength

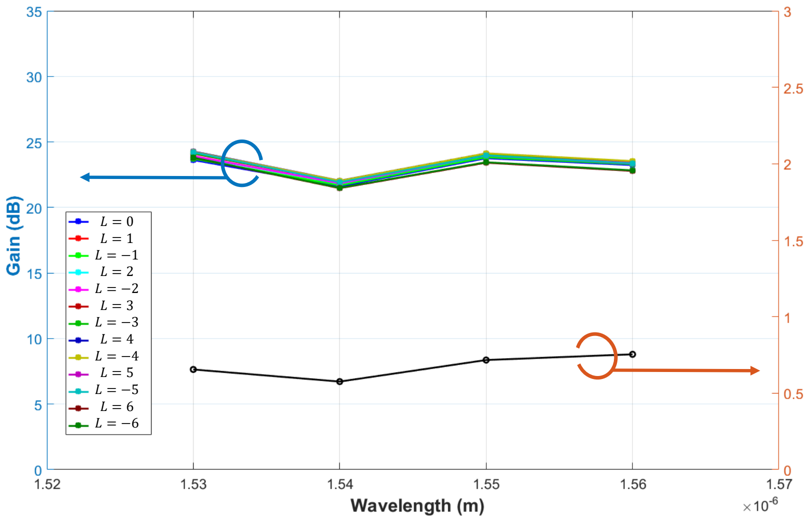

FIGURE 4.18: Spectral and modal gain and DMG provided by the 6 mode ring core FM-EDFA theoretical design in the optimized configuration.

spanned over the C-band, presented on the x-axis of the spectrum. Using the parameters of Table 4.4 as initial parameters, the optimal fiber length was $L_{opt} = 1.92$ m, delivering a gain of 22.61 dB with a total ΔG of 2.71 dB and a PCE of 38.42%. The $\Delta G/Gain_{mean}$ ratio has a value of 0.12. These values are very close to the best value for each parameter presented in Figure 4.17.

4.5.3 Manufactured fiber

During my PhD thesis, I had the chance to work with Arsene Tandje, a fellow PhD student whose thesis is based on the conception of specialty optical fibers optimized to better guide OAM modes [Tandjè, 2019]. Tandje deduced, thanks to multiple simulations on several fiber types, that, in order to lift the degeneracy of the OAM mode groups of an optical fiber, while trying to avoid the spin-orbit coupling, it is preferable to have a fiber with a refractive index difference between the core and the cladding around 20×10^{-3}. This lifting of degeneracy is necessary in order to fully exploit the maximal capacity of the spatial dimension of the fiber, dividing each OAM mode group into four separate channels (two spatial and two polarization degeneracy levels). Manufacturing an EDFA with such a Δn was quite challenging for us using the conventional methods, so our team developed a manufacturing method of MCVD preforms using a non-conventional approach: in addition to the usual aluminum ions doping, this method is based on the introduction of zirconium ions to the glass-lattice, in order to obtain a higher Δn. This method was first tested to manufacture a step index EDF with a high Δn. Figure 4.19(a) illustrates the RIP of the step index zirconium doped EDF, showing a step index like profile with a $\Delta n = 20 \times 10^{-3}$. Based on the good results of this fiber, our team proposed to use the same MCVD-based method in order to produce a ring core EDF. Figure 4.19(b) illustrates the RIP of the all solid ring core zirconium doped EDF. The obtained fiber shows a ring core with a $r_o = 5.7$ μm and a $r_i = 4.3$ μm, with a $\Delta n = 20 \times 10^{-3}$. Although the ring dimensions of the manufactured fiber do not match exactly the optimized ring dimensions presented in the previous section, the high Δn of this fiber shows a promising result. We should mention that the fiber presented in Figure 4.19(b) is a first test of using this non-conventional manufacturing method for a ring core design. At the time this manuscript is being written, another ring core preform is being manufactured, aiming to better match the theoretical dimensions of this design.

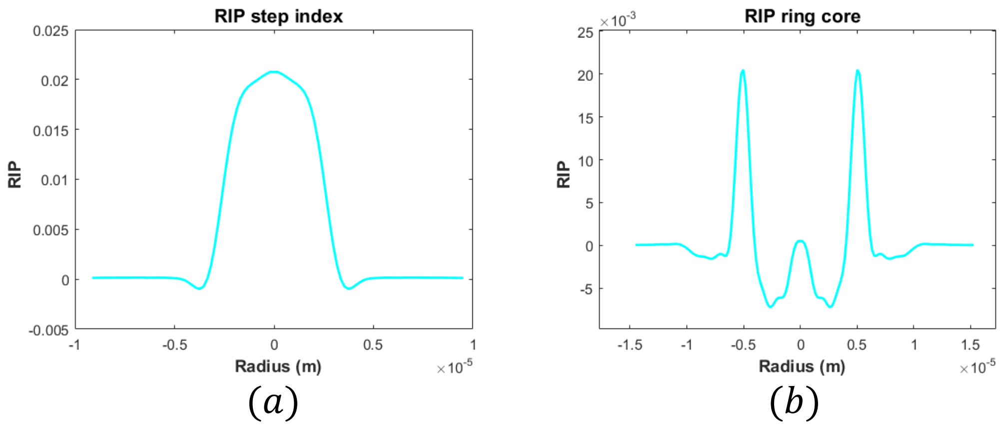

FIGURE 4.19: RIP of the realization of the geometry of the zirconium doped: (a) step index EDFA, (b) ring core EDFA.

4.6 Ring doped step index FM-EDFA

4.6.1 Design

As we have seen in Section 3.2, OAM modes can be efficiently guided using a step index FMF, presenting low coupling levels between these modes. Following this result, we were interested in investigating a step index FM-EDFA for OAM modes. As described in the previous section 4.2 of this chapter, the gain equalization of a FM-EDFA can be done either by shaping the pump beam, or by using a customized EDP. In an ideal long distance transmission, we can imagine having a succession of passive fibers spliced to the active fibers. Thus, the use of passive and active fibers having maximum matching quality between their mode groups enables us to establish a long distance line without the use of a MUX/DEMUX at each amplification stage, which can reduce drastically the losses caused by these devices. As seen in Section 4.4.4, a pair of MUX can add more than 14 dB of losses for each amplification stage, even if this result corresponds to a non-optimized case, more than 1 dB of loss is theoretically predicted in a best case scenario. In addition, the losses induced by these devices were also mode-dependent, with losses increasing with the order of the modes, adding another challenge to an equal amplification. From this prospect, we started with a RIP close to the FMF L113 studied in the experimental works in Section 3.2 in order to find the conditions that offer the highest overlap. Thus, the theoretical RIP of this fiber is a simple step index, having a $\Delta n = 17 \times 10^{-3}$ with a core radius of $r_c = 8\ \mu\mathrm{m}$. This fiber has the same experimentally detected modal content that the FMF L113 presented in Section 3.2, guiding up to $|L| = 4$ OAM mode groups for a short fiber length. The modes have a ring distribution inside the core of the fiber, with various radius depending on the topological charge $|L|$ of the mode. This passive fiber design was used as a basis to optimize an active version of this fiber. Due to the circular symmetry of the modes, we aimed to find a ring shaped EDP for this fiber, capable of equalizing the gain of a certain number of modes in one application, and capable, for another application, of compensating the different levels of accumulated losses for the different modes before the amplification phase.

4.6.2 Gain equalization

Theoretical performance

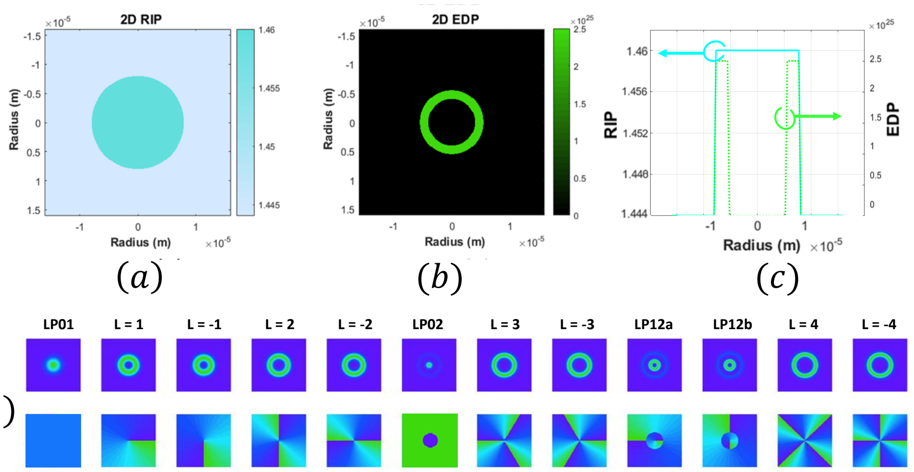

FIGURE 4.20: Two-dimensional representations of the (a) RIP and the (b) EDP, (c) one dimensional cut of the RIP and EDP,and (d) the intensity and phase distributions of the guided modes at $1550\mathrm{nm}$ of the step index ring doped FM-EDFA theoretical design.

Figure 4.20 shows the theoretical step index RIP, the ring shaped EDP of the fiber and intensity distributions of the guided modes at the signal wavelength $1550\ \mathrm{nm}$. These intensity distribution are calculated using a vector mode solver developed by our team. The overlap between the guided modes of the FMF L113 and the theoretical RIP is presented in Figure 4.21. These values were obtained using:

$$\Gamma_{k,i} = \iint E_i^{\mathrm{L113}}(x,y) E_j^{\mathrm{Step}}(x,y)dxdy \tag{4.2}$$

where E_i^{L113} is the $2D$ complex electric field of the guided mode i of the FMF L113 and E_j^{Step} is the $2D$ complex electric field of the guided mode j of the theoretical RIP presented in Figure 4.20. As we can see, the overlap values of the same modes of the 2 designs match pretty well with overlap values ranging from 69% for the $|L| = 4$ OAM mode group to 83% for the $|L| = 1$ mode group. However, in a long distance transmission, FMF L113 is supposed to guide up to $|L| = 3$ OAM mode groups at 1550 nm [Bigot-Astruc et al., 2019]. For that, we chose to limit the amplification study to the $|L| = 3$ OAM mode group.

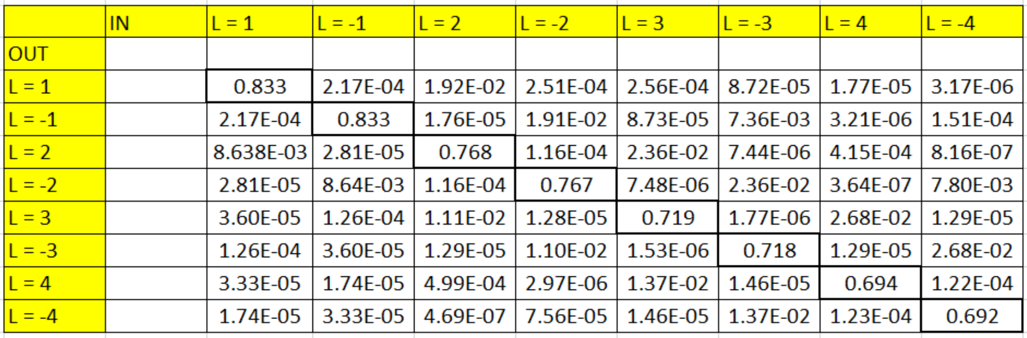

	IN	L = 1	L = -1	L = 2	L = -2	L = 3	L = -3	L = 4	L = -4
OUT									
L = 1		0.833	2.17E-04	1.92E-02	2.51E-04	2.56E-04	8.72E-05	1.77E-05	3.17E-06
L = -1		2.17E-04	0.833	1.76E-05	1.91E-02	8.73E-05	7.36E-03	3.21E-06	1.51E-04
L = 2		8.638E-03	2.81E-05	0.768	1.16E-04	2.36E-02	7.44E-06	4.15E-04	8.16E-07
L = -2		2.81E-05	8.64E-03	1.16E-04	0.767	7.48E-06	2.36E-02	3.64E-07	7.80E-03
L = 3		3.60E-05	1.26E-04	1.11E-02	1.28E-05	0.719	1.77E-06	2.68E-02	1.29E-05
L = -3		1.26E-04	3.60E-05	1.29E-05	1.10E-02	1.53E-06	0.718	1.29E-05	2.68E-02
L = 4		3.33E-05	1.74E-05	4.99E-04	2.97E-06	1.37E-02	1.46E-05	0.694	1.22E-04
L = -4		1.74E-05	3.33E-05	4.69E-07	7.56E-05	1.46E-05	1.37E-02	1.23E-04	0.692

FIGURE 4.21: Overlap table between the calculated OAM modes of the FMF L113 (IN) and the theoretical step index fiber (OUT).

The choice of the inner and outer radius of the doped ring, r_i and r_o respectively, are the subject of a study in order to find their optimized values enabling an equalized modal gain. The erbium concentration is fixed to 2.5×10^{25} ions/m^3. The pump configuration is chosen as a ring shaped beam having the dimension of the doped ring of the fiber as a start, with a power of 0.3 W and a flat phase, which can be easily done experimentally using a gaussian beam and an axicon. The choice of the pump beam shape will be investigated in the following section. The overlap fractions between the pump beam and the guided modes at the pump wavelength 980 nm are given in the tables shown in Figure 4.22, while the total overlap value is more than 85.5%. As can be seen, the flat phase leads to a high overlap with the centered mode groups LP$_{01}$, LP$_{02}$ and LP$_{03}$.

Figure 4.23 presents an illustration of the impact of the inner and outer radius values on the mean gain value of each OAM mode group and the standard deviation for these 3 mode groups. We conducted an extensive study, changing r_i from 2.5 μm to 7.5 μm and r_o from 3 μm to 8 μm, with a step of 0.5 μm. It is clear that when r_i and r_o match the inner and the outer radius of the intensity distribution of the amplified mode, the gain value of this mode is at its maximum, due to high overlap between the amplified mode and the spatial distribution of the excited Er^{3+} ions: for each mode map, the green area corresponds to a gain larger than 25 dB centered around the inner and outer radius of the mode itself.

The gain standard deviation of the OAM modes is then evaluated in order to find the values of r_i and r_o for which the differential gain between the modes is at its lowest, in addition to a flat gain spectrum with the highest mean gain value possible. As shown in Figure 4.23, a doped ring with $r_\mathrm{i} = 3.5$ μm and $r_0 = 8$ μm, marked by the orange marker, presents the lowest standard deviation value for the 3 OAM mode groups. For the purpose of having a well resolved study, we chose to re-evaluate the gain study around this position : r_i vary between 3 μm and 4 μm and r_o vary between 7 μm and 8 μm taking into account a smaller step of

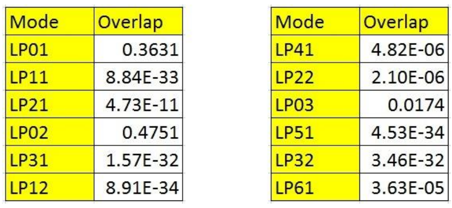

Mode	Overlap
LP01	0.3631
LP11	8.84E-33
LP21	4.73E-11
LP02	0.4751
LP31	1.57E-32
LP12	8.91E-34

Mode	Overlap
LP41	4.82E-06
LP22	2.10E-06
LP03	0.0174
LP51	4.53E-34
LP32	3.46E-32
LP61	3.63E-05

FIGURE 4.22: Overlap fractions tables between the pump beam and the guided modes at the pump wavelength 980 nm.

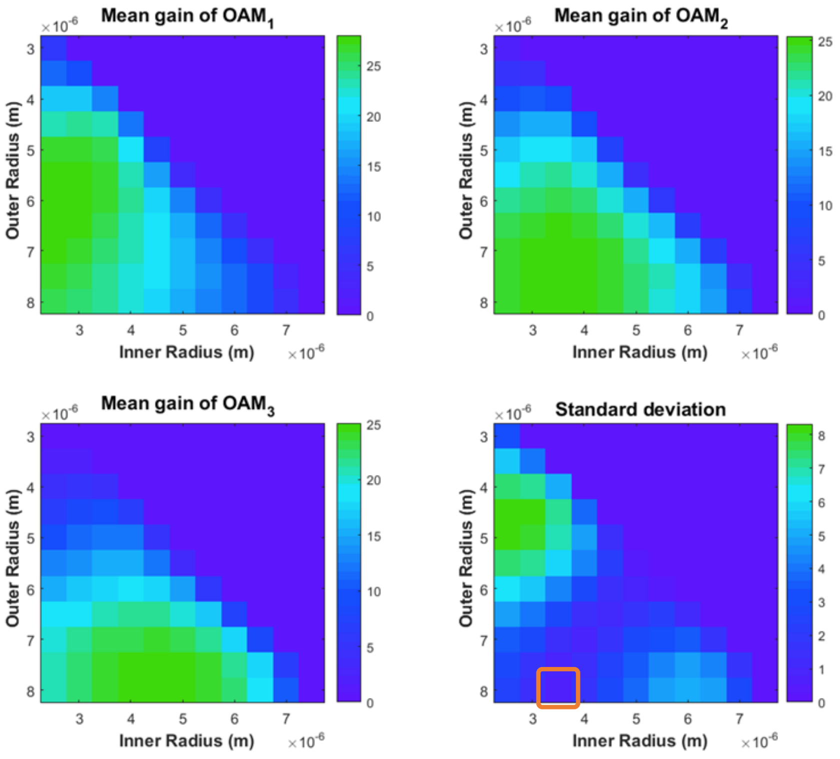

FIGURE 4.23: Impact of the inner and outer radius values on the mean gain values of each OAM mode group and the standard deviation of these gain values in the case of the step index ring doped FM-EDFA.

0.2 μm. This parameter can be reduced at wish when simulating the results, but we chose a reasonable resolution regarding the manufacturing constraints. Figure 4.24 shows the high re-evaluated mean gain values and the standard deviation for the 3 OAM mode groups. As a result, we obtained the optimized values of

$r_{\mathrm{i}} = 3.6\ \mu\mathrm{m}$ and $r_0 = 8\ \mu\mathrm{m}$

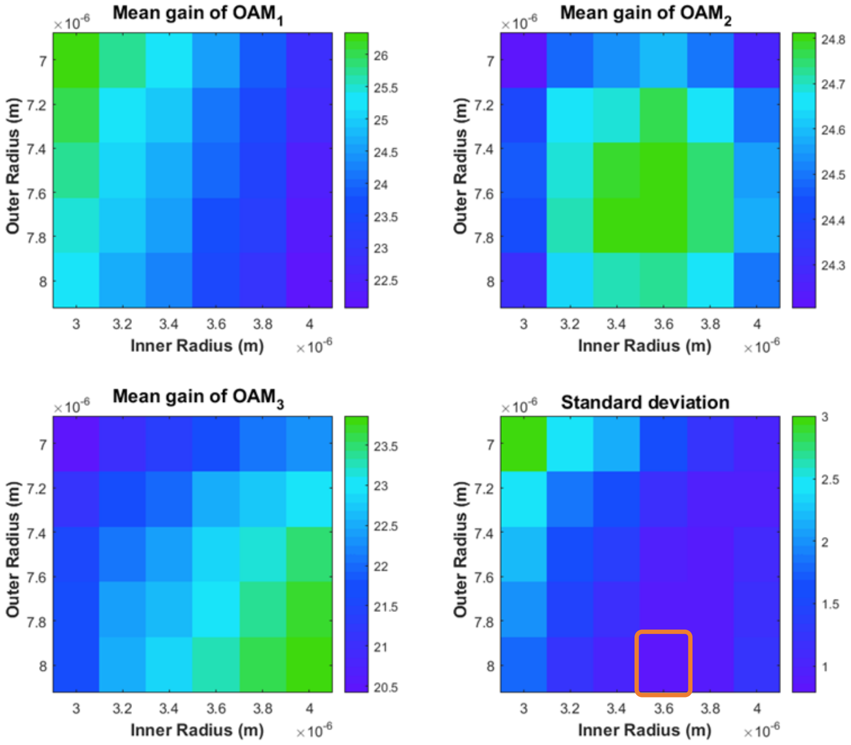

FIGURE 4.24: Re-evaluated mean gain values of each OAM mode group and their standard deviation delivered by the step index ring doped FM-EDFA.

Figure 4.25 shows the spectral and modal gain, as well as the differential modal gain for this fiber design. As we can see that the 3 mode groups have a quite flat gain spectrum all above 21 dB and a total differential gain of about 3.53 dB. The chosen design delivers a good compromise between the maximum delivered gain and the differential gain value: the maximal value of gain for each mode can be around 25 dB as described in Figure 4.23 and the mean gain of 23.11 dB delivered by this design is close to the optimized values. Thus the chosen configuration seems logical since it presents the lowest gain differential and a high mean gain at the same time.

In addition to the optimized values of r_{i} and r_{o} delivering similar amplification performances to the 3 OAM mode groups, we investigated deeper in the choice of the EDP radius in order to better understand its impact on the amplification process. More precisely, for each r_{i} and r_{o} pair, we have determined the number of modes having an equalized gain. Thus, two parameters were fixed in order to conduct this study:

- The modes must have a flat gain higher than 20 dB in order to be considered as amplified modes,
- The differential modal gain must be lower than 3 dB between the modes so their amplification can be considered equalized.

Figure 4.26 illustrates a map describing which set of mode group combinations respect our fixed conditions at a given r_{i} and r_{o} pair. Each color of the color scale

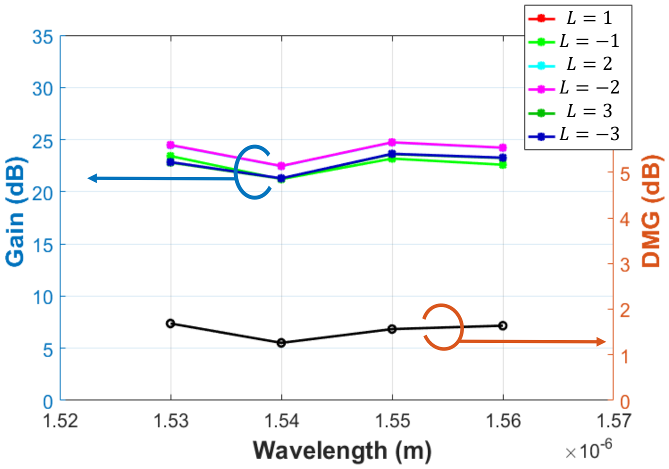

FIGURE 4.25: Spectral and modal gain and differential modal gain (DMG) provided by the ring doped step index 6 mode FM-EDFA manufactured design for gain equalization in the optimized configuration.

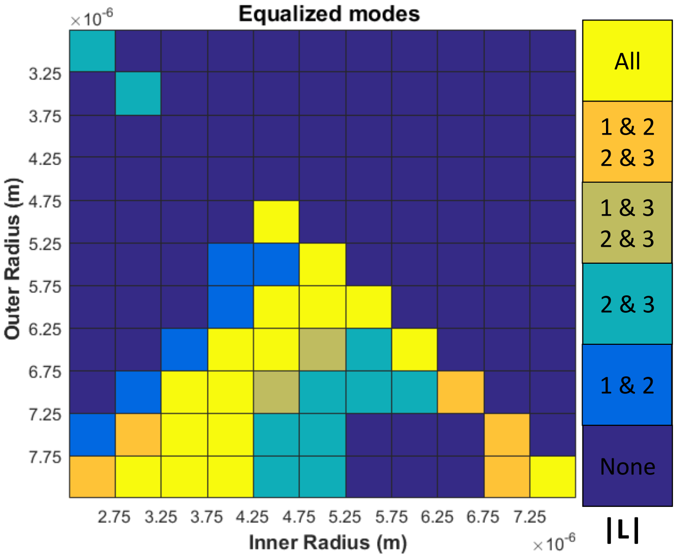

FIGURE 4.26: Equalized mode group combinations for the different radius pairs of the step index ring doped FM-EDFA.

on the right refers to a proper combination of modes: the blue square indicates a gain equalization for the OAM $|L| = 1$ and $|L| = 2$ groups, the orange one indicates a gain equalization for the $|L| = 1$ and $|L| = 2$ groups on one hand and the OAM $|L| = 2$ and $|L| = 3$ groups on the other hand. However, for the orange squares, the DMG between the $|L| = 1$ and $|L| = 3$ mode groups is higher than 3 dB. The yellow color indicates an equalization for the 3 mode groups. Thanks to this study, we can determine specific r_i and r_o values in order to equalize the gain of a given combination of mode groups, (i.e. not necessarily using all the guided modes) depending on the application's aims. Wen should mention that certain applications are more straightforward than others: as can be seen in Figure 4.26, the yellow color covers several neighboring r_i and r_o combinations for an EDFA able to equalize all 3 mode groups, which gives a range of options and a small margin for possible errors due to manufacturing reasons. However, the dark yellow color in Figure 4.26, presenting an EDFA able to equalize the OAM $|L| = 1$ and $|L| = 3$ on one hand and the OAM $|L| = 2$ and $|L| = 3$ on the other hand, covers just two precise combinations, which means that a small mismatch between the theoretical and the manufactured design can change the amplification behavior of the EDFA.

Pump beam study

We were also interested in better experimental approach for this fiber design, so we investigated more realistic pump beam shapes than the ideal ring shape used previously and matching perfectly the EDP. For that, we investigated the different guided modes at the pump wavelength $980\ \mathrm{nm}$, similarly to Section 4.5.3. The guided modes at the pump wavelength can be obtain using a SLM or series of propagation through phase plates, but this approach will have some additional losses, as we have shown in Section 4.4.4. We should mention that the second order OAM modes will not feature this study.

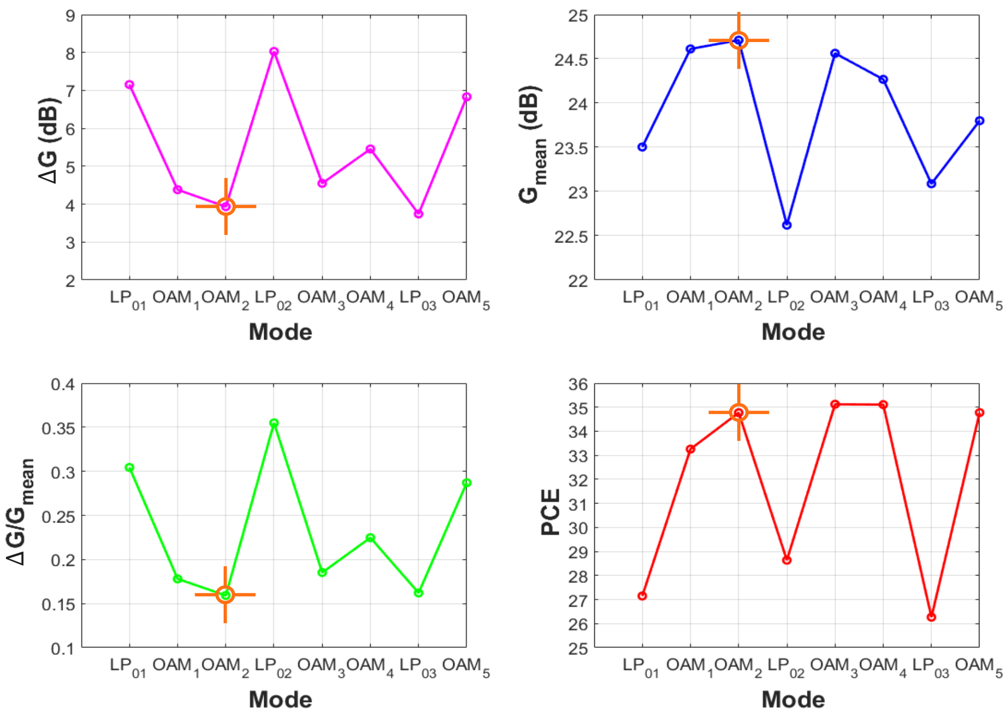

FIGURE 4.27: Evaluation of the performances of the step index ring doped FM-EDFA as a function of the pump beam mode order between the five guided OAM mode groups as well as the three centered LP modes at the pump wavelength.

As can be seen in Figure 4.27, the OAM $|L| = 2$ mode group represent the best choice for the pump beam from the guided modes at the pump wavelength: it offers the highest mean gain value of 24.71 dB and the second lowest ΔG value of 3.9 dB, thus having the best ΔG/mean gain ratio. In addition this mode offers a high PCE value of 34.7%. We also tested other pump schemes presenting lower experimental difficulty levels and less losses than generating the proper guided modes at the pump wavelength, notably a more realistic ring shaped beam and a gaussian beam. The ring shaped beam is obtain by a propagation of a gaussian beam with a diameter of 880 μm through an axicon with an angle of 5 degrees, resulting in a free space ring shaped beam with $r_{\mathrm{i}} = 360$ μm and $r_{\mathrm{o}} = 800$ μm which can be later re-scaled to the desired size using a telescope. The gaussian beam that will be considered is the fundamental mode of the HI1060 single-mode fiber ,with a mode-field diameter of 5.9 μm. We simulated a number of re-scaled ring shaped and gaussian beams, all aligned with the center of the core of the fiber, but we will be showing one of the results for each pump scheme for the sake of simplicity. The ring shaped and the gaussian pump beams are illustrated in Figure 4.28, as well as the overlap between them and the centered modes of the fiber at the pump wavelength.

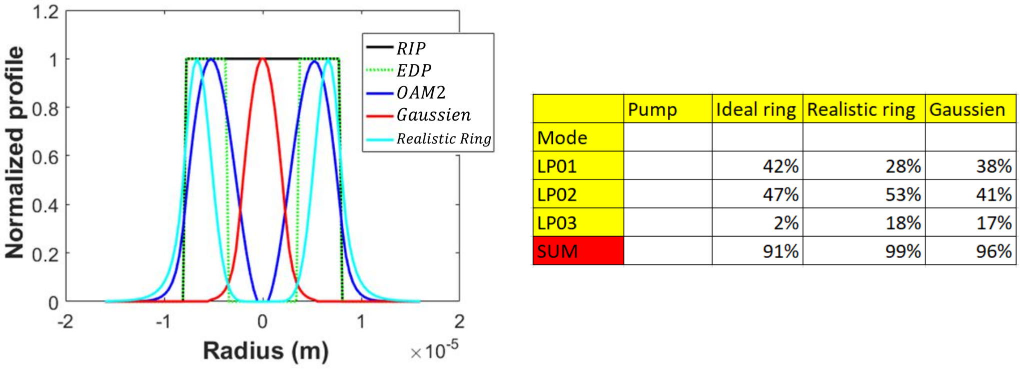

	Pump	Ideal ring	Realistic ring	Gaussien
Mode				
LP01		42%	28%	38%
LP02		47%	53%	41%
LP03		2%	18%	17%
SUM		91%	99%	96%

(a) (b)

FIGURE 4.28: (a) RIP, EDP, guided OAM $|L| = 2$ at the pump wavelength, gaussian and realistic ring pump beam traces and (b) Overlap between the pump beam and the guided modes at the pump wavelength 980 nm.

Table 4.6 show a comparison between the results of the 4 pump schemes.

TABLE 4.6: Simulated results of the gain equalization step index ring doped FM-EDFA design with different pump schemes.

Parameters	Idealring	OAM$\|L\| = 2$	Realisticring	Gaussian
$\mathrm{Gain}_{\mathrm{mean}}$	23.11 dB	24.71 dB	23.71 dB	23.52 dB
ΔG	3.53 dB	3.9 dB	3.91 dB	3.56 dB
PCE	24%	34.7%	28.4%	26.7%

As can be seen, the use of a realistic ring delivers nearly the same mean gain value, just 1 dB smaller than the OAM $|L| = 2$ pump beam, together with a similar ΔG of 3.9 dB. However, the PCE decrease of 6%. Using a centered gaussian beam as a pump mode, this design delivers a mean gain value of 23.52 dB with a of ΔG of 3.56 dB and a 8% lower PCE. The use of the guided OAM $|L| = 2$ mode group at the pump wavelength offers the best performance, delivering the best mean gain, ΔG values and the highest PCE. Therefore, if the OAM $|L| = 2$ can be properly generated and efficiently coupled into the fiber, this design will deliver its best gain equalizing performance. The use of easier and more accessible pump schemes experimentally offers nearly the same gain performances and mainly impact the power efficiency of the amplifier.

Manufactured fiber

Throughout the years, few-mode amplification was a focal part of our team's studies. During his thesis with our team, Le Cocq worked on several FM-EDFA designs. In 2012, he introduced a fiber design able to amplify four mode groups and to equally amplify the LP_{11} and LP_{21} mode groups with gains larger than 20 dB and with a DMG of less than 1 dB. This design, which we will call FMF GLC from now on, was later fabricated in our laboratory and the experimental results confirmed the simulations with a good concordance [Le Cocq et al., 2012]. The theoretical fiber design was a close-to step index doped in with a ring fashion at the periphery of the core. The similarities between this design and the design shown in the previous section are very interesting. Although the core radius of the two designs are different, preforms of FMF GLC still exists in our lab and can be used for our cause: the preform can be redrawn with different parameters to obtain the core radius of 8 μm of our design rather than the 5 μm of the original design. This core expansion is needed to guide up to $|L| = 3$ OAM mode groups in this fiber geometry. The fiber's RIP, EDP and the intensity distributions of the modal content are presented in Figure 4.29. These intensity distribution are calculated using a vector mode solver developed by our team. Even though the RIP presents a depletion zone in the center, it does not affect in any shape or form the modal content of the fiber.

Based on measurements of the actual RIP and EDP of the manufactured fiber, the index profile as well as the 2D erbium distribution were reconstructed in order to verify the performances of the fiber and compare it to the theoretical design. The amplification code described in appendix 4.8 is used for this study. The mean gain value delivered by the manufactured fiber is 19.78 dB with a ΔG of 7.24 dB, when using the guided OAM $|L| = 2$ at the pump wavelength as a pump beam for a fiber length of 3 m. These value are hardly comparable to the 24.71 dB mean gain and the 3.9 dB ΔG of the theoretical design. As a result, the PCE drastically decrease from 34.7% to 17.78%. Figure 4.30 illustrates the spectral and modal gain of this design and a one dimensional trace of the normalized RIP, EDP and pump beam. As we can see, the modal gain behavior is different than the one of the theoretical design shown in Figure 4.25: it seems that the fiber length is optimized regarding the gain flatness of the OAM $|L| = 2$ and OAM $|L| = 1$ mode groups. However, the behavior of the gain spectrum of the OAM $|L| = 3$ mode group gives an indication that this fiber length is longer than its optimized value. This can be seen by the absorption of the gain for the short wavelengths of the spectrum. The gain spectrum difference between the theoretical design and the manufactured fiber can be better understood by comparing the one dimensional

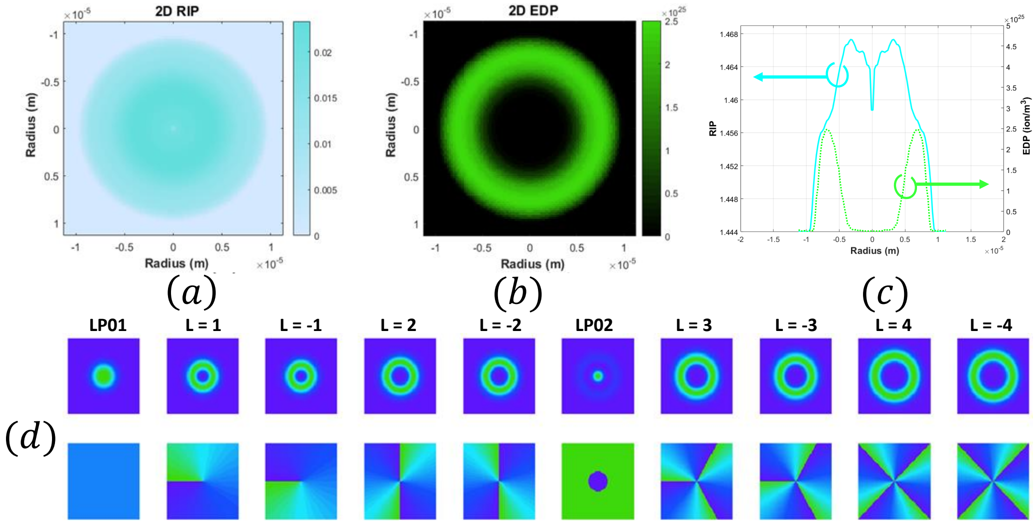

FIGURE 4.29: Two-dimensional representations of the (a) RIP and the (b) EDP, (c) one dimensional cut of the RIP and EDP and (d) the intensity and phase distributions of the guided modes at $1550\ \mathrm{nm}$ of the step index ring doped FM-EDFA manufactured design.

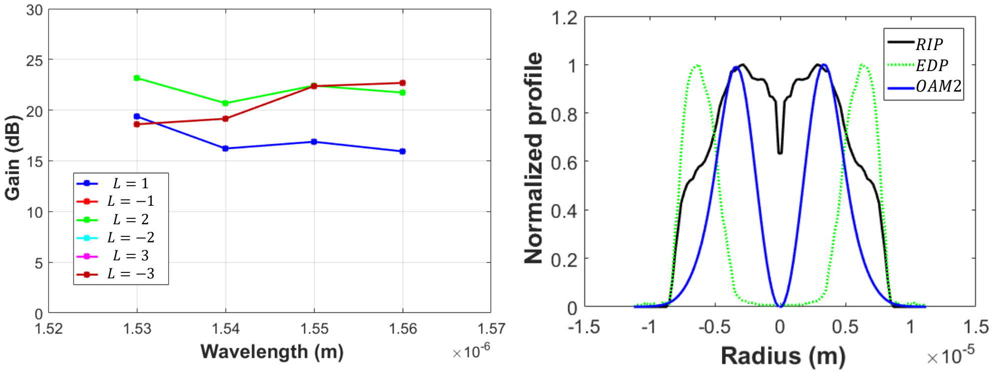

FIGURE 4.30: (a) Spectral and modal gain provided by the step index ring doped FM-EDFA manufactured design for attenuation compensation in the optimized configuration, (b) RIP, EDP and guided OAM $|L| = 2$ at the pump wavelength trace.

traces of the EDP and the pump beam presented in Figure 4.30 and Figure 4.28: the pump beam is better confined in the doped area for the theoretical design, enabling more excitation for the Er^{3+} ions. We attempted to use a larger pump beam for the manufactured fiber, but this choice favored the modes with larger mode field diameter, boosting the gain of the OAM $|L| = 3$ mode groups, while the gain of the more centered OAM $|L| = 1$ mode group decreases significantly, resulting in a ΔG value higher than $10\ \mathrm{dB}$. Thus, it is highly doubtful that this manufactured design matches the delivered performances of the theoretical design. We should remind that this fiber was not custom-made for this study, but for previous ones, and it matched greatly the performances of its theoretical design and application [Le Cocq et al., 2013].

4.6.3 Attenuation compensation

Another application of this kind of fiber design can be to compensate the different levels of losses seen by the different modes during their propagation along a long distance transmission line, which can ultimately limits the capacity increase. The FMF L111 previously studied present a modal content guiding up to $|L| = 4$ as seen in Section 3.2, while the FMF L113 guides up to $|L| = 3$ for long distances transmissions [Bigot-Astruc et al., 2019]. Given the fact that the FMF L111 presents a nearly ideal step index RIP, it presents different losses levels, with the attenuation significantly increasing with the order of the mode, due mainly to the different modal behavior for small angle light scattering (SALS) and the Rayleigh scattering. On the other hand, the FMF L113 has an inner depressed trapezoidal-index structure at the core-cladding interface which decrease the SALS of the modes, specially the HOMs [Bigot-Astruc et al., 2019]. Figure 4.31 illustrates a comparison of the mode attenuation levels of a FMF having nearly the same loss proprieties as the L111, named Fiber A and the FMF L113, referred to as Fiber B, while supposing that the losses of the OAM basis are at the same level of the losses of the LP basis (the losses of the L113 were measured for the LP basis modes.)

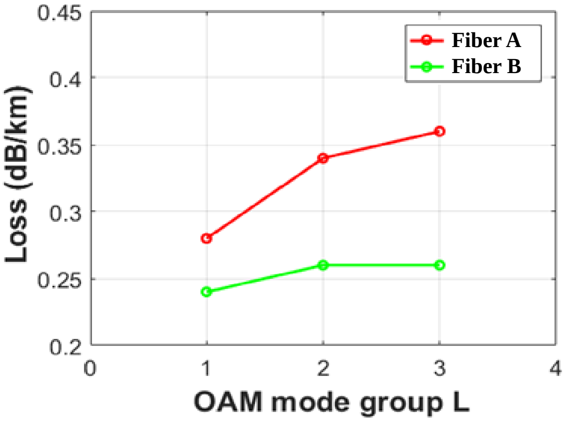

FIGURE 4.31: The modal losses per mode group of Fiber A (having similar loss proprieties as the L111) and Fiber B (L113) [Bigot-Astruc et al., 2019].

As we saw in the previous section 4.6.2, the use of the FMF L113, having the same levels of attenuation for all of its guided modes, requires a FM-EDFA with equalized gain. Nevertheless, the fact that this fiber presents a trapezoidal index structure limits its mode matching with a step index fiber, adding some additional losses to the modes while propagating from one fiber to the other. This can be seen in Figure 4.21, where the overlap between the FMF L113 and a perfect step index fiber can decrease to 69% for certain modes. The FMF L111 design, presenting a structure closer to the perfect step index, can match better with a theoretical step index fiber as shown by the overlap values of Figure 4.32. The values were calculated using Equation 4.2, replacing the complex fields of the L113 by those of the L111.

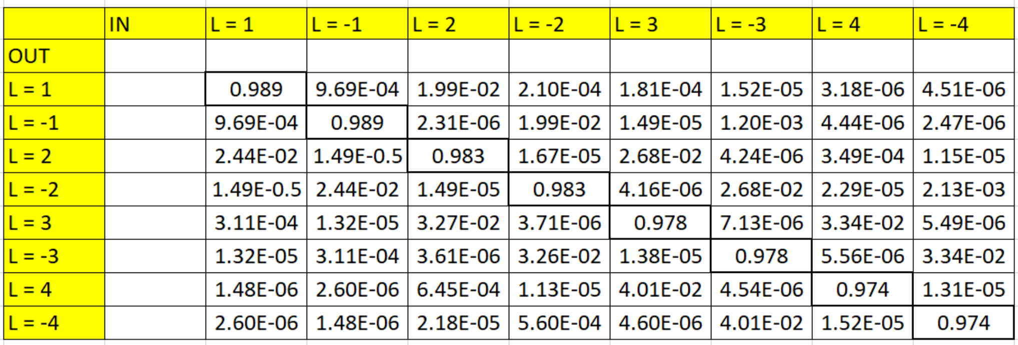

	IN	L = 1	L = -1	L = 2	L = -2	L = 3	L = -3	L = 4	L = -4
OUT									
L = 1		0.989	9.69E-04	1.99E-02	2.10E-04	1.81E-04	1.52E-05	3.18E-06	4.51E-06
L = -1		9.69E-04	0.989	2.31E-06	1.99E-02	1.49E-05	1.20E-03	4.44E-06	2.47E-06
L = 2		2.44E-02	1.49E-0.5	0.983	1.67E-05	2.68E-02	4.24E-06	3.49E-04	1.15E-05
L = -2		1.49E-0.5	2.44E-02	1.49E-05	0.983	4.16E-06	2.68E-02	2.29E-05	2.13E-03
L = 3		3.11E-04	1.32E-05	3.27E-02	3.71E-06	0.978	7.13E-06	3.34E-02	5.49E-06
L = -3		1.32E-05	3.11E-04	3.61E-06	3.26E-02	1.38E-05	0.978	5.56E-06	3.34E-02
L = 4		1.48E-06	2.60E-06	6.45E-04	1.13E-05	4.01E-02	4.54E-06	0.974	1.31E-05
L = -4		2.60E-06	1.48E-06	2.18E-05	5.60E-04	4.60E-06	4.01E-02	1.52E-05	0.974

FIGURE 4.32: Overlap between the calculated OAM modes of the FMF L111 (IN) and the theoretical step index fiber (OUT).

As can be seen in Figure 4.32, the lowest overlap value, presented between the $|L| = 4$ mode family of the FMF L111 and the step index fiber, is above 97%. In the following, we will be limiting ourselves to the $|L| = 3$ mode family since it is the last mode family guided for long distances. We performed the same study as the one presented in Section 4.6.2, simulating different ring shaped EDP inside our step fiber, while changing the transmission fiber from the L113 to the L111. Therefore, the output conditions must be modified, from having an equalized gain to having a gain dependent on the loss level of each mode group in the FMF L111: the $|L| = 1$ mode group, having the lowest attenuation level of about 0.26 dB/km will have the lowest gain in our FM-EDFA. Meanwhile, the $|L| = 3$ mode group, which presents the highest attenuation level of about 0.36 dB/km will necessitate the highest gain value. The gain delivered by our fiber should not only verify these two conditions, but also respect the differential modal loss (DML), which is the difference between the attenuation of two consecutive mode groups, while compensating the total accumulated losses for the propagation through the passive fiber. The group $|L| = 2$ presents an attenuation level of 0.34 dB/km. Hence, our design must deliver a gain respecting the following conditions: the DML between the $|L| = 2$ and $|L| = 1$ mode groups 0.08 dB/km and the DML between the $|L| = 3$ and $|L| = 2$ mode groups 0.02 dB/km.

We were able to isolate a fiber geometry able to verify these conditions if this FM-EDFA is deployed after 67 km of propagation through the FMF L111: a step index fiber with a radius of $r = 8$ μm and a $\Delta n = 0.014$, matching the passive

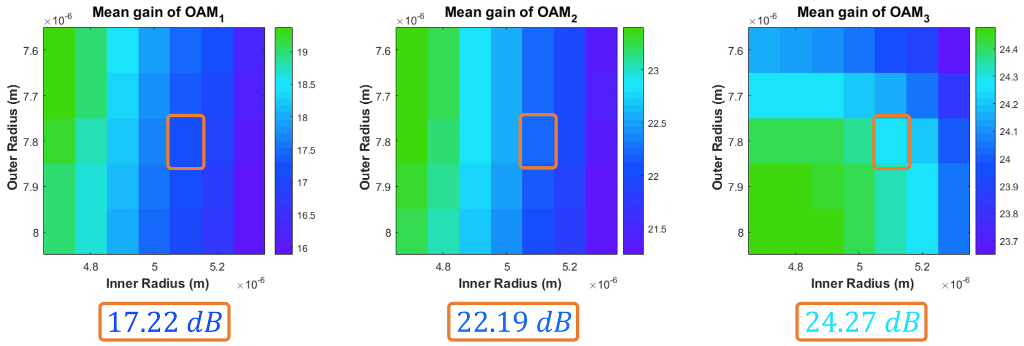

FIGURE 4.33: Impact of the inner and outer radius values on the mean gain values of each OAM mode group of the step index ring doped FM-EDFA.

fiber parameters, doped in a ring fashion with a $r_\mathrm{i} = 5.1\ \mu\mathrm{m}$ and a $r_\mathrm{o} = 7.8\ \mu\mathrm{m}$ as shown in Figure 4.33. The pump configuration is set to be a ring shaped beam that matches perfectly the EDP ring with a plane phase as described in the previous paragraph. Table 4.7 illustrates the characteristics of the proposed design: the pump and signal power as well as the erbium concentration. Under these conditions, the step index rind doped FM-EDFA delivers a mean gain value of 21.27 dB for an optimized fiber length of 2.61 m. Table 4.8 shows a comparison between the accumulated losses after a 67 km of propagation through the FMF L111, and the mean value of each mode gain delivered by this fiber design. Table 4.9 shows a comparison between the DML and the DMG of the 3 mode groups.

TABLE 4.7: Simulated results of the attenuation compensation step index ring doped FM-EDFA design.

Parameters	Values
$\mathrm{Power}_{\mathrm{pump}}$	0.3 W
$\mathrm{Power}_{\mathrm{Signal}}$	$12\ \mu\mathrm{W/mode/wavelength}$
Er^{3+}	$2.5 \times 10^{25}\mathrm{ions/m^3}$

TABLE 4.8: Comparison between the 67 km propagation losses and modal gains of our FM-EDFA geometry.

OAM	Propagation losses through L111	Gain FM − EDFA
$\lvert L \rvert = 1$	17.42 dB	17.22 dB
$\lvert L \rvert = 2$	22.78 dB	22.19 dB
$\lvert L \rvert = 3$	24.12 dB	24.27 dB

TABLE 4.9: Comparison between the accumulated DML of the 67 km propagation losses and the DMG of our FM-EDFA geometry.

OAM	DML	DMG
$\lvert L\rvert = 2 - \lvert L\rvert = 1$	5.36 dB	4.97 dB
$\lvert L\rvert = 3 - \lvert L\rvert = 2$	1.34 dB	2.08 dB

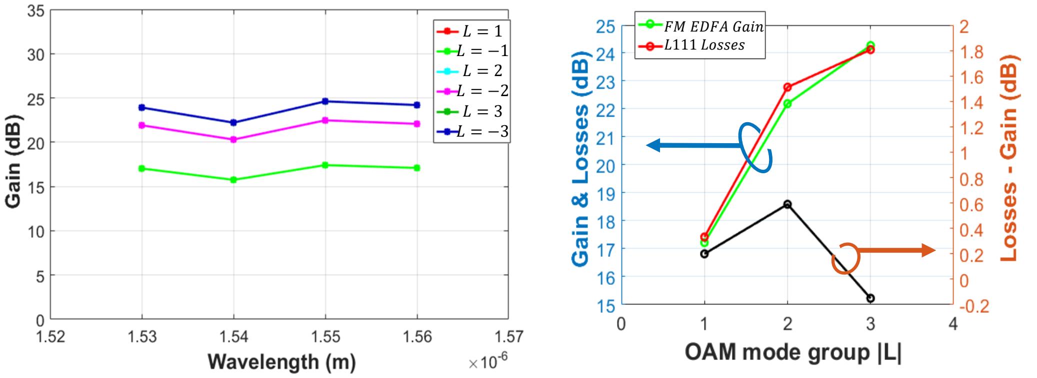

(a) (b)

FIGURE 4.34: (a) Spectral and modal gain provided by the step index ring doped FM-EDFA theoretical design for attenuation compensation in the optimized configuration, (b) Average modal gain of the design (green), total modal losses (red) and the Loss - Gain parameter after a 67 km propagation through the FMF L111.

The gain spectrum of the proposed geometry is illustrated in Figure 4.34, as well as a comparison between the total losses per mode and the total gain per mode. The mode losses in the doped fiber are supposed to be at the same level for a mode over the whole spectral band of interest. The amplification code described in appendix 4.8 is used for this study.

This design delivers a mean gain of 17.22 dB for the OAM_1 mode group, which presents a propagation loss of 17.42 dB. The mean gain value for the OAM_2 is 22.19 dB, while its propagation loss is 22.78 dB. For the OAM_3 a mean gain value of 24.27 dB is delivered compared to 24.12 dB of propagation loss.

This result sounds promising as we could hope to compensate the different losses of the mode groups directly by the fiber amplifier design, rather than using an equalized FM-EDFA followed by equalization filters that induce the needed losses in order to have the same power distributed over the different mode groups after the amplification. In an ideal transmission line, we could hope to splice this FM-EDFA to a 67 km of the FMF L111 fiber and know that after the beam propagates through this span, its losses suffered in the passive fiber and its added gains from the FM-EDFA can counterbalance each other, thus the signal power would be preserved throughout a number of passages through the same kind of splice. To put this idea in a more practical perspective, we chose to simulate a transmission line formed by two spans of the previous $67\ \mathrm{km}$ FMF L111 and its associated FM-EDFA. For that, the results presented in Figure 4.34 will be considered as the result of the first span, and the output signal power of this span will be considered as the input signal power for the second one. Figure 4.35 shows the spectral and modal gain provided by the second FM-EDFA, as well as a comparison between the losses and the gain of this span.

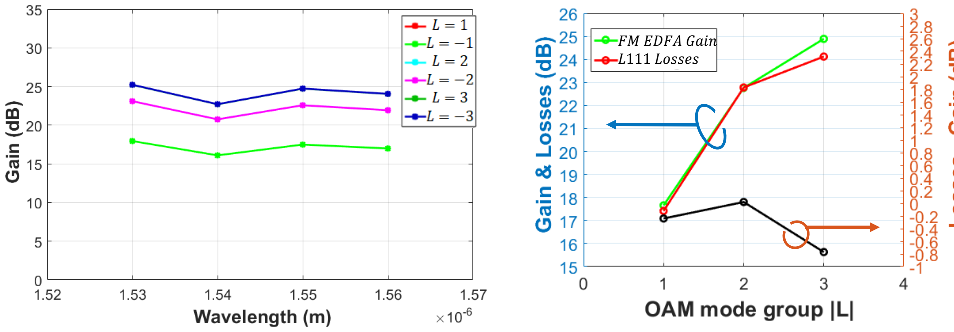

(a) (b)

FIGURE 4.35: (a) Spectral and modal gain provided by the step index ring doped FM-EDFA theoretical design for attenuation compensation in the optimized configuration, (b) Average modal gain of the design (green), total modal losses (red) and the Loss - Gain parameter after a second span of a $67\ \mathrm{km}$ propagation through the FMF L111.

As can be seen, the spectral and modal gain present the same behavior for both spans. The mean gain value for each mode slightly changes after the second span from $17.22\ \mathrm{dB}$ to $17.66\ \mathrm{dB}$ for the OAM $|L| = 1$ mode group and from $22.19\ \mathrm{dB}$ to $22.76\ \mathrm{dB}$ for the OAM $|L| = 2$ and from $24.27\ \mathrm{dB}$ to $24.89\ \mathrm{dB}$ for the OAM $|L| = 3$. This result shows that this approach can maintain the same gain levels for a multi-span transmission, delivering the same amplification as a single span scheme.

In addition, the $0.59\ \mathrm{dB}$ of difference between the losses and the gain for the OAM $|L| = 2$ at the output of the first span will be compensated at the output of the second span. The same process can be observed for the OAM $|L| = 1$. However, the difference between the mean gain value and the propagation losses of OAM $|L| = 3$ have grown larger, from $0.15\ \mathrm{dB}$ to $0.77\ \mathrm{dB}$. These difference variations must be evaluated for each consecutive span in order to characterize the final output gain. We will limit this study to a two spans transmission, given the fact that we are not proposing a finalized experimental set-up. This design can be the subject of more optimization through future works, in order to obtain an EDP ring closer to the experimental profiles, an optimized pump beam and pumping scheme for a multi-span transmission and even including the passive/active fiber splice losses of each mode. The subject of a custom-made fabrication for the attenuation compensation application remains a perspective which could be a part of a future work for our team.

4.7 Power conversion efficiency

The power conversion efficiency of a single-mode EDFA is generally calculated to compare the performance of two such amplifiers [Anthony, Lahiri, and Biswas, 2012]. Based on the method used to calculate the PCE for single-mode EDFAs, this efficiency can be calculated for FM-EDFAs as shown in Equation 4.1.

$$\text{PCE} = \frac{\sum_n \sum_k \text{Power}_{\text{Signal,out}} - \sum_n \sum_k \text{Power}_{\text{Signal,in}}}{\text{Power}_{\text{Pump}}} \tag{4.3}$$

where n is the mode index and k is the wavelength index. In our case, using a pump wavelength at $980\ \text{nm}$ and signal wavelengths centered around $1550\ \text{nm}$, the best efficiency we can hope for is around 63.23%, corresponding to the $\lambda_{\text{Pump}}/\lambda_{\text{Signal}}$ ratio, which is experimentally never reached. In order to offer a better understanding of the PCE of the FM-EDFAs studied in the previous sections 4.5 and 4.6, the PCE of each design was calculated for the same pump power $0.3\ \text{W}$, same signal power $12\ \mu\text{W}/\text{mode}/\text{wavelength}$ and the corresponding optimal configuration of each design. These values were later compared to the ones of a single-mode EDF, a doped version of the SMF28 and the micro-structured FM-EDFA discussed in the section 4.4 under the same conditions. The different fiber designs and their parameters are presented in Figure 4.36. The amplification code described in appendix 4.8 is used for this study.

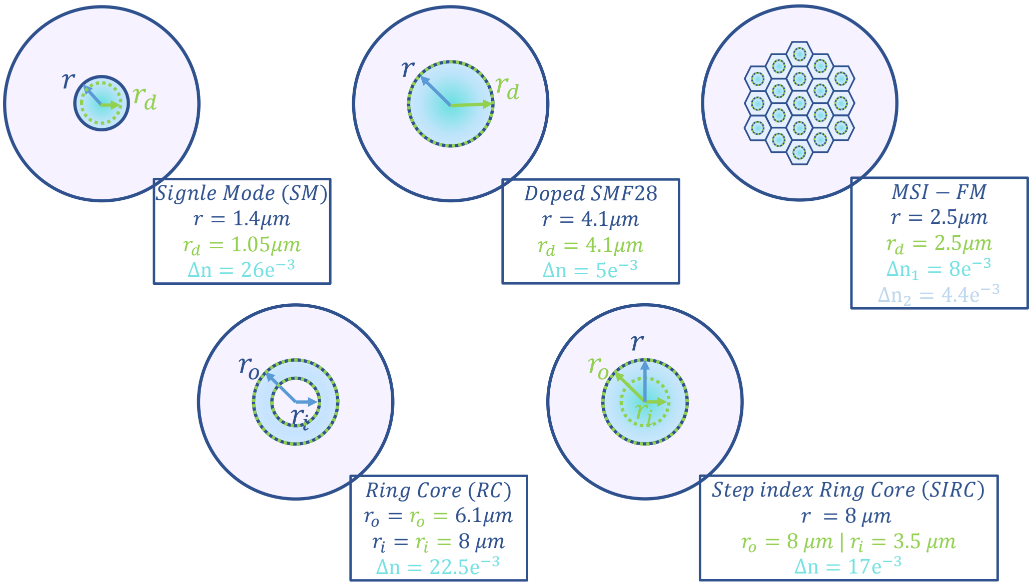

FIGURE 4.36: EDF designs and their parameters used to compare the PCE.

We should mention that in order to better compare the different FMFs, we chose to fix the number of guided modes up to the LP_{31} (OAM $|L| = 3$ in the case of the fibers studied in the OAM base). As a consequence, the outer radius of the ring core FM-EDFA is considered to be $8\ \mu\text{m}$ instead of $9\ \mu\text{m}$ given in the section 4.5. The results are presented in Table 4.10.

TABLE 4.10: Amplification results for the different fiber designs shown in figure 4.23, showing the optimal length of the fiber, the mean gain value, the total gain excursion and the PCE.

Fiber type	SM	SMF28	MSI − FM	RC	SIRC
L_{opt}	6.06 m	3.23 m	1.68 m	1.92 m	2.06 m
Gain_{mean}	35.7 dB	35.1 dB	19.2 dB	22.61 dB	24.71 dB
ΔG	3.4 dB	3.4 dB	2.4 dB	2.71 dB	3.9 dB
PCE	52.6%	45.3%	22%	38.42%	34.7%

As we can see, the single-mode EDF has the highest PCE value of about $52,6\%$, with only 10% difference from the maximal value. The SMF28 presents the second highest PCE of 45.3%. The FMF designs all present smaller PCE values: both ring core and step index FM-EDFA offer PCE higher than 34%. Another way to better describe this is the evaluation of the pump budget needed to provide the same gain for both the single-mode EDF and the ring core one. If we should consider the mean gain value of 22.61 dB delivered by the ring core FM-EDFA with 0.3 W as the targeted value, a single-mode EDF will necessitate a pump power of 0.03 W to delivered such mean gain value. Now regarding the modal content of those two fiber amplifiers, the single-mode EDF can amplify the fundamental mode having a polarization degeneracy, thus a total of two modes, while the ring core FM-EDFA guides up to $|L| = 6$ OAM mode groups, thus 26 spatial and polarized degenerated modes. Hence, the ring core FM-EDFA can amplify 13 times the capacity of a single-mode EDF using only 10 times more pump power. Such a result put in evidence the advantage of using a FM-EDFA in terms of operating costs. This can be seen as a starting point in the quest of a doped FMF design having nearly the same PCE as a single-mode EDF.

4.8 Conclusion

All along this chapter, different possible fiber designs of FM-EDFAs were reviewed. The fiber geometry associated with conventional manufacturing methods does not allow gains to be equalized when the number of modes becomes large in a classical step FMF, which is why micro-structured core fibers are considered as an interesting alternative. This type of fibers makes it possible to overcome the limitations of the conventional manufacturing methods, in particular from the point of view of controlling the EDP, as it offers the ability to control the doping geometry outside of a circular fashion. Another alternative geometry that can be explored is the ring core one that is technologically easier to achieve. This type of design enhances the overlap between the EDP and the beams at the pump and signal wavelengths, delivering equalized gain between mode with low total excursion levels. Step index fibers with a ring shaped EDP were also investigated in order to amplify OAM modes guided in this type of fiber. Gain equalization for up to $|L| = 3$ OAM mode groups has been theoretically investigated. This geometry was also investigated in an alternative approach, having a modal gain scheme proportional to the modal propagation losses through a passive fiber, enabling their compensation. At the end of this chapter, the PCE of all the fiber designs studied in this chapter is compared to single-mode EDF, opening the perspective of finding new fiber designs having PCE comparable to the single-mode EDF as well as the fabrication of the proposed designs in order to characterize them experimentally.

Conclusion and perspectives

During this thesis, we have worked on several fronts in order to get closer to a long-haul transmission system based on the use of few-mode fibers employing the modal division multiplexing technology with the aim to surpass the limits set by the single-mode fiber used in the actual used long distance networks. From a technological standpoint, a remarkable gap exists between these two transmission systems. As described throughout this manuscript, two major factors increase the difficulties facing the use of the few-mode fiber based networks: the mode coupling that can occur during the propagation of the beam through the optical fiber and the amplification of the signal vital for a long distance transmission. Both these factors fall into the research axes of the project FUI-MODAL, under which this thesis was conducted. Hence, these factors were the subject of my works, combining theoretical and experimental approaches, inspired from the precedent works of past team members, as well as my personal contributions leading up to this PhD manuscript.

We started this manuscript by recalling some of the necessary theories and notions throughout the first chapter necessary to understand the rest of the chapters. Chapters 2 and 3 covered the modal content characterization axis of the thesis. We started the second chapter by the notion of the transmission matrix that we used to develop our modal content characterization method. Then we presented the state of the art regarding the existing methods able to study the modal behavior of few-mode and multi-mode fibers. After that, we introduced the method that we developed during the first part of this thesis, inspired by the previous works presented in the state of the art section. This method does not necessarily present any novelty compared to the already existing methods, but such a method did not exist in our laboratory before the start of this thesis. In addition, as can be seen in the third chapter where we described and detailed the results of this method, we can proudly say that we matched the other methods of the state of the art. Our set-up was used in order to characterize multiple types of fibers : we studied two generations of a few-mode fiber designed and manufactured by Draka/Prysmian group, a partner of the Project FUI-MODAL. The two generations had the same modal content but with different modal losses behavior due to different refractive index profiles. Our method successfully detected the proper modes of these fibers with high matching to their numerically calculated modes, for a linearly polarized mode basis as well as a orbital angular momentum one. We also used our set-up in order to selectively inject a specific mode at the input face of the fiber, obtaining an electric field at the output face of the fiber that highly matched the selected mode. We also used this technique to characterize a specialty ring-core fiber that was manufactured by our team members at the Fibertech Lille platform in our laboratory. In addition to characterizing the modal content via the transmission matrix of this fiber, we conducted a time evolution study of its transmission matrix over a two days span in order to better understand the variations of the coupling properties of this fiber. The results showed low variations mainly attributed to the phase contribution rather than anything else. Following this result, we developed a parametrize transmission matrix model able to highly predict these variations even when using a single parameter, reducing thus the dimensions of the problem to a single dimension. We showed that adding more parameters can not but help increasing the quality of the prediction, although a single parameter gave very good results.

This method can be subject for many upgrades and updates in the future. The modal content characterization in the third chapter was conducted on short fiber length (less than 2 m). Although this length is comparable to some transmission systems components such as FM-EDFAs, the ability to use this method to study long distance fibers is still considered as a primary objective. This can be achieved by reducing the measurement time of the transmission matrix, which can be done using a variety of approaches. The use of a spatial light modulator with shorter response time, or any other device than can deviate the propagation of a light beam, such as acousto-optic deflectors. A version of this method using an acousto-optic device was the objective of a Master 2 internship and it is described at the end of the third chapter. The use of a camera with higher refreshing frequency can also reduce the measurement time of the transmission matrix. Another approach for a faster measurement can be to measure the different combinations of polarization states simultaneously which can make the measurement four times faster. This can be done by injecting both horizontal and vertical states at the same time and collecting the emerging beam on two separate cameras, one for each output polarization state. Another perspective than could be applied to our method is to develop accurate channel models for few-mode fiber optical transmission systems based on our parametrized model for the time evolution of the transmission matrix.

The second part on the thesis was focused on the other factor mentioned above: the few-mode amplification. The fourth chapter of this manuscript was dedicated to describe our works on this problematic. We started by describing the properties and characteristics of a few-mode amplifier and then detailing the state of the art for the few-mode erbium doped fiber amplifier, limiting ourselves to the works where an actual fiber was produced and characterized. In the first months of my arrival at the laboratory, a new micro-structured few-mode amplifier was already designed by Trinel during his thesis and manufactured at Fibertech Lille platform. This fiber was combined with a pair of spatial multiplexers, produced by CAILabs, another partner of the project FUI-MODAL, in order to build a prototype of few mode amplifier. The tests and characterizations of this system, in which I participated, are described in the fourth chapter. The results show high acceptable X-talk values and a flat gain for the different modes. High levels of losses were also presented for this system, with multiple probable origins such as temperature effects, questionable mode shaping and injection. However, we proved the feasibility of such systems, while mentioning that it is a first prototype based on all new devices using a single phase plate to modify both the signal and pump beams. Future work and upgrades on these devices can lead to lower losses levels and better mode shaping which will improve the system performances. My works were not limited in pursuing the works of the preceding team member on this topic: I also worked on new designs of few-mode erbium doped fibers in the context of a long distance transmission. Having the chance to work with other fellow PhD students of our team, especially Tandje who worked on ring-core fiber designs and conceptions, we developed a ring-core erbium doped design able to amplify up to 6 orbital angular momentum mode groups (equivalent to 26 if we consider polarization and spatial degeneracy modes), with equalized flat gain and low differential modal gain. This design presents a remarkable advantage compared to the manufactured fiber guiding just one orbital angular momentum mode presented in the state of art. The performances of this design were simulated numerically using a code developed by Le Cocq during his thesis with our team and presented in the Appendix A, which was adapted and upgraded to suite our needs. Theoretical studies of this design showed promising results, with a mean gain value of 22.61 dB, a differential gain of only 2.7 dB and a power conversion efficiency value of 38.42%, which can be considered high for these kinds of fibers. In order to transform this design from a numerical idea to an actual fiber, our team at Fibertech Lille platform developed a non-conventional preform fabrication method, with complementary zirconium doping, in order to achieve the refractive index profile of our theoretical model. As presented in the fourth chapter, we managed to manufacture a ring-core alumino-silicate fiber with erbium and zirconium co-doping that had the required refractive index difference between the core and the cladding. However, both radius of the ring did not match our design for this first test. At the time this manuscript was written, another fiber was at the production stage and we hope to characterize it and present it in our future works. Following the promising theoretical results of our ring-core erbium doped design, as well as the proof that a step-index fiber can guide orbital angular momentum modes, with even less coupling levels than the linearly polarized modes, we were interested in a step-index fiber doped with erbium ions in a ring fashion, in order to better amplify such modes. The same code presented in Appendix A was used to numerically simulate the performances of such a design. A resulting mean gain value of 24.71 dB, a differential gain of 3.9 dB and a power conversion efficiency value of 34.7% was obtained for such a design, amplifying the first 3 orbital angular momentum mode groups. Le Cocq had developed and manufactured during his thesis a nearly step-index fiber with a ring-shape erbium doping. Although this fiber and our design did not present a matching radius for the erbium doping profile, the experimental measurement of the refractive index profile and the erbium doping profile of Le Cocq's fiber were used in order to find a rescaling factor that can lead to a fiber matching our theoretical design. However, our erbium doping profile radius and the one of the manufactured fiber did not perfectly match, resulting in lower mean gain values and higher differential gain values. We could hope and start a new process for this fiber in order to better match our theoretical design and thus characterize experimentally the liability of our design. At the end of this chapter, we compared the different power conversion efficiencies of all the presented few-mode fiber amplifier with the ones of single-mode fiber amplifier. We can conclude that our ring-core fiber can be a starting point of a new generation of few-mode fiber amplifiers having high power conversion efficiencies, thus reducing the pump power budget and limiting the energy losses observed in other few-mode amplifiers.

Although the works of this thesis can be considered as two separate parts, one could not help but notice the common points between this two parts. A main objective of our future works is to use our modal content characterization method in order to study the modal behavior and coupling of the modes of an erbium doped few-mode fiber. To the best of our knowledge, an experimental modal characterization of an active fiber has not been done yet, and we believe that our method is able to accomplish such an objective.

Appendix A: Numerical modeling of FM-EDFAs

.1 Introduction

The increasing need for outperforming telecommunications networks relies on developing new tools and components such as optical amplifiers. During EDFAs designing stages, the implementation of fiber profiles and amplifications modules makes it a time-consuming and costing process. However, these encountered issues can be coped by numerical modeling. This latter predictive tool, having to be representative of the reality as much as possible, requires advanced developments.

This chapter will be dedicated to describe in details the multiple-steps workflow allowing to translate the physical questions to a numerical model. The description will start by a step of physical discretization of the amplifiers dimensions followed by the treatment of the population equations as well as the equations of propagation, to continue by explaining the used approximations in our code and finish with this code converging conditions for an intensity model conventionally used to study FM-EDFAs.

In order you give a better understanding of this model, developed by former member of our team Guillaume Le Cocq, presenting their code explanation is of a great interest, since it allowed us to obtain highly similar results to the experimental ones. It should be mentioned that during this thesis, several upgrades and adaptations were applied to this code thanks to which the study of our new doped designs, presented previously in Chapter 4, was possible.

.2 Physical discretization

The discretization of the amplification including its spatial, spectral and modal dimensions is needed to have a complete digital resolution. Concerning the spatial dimensions of the fiber, we used a division into 3 small elements Nx, Ny and Nz, where z is the lengthwise dimension and x, y are the transversal ones as indicated in Figure (37). Due to the fact that the amplification occurs only in the presence of erbium Er^{3+} ions, the transverse resolution could be restricted to the core dimensions or even to its doped areas in case of partial doping. In addition, the discretization of the spectral dimension is performed by subdividing the entire spectrum into small width elements, knowing that the spectral dimension corresponds to the spectrum of the high effective cross-sections of the ions as shown in Figure (1.15). This latter consideration should be addressed since the amplification mechanism affects all the wavelengths. Indeed, when the signal is in the C-band, these spectral bands can be narrowed to include the range from $1500\ \mathrm{nm}$ to $1600\ \mathrm{nm}$ for the wavelengths of the signal beams. The pump beam is considered separately since it propagates at a different wavelength, commonly around $980\ \mathrm{nm}$ or even $1480\ \mathrm{nm}$.

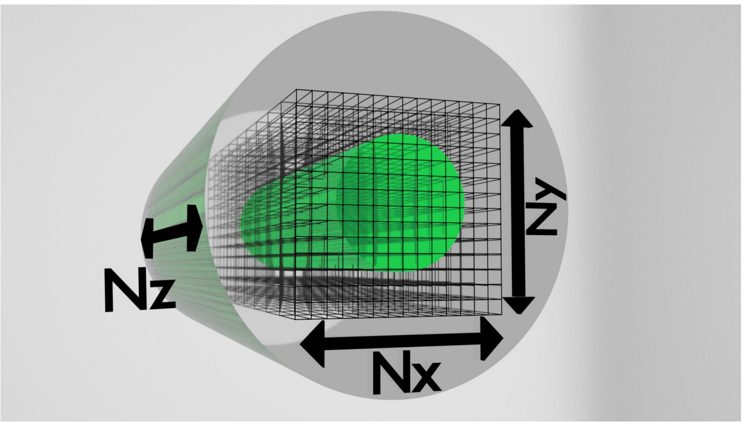

FIGURE 37: Spatial discretization of the fiber [Trinel, 2017].

.3 Amplification equations

Population equations

At a given moment t, the Equation 1.45 becomes:

$$N_T(x,y) = N_1(x,y,z,t) + N_2(x,y,z,t) \tag{4}$$

The population inversion, driven by the absorption as well as the stimulated and the spontaneous emission phenomenons (described in Chapter 1.3.2), is not homogeneous taking into account its dependence on the considered point position (x,y,z) and the amount of photons crossing this point. The quantification of these latter dependencies is expressed as function of photons flux $\phi_{k,i,\pm}$, where k is the wavelength index, i is the mode index, $\pm$ reflects the two directions of beam propagation with $+$ represent the direction of the signal propagation, called co-propagation and $-$ is the opposite one known as the countra-propagarion:

- the quantity of photons absorbed at the (x,y,z) point per second and per volume unit: $\phi_{k,i,\pm}(z,t)I_{k,i}(x,y)\sigma_{a,k}N_1(x,y,z,t)$,
- the number of photons created by stimulated emission per second and per volume unit: $\phi_{k,i,\pm}(z,t)I_{k,i}(x,y)\sigma_{e,k}N_2(x,y,z,t)$,
- the number of photons created by spontaneous emission: $A_{21}N_2(x,y,z,t)$,

$I_{k,i}(x,y)$ is the normalized intensity distribution of the mode i at the wavelengthλ_k at the (x,y) point in the transversal plane, $\sigma_{a,k}$ and $\sigma_{e,k}$ are the effective cross-section of absorption and emission respectively at λ_k and $A_{21} = \frac{1}{\tau_{21}}$ with τ_{21} representing relaxation time or the life time of the level $4I_{13/2}$. Thus, the population equation can be written as:

$$\begin{aligned}\frac{N_2(x,y,z,t)}{dt} &= \sum_k \sum_i \sum_{\pm} \phi_{k,i,\pm}(z,t) I_{k,i}(x,y) \sigma_{a,k} N_1(x,y,z,t) \\ &\quad - \sum_k \sum_i \sum_{\pm} \phi_{k,i,\pm}(z,t) I_{k,i}(x,y) \sigma_{e,k} N_2(x,y,z,t) \\ &\quad - A_{21} N_2(x,y,z,t)\end{aligned}$$

Propagation equations

The Equation 4 allowed us to observe that any population change at the N_2 level is oppositely equal to the population change at the N_1 level. The reason why it is possible to establish the propagation equations. During its propagation in an elementary section $dx \times dy \times dz$ through the fiber, the beam will undergo the effects of the absorption, the stimulated emission and the spontaneous emission. thus, for this section, we will have

- the number of added photons to the incident photon flux due to the duplication by stimulated emission: $\iint \phi_{k,i,\pm}(z,t) I_{k,i}(x,y) \sigma_{e,k} N_2(x,y,z,t) dxdy$
- the number of subtracted photons from the incident flux due to the absorption: $\iint \phi_{k,i,\pm}(z,t) I_{k,i}(x,y) \sigma_{a,k} N_1(x,y,z,t) dxdy$
- the number of parasitic photons added to the incident flux due to the spontaneous emission: $\iint m_i \Delta\nu_k I_{k,i}(x,y) \sigma_{e,k} N_2(x,y,z,t) dxdy$

where m is the mode degeneracy of the mode i and $\Delta\nu_k$ is the elementary spectral band of the spontaneous emission [Giles and Desurvire, 1991].

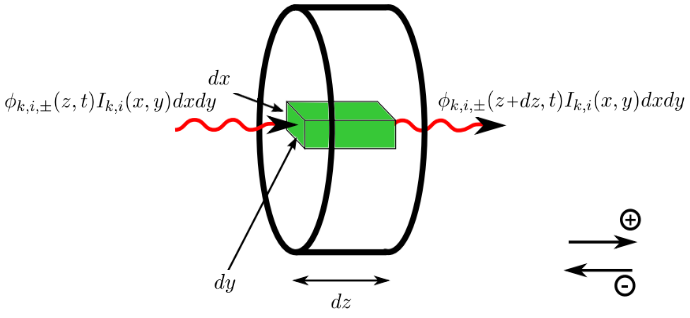

FIGURE 38: Photons flux propagation through an elementary volume of the fiber [Le Cocq, 2014].

The propagation equation is obtained as follows through combining these elements and adding the linear losses $l_{k,i}$ (due to poor containment, curvature losses, material absorption, etc.) depending on the length and the propagation mode:

$$\begin{aligned}\frac{\phi_{k,i,\pm}(z,t)}{dz} &= u\iint \phi_{k,i,\pm}(z,t)I_{k,i}(x,y)\sigma_{e,k}N_2(x,y,z,t)dxdy\\ &\quad -u\iint \phi_{k,i,\pm}(z,t)I_{k,i}(x,y)\sigma_{a,k}N_1(x,y,z,t)dxdy\\ &\quad +u\iint m_i\Delta\nu_k I_{k,i}(x,y)\sigma_{e,k}N_2(x,y,z,t)dxdy\\ &\quad -ul_{k,i}\phi_{k,i,\pm}(z,t)\end{aligned}$$

where u is the beam propagation direction, with values that can be $+1$ for the beams propagating in the same direction as the z axis and -1 for the opposite direction.

.4 Light-matter interaction

The amplification process depends on the overlap integrals between different modes (pump and signal) and erbium ions distribution. The overlap integrals, based on normalized intensity transverse distribution and within the interval $[01]$, are written as [Becker, Olsson, and Simpson, 1999; Giles and Desurvire, 1991;Digonnet and Gaeta, 1985]:

$$\Gamma_{k,i} = \iint I_{k,i}(x,y)\frac{N_T(x,y)}{N_{T,max}(x,y)}dxdy \tag{5}$$

$$\Gamma^1_{k,i} = \iint I_{k,i}(x,y)\frac{N_1(x,y,z,t)}{N_{T,max}(x,y)}dxdy \tag{6}$$

$$\Gamma^2_{k,i} = \iint I_{k,i}(x,y)\frac{N_2(x,y,z,t)}{N_{T,max}(x,y)}dxdy \tag{7}$$

Where $N_{T,max}(x,y)$ is the maximal value of N_T. The overlap integrals are always within the interval $[0,1]$.

.5 Gain and noise figure

We have previously described the optical gain of EDFAs, given by the equation 1.44. Noise generation is another important aspect of EDFAs. An simple factor to quantify this noise is the signal to noise ratio (SNR) which is the ratio between the signal power and the noise power. The difference between the SNR before and after the amplification is called noise figure (NF):

$$NF_{lin} = \frac{SNR_{in}}{SNR_{out}}$$

$$NF_{dB} = SNR_{in,dB} - SNR_{out,dB}$$

.6 Approximation of the steady state

In the context of the steady state approximation, the amplifier is at a stationary regime, thus the derivatives by time are zero. The population and propagation equations become respectively:

$$
N_2(x,y,z) = N_T(x,y)\frac{\sum_k \sum_i \sum_\pm \phi_{k,i,\pm}(z,t) I_{k,i}(x,y)\sigma_{a,k}}{A_{21} + \sum_k \sum_i \sum_\pm \phi_{k,i,\pm}(z,t) I_{k,i}(x,y)(\sigma_{a,k}+\sigma_{e,k})}
$$

$$
\begin{aligned}
\frac{\phi_{k,i,\pm}(z,t)}{dz} &= u\phi_{k,i,\pm}(z)\sigma_{e,k}N_{T,max}\Gamma_{k,i}^2 \\
&\quad -u\phi_{k,i,\pm}(z)\sigma_{a,k}N_{T,max}(\Gamma_{k,i}-\Gamma_{k,i}^2) \\
&\quad +u(m_i\Delta\nu_k)\sigma_{e,k}N_{T,max}\Gamma_{k,i}^2 \\
&\quad -ul_{k,i}\phi_{k,i,\pm}(z)
\end{aligned}
$$

.7 Integration of the equations

These coupled differential equations do not have analytical solutions since optical beams propagate in both directions of propagation. Using an analytical approach can significantly reduce the number of equations in the system in the case of a single-mode EDFAs. However, these models are not sufficient to describe the FM-EDFAs for which it is necessary to use numerical integration methods.

The Runge-Kutta of order 4 (RK4) method can be used in order to solve the equations by recurrence along the propagation axis (Oz). To initiate recurrence, it is necessary to know the initial conditions of the system:

- the power coupled in each pump mode at z=0 (co-propagative pump),
- the power coupled in each pump mode at in z=L (counter-propagative pump) with L the length of the fiber,
- the power coupled in each signal modes at z=0 (co-propagative signal),
- the power coupled in each signal modes at z=L (counter-propagative signal),
- the level of optical noise carried by each mode at each wavelength when injected into the EDF, or the noise of the laser source used. Most of the time we neglect this noise since it is very low compared to that generated by the amplifier itself through ASE. The noise level is then set to zero at z=0 for co-propagative beams and at z=L for contra-propagative beams.

The iterative process of solving the equations consists in calculating the population inversion at any transverse point $(x, y, z = z_i)$ by knowing the value of the photons flux $\phi_{k,i,\pm}(z_i)$, then the RK4 method is used to determine $\phi_{k,i,\pm}(z_i + dz)$, which will give us the population inversion for the point $(x, y, z = z_i + dz)$ and so on. However, using the RK4 method can only be resolved the in the direction of the propagation, neglecting thus the counter propagative beams. Later in this appendix, we will see how we can surpass this problem by employing convergence loops.

.8 Implementation of the code

In this section we will describe the code developed by Le Cocq during his thesis in our laboratory [Le Cocq et al., 2012]. This code is based on the propagation invariable intensity profiles at different wavelengths. We should mention that another code was developed in our laboratory by Trinel during his thesis, taking into account the electric field of the modes and not only the intensity profile, adding the mode beating and the coupling between the different modes, but we would not describe this code in details since we have used the intensity code for our studies shown in chapter 4.

First approximation

First, based on the initial parameters defined by the user, the code leads to a first approximation that is carried out in several steps:

- from the initial conditions in $z = 0$, we calculate the population inversion and the co-propagative photon flux $\phi_{k,i,+}(z = 0)$, neglecting the contra-propagative beams $\phi_{k,i,-}(z = 0)$,
- then, by considering the population inversion fixed, using the initial conditions in $z = L$, we can calculate the countra-propagative photon flux $\phi_{k,i,-}(z = 0)$ by integrating the equations in the opposite direction.

The results obtained during this first approximation are obviously not correct and must be refined using a convergence loop.

Convergence loop

Following the first calculation of the co-propagative beam, it is necessary to evaluate the beam propagating in the opposite direction. For that, a convergence loop is used. For each loop, the following calculation are successively done:

- first, using the co and countra-propagative photon flux $\phi_{k,i,\pm}(z)$ calculated at the previous iteration, the population inversion can be re-evaluated thus determining a more "realistic" values since it takes into account all beams at this stage,
- then, using the re-evaluated population inversion, co-propagative photon flux $\phi_{k,i,+}(z)$ are re-calculated without taking into account the countra-propagative,
- once the beam completes its propagation in the first direction, the population inversion is re-evaluated using the more optimized photon flux $\phi_{k,i,+}(z)$,
- at last, the countra-propagative photon flux $\phi_{k,i,-}(z)$ is re-calculated using the new population inversion values.

Since the RK4 can only be calculated for a single propagation direction, this convergence loop offers the ability to evaluate both propagation direction: after a number of loops, the values of the population inversion and the photon flux in the co-propagative direction take into account their values in the opposite direction. The code converges to the optimized solution when the calculated values of the population inversion and the photon flux during two consecutive loops show little to no difference. The different calculation steps are summarized in the figure 39

Results

Once the code has converged, we will have access to the longitudinal and transverse evolution of:

- the density of erbium ions in the different states, especially in the excited state: $N_2(x, y, z)$,
- the photon flux of the signal, pump and ASE, both co- and counter-propagative: $\phi_{k,i,\pm}(z)$.

These results are then used to calculate the gain for each mode at each wavelength signal λ_k. Other parameters can be analyzed such as the average gain G_{ave}, the differential modal gain $DMG(k)$, the differential spectral gain $DSG(i)$. These numerical results also make it possible to calculate the SNR and NF.

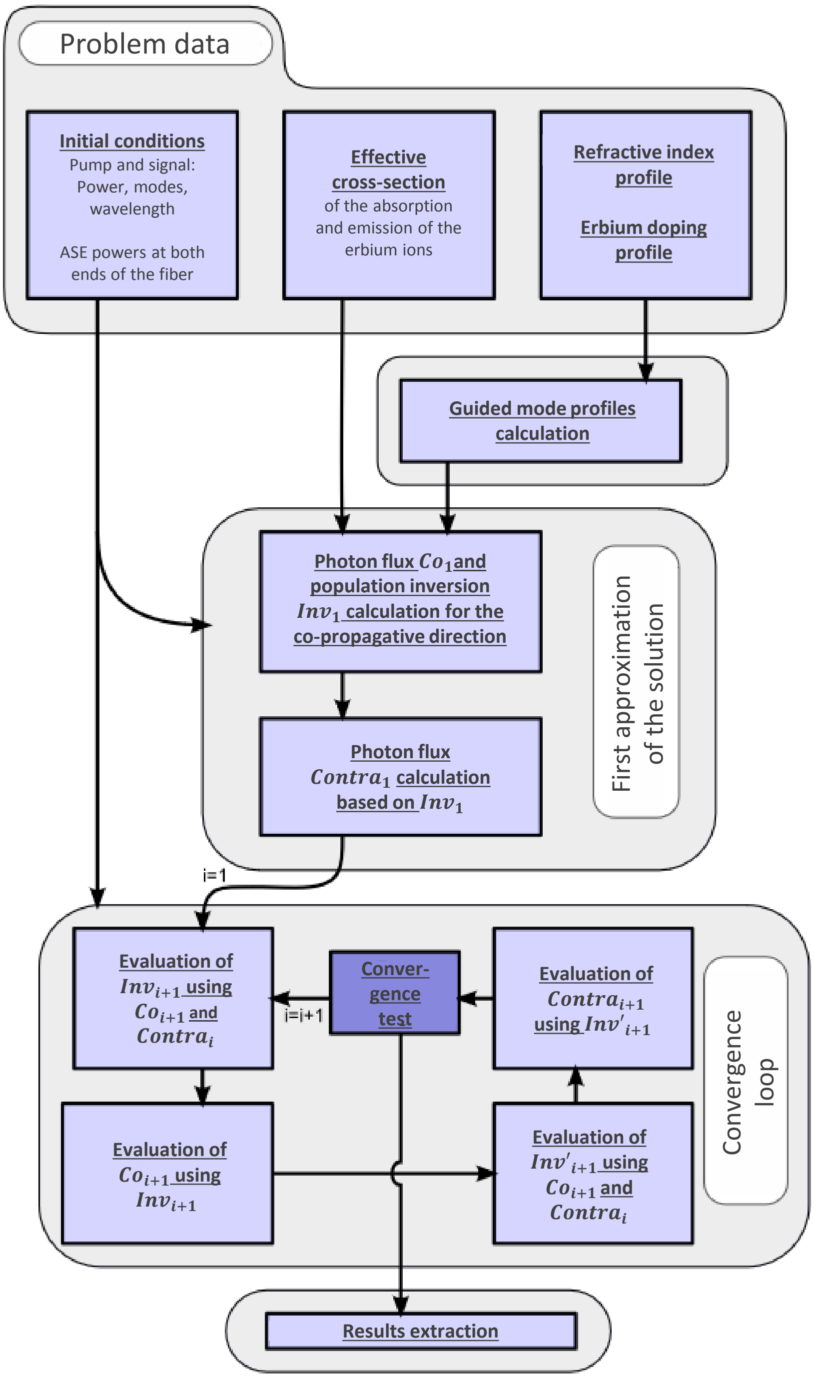

FIGURE 39: Diagram representing the calculation steps for the simulation of an EDFA [Le Cocq, 2014].

Bibliography

Agrawal, G. P (2002). *Fiber-optic communication systems*. en. OCLC: 58437991. New York: Wiley-Interscience. ISBN: 978-0-471-22114-2. URL: http://public.eblib.com/choice/publicfullrecord.aspx?p=5247720 (visited on 06/12/2019).

Agrawal, Govind (Oct. 2012). *Nonlinear Fiber Optics - 5th Edition*. URL: https://www.elsevier.com/books/nonlinear-fiber-optics/agrawal/978-0-12-397023-7 (visited on 01/16/2019).

Allen, L. et al. (June 1992). "Orbital angular momentum of light and the transformation of Laguerre-Gaussian laser modes". In: *Physical Review A* 45.11, pp. 8185–8189. DOI: 10.1103/PhysRevA.45.8185. URL: https://link.aps.org/doi/10.1103/PhysRevA.45.8185 (visited on 05/27/2019).

Alves, Tiago M. F. and Adolfo V. T. Cartaxo (Feb. 2018). "Characterization of the stochastic time evolution of short-term average intercore crosstalk in multicore fibers with multiple interfering cores". EN. In: *Optics Express* 26.4, pp. 4605–4620. ISSN: 1094-4087. DOI: 10.1364/OE.26.004605. URL: https://www.osapublishing.org/oe/abstract.cfm?uri=oe-26-4-4605 (visited on 05/29/2019).

Alves, Tiago M. F. et al. (July 2017). "Performance of adaptive DD-OFDM multicore fiber links and its relation with intercore crosstalk". EN. In: *Optics Express* 25.14, pp. 16017–16027. ISSN: 1094-4087. DOI: 10.1364/OE.25.016017. URL: https://www.osapublishing.org/oe/abstract.cfm?uri=oe-25-14-16017 (visited on 05/28/2019).

Alves, Tiago M. Ferreira and Adolfo V. T. Cartaxo (Nov. 2017). "Intercore Crosstalk in Homogeneous Multicore Fibers: Theoretical Characterization of Stochastic Time Evolution". EN. In: *Journal of Lightwave Technology* 35.21, pp. 4613–4623. URL: https://www.osapublishing.org/jlt/abstract.cfm?uri=jlt-35-21-4613 (visited on 05/28/2019).

Amphawan, Angela (Oct. 2011). "Review of optical multiple-input-multiple-output techniques in multimode fiber". In: *Optical Engineering* 50.10, p. 102001. ISSN: 0091-3286, 1560-2303. DOI: 10.1117/1.3631045. URL: https://www-spiedigitallibrary-org.ressources-electroniques.univ-lille.fr/journals/Optical-Engineering/volume-50/issue-10/102001/Review-of-optical-multiple-input-multiple-output-techniques-in-multimode/10.1117/1.3631045.short (visited on 06/27/2019).

Anthony, Ricky, Rini Lahiri, and Sambhunath Biswas (Apr. 2012). "Study of Power Conversion Efficiency of a Novel Hybrid L-Band Erbium Doped Fiber Amplifier". en. In: *International Journal of Computer Applications* 44.14, pp. 1–4. ISSN: 09758887. DOI: 10.5120/6328-8688. URL: http://research.ijcaonline.org/volume44/number14/pxc3878688.pdf (visited on 05/28/2019).

Antonelli, Cristian et al. (Apr. 2013). "Random coupling between groups of degenerate fiber modes in mode multiplexed transmission". EN. In: *Optics Express* 21.8, pp. 9484–9490. ISSN: 1094-4087. DOI: 10.1364/OE.21.009484.

URL: https://www.osapublishing.org/oe/abstract.cfm?uri=oe-21-8-9484 (visited on 06/23/2019).

Bai, Neng et al. (Aug. 2011). "Multimode fiber amplifier with tunable modal gain using a reconfigurable multimode pump". EN. In: *Optics Express* 19.17, pp. 16601–16611. ISSN: 1094-4087. DOI: 10.1364/OE.19.016601. URL: https://www.osapublishing.org/oe/abstract.cfm?uri=oe-19-17-16601 (visited on 05/28/2019).

Bai, Neng et al. (Mar. 2012). "Experimental Study on Multimode Fiber Amplifier Using Modal Reconfigurable Pump". EN. In: *Optical Fiber Communication Conference (2012), paper OW1D.3*. Optical Society of America, OW1D.3. DOI: 10.1364/OFC.2012.OW1D.3. URL: https://www.osapublishing.org/abstract.cfm?uri=OFC-2012-OW1D.3 (visited on 05/28/2019).

Becker, Philippe M., Anders A. Olsson, and Jay R. Simpson (Mar. 1999). *Erbium-Doped Fiber Amplifiers: Fundamentals and Technology*. en. Google-Books-ID: uAOq75yt5CcC. Elsevier. ISBN: 978-0-08-050584-8.

Beenakker, C. W. J. (July 1997). "Random-Matrix Theory of Quantum Transport". en. In: *Reviews of Modern Physics* 69.3. arXiv: cond-mat/9612179, pp. 731–808. ISSN: 0034-6861, 1539-0756. DOI: 10.1103/RevModPhys.69.731. URL: http://arxiv.org/abs/cond-mat/9612179 (visited on 07/23/2019).

Beth, Richard A. (Jan. 1936). *Mechanical Detection and Measurement of the Angular Momentum of Light*. en. URL: https://www.researchgate.net/publication/220029883_Mechanical_Detection_and_Measurement_of_the_Angular_Momentum_of_Light (visited on 05/27/2019).

Bigot, Laurent (Jan. 2002). "Structure homogène et inhomogène de la transition 4I 13/2 - 4I 15/2 de l'amplificateur à fibre dopée erbium dans des verres d'oxydes, de fluorures et de sulfures". thesis. Lyon 1. URL: http://www.theses.fr/2002LYO10035 (visited on 05/27/2019).

Bigot, Laurent, Guillaume Le Cocq, and Yves Quiquempois (Feb. 2015). "Few-Mode Erbium-Doped Fiber Amplifiers: A Review". EN. In: *Journal of Lightwave Technology* 33.3, pp. 588–596. URL: https://www.osapublishing.org/jlt/abstract.cfm?uri=jlt-33-3-588 (visited on 05/28/2019).

Bigot-Astruc, M. et al. (Mar. 2019). "Weakly-Coupled 6-LP-Mode Fiber with Low Differential Mode Attenuation". EN. In: *Optical Fiber Communication Conference (OFC) 2019 (2019), paper M1E.3*. Optical Society of America, M1E.3. DOI: 10.1364/OFC.2019.M1E.3. URL: https://www.osapublishing.org/abstract.cfm?uri=OFC-2019-M1E.3 (visited on 06/07/2019).

Boyer, K. et al. (Aug. 1996). "Biomedical three–dimensional holographic microimaging at visible, ultraviolet and X–ray wavelengths". en. In: *Nature Medicine* 2.8, pp. 939–941. ISSN: 1078-8956, 1546-170X. DOI: 10.1038/nm0896-939. URL: http://www.nature.com/articles/nm0896-939 (visited on 06/05/2019).

Bozinovic, N. et al. (June 2013). "Terabit-Scale Orbital Angular Momentum Mode Division Multiplexing in Fibers". en. In: *Science* 340.6140, pp. 1545–1548. ISSN: 0036-8075, 1095-9203. DOI: 10.1126/science.1237861. URL: http://www.sciencemag.org/cgi/doi/10.1126/science.1237861 (visited on 06/27/2019).

Brunet, Charles and Leslie Rusch (Oct. 2016). "Optical fibers for the transmission of orbital angular momentum modes". In: *Optical Fiber Technology* 35. DOI: 10.1016/j.yofte.2016.09.016.

Bures, Jacques (2009). *Optique guidée*. fr. URL: https://www.chapitre.com/BOOK/bures-jacques/optique-guidee,22452425.aspx.

Carpenter, J. and T. D. Wilkinson (May 2012). “Characterization of Multimode Fiber by Selective Mode Excitation”. In: *Journal of Lightwave Technology* 30.10, pp. 1386–1392. ISSN: 0733-8724. DOI: `10.1109/JLT.2012.2189756`.

Carpenter, Joel, Benjamin J. Eggleton, and Jochen Schröder (Jan. 2014). “110x110 optical mode transfer matrix inversion”. EN. In: *Optics Express* 22.1, pp. 96–101. ISSN: 1094-4087. DOI: `10.1364/OE.22.000096`. URL: `https://www.osapublishing.org/oe/abstract.cfm?uri=oe-22-1-96` (visited on 06/14/2019).

— (Dec. 2016). “Complete spatiotemporal characterization and optical transfer matrix inversion of a 420 mode fiber”. EN. In: *Optics Letters* 41.23, pp. 5580–5583. ISSN: 1539-4794. DOI: `10.1364/OL.41.005580`. URL: `https://www.osapublishing.org/ol/abstract.cfm?uri=ol-41-23-5580` (visited on 06/14/2019).

Carpenter, Joel and Timothy D. Wilkinson (Mar. 2011). “Holographic Mode-Group Division Multiplexing”. EN. In: *Optical Fiber Communication Conference/National Fiber Optic Engineers Conference 2011 (2011), paper OThN3*. Optical Society of America, OThN3. DOI: `10.1364/OFC.2011.OThN3`. URL: `https://www.osapublishing.org/abstract.cfm?uri=OFC-2011-OThN3` (visited on 06/15/2019).

Cizmar, Tomas and Kishan Dholakia (Sept. 2011). “Shaping the light transmission through a multimode optical fibre: complex transformation analysis and applications in biophotonics”. EN. In: *Optics Express* 19.20, pp. 18871–18884. ISSN: 1094-4087. DOI: `10.1364/OE.19.018871`. URL: `https://www.osapublishing.org/oe/abstract.cfm?uri=oe-19-20-18871` (visited on 07/25/2019).

Coquoz, Olivier et al. (Nov. 1995). “Performances of endoscopic holography with a multicore optical fiber”. EN. In: *Applied Optics* 34.31, pp. 7186–7193. ISSN: 2155-3165. DOI: `10.1364/AO.34.007186`. URL: `https://www.osapublishing.org/ao/abstract.cfm?uri=ao-34-31-7186` (visited on 06/05/2019).

Deng, Yifan et al. (Feb. 2017). “Erbium-doped amplification in circular photonic crystal fiber supporting orbital angular momentum modes”. EN. In: *Applied Optics* 56.6, pp. 1748–1752. ISSN: 2155-3165. DOI: `10.1364/AO.56.001748`. URL: `https://www.osapublishing.org/ao/abstract.cfm?uri=ao-56-6-1748` (visited on 05/28/2019).

Desurvire, E. (Oct. 1990). “Study of the complex atomic susceptibility of erbium-doped fiber amplifiers”. In: *Journal of Lightwave Technology* 8.10, pp. 1517–1527. ISSN: 0733-8724. DOI: `10.1109/50.59191`.

Desurvire, E., J. R. Simpson, and P. C. Becker (Nov. 1987). “High-gain erbium-doped traveling-wave fiber amplifier”. EN. In: *Optics Letters* 12.11, pp. 888–890. ISSN: 1539-4794. DOI: `10.1364/OL.12.000888`. URL: `https://www.osapublishing.org/ol/abstract.cfm?uri=ol-12-11-888` (visited on 01/16/2019).

Digonnet, M. J. F. and C. J. Gaeta (Feb. 1985). “Theoretical analysis of optical fiber laser amplifiers and oscillators”. EN. In: *Applied Optics* 24.3, pp. 333–342. ISSN: 2155-3165. DOI: `10.1364/AO.24.000333`. URL: `https://www.osapublishing.org/ao/abstract.cfm?uri=ao-24-3-333` (visited on 05/28/2019).

Eznaveh, Z. Sanjabi (Mar. 2017). *Ultra-low DMG multimode EDFA - IEEE Conference Publication*. URL: `https://ieeexplore.ieee.org/abstract/document/7937086` (visited on 05/28/2019).

Florentin, R. et al. (Oct. 2018). “Fast Transmission Matrix Measurement of a Multimode Optical Fiber With Common Path Reference”. In: *IEEE Photonics Journal* 10.5, pp. 1–6. ISSN: 1943-0655. DOI: 10.1109/JPHOT.2018.2866681.

Fontaine, Nicolas K. et al. (Mar. 2016). “Multi-mode Optical Fiber Amplifier Supporting over 10 Spatial Modes”. EN. In: *Optical Fiber Communication Conference Postdeadline Papers (2016), paper Th5A.4*. Optical Society of America, Th5A.4. DOI: 10.1364/OFC.2016.Th5A.4. URL: https://www.osapublishing.org/abstract.cfm?uri=OFC-2016-Th5A.4 (visited on 05/28/2019).

Foschini, Gerard J. (Aug. 2002). “Layered space-time architecture for wireless communication in a fading environment when using multi-element antennas”. en. In: *Bell Labs Technical Journal* 1.2, pp. 41–59. ISSN: 10897089. DOI: 10.1002/bltj.2015. URL: http://ieeexplore.ieee.org/lpdocs/epic03/wrapper.htm?arnumber=6770094 (visited on 01/16/2019).

Frignac, Yann (Apr. 2003). “Contribution à l’ingénierie des systèmes de transmission terrestres sur fibre optique utilisant le multiplexage en longueur d’onde de canaux modulés au débit de 40 Gbit/s.” en. In: URL: https://pastel.archives-ouvertes.fr/pastel-00000688 (visited on 05/28/2019).

Gan, Lin et al. (Mar. 2018). “Investigation of channel model for weakly coupled multicore fiber”. EN. In: *Optics Express* 26.5, pp. 5182–5199. ISSN: 1094-4087. DOI: 10.1364/OE.26.005182. URL: https://www.osapublishing.org/oe/abstract.cfm?uri=oe-26-5-5182 (visited on 05/29/2019).

Gaur, Ankita, Gyanendra Kumar, and Vipul Rastogi (Jan. 2018). “Dual-core few mode EDFA for amplification of 20 modes”. en. In: *Optical and Quantum Electronics* 50.2, p. 66. ISSN: 1572-817X. DOI: 10.1007/s11082-018-1322-6. URL: https://doi.org/10.1007/s11082-018-1322-6 (visited on 05/28/2019).

Giles, C.R. and E. Desurvire (Feb. 1991). *Modeling erbium-doped fiber amplifiers - IEEE Journals & Magazine*. URL: https://ieeexplore.ieee.org/document/65886 (visited on 01/16/2019).

Glance, B. (Feb. 1987). “Polarization independent coherent optical receiver”. In: *Journal of Lightwave Technology* 5.2, pp. 274–276. ISSN: 0733-8724. DOI: 10.1109/JLT.1987.1075494. URL: https://ieeexplore.ieee.org/abstract/document/1075494.

Ho, Keang-Po and Joseph M. Kahn (Aug. 2011). “Mode-dependent loss and gain: statistics and effect on mode-division multiplexing”. en. In: *Optics Express* 19.17, p. 16612. ISSN: 1094-4087. DOI: 10.1364/OE.19.016612. URL: https://www.osapublishing.org/oe/abstract.cfm?uri=oe-19-17-16612 (visited on 07/19/2019).

Ingerslev, Kasper et al. (Aug. 2018). “12 mode, WDM, MIMO-free orbital angular momentum transmission”. EN. In: *Optics Express* 26.16, pp. 20225–20232. ISSN: 1094-4087. DOI: 10.1364/OE.26.020225. URL: https://www.osapublishing.org/oe/abstract.cfm?uri=oe-26-16-20225 (visited on 06/27/2019).

Ip, E. (Nov. 2012). “Gain Equalization for Few-Mode Fiber Amplifiers Beyond Two Propagating Mode Groups”. In: *IEEE Photonics Technology Letters* 24.21, pp. 1933–1936. ISSN: 1041-1135. DOI: 10.1109/LPT.2012.2219521.

Ip, Ezra et al. (Sept. 2011). “88x3x112-Gb/s WDM Transmission over 50 km of Three-Mode Fiber with Inline Few Mode Fiber Amplifier”. EN. In: *37th European Conference and Exposition on Optical Communications (2011), paper Th.13.C.2*. Optical Society of America, Th.13.C.2. DOI: 10.1364/ECOC.2011.Th.13.

C.2. URL: https://www.osapublishing.org/abstract.cfm?uri=ECOC-2011-Th.13.C.2 (visited on 05/28/2019).

Ip, Ezra et al. (Feb. 2013). "Few-mode fiber transmission with in-line few-mode erbium-doped fiber amplifier". In: *Next-Generation Optical Communication: Components, Sub-Systems, and Systems II*. Vol. 8647. International Society for Optics and Photonics, p. 864709. DOI: 10.1117/12.2008913. URL: https://www.spiedigitallibrary.org/conference-proceedings-of-spie/8647/864709/Few-mode-fiber-transmission-with-in-line-few-mode-erbium/10.1117/12.2008913.short (visited on 05/28/2019).

Jackson, John David (1998). *Classical Electrodynamics, 3rd Edition*. en-us. URL: https://www.wiley.com/en-us/Classical+Electrodynamics%2C+3rd+Edition-p-9780471309321 (visited on 01/16/2019).

Jacquier, Bernard (June 2012). *Nano-optique du solide*. URL: https://www.lavoisier.fr/livre/physique/nano-optique-du-solide/jacquier/descriptif-9782746219809.

Jin, Cang et al. (Oct. 2013). "Tailored modal gain in a multi-mode erbium-doped fiber amplifier based on engineered ring doping profiles". In: *Photonics North 2013*. Vol. 8915. International Society for Optics and Photonics, 89150A. DOI: 10.1117/12.2033945. URL: https://www.spiedigitallibrary.org/conference-proceedings-of-spie/8915/89150A/Tailored-modal-gain-in-a-multi-mode-erbium-doped-fiber/10.1117/12.2033945.short (visited on 05/28/2019).

Jung, Y. et al. (Dec. 2011). "First demonstration and detailed characterization of a multimode amplifier for space division multiplexed transmission systems". EN. In: *Optics Express* 19.26, B952–B957. ISSN: 1094-4087. DOI: 10.1364/OE.19.00B952. URL: https://www.osapublishing.org/oe/abstract.cfm?uri=oe-19-26-B952 (visited on 05/28/2019).

Jung, Y. et al. (Sept. 2013a). "Few-mode EDFA supporting 5 spatial modes with reconfigurable differential modal gain control". In: *39th European Conference and Exhibition on Optical Communication (ECOC 2013)*, pp. 1–3. DOI: 10.1049/cp.2013.1467.

Jung, Y. et al. (Apr. 2013b). "Three mode Er3+ ring-doped fiber amplifier for mode-division multiplexed transmission". EN. In: *Optics Express* 21.8, pp. 10383–10392. ISSN: 1094-4087. DOI: 10.1364/OE.21.010383. URL: https://www.osapublishing.org/oe/abstract.cfm?uri=oe-21-8-10383 (visited on 05/28/2019).

Jung, Y. et al. (Nov. 2014a). "Cladding pumped few-mode EDFA for mode division multiplexed transmission". EN. In: *Optics Express* 22.23, pp. 29008–29013. ISSN: 1094-4087. DOI: 10.1364/OE.22.029008. URL: https://www.osapublishing.org/oe/abstract.cfm?uri=oe-22-23-29008 (visited on 05/28/2019).

Jung, Y. et al. (June 2014b). "Reconfigurable Modal Gain Control of a Few-Mode EDFA Supporting Six Spatial Modes". In: *IEEE Photonics Technology Letters* 26.11, pp. 1100–1103. ISSN: 1041-1135. DOI: 10.1109/LPT.2014.2315500.

Jung, Y. et al. (Sept. 2017a). "Few Mode Ring-Core Fibre Amplifier for Low Differential Modal Gain". In: *2017 European Conference on Optical Communication (ECOC)*, pp. 1–3. DOI: 10.1109/ECOC.2017.8345893.

Jung, Yongmin et al. (Feb. 2017b). "Optical Orbital Angular Momentum Amplifier Based on an Air-Hole Erbium-Doped Fiber". EN. In: *Journal of Lightwave*

Technology 35.3, pp. 430–436. URL: https://www.osapublishing.org/jlt/abstract.cfm?uri=jlt-35-3-430 (visited on 05/28/2019).

Kang, Qiongyue et al. (Sept. 2012). "Accurate modal gain control in a multimode erbium doped fiber amplifier incorporating ring doping and a simple LP_{01} pump configuration". EN. In: *Optics Express* 20.19, pp. 20835–20843. ISSN: 1094-4087. DOI: 10.1364/OE.20.020835. URL: https://www.osapublishing.org/oe/abstract.cfm?uri=oe-20-19-20835 (visited on 05/28/2019).

Kang, Qiongyue et al. (Mar. 2013). "Design of Four-Mode Erbium Doped Fiber Amplifier with Low Differential Modal Gain for Modal Division Multiplexed Transmissions". EN. In: *Optical Fiber Communication Conference/National Fiber Optic Engineers Conference 2013 (2013), paper OTu3G.3*. Optical Society of America, OTu3G.3. DOI: 10.1364/OFC.2013.OTu3G.3. URL: https://www.osapublishing.org/abstract.cfm?uri=OFC-2013-OTu3G.3 (visited on 05/28/2019).

Kang, Qiongyue et al. (Nov. 2015). "Amplification of 12 OAM Modes in an air-core erbium doped fiber". EN. In: *Optics Express* 23.22, pp. 28341–28348. ISSN: 1094-4087. DOI: 10.1364/OE.23.028341. URL: https://www.osapublishing.org/oe/abstract.cfm?uri=oe-23-22-28341 (visited on 05/28/2019).

Labroille, G. et al. (Sept. 2016). "Multi-Wavelength Multiplexer with Independent Mode Control Based on Multi-Plane Light Conversion". In: *ECOC 2016; 42nd European Conference on Optical Communication*, pp. 1–3.

Le Cocq, Guillaume (Nov. 2014). "Nouvelle génération d'amplificateurs à fibres dopées Erbium : amplificateurs multimodes adaptés aux transmissions multiplexées modalement". thesis. Lille 1. URL: http://www.theses.fr/2014LIL10107 (visited on 05/28/2019).

Le Cocq, Guillaume et al. (Nov. 2012). "Modeling and characterization of a few-mode EDFA supporting four mode groups for mode division multiplexing". EN. In: *Optics Express* 20.24, pp. 27051–27061. ISSN: 1094-4087. DOI: 10.1364/OE.20.027051. URL: https://www.osapublishing.org/oe/abstract.cfm?uri=oe-20-24-27051 (visited on 05/28/2019).

Le Cocq, Guillaume et al. (Dec. 2013). "Few mode Er3+ doped fiber with micro-structured core for mode division multiplexing in the C-band". EN. In: *Optics Express* 21.25, pp. 31646–31659. ISSN: 1094-4087. DOI: 10.1364/OE.21.031646. URL: https://www.osapublishing.org/oe/abstract.cfm?uri=oe-21-25-31646 (visited on 05/28/2019).

Leith, Emmett N., Juris Upatnieks, and Kenneth A. Haines (Aug. 1965). "Microscopy by Wavefront Reconstruction*". EN. In: *JOSA* 55.8, pp. 981–986. DOI: 10.1364/JOSA.55.000981. URL: https://www.osapublishing.org/josa/abstract.cfm?uri=josa-55-8-981 (visited on 06/05/2019).

Li, Cheng and Bingyu Wang (Nov. 2014). "Principal Components Analysis". en. In: p. 6.

Lopez-Galmiche, G. et al. (June 2016). "Few-mode erbium-doped fiber amplifier with photonic lantern for pump spatial mode control". EN. In: *Optics Letters* 41.11, pp. 2588–2591. ISSN: 1539-4794. DOI: 10.1364/OL.41.002588. URL: https://www.osapublishing.org/ol/abstract.cfm?uri=ol-41-11-2588 (visited on 05/28/2019).

Luís, R. S. et al. (Jan. 2016). "Time and Modulation Frequency Dependence of Crosstalk in Homogeneous Multi-Core Fibers". In: *Journal of Lightwave Technology* 34.2, pp. 441–447. ISSN: 0733-8724. DOI: 10.1109/JLT.2015.2474128. URL: https://ieeexplore.ieee.org/abstract/document/7229243.

Macho, Andrés, Maria Morant, and Roberto Llorente (July 2015). "Experimental evaluation of nonlinear crosstalk in multi-core fiber". EN. In: *Optics Express* 23.14, pp. 18712–18720. ISSN: 1094-4087. DOI: `10.1364/OE.23.018712`. URL: `https://www.osapublishing.org/oe/abstract.cfm?uri=oe-23-14-18712` (visited on 05/28/2019).

Martin, Th. and R. Landauer (Jan. 1992). "Wave-packet approach to noise in multichannel mesoscopic systems". In: *Physical Review B* 45.4, pp. 1742–1755. DOI: `10.1103/PhysRevB.45.1742`. URL: `https://link.aps.org/doi/10.1103/PhysRevB.45.1742` (visited on 07/23/2019).

Mears, R. J. et al. (Sept. 1987). "Low-noise erbium-doped fibre amplifier operating at 1.54m". In: *Electronics Letters* 23.19, pp. 1026–1028. ISSN: 0013-5194. DOI: `10.1049/el:19870719`.

Mecozzi, Antonio and René-Jean Essiambre (2012). *Nonlinear Shannon Limit in Pseudolinear Coherent Systems - IEEE Journals & Magazine*. URL: `https://ieeexplore.ieee.org/document/6175093` (visited on 01/16/2019).

Mello, P. A, P Pereyra, and N Kumar (Feb. 1988). "Macroscopic approach to multichannel disordered conductors". In: *Annals of Physics* 181.2, pp. 290–317. ISSN: 0003-4916. DOI: `10.1016/0003-4916(88)90169-8`. URL: `http://www.sciencedirect.com/science/article/pii/0003491688901698` (visited on 07/23/2019).

MIT OpenCourseWare (May 2016). *Singular Value Decomposition (the SVD)*. URL: `https://www.youtube.com/watch?v=mBcLRGuAFUk` (visited on 07/23/2019).

Mitra, P. P. and J. B. Stark (June 2001). "Nonlinear limits to the information capacity of optical fibre communications". eng. In: *Nature* 411.6841, pp. 1027–1030. ISSN: 0028-0836. DOI: `10.1038/35082518`. URL: `https://www.nature.com/articles/35082518`.

Molin, D. et al. (Mar. 2018). "Recent Advances on MMFs for WDM and MDM". In: *2018 Optical Fiber Communications Conference and Exposition (OFC)*, pp. 1–3.

Nicholson, J. W. et al. (May 2008). "Spatially and spectrally resolved imaging of modal content in large-mode-area fibers". EN. In: *Optics Express* 16.10, pp. 7233–7243. ISSN: 1094-4087. DOI: `10.1364/OE.16.007233`. URL: `https://www.osapublishing.org/oe/abstract.cfm?uri=oe-16-10-7233` (visited on 05/28/2019).

Nykolak, G. et al. (Dec. 1991). "An erbium-doped multimode optical fiber amplifier". In: *IEEE Photonics Technology Letters* 3.12, pp. 1079–1081. ISSN: 1041-1135. DOI: `10.1109/68.118007`.

Ono, H. et al. (Jan. 2015). "Improvement of differential modal gain in few-mode fibre amplifier by employing ring-core erbium-doped fibre". en. In: *Electronics Letters* 51.2, pp. 172–173. ISSN: 1350-911X. DOI: `10.1049/el.2014.3411`. URL: `https://digital-library.theiet.org/content/journals/10.1049/el.2014.3411` (visited on 05/28/2019).

Plöschner, Martin, Tomáš Tyc, and Tomáš Čižmár (Aug. 2015). "Seeing through chaos in multimode fibres". en. In: *Nature Photonics* 9.8, pp. 529–535. ISSN: 1749-4885, 1749-4893. DOI: `10.1038/nphoton.2015.112`. URL: `http://www.nature.com/articles/nphoton.2015.112` (visited on 05/31/2019).

Popoff, S. M. et al. (Mar. 2010a). "Measuring the Transmission Matrix in Optics: An Approach to the Study and Control of Light Propagation in Disordered Media". en. In: *Physical Review Letters* 104.10. ISSN: 0031-9007, 1079-7114. DOI: `10.1103/PhysRevLett.104.100601`. URL: `https://link.aps.org/doi/10.1103/PhysRevLett.104.100601` (visited on 06/14/2019).

Popoff, Sébastien (Feb. 2012). “Contrôle spatio-temporel de la lumière en milieux complexes”. en. PhD thesis. (Visited on 06/03/2019).

Popoff, Sébastien et al. (Dec. 2010b). “Image transmission through an opaque material”. en. In: *Nature Communications* 1.1. ISSN: 2041-1723. DOI: 10.1038/ncomms1078. URL: http://www.nature.com/articles/ncomms1078 (visited on 06/14/2019).

Puttnam, B. J. et al. (Sept. 2015). “2.15 Pb/s transmission using a 22 core homogeneous single-mode multi-core fiber and wideband optical comb”. In: *2015 European Conference on Optical Communication (ECOC)*, pp. 1–3. DOI: 10.1109/ECOC.2015.7341685.

Puttnam, B. J. et al. (Sept. 2017). “Inter-Core Crosstalk Spectrum and Penalty Measurements in 7-Core Fiber”. In: *2017 European Conference on Optical Communication (ECOC)*, pp. 1–3. DOI: 10.1109/ECOC.2017.8346241. URL: https://ieeexplore.ieee.org/abstract/document/8346241.

Ramachandran, S. and P. Kristensen (2013). “Optical Vortices in Fiber”. In: DOI: 10.1515/nanoph-2013-0047.

Ramachandran, S., P. Kristensen, and Man F. Yan (Aug. 2009). “Generation and propagation of radially polarizedbeams in optical fibers”. In: DOI: 10.1364/OL.34.002525. URL: https://www.osapublishing.org/DirectPDFAccess/0DF36F40-0718-C76B-67B6598623786205_184799/ol-34-16-2525.pdf?da=1&id=184799&seq=0&mobile=no.

Richardson, D. J., J. M. Fini, and L. E. Nelson (May 2013). “Space-division multiplexing in optical fibres”. en. In: *Nature Photonics* 7.5, pp. 354–362. ISSN: 1749-4893. DOI: 10.1038/nphoton.2013.94. URL: https://www.nature.com/articles/nphoton.2013.94 (visited on 06/23/2019).

Rotter, Stefan and Sylvain Gigan (Mar. 2017). “Light fields in complex media: mesoscopic scattering meets wave control”. en. In: *Reviews of Modern Physics* 89.1. arXiv: 1702.05395, p. 015005. ISSN: 0034-6861, 1539-0756. DOI: 10.1103/RevModPhys.89.015005. URL: http://arxiv.org/abs/1702.05395 (visited on 07/23/2019).

Ryf, R. et al. (Sept. 2011). “Mode-equalized distributed Raman amplification in 137-km few-mode fiber”. In: *2011 37th European Conference and Exhibition on Optical Communication*, pp. 1–3.

Ryf, R. et al. (Sept. 2016). “10-Mode Mode-Multiplexed Transmission with Inline Amplification”. In: *ECOC 2016; 42nd European Conference on Optical Communication*, pp. 1–3.

Salsi, M. et al. (Sept. 2012). “A Six-Mode Erbium-Doped Fiber Amplifier”. EN. In: *European Conference and Exhibition on Optical Communication (2012), paper Th.3.A.6*. Optical Society of America, Th.3.A.6. DOI: 10.1364/ECEOC.2012.Th.3.A.6. URL: https://www.osapublishing.org/abstract.cfm?uri=ECEOC-2012-Th.3.A.6 (visited on 05/28/2019).

Schimpf, D. N., R. A. Barankov, and S. Ramachandran (July 2011). “Cross-correlated C2 imaging of fiber and waveguide modes”. EN. In: *Optics Express* 19.14, pp. 13008–13019. ISSN: 1094-4087. DOI: 10.1364/OE.19.013008. URL: https://www.osapublishing.org/oe/abstract.cfm?uri=oe-19-14-13008 (visited on 05/28/2019).

Simonneau, C. et al. (Sept. 2015). “5-Mode amplifier with low modal crosstalk for spatial mode multiplexing transmission with low signal processing complexity”. In: *2015 European Conference on Optical Communication (ECOC)*, pp. 1–3. DOI: 10.1109/ECOC.2015.7341980.

Sleiffer, V. a. J. M. et al. (Dec. 2012). "73.7 Tb/s (96 x 3 x 256-Gb/s) mode-division-multiplexed DP-16QAM transmission with inline MM-EDFA". EN. In: *Optics Express* 20.26, B428–B438. ISSN: 1094-4087. DOI: 10.1364/OE.20.00B428. URL: https://www.osapublishing.org/oe/abstract.cfm?uri=oe-20-26-B428 (visited on 05/28/2019).

Snyder, Allan W. (Nov. 1972). "Coupled-Mode Theory for Optical Fibers". EN. In: *JOSA* 62.11, pp. 1267–1277. DOI: 10.1364/JOSA.62.001267. URL: https://www.osapublishing.org/josa/abstract.cfm?uri=josa-62-11-1267 (visited on 05/28/2019).

Soma, Daiki et al. (2018). "10.16-Peta-bit/s Dense SDM/WDM Transmission over 6-Mode 19-Core Fiber across the C+L Band". en. In: *Journal of Lightwave Technology*, pp. 1–1. ISSN: 0733-8724, 1558-2213. DOI: 10.1109/JLT.2018.2799380. URL: http://ieeexplore.ieee.org/document/8274947/ (visited on 06/27/2019).

Spellmeyer, N. W. (Oct. 2000). "Communications performance of a multimode EDFA". In: *IEEE Photonics Technology Letters* 12.10, pp. 1337–1339. ISSN: 1041-1135. DOI: 10.1109/68.883822.

Stuart, Howard R. (July 2000). "Dispersive Multiplexing in Multimode Optical Fiber". en. In: *Science* 289.5477, pp. 281–283. ISSN: 0036-8075, 1095-9203. DOI: 10.1126/science.289.5477.281. URL: https://science.sciencemag.org/content/289/5477/281 (visited on 09/02/2019).

Sévigny, Benoit et al. (Dec. 2014). "Advanced S2 Imaging: Application of Multivariate Statistical Analysis to Spatially and Spectrally Resolved Datasets". EN. In: *Journal of Lightwave Technology* 32.23, pp. 4004–4010. URL: https://www.osapublishing.org/jlt/abstract.cfm?uri=jlt-32-23-4004 (visited on 05/28/2019).

Tandjè, A. (Nov. 2019). "Conception et caractérisation de fibres optiques à modes à moment angulaire orbital". PhD thesis. University of lille.

Trinel, Jean-Baptiste (Oct. 2017). "Amplificateurs à fibres dopées erbium légèrement multimodes pour les futurs réseaux de télécommunications". thesis. Lille 1. URL: http://www.theses.fr/2017LIL10094 (visited on 05/27/2019).

Trinel, Jean-Baptiste et al. (Feb. 2018). "Design and characterization of a 10-mode few-mode erbium-doped fiber with multicore pedestal core". In: *Optical Components and Materials XV*. Vol. 10528. International Society for Optics and Photonics, p. 1052813. DOI: 10.1117/12.2290118. URL: https://www.spiedigitallibrary.org/conference-proceedings-of-spie/10528/1052813/Design-and-characterization-of-a-10-mode-few-mode-erbium/10.1117/12.2290118.short (visited on 05/28/2019).

Trischitta, P. et al. (Feb. 1996). "The TAT-12/13 Cable Network". In: *IEEE Communications Magazine* 34.2, pp. 24–28. ISSN: 0163-6804. DOI: 10.1109/35.481240.

Venghaus, Herbert and Norbert Grote, eds. (2017). *Fibre Optic Communication: Key Devices*. en. 2nd ed. Springer Series in Optical Sciences. Springer International Publishing. ISBN: 978-3-319-42365-4. URL: //www.springer.com/fr/book/9783319423654 (visited on 01/16/2019).

Wada, M. et al. (Sept. 2016). "Core-pumped 10-mode EDFA with Cascaded EDF Configuration". In: *ECOC 2016; 42nd European Conference on Optical Communication*, pp. 1–3.

Wakayama, Y. et al. (Sept. 2016). "Novel 6-Mode Fibre Amplifier with Large Erbium-Doped Area for Differential Modal Gain Minimization". In: *ECOC 2016; 42nd European Conference on Optical Communication*, pp. 1–3.

Wakayama, Y. et al. (Sept. 2017). "Dual C+L-Band Six-Mode Optical Amplifier with Widely Erbium-Doped Fibre". In: *2017 European Conference on Optical Communication (ECOC)*, pp. 1–3. DOI: `10.1109/ECOC.2017.8346214`.

Wang, Ning et al. (May 2017). "Erbium-Doped Fiber Amplifier for OAM Modes Using an Annular-Core Photonic Lantern". EN. In: *Conference on Lasers and Electro-Optics (2017), paper STu4K.4*. Optical Society of America, STu4K.4. DOI: `10.1364/CLEO_SI.2017.STu4K.4`. URL: `https://www.osapublishing.org/abstract.cfm?uri=CLEO_SI-2017-STu4K.4` (visited on 05/28/2019).

Weerdenburg, John van et al. (Mar. 2018). "138-Tb/s Mode- and Wavelength-Multiplexed Transmission Over Six-Mode Graded-Index Fiber". EN. In: *Journal of Lightwave Technology* 36.6, pp. 1369–1374. URL: `https://www.osapublishing.org/jlt/abstract.cfm?uri=jlt-36-6-1369` (visited on 06/27/2019).

Winzer, Peter J (2017). "Fiber-optic transmission and networking: the previous 20 and the next 20 years". en. In: p. 50. URL: `https://www.osapublishing.org/oe/abstract.cfm?URI=oe-26-18-24190`.

Yamada, E. et al. (Mar. 2001). "A high SNR, 150 ch supercontinuum CW optical source with precise 25 GHz spacing for 10 Gbit/s DWDM systems". In: *OFC 2001. Optical Fiber Communication Conference and Exhibit. Technical Digest Post-conference Edition (IEEE Cat. 01CH37171)*. Vol. 1, ME2–ME2. DOI: `10.1109/OFC.2001.927838`. URL: `https://ieeexplore.ieee.org/document/927838`.

Yammine, J. et al. (Feb. 2019). "Time-dependence of the transmission matrix of a specialty few-mode fiber". In: *Next-Generation Optical Communication: Components, Sub-Systems, and Systems VIII*. Vol. 10947. International Society for Optics and Photonics, p. 1094702. DOI: `10.1117/12.2508301`. URL: `https://www.spiedigitallibrary.org/conference-proceedings-of-spie/10947/1094702/Time-dependence-of-the-transmission-matrix-of-a-specialty-few/10.1117/12.2508301.short` (visited on 06/21/2019).

Yariv, Amnon (1997). *Optical Electronics in Modern Communications*. en. Oxford University Press. ISBN: 978-0-19-510626-8.

Zhang, Zhenzhen et al. (Apr. 2018). "21 spatial mode erbium-doped fiber amplifier for mode division multiplexing transmission". EN. In: *Optics Letters* 43.7, pp. 1550–1553. ISSN: 1539-4794. DOI: `10.1364/OL.43.001550`. URL: `https://www.osapublishing.org/ol/abstract.cfm?uri=ol-43-7-1550` (visited on 05/28/2019).

Zhao, Ningbo et al. (Mar. 2013). "Few-Mode Fiber Optical Parametric Amplifier". EN. In: *Optical Fiber Communication Conference/National Fiber Optic Engineers Conference 2013 (2013), paper OTu2D.5*. Optical Society of America, OTu2D.5. DOI: `10.1364/OFC.2013.OTu2D.5`. URL: `https://www.osapublishing.org/abstract.cfm?uri=OFC-2013-OTu2D.5` (visited on 05/28/2019).